SISSA - SCUOLA
INTERNAZIONALE
SUPERIORE
DI STUDI AVANZATI
TRIESTE
Strada Costiera 11

ISAS - INTERNATIONAL SCHOOL
FOR ADVANCED STUDIES

A Study of a Sample of Optically Selected AGNs

Thesis submitted to the
International School for Advanced Studies, Trieste, Italy
- Astrophysics Sector -
in partial fulfillment of the requirements for the degree of

Doctor Philosophiæ

Candidate:
Gian Luigi Granato

Supervisors:
Prof. Aldo Treves
Prof. Luigi Danese

Academic Year 1992/93

TRIESTE

Contents

Preface

This PhD thesis collects the results of my research activity as a student at the International School for Advanced Studies (ISAS). I have investigated the properties of a sample of optically selected local Active Galactic Nuclei (AGNs), in practise Seyfert 1 nuclei, with particular interest to the possible role of dust in shaping the continuum radiation.

Seyfert galaxies give important clues on nuclear activity. Besides their relative proximity, the power of their nuclei by definition do not overwhelms that of host galaxies, giving us the opportunity to investigate the links between nuclear activity and the properties of the host. On the other hand, this same circumstance often constitutes a problem in interpreting the data, since the contamination of nuclear observable quantities, due to other galactic components, is not negligible, especially in optical and infrared bands. Part of my activity has been devoted to the development of analysis methods to reliably separate the nuclear and galactic emission in these bands. These techniques, as well as the results obtained by using them, are presented and discussed in Chapters 1, 2 and 3, which are adapted versions of three papers recently published in collaboration with other authors (Zitelli et al. 1993, Danese et al. 1992, Granato et al. 1993). Chapter 4 is devoted to the computation of the optical, near infrared and 12 μm luminosity function of Seyfert 1 nuclei. The effects of the use of nuclear magnitudes, as opposed to integrated ones, are considered. Finally, in Chapter 5 I present detailed calculations of the 0.1 to 100 μm Spectral Energy Distributions for the case of AGNs surrounded by optically thick and thin dust torii. The results are compared to the observed spectra of our sample nuclei and discussed in the context of unified schemes for broad and narrow–line AGNs.

All the quantities reported in this thesis have been normalized to $H_o = 50$ km s^{-1} Mpc^{-1} and $q_0 = 0.5$ whenever necessary.

To my wife Chiara and my parents Grazia Maria and Giorgio

Chapter 1

Near–IR: Observations

Summary. We[1] present IR observations of a homogeneous sample of Seyfert 1 galaxies, that we also observed with CCDs in optical bands (Chapter 3). We have K band frames for 41 objects, and JHKL photometry for 27 of these with the UK Infrared Telescope. Methods of separating the galaxian and nuclear fluxes are presented and discussed. The nuclear and galaxian K magnitudes are derived with their errors. The frequent presence of large bulge components suggests that the host galaxies are early type spirals or S0's.

1.1 Introduction

In the last few years the astronomical detectors in the near IR bands have been remarkably improving both in sensitivity as well as in spatial resolution, approaching the performances of the optical CCDs. As for studies of AGNs, these improvements allow much better measurements of IR nuclear fluxes after reliable subtraction of the galaxy contributions. Nevertheless the origin of the IR emission of the AGNs is still debated. In particular the importance of thermal dust reradiation is still an open question.

Many authors pointed out the role of dust in shaping the continuum emission (Rieke 1978; Lawrence and Elvis 1982; Cheng et al. 1983; Lawrence

[1]This Chapter is based on a paper published in collaboration with V. Zitelli, N. Mandolesi, R. Wade and L. Danese (Zitelli et al. 1993)

et al. 1985; Ward et al. 1987) as well as in determining the emission-line ratios and polarization (Wampler 1971; De Zotti and Gaskell 1985; Antonucci and Miller 1985; Ward et al. 1987; Dahari and De Robertis 1988; Berriman 1989).

The presence of a bump around 3.5–5 μm in several AGNs has been noticed by many authors (see e.g. Neugebauer et al. 1979; Edelson and Malkan 1986; Edelson et al. 1987). Barvainis (1987) proposed a model which naturally explains the bump in the near IR with reradiation by dust heated to the evaporation temperature by primary optical and ultraviolet continuum emissions; more recently, the same author has successfully fitted with this model the spectral energy distributions (SEDs) of 11 radio-quiet QSOs from 0.3 to 100 μm (Barvainis 1990).

Sanders et al. (1989) claimed that the SEDs of 109 bright QSOs of the Palomar-Green survey usually exhibit a minimum at around 1 μm. They concluded that dust heated to the sublimation temperature can account for the observed spectra and suggested that the absorbing material is distributed in a warped disc.

In the above mentioned studies the contribution to the far-IR emission from the host galaxies is either neglected, or it enters as an uncertain parameter in fitting the SEDs. However in the IR band the contributions of the host galaxies are often relevant, even in the case of QSOs observed with small apertures. The determination of truly nuclear fluxes of a well defined and statistically significant sample of AGNs is extremely important, when discussing the possible emission mechanisms operating in the IR bands.

Cheng et al. (1985) have defined a sample of Seyfert 1 and 1.5 galaxies, from which they derived the luminosity function of low luminosity AGNs. This optical luminosity function matches remarkably well with that of optically selected QSOs and it also compares favorably with the local luminosity function of X-ray selected active galactic nuclei. Moreover about 70% of the sample objects have been detected in one of the IRAS bands and the same percentage has been detected also in radio. X-ray observations allow the computation of 2 keV fluxes for about 60% of the objects.

It is therefore quite informative to investigate the IR properties of this well defined sample of faint active galactic nuclei harbored in Seyfert 1 galaxies with techniques which allow a reliable separation of the emissions of nuclei and of galaxies. In this Chapter we will present the observations obtained with the UK Infrared Telescope (UKIRT) using both photoelectric photometer and imaging camera. Particular attention will be paid to the discussion of the method of deriving nuclear and galaxian fluxes from the

camera images. Chapter 2 is devoted to analysis and interpretations of the results. We have also obtained optical CCD frames of the same objects; the results are presented in Chapter 3.

1.2 Observations

The sample of Cheng et al. (1985, see also Chapter 4) comprises 56 AGNs in the area covered by the first nine Markarian lists, with the restrictions $U \leq 16.3$, $M_u \leq -18.5$ and $z \leq 0.08$. It has been shown that there is no significant correlation of the apparent magnitudes with the absolute magnitudes, or with the ratios of the fluxes of the nuclei to those of the underlying galaxies. The probability for an objects to be included in the sample depends solely on its apparent magnitude. Such a sample is *homogeneous*, following the definition of Neyman & Scott (1961, 1974).

We observed 45 objects, with the photoelectric photometer and/or with the IR camera on the 3.8 m UK Infrared Telescope at Mauna Kea. One of these (Tol 1059+105), however, does not belong to the homogeneous sample. The images of two objects (Mrk 124 and Mrk 595) could not be calibrated because of lack of photometric data. In the following analysis, we will deal with the remaining 42 objects. For all but one of them (Mrk 142) we got a K-band image.

1.2.1 IR photometry

Our photoelectric data were obtained using the photometer UKT9 in two nights in April and UKT6 in two nights in August 1987. We observed the galaxies in the J H K L' bands using 5″ and 7.8″ apertures. In order to avoid contributions from the galaxy to the sky-observation we used a focal-plane chopper giving a beam throw of 40 arcsec in R.A. Each observation was usually stopped when the statistics of the measurements gave estimated errors of the mean smaller than 0.02 magnitudes. This precision was generally reached with 10-20 couples (object plus sky) of 5 seconds exposures. When the error of the mean remained larger than 0.02 after 30 couples, then we stopped the observation. Anyway, even in these few cases errors of the mean ≤ 0.03 mag were achieved. The observed standard stars were selected from the available lists defined on the UKIRT system. The photoelectric data were reduced in Edinburgh using the local facilities.

We observed 27 objects from the sample of Cheng et al. (1985), plus Tol 1059+105. No IR image was obtained for one of them (Mrk 142).

Name	z	E_{B-V}	J(5″)	H(5″)	K(5″)	L(5″)	J(7.8″)	H(7.8″)	K(7.8″)	L(7.8″)	Date (87)
(1)	(2)	(3)	(4)	(5)	(6)	(7)	(8)	(9)	(10)	(11)	(12)
0048+29	.036	.00	12.99	12.16	11.61	10.90	12.74	11.98	11.48	10.70	Aug 16
2237+07	.025	.00	13.05	12.12	11.44	10.35	12.70	11.91	11.32	10.24	Aug 16
II Zw 1	.054	.01	14.25	13.45	12.69	11.34	13.85	13.05	12.40	11.09	Aug 16
II Zw 136	.062	.03	13.38	12.42	11.27	9.57	13.22	12.25	11.14	9.34	Aug 15
Mrk 9	.040	.03	12.95	12.00	10.86	8.77	12.87	11.93	10.81	...	Apr 5
Mrk 110	.036	.01	13.67	13.02	11.93	10.10	13.48	12.68	11.72	9.97	Apr 4
Mrk 142	.045	.00	14.16	13.31	12.49	11.39	...	...	...	...	Apr 5
Mrk 290	.031	.01	13.26	12.56	11.76	10.04	13.16	12.45	11.62	...	Apr 4
Mrk 304	.067	.05	13.39	12.60	11.68	10.09	13.20	12.42	11.55	10.11	Aug 16
Mrk 374	.044	.08	13.31	12.61	11.94	10.44	...	...	...	...	Apr 5
Mrk 376	.056	.09	12.84	11.95	10.76	8.85	...	...	10.76	...	Apr 5
Mrk 382	.034	.04	13.85	13.29	12.77	11.91	13.81	13.11	12.65	11.64	Apr 4
Mrk 464	.051	.00	14.31	13.65	12.94	11.12	...	13.59	12.69	...	Apr 4
Mrk 478	.079	.00	12.84	11.90	10.88	9.37	...	...	10.94	...	Apr 4
Mrk 478	.079	.00	12.93	12.05	10.98	9.42	...	...	10.93	...	Apr 5
Mrk 486	.039	.01	13.05	12.25	11.16	...	...	...	...	...	Apr 4
Mrk 506	.043	.03	13.58	12.71	11.97	10.52	13.26	12.44	11.79	10.52	Aug 15
Mrk 509	.036	.04	12.03	11.15	10.20	8.58	11.89	11.05	10.14	8.52	Aug 15
Mrk 530	.029	.03	12.46	11.61	10.89	9.35	12.12	11.29	10.63	9.29	Aug 15
Mrk 584	.078	.00	...	...	...	...	13.92	13.19	12.60	12.33	Aug 16
Mrk 634	.066	.00	14.30	13.37	12.65	11.35	...	...	12.55	...	Apr 5
Mrk 704	.029	.01	12.95	12.10	10.91	8.91	12.68	11.80	10.76	...	Apr 4
Mrk 705	.028	.01	12.77	11.95	11.23	9.84	...	...	11.15	...	Apr 5
Mrk 739	.030	.00	13.46	12.41	11.38	...	12.88	12.02	11.13	9.52	Apr 4
Mrk 783	.067	.01	...	...	13.68	...	14.73	14.04	13.40	13.04	Apr 4
Mrk 845	.046	.01	13.59	12.87	12.38	11.49	...	...	12.01	...	Apr 5
Mrk 975	.050	.04	13.38	12.33	11.34	9.54	13.07	12.12	11.20	9.56	Aug 15
NGC 5940 ...	.034	.00	13.44	12.66	11.88	10.65	...	...	11.75	...	Apr 5
Tol 1059+105	.034	.00	14.50	13.84	13.39	12.18	...	...	13.19	...	Apr 5

Table 1.1: Observed near–infrared magnitudes

The data, corrected for galactic extinction, using the values of $E(B-V)$ listed by Cheng et al. (1985), are reported in Table 1.1. We have obtained JHKL photometry with at least one aperture for all objects except Mrk 486 which is lacking only L-band observations; 15 galaxies were observed with two apertures at least in JHK bands, and 11 of them also in the L band; one galaxy has two-aperture photometry in J and K bands; 8 galaxies only in the K band. Repeated observations of standard stars throughout a single night have rms ≤ 0.03 magnitudes in JHK bands. Moreover we have observed several standards in different nights during the same run (on April and August 1987) and we have found that the measurements exhibit standard deviations not exceeding the values found troughout single night. Thus we can estimate that the typical internal photometric errors are about 0.03 magnitudes in JHK bands. On the other hand we have found rms ≤ 0.1 in the L band. We have used the absolute calibrations proposed by Campins et al. (1985) and have reduced other authors' data to the same system whenever possible.

One object (Mrk 478) has been observed on two different nights, since in the first observation we found a larger flux within the smaller aperture in the K band. This happened once in a set of 25 double aperture measurements in the K band. We got a difference of 0.1 mag (i.e. about 10% in fluxes) in the observations with the $5''$ aperture, while the difference reduces to only 0.01 mag in the case of $7.8''$ aperture. This suggests the possibility that the photometric errors are larger for observations done with the smaller aperture. On the other hand the observations of the standards do not support this hypothesis. No significant variations and trends have been found in the standards changing aperture. Fortunately Mrk 478 has been observed by Neugebauer et al. (1987) in different epochs with a $5.5''$ aperture and with typical quoted errors $\Delta m \leq 0.07$. There is no evidence of variability in their data. Our measurements redone in April 5 are in good agreement with theirs, the differences being $\Delta J \simeq 0.07$, $\Delta H \simeq 0.02$, and $\Delta K \simeq 0.05$. In the following only the data taken on april 5 have been used for Mrk 478.

We have three more objects in common with the sample of Neugebauer et al. (1987). They have done one measurement of the J, H and K fluxes of Mrk 290; the differences are also in this case within the quoted errors $\Delta J \simeq 0.09$, $\Delta H \simeq 0.03$, and $\Delta K \simeq 0.10$. In the other two cases, Mrk 486 and II ZW 136, their data taken at different epochs show that the fluxes significantly changed with the time.

The comparison among data collected in different epochs is hampered mainly by time variability and seeing. Systematic differences are also added

by use of different photometric systems, and of different apertures. When dealing with observations performed with different apertures, we took into account the host galaxy contribution, by the use of the mean growth curves for early type spirals proposed by Griersmith et al. (1982). The corrections amount to few hundredths of magnitude, if we limit the comparison to data taken with small apertures.

We have found in the literature JHK photometry with apertures ranging from 7.5″ to 9″ for ten objects of our samples. The average magnitude difference in the K band is $\Delta K = 0.03 \pm 0.13$ (s.d.) and similar values are obtained for ΔJ and ΔH.

The comparison of K band fluxes of objects observed in different epochs by Glass (1981), McAlary et al. (1983), Edelson, Malkan and Rieke (1987) and by Simons et al. (1988) shows that differences of 0.1-0.2 magnitudes are quite common. Time variability is the most probable explanation. For instance flux variations of 10-20% are present in observations done by the same authors at different times (see e.g. Neugebauer et al. 1987). Therefore it is not surprising that the comparison of results of different authors usually show flux differences larger than the errors quoted by the authors themselves.

Taking into account of possible problems in pointing and guiding the telescope we conclude that 0.06 mag is a reliable estimate of our photometric errors.

It is also worth noticing that in our case the time elapsed between the observations of each object with both apertures was always shorter than 30 minutes. Therefore possible seeing variations are minimized.

1.2.2 K-band Imaging with IRCAM

As already mentioned, high resolution K band images have been obtained on January and on July 1988 with the IRCAM system (McLean et al. 1986) for 43 galaxies from the Cheng et al. (1985) sample; two of them, however, could not be calibrated and will not be considered further. We selected the high resolution mode with a scale of 0.62″/pixel, to obtain detailed maps of the innermost regions. This choice has the drawback that the images of the nearest objects extend over a large fraction of the available pixels (62×58), complicating the background subtraction, which is particularly subject to errors in the outer regions. Particular attention has been devoted to obtain a good dynamic range and a reliable background subtraction.

Bias and dark frames must be subtracted from IRCAM astronomical images. We have repeatedly taken bias frames during the night and we have

used them for the subtraction. Dark frames with exposure time equal to the integration time of the astronomical images have been taken and used for dark subtraction.

Observations of standard stars were done just before the observation of a galaxy of our sample. Then the integration on the astronomical object were done, with exposure times ranging from 20 to 40 seconds and total integration times ranging from 300 to 900 seconds. Afterwards sky frames with the same integration time were taken with an offset of about 60″ from the nucleus of the galaxy, in regions with no apparent object.

The sky frames were bias and dark subtracted and then used as flat–fields for the galaxy images. The image reduction package MIDAS has been used to produce the final images. The removal of bad pixels has been done interactively, by replacing the pixel value with that interpolated from adjacent pixels.

To determine the background level, we usually choose 4 boxes widely spaced (one in each quadrant of the astronomical frame) of at least 30 pixels each in regions away from the galaxy, but possibly not just in the outermost areas of the frame. The boxes were selected interactively on the images produced by the image reduction package MIDAS, after bias and dark subtraction and division by flat field. The distributions of the pixel values are usually narrow with standard deviations that are on average 4×10^{-4} relative to the means, implying a remarkable uniformity of the sky background. The background level ranges from 12.13 to 13.22 mag arcsec^{-2}, with a median of 12.6 mag arcsec^{-2}. This value is in agreement with the estimate of Cowie et al. (1990). On January 27th 1988 the median was 12.9 mag arcsec^{-2}, while on July 3th it was 12.4 mag arcsec^{-2}.

Our capability of reliably tracing the outer parts of the intensity profiles depends on the precision in estimating the background intensity. The background evaluation is hampered by our small field of view (36″), at least for objects with redshift $z \leq 0.03$. Not surprisingly the worst case is that of Mrk 766, the nearest object, for which we likely were not able to find in the frame regions free from significant contamination by the hosting galaxy. As a result the background intensity has a higher rms $\simeq 2 \times 10^{-2}$ relative to the mean.

For NGC 5548 (z=0.019) we have a mosaic of 4 frames each with the nucleus in a corner, in addition to the usual nucleus centered frame. We checked that the differences of surface brightness between the regions we used to determine the background in the latter frame and regions up to 40″ (corresponding to 22 kpc) away from the nucleus, are well within our

estimate of the error on the background level.

A further example is given by NGC 5940 (z=0.034). In this case we have got a frame with the nucleus in the center and a second one with the nucleus in a corner. Even in this case the differences of surface brightness of regions far from the nucleus 20 and 40 arcsec respectively are within the errors. However in this case 1″ corresponds to 1 kpc. It is worth noticing that only 7 objects in our sample are at $z \leq 0.025$ and only 3 at $z \leq 0.022$.

Skrutskie, Shure and Beckwith (1985) have done accurate K photometry along the major axis of 3 spiral galaxies. They have found that in two cases the K surface brightness at distance from the the center $r \geq 10$ kpc is $\mu_K \geq 22$ mag arcsec^{-2}, and in one case $\mu_K \geq 22$ mag arcsec^{-2} only at $r \geq 25$ kpc. They also found that the colors tend to be bluer in the outermost regions. Giovanardi and Hunt (1988) observed 7 Sa-Sb galaxies along the major axis in JHK bands. Their results are consistent with $\mu_K \geq 21.5$ mag arcsec^{-2} at $r \geq 15$ kpc.

The above findings suggest that at least for frames of objects at $z \geq 0.030$ systematic errors in the background due to the small field of view should not severely affect the estimates of the integrated galactic magnitudes. Actually for the 31 objects with $z \geq 0.030$ there is no correlation between redshift and disc scale. For the nearest objects the interactive choice of the regions for background subtraction is useful in avoiding large errors, as the case of NGC 5548 demonstrates. On the other hand the situation of Mrk 766 is likely to be representative for objects at $z \leq 0.020$.

The data on individual pixels have been reduced to intensity profiles with the aim of increasing the signal to noise ratio in the outer regions and to smooth out small scale irregularities. The radial intensity profiles have been computed from the two-dimensional images, properly averaging the intensity in concentric rings, and the surface brightness μ (mag arcsec^{-2}) have been reported in Table 1.5.

The center of the galaxy is determined by the use of the first moment of the brightness distribution on a 20×20 pixels grid around the brightest one. The rings are spaced by 1 pixel, i.e. by 0.62 arcsec. The brightness in a ring is the sum of the contributions from the individual pixels weighted by the area in common between the ring and the pixels. Of course an accurate weighting procedure is extremely important in the central regions of the objects, where the pixel size is comparable to the scale of a significant variation of the intensity profile.

The errors $\delta\mu$ quoted in Table 1.5 are comprehensive of the photon noise, of the read-out noise of the detectors, and of the uncertainty in the back-

ground subtraction.

The small errors of the surface brightness in external regions of some objects in Table 1.5 (e.g. IIZW 136, Mrk 79, Mrk 374, Mrk 739) are the consequence of the uniformity of the sky background.

In Fig. 1.1 we have reported three examples of the surface brightness intensity profiles with the computed errors. It is apparent that the seeing is a major problem in our observations. In fact, despite of the widely recognized good atmospheric seeing on Mauna Kea, the average *total* seeing during our observations was about 1.6″ (FWHM) mainly due to the optical alignment of the telescope at the time of the observations.

We checked that the seeing profile of our standard stars is well reproduced by a double gaussian PSF,

$$I(r) = \frac{F_T}{2\pi\sigma^2(1+as^2)}\left[\exp\left(\frac{-r^2}{2\sigma^2}\right) + a\exp\left(\frac{-r^2}{2s^2\sigma^2}\right)\right] \qquad (1.1)$$

where F_T is the total flux of the star and σ is the standard deviation of the main gaussian, a and s are the ratios of the central peaks and of the standard deviations of the two gaussians, respectively (Granato 1988). As for the last two parameters, the profiles of the standard stars gave almost constant values, $a \simeq 0.05$ and $s \simeq 2.2$ respectively. We assumed that the intensity profiles of the active nuclei are described by the above formula.

1.3 Data Analysis

Our primary aim in analyzing the K-band imaging data is to obtain reliable nuclear fluxes. Secondarily we are interested in the main characteristics of the galaxies hosting the AGNs, such as their total luminosity, and, possibly, the relative importance of the bulge and the disk components. The photometric data will be used to derive nuclear fluxes by independent methods, as a check for the results obtained by the analysis of the frames.

1.3.1 Analysis of the Imaging Data

To separate the nuclear from the galactic fluxes, a model for the profile of the host galaxies is needed. A first general assumption is that the host galaxies are *regular* galaxies, with bulge and disc. Of course this is an oversimplification of the real situation. In the CCD frames of our objects complex structures like rings or disturbances frequently show up. Similar

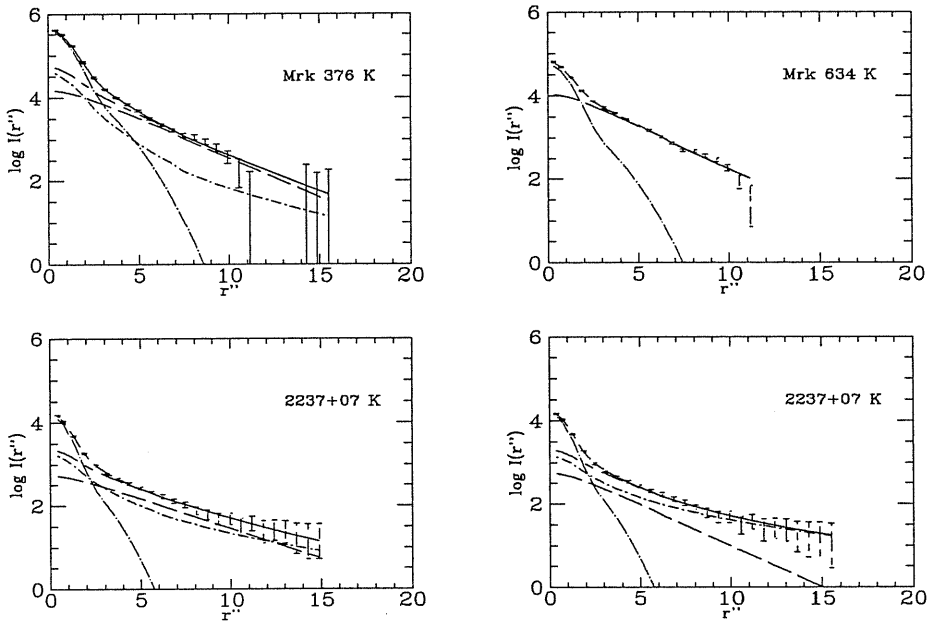

Figure 1.1: Intensity profile data (arbitrary units) and fits for three objects. The global best fit (solid lines), the nuclear (dotted long dashed), the bulge (dotted dashed), and disc profiles (dashed) are reported. As for 2237+07, the best-fit is shown in the lower left panel, while in the lower right panel we have reported a fit obtained fixing the disc scale length to a value lower than the best-fit one by about 30%, and minimizing the χ^2 with respect to the other 4 free parameters. Both the nuclear and galactic luminosities computed from the two fits differ by no more than a few percent.

features have been noticed also by other authors (Dahari 1985; MacKenty 1990). However it is reasonable to assume that these structures do not contribute significantly to the total luminosity of the host galaxies. Moreover the procedure of averaging the surface brightness over concentric rings largely smoothes out irregularities and weakens their influence in the determination of the fluxes of galaxies and nuclei. The most intriguing possibility is the presence of a bar, although Kent (1985) has cast some doubt on the possibility of discriminating between the presence of a bar or of a bulge on the basis of the intensity profiles.

A second assumption is that the thickness of the galaxies is negligible and that the surface brightness is symmetric with respect to the central axis perpendicular to the galactic plane. This is equivalent to assume that the isophotes are concentric circles on the galactic plane. The isophotes of a galaxy tilted by an angle i with respect to the line of sight become concentric ellipses with axial ratio $\epsilon = b/a = \sin i$.

We have represented the intrinsic intensity profile of the host galaxies as the sum of a bulge following the $r^{1/4}$ law and an exponential disc:

$$I_b(r) = I_e \exp\left[-3.33 \ln 10 \left(\left(\frac{r}{r_e}\right)^{1/4} - 1\right)\right] \tag{1.2}$$

$$I_D(r) = I_D \exp\left(-\frac{r}{r_D}\right) \tag{1.3}$$

where r_e is the effective radius, which encloses half of the total light of the bulge, I_e is the surface brightness at r_e, and r_D is the scale length, I_D the central surface brightness of the disc. By adding the nuclear total flux F_n, we get a model of Seyfert galaxies fully described by 5 parameters.

To compare the model to the intensity profiles obtained from the observations, we must properly take into account the effects of seeing and of inclination of the galaxian planes with respect to the line of sight (Granato 1988). The seeing profile of the nucleus is given by Eq. 1.1, where F_T must be replaced by F_n. The problem is more complex for the hosting galaxy. Using the PSF given by Eq. 1.1 and introducing a cartesian reference frame with x axis defined by the intersection of the plane of the sky with that of the galaxy, z axis directed along the line of sight and y axis in the plane of the sky, the expected surface brightness of a hosting galaxy at a point (x, y) in the sky is given by,

$$I_{obs}(x,y) = \frac{1}{2\pi\sigma^2(1+as^2)\epsilon} \times \tag{1.4}$$
$$\times \int\int_{-\infty}^{\infty} I(r') \left[\exp\left(-\frac{\rho'^2}{2\sigma^2}\right) + a\exp\left(-\frac{\rho'^2}{2s^2\sigma^2}\right)\right] dx'dy'$$

where $\rho'^2 = (x-x')^2 + (y-y')^2$, and $r' = \left(x'^2 + (y'/\epsilon)^2\right)^{1/2}$. The surface brightness is then integrated to obtain the expected intensity profile. In such a way we reduce the dimensionality of the problem, significantly decreasing the required computing time. On the other hand we do not completely loose the bidimensional information, and we increase the signal to noise ratio in the outer regions. The symmetry of the problem allows us to compute the expected surface brightness in only one quadrant.

In spite of these simplifications, the computing time needed to take into account for the seeing effect would still be huge. On the other hand the relevance of the effect strongly decreases in regions with relatively shallow gradient of the surface brightness. We have checked that with our typical observational conditions, the seeing effect on the galactic component is negligible at distances from the center $r \geq 8\sigma$. As for the inner regions, we computed the surface brightness in 100 points of the quadrant, distributed in an appropriate way, and used this 10 by 10 array in the x–y plane to interpolate the values required to calculate the intensity profile of the galaxy. Finally the nuclear and galaxian profiles are added together to obtain the expected global intensity profile. The galaxy inclinations have been determined from the axial ratios of the outermost isophotes in R CCD frames.

The best fit parameters have been obtained by χ^2 minimizations. The initial values of the parameters have been selected using tentative fits by eye. Then the final parameters have been computed using the subroutine MRQMIN described by Press et al. (1986). The typical computing time was about 1 hour on a VAX 8530. In Table 1.2 we have reported for each observed object the best fit values of the parameters, the seeing during the observing time and the axial ratio b/a.

To accurately determine the luminosities of nuclei and galactic bulges it is essential to have a good seeing and a good sampling of the PSF. A reliable estimate of the background is necessary to derive the disc parameters. These conditions are not all always fulfilled by our data. When the intensity profile at small radii is strongly dominated by the PSF of the nucleus, we usually can get a good determination of the nuclear flux, but the information on

Name	z	E_{B-V}	b/a	σ	μ_e	r_e	μ_D	r_D	μ_n	Date
				sec	$\frac{mag}{sec^2}$	kpc	$\frac{mag}{sec^2}$	kpc	$\frac{mag}{sec^2}$	1988
(1)	(2)	(3)	(4)	(5)	(6)	(7)	(8)	(9)	(10)	(11)
0048+29 ..	.036	.00	.80	.93	17.97	3.33	16.86	2.68	14.09	Jul 1
2237+07 ..	.025	.00	.90	.72	18.89	3.65	16.63	2.24	13.27	Jul 2
I Zw 1	.061	.03	.88	.65	16.91	4.83	17.00	3.18	11.35	Jul 1
II Zw 1 ...	.054	.01	.67	.60	17.19	1.99	17.50	6.35	14.88	Jul 3
II Zw 136 .	.062	.03	.50	.63	19.51	7.13	16.55	3.40	12.55	Jul 1
Mrk 009 ..	.040	.03	.90	.93	...	...	15.87	3.42	13.00	Jan 27
Mrk 079 ..	.022	.06	.57	.95	17.78	2.41	18.26	6.27	13.23	Jan 27
Mrk 110* .	.036	.01	.83	.85	17.73	2.39	18.96	27.06	14.17	Jan 27
Mrk 290 ..	.031	.01	.99	.65	16.27	.89	17.97	4.98	13.35	Jul 3
Mrk 304 ..	.067	.05	.95	.80	17.25	3.15	17.95	5.93	13.55	Jul 1
Mrk 335 ..	.025	.03	.90	.75	13.62	.35	16.42	2.31	11.54	Jul 1
Mrk 352 ..	.025	.03	.65	.66	17.76	.67	17.05	1.65	13.64	Jul 3
Mrk 359 ..	.017	.01	.68	.65	17.27	1.35	16.48	2.03	13.53	Jul 3
Mrk 374 ..	.044	.08	.64	.95	23.57	.60	16.17	4.07	14.34	Jan 27
Mrk 376 ..	.056	.09	.99	.88	16.20	1.60	15.93	3.46	12.74	Jan 27
Mrk 382 ..	.034	.04	.86	.97	...	...	16.71	2.16	15.16	Jan 27
Mrk 464* .	.051	.00	.79	.60	16.94	1.32	21.19	19.44	14.49	Jul 3
Mrk 478 ..	.079	.00	.85	.68	16.73	3.58	18.07	6.17	12.40	Jul 1
Mrk 486* .	.039	.01	.63	.60	20.64	9.93	13.75	.53	12.46	Jul 3
Mrk 493 ..	.031	.00	.83	.60	17.05	1.83	18.30	5.53	13.69	Jul 2
Mrk 504 ..	.036	.03	.44	.60	18.05	2.64	18.52	5.64	15.28	Jul 3
Mrk 506 ..	.043	.03	.95	.62	17.31	2.04	17.37	8.57	13.56	Jul 2
Mrk 509 ..	.036	.04	.85	.78	16.19	1.96	17.45	11.69	12.08	Jul 1
Mrk 530 ..	.029	.03	.80	.85	15.64	1.34	15.62	2.91	13.77	Jul 1
Mrk 584 ..	.078	.00	.80	.60	16.68	1.73	16.82	6.61	15.76	Jul 3
Mrk 618 ..	.034	.05	.60	1.00	19.96	1.50	17.18	5.35	13.69	Jan 27
Mrk 634 ..	.066	.00	.67	.85	...	...	16.61	4.35	14.99	Jan 27
Mrk 704 ..	.029	.01	.57	.90	19.16	2.86	16.48	2.77	13.02	Jan 27
Mrk 705* .	.028	.01	.74	.85	24.99	78	15.06	1.31	13.34	Jan 27
Mrk 734 ..	.050	.01	.80	.85	...	...	15.92	2.62	13.77	Jan 27
Mrk 739 ..	.030	.00	.58	.90	...	...	15.81	3.61	13.76	Jan 27
Mrk 766* .	.013	.01	.80	.70	17.71	1.26	15.46	1.12	12.66	Jul 1
Mrk 771 ..	.064	.02	.70	.80	16.80	3.82	18.37	6.76	14.40	Jul 1
Mrk 783* .	.067	.01	.75	.65	20.56	5.41	16.53	1.62	15.27	Jul 2
Mrk 817 ..	.032	.01	.80	.60	13.13	.44	16.25	4.10	12.18	Jul 3
Mrk 841 ..	.036	.00	.95	.64	18.32	5.86	14.52	.49	12.71	Jul 2
Mrk 845 ..	.046	.01	.14	.65	20.38	3.17	16.90	6.30	14.71	Jul 2
Mrk 871 ..	.034	.03	.57	.68	15.13	.74	16.18	4.00	13.80	Jul 1
Mrk 975 ..	.050	.04	.61	.67	17.75	3.06	17.43	6.56	12.92	Jul 3
NGC 5548	.019	.00	.90	.65	16.18	.97	15.34	1.89	11.82	Jul 3
NGC 5940*	.034	.00	1.00	.68	21.13	36.93	17.61	2.46	13.68	Jul 3

Table 1.2: Derived fitting parameters. Asterisks denote objects with no reliable estimates of the galactic magnitudes.

Name (1)	K_n (2)	δK_n (3)	K_g (4)	δK_g (5)	$K_g(20)$ (6)	$\delta K_g(20)$ (7)
0048+29 .	12.15	.27	11.50	.24	11.57	.23
2237+07 .	11.83	.23	11.30	.24	11.37	.23
I Zw 1 ...	10.20	.22	11.02	.45	11.06	.46
II Zw 1 ...	13.77	.32	11.85	.20	11.90	.18
II Zw 136	11.49	.23	12.19	.42	12.25	.44
Mrk 9	11.03	.21	11.38	.33	11.40	.34
Mrk 79 ...	11.19	.23	10.57	.37	10.94	.26
Mrk 110 ..	12.33	.24	...	...	...	...
Mrk 290 ..	12.06	.29	11.66	.37	11.77	.34
Mrk 304 ..	12.00	.24	12.11	.31	12.16	.33
Mrk 335 ..	10.04	.30	11.02	.60	11.04	.61
Mrk 352 ..	12.42	.29	11.77	.24	11.82	.24
Mrk 359 ..	12.35	.24	10.74	.18	10.80	.18
Mrk 374 ..	12.30	.23	11.48	.22	11.53	.21
Mrk 376 ..	11.07	.24	11.58	.42	11.81	.57
Mrk 382 ..	13.16	.29	12.89	.28	12.90	.28
Mrk 464 ..	13.35	.27	...	...	...	...
Mrk 478 ..	11.28	.23	11.88	.42	11.90	.43
Mrk 486 ..	11.39	.23	...	...	...	...
Mrk 493 ..	12.69	.27	11.36	.23	11.48	.20
Mrk 504 ..	14.27	.68	11.86	.23	11.98	.18
Mrk 506 ..	12.55	.28	10.82	.42	11.08	.32
Mrk 509 ..	10.50	.23	9.79	.47	10.31	.31
Mrk 530 ..	11.99	.34	10.20	.18	10.24	.18
Mrk 584 ..	14.71	.74	11.94	.17	11.97	.17
Mrk 618 ..	11.54	.22	11.34	.33	11.52	.29
Mrk 634 ..	13.24	.31	12.60	.24	12.60	.24
Mrk 704 ..	11.07	.23	11.49	.36	11.53	.37
Mrk 705 ..	11.58	.22	...	...	...	...
Mrk 734 ..	11.98	.22	12.36	.35	12.40	.35
Mrk 739 ..	11.80	.24	10.64	.23	10.69	.21
Mrk 766 ..	11.30	.28	...	...	...	...
Mrk 771 ..	12.74	.32	11.42	.20	11.46	.19
Mrk 783 ..	14.06	.41	...	...	...	...
Mrk 817 ..	11.21	.32	10.31	.22	10.36	.22
Mrk 841 ..	11.59	.23	11.03	.27	11.20	.24
Mrk 845 ..	13.51	.41	11.34	.20	11.44	.17
Mrk 871 ..	12.50	.25	10.70	.18	10.76	.17
Mrk 975 ..	11.64	.27	11.46	.30	11.55	.29
NGC 5548	10.64	.23	10.19	.24	10.22	.24
NGC 5940	12.53	.23	...	...	...	...

Table 1.3: Derived nuclear and galactic magnitudes. All the quoted uncertainties on the magnitudes are downward errors. The corresponding upward errors are given by $\delta m^+ = -2.5\log(2 - 10^{0.4\delta m^-})$.

the bulge is poor. Therefore the values of the galactic parameters reported in Table 1.2 must be considered with caution. Actually we have reported them because they allow to compute galactic fluxes within fixed apertures, which are much less uncertain quantities than the single parameters (see discussion below).

To mimic the effects of possible uncertainties of the seeing, we have repeated the numerical fits of the profiles of many objects, changing the seeing parameter σ evaluated from the standards in both directions by 0.05 and 0.13, the rms of the seeing parameters of a single night and of all the nights respectively. The best fits obtained varying the parameter by 0.13 give χ^2 larger by more than a factor of two respect to the minimum χ^2_{min} found with the seeing evaluated from the standards. Conversely, if the seeing parameters are varied only by 0.05, sometimes we get best fits with $\chi^2 \leq \chi^2_{min} + 1$. However, in these cases the galactic and nuclear fluxes change by no more than 20%.

In Table 1.3 we have reported the nuclear magnitudes with their errors. The errors on the fluxes are comprehensive of the following contributions added up in quadrature: *i)* uncertainties due to possible variation of the seeing parameter $\Delta\sigma = \pm 0.05$, *ii)* uncertainties in the final values of the fitting parameters, and *iii)* uncertainties of calibration.

The uncertainties in the estimated nuclear fluxes range from 20 to 45%, apart from 2 objects with particularly faint nuclei (Mrk 504 and Mrk 584) for which the relative uncertainties amount to 1.8 and 2.0, respectively.

Koitilainen et al. (1992a) have observed with IR arrays hard X-ray selected Seyfert galaxies. Their analysis of the data are quite similar to ours, and they have two objects in common with our sample. Their estimate (Koitilainen et al. 1992b) of the flux of the nucleus of NGC 5548 is only 0.04 magnitudes fainter than ours. For the other object in common with us, Mrk 509, they have found $K_n = 10.49$, while we have found $K_n = 10.50$. The agreement is therefore very good in both cases, and well within our estimate of the errors (0.23 mag.).

McAlary and Rieke (1988) have estimated the nuclear magnitude and the ratio of the nuclear to the total flux in a 10″ aperture of several hard X-ray selected objects. They have used multiaperture, multicolor photometry plus a model which take advantage of assumptions about the growth curve and colours of the hosting galaxy. We have two objects in common with them, Mrk 79 and NGC 5548. They have estimated the nuclear magnitude of the latter galaxy $K_n = 10.31$, about 0.3 magnitudes brighter than our estimate, that conversely is in good agreement with the above mentioned

A

Name	f_b	$\Delta\chi^2$	δL_b	δL_d	δL_g	δL_n
(1)	(2)	(3)	(4)	(5)	(6)	(7)
0048+29	2.0	1.1	60%	70%	4%	2%
2237+07	2.5	0.8	24%	25%	2%	4%
Mkn 352	1.7	1.1	25%	12%	3%	7%
Mkn 530	2.0	1.1	20%	20%	2%	12%
Mkn 975	4.0	0.8	100%	60%	1%	2%

B

Name	f_d	$\Delta\chi^2$	δL_b	δL_d	δL_g	δL_n
(1)	(2)	(3)	(4)	(5)	(6)	(7)
0048+29	1.4	4.1	27%	28%	7%	5%
2237+07	1.4	3.4	40%	28%	6%	4%
Mkn 352	1.1	1.3	31%	8%	12%	12%
Mkn 530	1.1	1.2	12%	12%	3%	9%
Mkn 975	1.2	1.0	38%	6%	10%	9%

Table 1.4: See text.

result of Koitilainen et al. (1992a,b).

In the case of the nucleus of Mrk 79 they have found $K_n = 11.14$ quite close to our estimate $K_n = 11.19$.

Extrapolating the stellar flux from the V-band with the assumption $(V - K) = 3.2$, Ward et al. (1987) have estimated the a nonstellar flux of Mrk 79 corresponding to $K_n = 11.08$, in good agreement with the above results.

Regarding the hosting galaxies, our main concern was to estimate as reliably as possible their total K magnitude. It is therefore very important to understand the effect of the statistically allowed deviations of the parameters from their best fit values on the estimate of total magnitudes. Table 1.4 illustrates that the bulge or disc luminosities, and even more those of the whole galaxies and of the nuclei, are much better constrained than the single

galactic parameters. To check this point, we have repeated the fits of several profiles, fixing the parameter r_e to a value equal to the best-fit one multiplied or divided by a factor f_b, which corresponds to its statistical uncertainty as estimated by the fitting program, and minimizing the χ^2 with respect to the other 4 parameters. In Table 1.4A we have reported, for 5 representative objects, the factor f_b, the corresponding increase of the χ^2 and the maximum percentage variation of the bulge, disc, galactic (bulge + disc) and nuclear luminosity with respect to the best-fit value. The data reported in Table 1.4B refer to a similar computation, in which however the disc scale length r_D has been fixed, and the χ^2 has been minimized with respect to the other 4 parameters. As can be seen, we have found that galactic and nuclear fluxes differ by no more than 15% respect to the values computed with the best fit parameters, though the bulge and disc contributions may vary by more than a factor of two.

Our results confirm that the correlations among the disc and bulge parameters are such that the total magnitudes of the hosting galaxies are estimated more precisely than the individual parameters (Malkan 1984; Kent 1985; Veron-Cetty and Woltjer 1990).

In few cases we can compare our estimates of the galactic flux with those derived by other authors with different methods. Neugebauer et al. (1985) used aperture photometry with an annular diaphragm in the attempt to infer the flux of the nebulosity around the nucleus of several QSOs. We have in our sample Mrk 841 in common with them. For this object we have found $K_n = 11.59$ and galactic magnitude $K_g = 11.03$, while Neugebauer et al. (1985) obtained $K_n = 11.37$ and $K_g = 12.27$. Discrepancies are already present in the data. Actually we have found that on the basis of our calibration the flux in 5″ aperture is $K(5'') = 11.14$, in agreement with Neugebauer et al. (1985) who have found $K(5'') = 11.16$. On the other hand using their Table 1 we have also computed their estimate of the magnitude within 10″, $K(10'') = 11.07$, while we have found $K(10'') = 10.91$. This difference may arise from the quite complex technique used by Neugebauer et al. (1985). Moreover in computing the total galactic flux from the inner and outermost regions they have to extrapolate the contributions both from the regions inside 5″ as well as from the regions outside 10″.

As mentioned above, McAlary & Rieke (1988) have estimated the galactic contribution to the observed fluxes within a 10″ aperture of several hard X-ray selected AGNs. As for Mrk 79 they have found that the galactic flux within 10″ is 32% of the total, while we have estimated that the galactic flux amounts to 39%. Our estimate of the total flux within 10″ aperture

$K = 10.70$ is in nice agreement with their finding $K = 10.72$. In the case of NGC 5548 McAlary and Rieke (1988) have found that the galaxy magnitude within 10″ aperture is $K_g(10'') = 11.63$, while we have found $K_g(10'') = 10.86$. In this case the difference is mainly due to different partition of the flux between the nucleus and the galaxy. Actually our estimate of the total flux within 10″ aperture $K = 9.99$ is close to the value $K = 10.03$ found by McAlary and Rieke (1988). A trade-off between galactic and nuclear fluxes is evident. This is somewhat expected and has been taken into account in evaluating the errors. On the other hand our data contain much more information than the multiaperture photometry used by McAlary & Rieke (1988) and thus allow a more reliable separation of stellar and non-stellar fluxes.

As for NGC 5548 Koitilainen et al. (1992a) with data and analysis similar to ours have found $K_n = 10.68$ in agreement with our results, but $K_g = 11.66$ in 10″ aperture, closer to the value found by McAlary and Rieke (1988). On the other hand their estimate of the total flux within a 10″ aperture is $K(10'') \simeq 10.2$ (see Table 3 of Koitilainen et al. 1992a).

Only in the case of Mrk 79 the agreement is fully satisfactory. However it is interesting to notice that in the other two cases our estimates of the galactic fluxes are larger than those given by other authors. This circumstance at least suggests that we have not grossly underestimated the galactic fluxes because of an overestimate of the background.

As a further check on galactic fluxes we can add that the distribution of $(B-K)$ integrated colours of the hosting galaxies is quite similar to that of normal early type spirals (Granato et al. 1993 and Chapter 3).

The single galactic parameters are very uncertain. In particular in the K band the disc profiles look steeper than in B band; the disc central brightness I_D is on average brighter than the corresponding value in B band, adopting $(B-K) = 4.2$ (Griersmith et al. 1982), whereas the disc scale is on average larger in B band (see Granato et al. 1993 and Chapter 3).

In Table 1.2 we have reported the total magnitudes of the hosting galaxies (column 4). They have been computed by integrating the intensity profiles of bulge and disc as they resulted from the best fitting procedure. For each objects we have also computed and reported in column 6 the galactic magnitudes within $r \leq 20$ kpc.

We have not been able to derive reliable estimates of the galactic magnitudes of 7 objects (Mrk 110, 464, 486, 705, 766, 783 and NGC 5940). In the case of Mrk 766 we have found large uncertainties in the estimate of the background, due to the dimension of the array and the small distance of the

object (see above discussion and Table 1.5). The profiles of Mrk 464, Mrk 486 and Mrk 783 are almost starlike, with a hosting galaxy poorly defined. An unusually large value of the disc scale (r_D = 25 kpc) has been found fitting the profile of Mrk 110; this result could be affected by the underestimate of the background in the frame. Because of the importance of the disc component of the hosting galaxy this entails a large difference between the total magnitude and that within 20 kpc (Δm = 1.2). Quite similar cases are those of Mrk 705 and NGC 5940. In these two objects the bulges, that are the dominant components of the galaxies, are extremely wide ($r_e \geq 36$ kpc).

To evaluate the errors on the galactic fluxes we have added in quadrature four contributions: *i)* the uncertainty due to possible variation of the seeing parameter $\Delta\sigma = \pm 0.05$, *ii)* the uncertainty in the final values of the fitting parameters, *iii)* the uncertainty of calibration and *iv)* the uncertainty in the surface brightness in the external regions. The first three contributions have been widely discussed above. The difference between the galactic flux within the last observed point of the profile and the reported galactic flux has been taken as a possible evaluation of *iv)*. The resulting global errors expressed in magnitudes have been reported in column 5 and 7 of Table 1.2.

No K–correction have been applied to the results of Table 1.2, so that they refer to observer's frame. On the other hand, owing to the relatively low redshifts of the galaxies, such corrections are bound to be small.

Using the K band frames we have determined the ratios between the nuclear flux F_{Kn} and the galactic flux F_{Kg} within the 5″ and 7.8″ apertures of the photometric observations. The ratios in the 5″ aperture range from .3 to 7.3 with a median value of 2.1; thus, neglecting the galaxy contribution within this small aperture would lead to an overestimate of the nuclear flux of half of the objects by more than 50%. The median value for the ratios within 7.8″ aperture is 1.4.

1.4 Analysis of the Photometric Data

With the multiaperture and multicolor photometry we can exploit two further methods for separating the nuclear and the galaxy contributions. The *color given* method (Sandage 1973) is based on the assumption that the intrinsic colors of both the nuclei and the galaxies have very narrow distributions. However, the correlation of the IR colors observed with the small apertures with the ratios of the nuclear to the galactic flux derived on the

basis of the K frames turns out to be weak. Moreover, the $J-K$ colors of objects where the nuclear emission dominates ($F_{Kn}/F_{Kg} > 2$) show a considerable spread: they range from 1.4 to 2.1. Therefore the *color given* method is quite unreliable in the near IR.

The second method, the *template profile method*, is based on the assumption of a standard profile for the underlying galaxies. The adopted template intensity profile is described by 3 parameters: the disc radial scale r_D, the effective radius of the bulge r_e and the ratio I_e/I_D. We have used the median values of these parameters for a sample of about 30 early spiral galaxies studied by Kent (1985) using accurate surface photometry from CCD images in the J and F optical bands. The adopted values are $r_D = 5.2$ kpc, $r_e = 3.2$ kpc and $I_e/I_D = 0.38$.

As a check on whether such parameter values are appropriate also for the K band, we have compared the growth curve in this band, corresponding to the adopted profile, with that derived by Griersmith, Hyland & Jones (1982) from multiaperture J, H, K photometry of 65 early-type spirals (see Fig. 1.2). It is apparent that the two curves match well; the discrepancies are less than few hundreds of a magnitude in the range of A/D_1 values which correspond to apertures of 5″ to 15″ at the median redshift of the Seyferts in our sample ($z = 0.035$).

The total flux, $F_c(r)$, within an apertures r can be written as

$$F_c(r) = f_n(r)F_n + f_g(r)F_g \tag{1.5}$$

where F_g and F_n are the total fluxes of the host galaxy and the nucleus, respectively, and $f_g(r)$ and $f_n(r)$ are the fractions comprised within the aperture r. If photometric data with two apertures are available, the total nuclear flux F_n can be derived from the observed fluxes $F_c(r_{1,2})$:

$$F_n = F_c(r_2)\frac{F_c(r_1)/F_c(r_2) - f_g(r_1;r_2)}{f_n(r_1) - f_g(r_1;r_2)f_n(r_2)} \tag{1.6}$$

where $f_g(r_1;r_2) = f_g(r_1)/f_g(r_2)$ can be derived from the assumed galaxy profile, taking into account the PSF; $f_n(r_1)$ and $f_n(r_2)$ are determined only by the PSF.

This method is a generalization of the *galaxy growth curve given* proposed by Sandage (1973), and discussed and extended by McAlary and Rieke (1988).

We applied the *template profile method* whenever photometry with at least two apertures was available. In the K band, the method could be

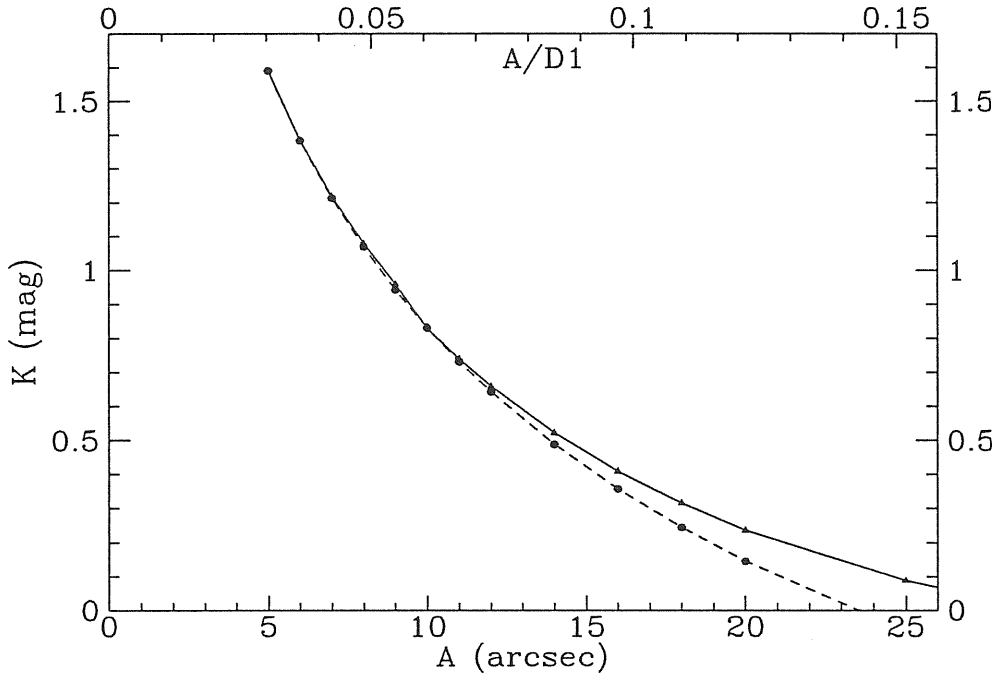

Figure 1.2: Comparison between the K-band growth curve corresponding to our template profile (solid line) and that determined by Griersmith et al. (1982) (dashed line). A is the aperture and D_1 is the angular diameter of the reference isophote at $\mu_B = 25$ mag arcsec^{-2}. The curve of Griersmith et al. (1982) refers to $D_1 = 165''$, the median values for their galaxies, and it is normalized about $\log(A/D_1) = -0.85$; the solid line refers to a galaxy at $z = 0.035$, the median redshift of our sample, and has been normalized to match the previous curve at $A = 5''$.

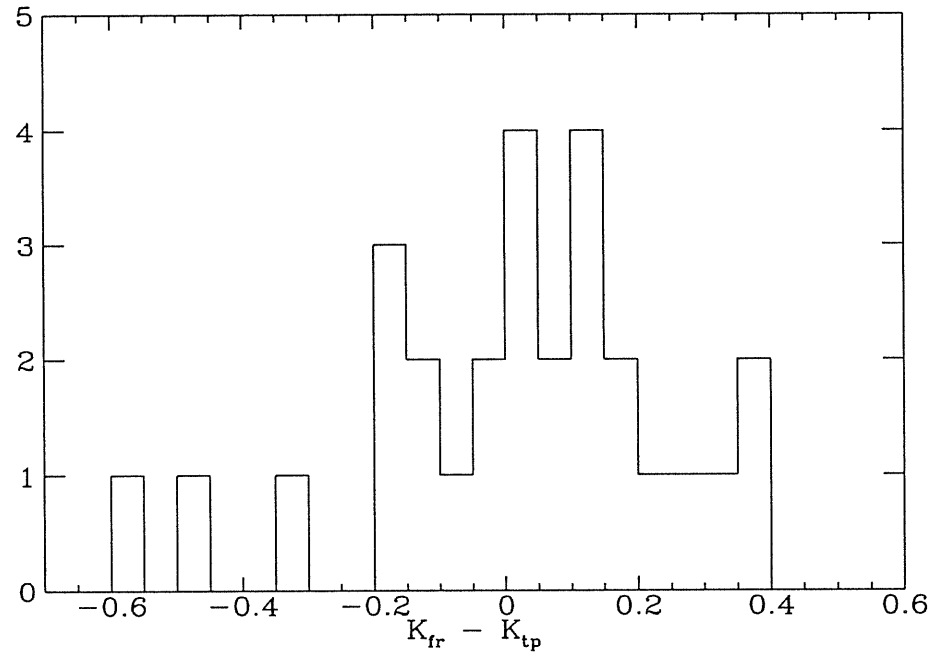

Figure 1.3: Distribution of the differences between the nuclear magnitudes derived from the best fit of the intensity profiles, K_{fr}, and those computed with the *template profile* method, K_{tp}.

applied using only our own data for 22 sources. By searching the literature we have brought together K–band photometry with two apertures for 5 additional objects. For 27 objects we could thus compare nuclear magnitudes estimated with the *template profile method* with those derived from IRCAM frames. The histogram of the magnitude differences is shown in Fig. 1.3. In about 75% of the cases the absolute value of the difference is less than 0.25 magnitudes.

The errors in our photometry are small enough ($\Delta m \leq 0.06$) to allow a reasonable use of the method. However it is important to stress that our main purpose in these calculations was to obtain independent estimates of the nuclear magnitudes to be compared with those obtained from the analysis of the frames.

Thus the consistency found among results based on IRCAM frames and those based on photometric data is reassuring.

1.5 Summary and Conclusions

In this Chapter we have presented IR observations of a *homogeneous* sample of optically selected AGNs. High resolution K band images have been obtained for 41 objects using the IRCAM system and the respective intensity profiles have been computed. We have also observed 27 objects of the sample with the UKT9 and UKT6 photometers in JHKL bands, with 5″ and 7.8″ apertures.

A method for reliable determinations of nuclear and galaxian fluxes using K band frames has been presented. To save computing time without loosing much information, the use of the intensity profiles has been suggested. The host galaxies have been modeled as a combination of bulge and disc. Their intensity profiles have been derived taking into account the effects of seeing and inclination. The nuclear profiles shaped by the seeing has then been added to get the global profiles, that depend on 5 parameters. The best fit parameters have been obtained by χ^2 minimizations. Two main problems hampered the evaluations of the parameters, the total seeing and the background subtraction.

Because of paucity of previous comparable results, we resorted to test the reliability of the nuclear fluxes by comparison to the fluxes derived by a different method, based on multiaperture photometry. We have shown that the galactic profile can be well represented in the inner parts by a template. In the *template profile* method only the normalization is a free parameter; thus two apertures are enough to estimate the nuclear and galactic fluxes. The results obtained using the *template profile* method are in good agreement with those derived from the frames.

We have also obtained reliable values of the total magnitudes of 35 host galaxies. It is the first statistically significant sample of total K band magnitudes of galaxies hosting AGNs.

The morphologies of Seyfert galaxies have been studied by many authors (Adams 1977; Simkin et al. 1980; Yee 1983; MacKenty 1990) who concluded that the large majority of the Seyfert nuclei reside in early type spiral or S0 galaxies. More recently these studies have been extended to galaxies hosting QSOs and have found evidence of a rather generalized presence of disturbed morphologies and/or bars (see MacKenty 1990 and references therein).

The problems generated by the effective seeing and by the subtraction of the background in our K frames do not allow a detailed discussion of morphological properties. However it is worth noticing that our results support previous conclusions. A significant contribution from a bulge is not

required by the fit of K–band intensity profiles in only 6 cases out of 41; for only one galaxy there is no evidence for a significant disc.

The ratios of nuclear to galactic fluxes in 5″ and 7.8″ apertures showed that the galactic contributions are of the same order of the nuclear flux in half of the analyzed cases.

The discussion of these results in the frame of the IR emission in optically selected AGNs is presented in Chapter 2, in which we use the photometry to estimate the IR colors of the nuclei and of the surrounding galaxies.

	0048+29		2237+07		I Zw 1		II Zw 1		II Zw 136		Mrk 9		Mrk 79	
r''	μ	$\delta\mu^-$	μ	$\delta\mu^-$	μ	$\delta\mu^-$	μ	$\delta\mu^-$	μ	$\delta\mu^-$	μ	$\delta\mu^-$	μ	$\delta\mu^-$
.40	13.87	.04	13.30	.04	11.54	.04	14.40	.06	13.14	.04	13.08	.04	13.10	.04
.73	14.14	.04	13.65	.04	12.10	.04	14.85	.05	13.45	.04	13.33	.04	13.35	.04
1.29	14.70	.04	14.54	.04	12.99	.04	15.75	.06	14.14	.04	13.93	.04	13.92	.04
1.88	15.43	.04	15.57	.04	14.26	.04	16.70	.08	15.07	.04	14.79	.04	14.72	.04
2.49	16.13	.05	16.29	.05	15.40	.04	17.29	.11	16.01	.04	15.65	.04	15.55	.04
3.11	16.73	.05	16.80	.05	16.31	.05	17.64	.13	16.74	.05	16.32	.04	16.25	.04
3.73	17.19	.05	17.11	.06	16.88	.06	17.88	.15	17.27	.06	16.79	.05	16.75	.04
4.35	17.60	.07	17.39	.07	17.24	.07	18.07	.16	17.43	.06	17.12	.05	17.11	.04
4.97	17.91	.08	17.64	.08	17.54	.08	18.23	.18	17.61	.06	17.43	.05	17.41	.04
5.59	18.13	.09	17.92	.09	17.82	.09	18.51	.21	17.81	.07	17.71	.05	17.62	.04
6.21	18.44	.11	18.15	.11	18.23	.12	18.64	.22	17.89	.07	17.99	.06	17.81	.05
6.83	18.57	.12	18.42	.13	18.61	.17	18.86	.26	17.96	.08	18.21	.07	17.99	.05
7.45	19.02	.17	18.64	.15	19.08	.24	19.14	.31	18.06	.08	18.47	.08	18.19	.05
8.07	19.27	.21	19.01	.21	19.33	.30	19.42	.38	18.12	.08	18.60	.08	18.36	.05
8.69	19.83	.33	19.23	.24	20.20	.57	19.64	.44	18.15	.09	18.88	.10	18.55	.05
9.31	20.14	.42	19.44	.29	20.23	.58	20.10	.60	18.22	.09	19.05	.11	18.66	.05
9.93	20.59	.58	19.47	.30	...	...	20.39	.72	18.29	.09	19.21	.13	18.77	.06
10.54	...	...	19.88	.41	...	...	20.47	.74	18.30	.10	19.52	.16	18.88	.06
11.16	...	...	19.71	.36	20.36	.64	20.39	.69	18.38	.10	19.90	.22	18.96	.06
11.78	...	...	20.09	.47	19.96	.48	...	...	18.50	.11	20.01	.24	19.10	.06
12.40	...	...	20.03	.45	20.25	.59	...	...	18.49	.11	20.34	.31	19.19	.07
13.02	...	...	20.10	.48	...	...	...	...	18.44	.11	20.54	.37	19.32	.07
13.64	...	...	20.34	.57	...	...	...	...	18.40	.10	21.10	.56	19.35	.07
14.26	...	...	20.43	.61	...	...	...	...	18.48	.11	21.12	.57	19.41	.08
14.88	...	...	20.43	.61	...	...	...	...	18.44	.10	...		19.51	.08
15.50	...	...	20.56	.66	...	...	...	...	18.43	.10	...		19.72	.09

Table 1.5: A. Observed surface brightness profiles. $\delta\mu^-$ is the downerror of μ. The upward error is given by $\delta\mu^+ = -2.5\log(2 - 10^{0.4\delta\mu^-})$

	Mrk 110		Mrk 290		Mrk 304		Mrk 335		Mrk 352		Mrk 359		Mrk 374	
r''	μ	$\delta\mu^-$	μ	$\delta\mu^-$	μ	$\delta\mu^-$	μ	$\delta\mu^-$	μ	$\delta\mu^-$	μ	$\delta\mu^-$	μ	$\delta\mu^-$
.40	14.01	.04	13.42	.05	13.54	.04	11.67	.04	13.68	.04	13.20	.05	14.32	.04
.73	14.25	.04	13.77	.04	13.94	.04	11.97	.04	14.06	.04	13.76	.04	14.49	.04
1.29	14.89	.04	14.83	.05	14.72	.04	12.81	.04	15.07	.04	14.56	.04	14.93	.04
1.88	15.79	.05	16.14	.07	15.72	.04	14.00	.04	16.19	.05	15.40	.05	15.53	.04
2.49	16.67	.06	17.07	.12	16.66	.04	15.25	.04	16.86	.05	15.97	.05	16.16	.04
3.11	17.33	.08	17.66	.17	17.35	.05	16.17	.05	17.29	.06	16.36	.06	16.74	.04
3.73	17.75	.10	17.96	.20	17.81	.05	16.83	.05	17.61	.06	16.68	.07	17.21	.04
4.35	18.00	.12	18.27	.24	18.26	.06	17.16	.05	17.89	.07	17.00	.07	17.54	.04
4.97	18.21	.14	18.58	.29	18.76	.08	17.51	.06	18.22	.09	17.22	.08	17.75	.05
5.59	18.41	.17	18.76	.32	18.94	.09	17.91	.07	18.27	.09	17.41	.09	17.91	.05
6.21	18.52	.19	19.09	.40	19.06	.10	18.28	.09	18.47	.11	17.68	.10	18.02	.05
6.83	18.66	.21	19.10	.39	19.27	.11	18.49	.11	18.75	.13	17.93	.12	18.11	.05
7.45	18.78	.23	18.91	.33	20.05	.21	18.76	.13	18.98	.16	18.13	.14	18.39	.05
8.07	18.88	.25	18.72	.28	20.04	.20	19.11	.17	19.12	.17	18.31	.16	18.70	.05
8.69	18.96	.26	18.90	.31	20.09	.21	19.28	.20	19.54	.24	18.47	.17	18.94	.06
9.31	18.93	.26	19.45	.46	20.48	.29	19.51	.24	19.70	.28	18.70	.20	19.16	.07
9.93	18.99	.27	...	...	20.78	.36	20.50	.51	20.43	.48	18.81	.22	19.48	.08
10.54	19.10	.30	...	...	20.93	.40	20.17	.40	20.59	.54	18.96	.24	19.64	.09
11.16	19.18	.31	...	...	21.45	.59	...	...	20.67	.57	19.22	.29	19.79	.10
11.78	19.17	.31	...	...	...	...	20.05	.36	20.67	.57	19.43	.33	20.28	.14
12.40	19.28	.34	...	...	21.40	.57	20.69	.58	...	...	19.48	.34	21.06	.27
13.02	19.26	.33	...	...	21.55	.63	...	...	...	...	19.84	.45	...	...
13.64	19.29	.34	...	...	21.15	.47	20.61	.55	...	...	20.27	.60	22.08	.57
14.26	19.25	.33	...	...	21.77	.73	21.04	.74	...	...	20.58	.73	22.10	.58
14.88	19.24	.33	...	...	...	...	...	...	...	...	20.57	.72	...	...
15.50	19.53	.41	...	...	...	...	...	...	...	...	...	...	...	...

Table 1.5: B. Continued

	Mrk 376		Mrk 382		Mrk 464		Mrk 478		Mrk 486		Mrk 493		Mrk 504	
r''	μ	$\delta\mu^-$	μ	$\delta\mu^-$	μ	$\delta\mu^-$	μ	$\delta\mu^-$	μ	$\delta\mu^-$	μ	$\delta\mu^-$	μ	$\delta\mu^-$
.40	12.89	.04	15.11	.04	14.19	.04	12.69	.04	12.39	.04	13.51	.04	14.66	.07
.73	13.17	.04	15.35	.04	14.77	.04	13.03	.04	13.10	.04	13.96	.04	14.97	.05
1.29	13.86	.04	15.91	.04	15.91	.04	14.02	.04	14.37	.04	15.02	.04	15.80	.06
1.88	14.82	.04	16.61	.05	17.26	.06	15.28	.04	15.82	.06	16.08	.05	16.65	.09
2.49	15.74	.04	17.24	.06	18.11	.08	16.36	.04	17.01	.10	16.78	.05	17.19	.11
3.11	16.44	.04	17.79	.08	18.99	.16	17.16	.05	17.69	.16	17.22	.07	17.60	.14
3.73	16.94	.05	18.25	.11	19.42	.22	17.67	.05	18.19	.22	17.55	.08	17.96	.18
4.35	17.34	.05	18.72	.16	19.43	.21	18.15	.06	18.66	.30	17.87	.10	18.32	.23
4.97	17.73	.05	18.89	.19	20.05	.35	18.48	.06	18.94	.36	18.36	.14	18.52	.25
5.59	18.19	.06	19.00	.20	20.70	.56	18.84	.08	19.38	.48	18.45	.15	18.82	.31
6.21	18.58	.08	19.42	.29	...	...	19.12	.09	19.99	.72	18.71	.18	19.00	.34
6.83	18.90	.09	19.73	.37	...	...	19.59	.13	...	...	18.84	.20	19.07	.35
7.45	19.20	.12	19.97	.44	21.00	.67	19.99	.18	...	...	18.90	.21	19.29	.40
8.07	19.29	.13	20.46	.63	...	...	20.47	.25	...	...	19.13	.25	19.66	.52
8.69	19.56	.15	...	...	...	...	20.06	.18	...	...	20.43	.67	19.88	.59
9.31	19.93	.21	...	...	...	...	20.70	.30	...	...	20.34	.63	20.09	.67
9.93	20.47	.32	...	...	...	...	...	...	...	...	19.22	.27	20.15	.69
10.54	21.19	.55	...	...	...	...	21.88	.71	...	...	19.47	.33	...	...
11.16	...	...	...	...	...	...	21.80	.67	...	...	19.31	.29	...	...
11.78	...	...	...	...	...	...	20.86	.33	...	...	19.56	.36	...	...
12.40	...	...	...	...	...	...	21.15	.41	...	...	19.80	.42	...	...
13.02	...	...	...	...	...	...	21.77	.64	...	...	19.79	.42	...	...
13.64	...	...	...	...	...	...	...	...	...	...	20.10	.53	...	...
14.26	...	...	...	...	...	...	...	...	...	...	...	...	...	...
14.88	...	...	...	...	...	...	...	...	...	...	...	...	...	...
15.50	...	...	...	...	...	...	...	...	...	...	...	...	...	...

Table 1.5: C. Continued

	Mrk 506		Mrk 509		Mrk 530		Mrk 584		Mrk 618		Mrk 634		Mrk 704	
r''	μ	$\delta\mu^-$	μ	$\delta\mu^-$	μ	$\delta\mu^-$	μ	$\delta\mu^-$	μ	$\delta\mu^-$	μ	$\delta\mu^-$	μ	$\delta\mu^-$
.40	13.58	.04	12.04	.04	13.16	.04	14.83	.04	13.72	.04	14.90	.04	13.11	.04
.73	14.06	.04	12.42	.04	13.42	.04	15.30	.04	13.93	.04	15.20	.04	13.31	.04
1.29	15.18	.05	13.26	.04	13.94	.04	16.03	.04	14.49	.04	15.85	.04	13.90	.04
1.88	16.19	.09	14.39	.04	14.61	.04	16.76	.05	15.28	.04	16.61	.04	14.75	.04
2.49	16.87	.15	15.37	.04	15.24	.04	17.21	.05	16.10	.05	17.24	.05	15.66	.04
3.11	17.18	.20	16.01	.04	15.71	.05	17.52	.06	16.74	.05	17.62	.05	16.39	.05
3.73	17.40	.24	16.46	.04	16.08	.05	17.81	.06	17.18	.06	17.95	.05	16.94	.05
4.35	17.58	.27	16.81	.04	16.40	.05	18.16	.08	17.48	.07	18.33	.06	17.32	.06
4.97	17.88	.35	17.09	.05	16.65	.06	18.21	.08	17.73	.07	18.70	.07	17.64	.08
5.59	18.14	.42	17.29	.05	16.88	.06	18.42	.09	17.97	.09	18.99	.09	17.91	.09
6.21	18.24	.46	17.52	.05	17.15	.07	18.79	.12	18.14	.10	19.38	.12	18.18	.11
6.83	18.49	.55	17.75	.05	17.38	.08	19.03	.14	18.29	.11	19.76	.16	18.40	.13
7.45	18.41	.52	17.79	.05	17.60	.10	19.29	.17	18.42	.12	20.18	.22	18.65	.16
8.07	18.32	.48	17.83	.05	17.78	.11	19.36	.18	18.57	.14	20.22	.23	18.95	.20
8.69	18.32	.48	17.91	.05	18.02	.13	19.81	.26	18.68	.15	20.53	.29	19.11	.23
9.31	18.68	.63	18.07	.05	18.28	.17	20.31	.38	18.77	.16	20.77	.35	19.40	.29
9.93	18.79	.68	18.11	.05	18.48	.19	20.84	.56	18.88	.18	21.24	.50	19.69	.36
10.54	...	...	18.19	.05	18.80	.25	20.27	.37	19.04	.20	...	...	20.13	.51
11.16	...	...	18.25	.05	19.05	.31	20.70	.51	19.20	.23	...	...	20.59	.70
11.78	...	...	18.37	.06	19.51	.44	20.16	.34	19.36	.26	...	...	...	...
12.40	...	...	18.46	.06	19.45	.42	...	...	19.52	.29	...	...	...	...
13.02	...	...	18.38	.06	19.62	.48	...	...	19.73	.34	...	...	...	...
13.64	...	...	18.42	.06	19.84	.56	...	...	...	...	...	...	...	...
14.26	...	...	18.57	.06	...	...	...	...	...	...	...	...	...	...
14.88	...	...	18.73	.06	...	...	...	...	...	...	...	...	...	...
15.50	...	...	18.87	.07	...	...	...	...	...	...	...	...	...	...

Table 1.5: D. Continued

	Mrk 705		Mrk 734		Mrk 739		Mrk 766		Mrk 771		Mrk 783		Mrk 817	
r''	μ	$\delta\mu^-$	μ	$\delta\mu^-$	μ	$\delta\mu^-$	μ	$\delta\mu^-$	μ	$\delta\mu^-$	μ	$\delta\mu^-$	μ	$\delta\mu^-$
.40	13.33	.04	13.73	.04	13.67	.04	12.64	.04	13.84	.04	15.18	.05	11.98	.04
.73	13.60	.04	14.03	.04	13.87	.04	13.03	.04	14.10	.04	15.61	.04	12.49	.04
1.29	14.30	.04	14.72	.04	14.40	.04	13.84	.05	14.75	.04	16.63	.05	13.59	.04
1.88	15.23	.04	15.65	.04	15.08	.04	14.75	.07	15.54	.04	17.72	.08	14.90	.05
2.49	15.99	.04	16.54	.04	15.74	.04	15.47	.11	16.26	.04	18.50	.14	15.79	.06
3.11	16.64	.04	17.20	.05	16.23	.04	15.96	.17	16.93	.05	19.32	.26	16.31	.08
3.73	17.14	.05	17.69	.05	16.56	.05	16.37	.23	17.39	.05	19.90	.41	16.66	.09
4.35	17.54	.05	18.10	.06	16.73	.05	16.68	.30	17.72	.06	20.74	.74	16.94	.11
4.97	17.94	.05	18.48	.07	16.84	.05	16.88	.35	18.13	.08	...	...	17.05	.11
5.59	18.37	.06	18.91	.09	16.96	.05	17.18	.44	18.41	.09	...	...	17.19	.12
6.21	18.76	.08	19.27	.12	17.10	.05	17.56	.58	18.37	.09	...	...	17.46	.14
6.83	19.35	.11	19.98	.21	17.34	.05	17.52	.56	18.93	.13	...	...	17.69	.17
7.45	19.72	.15	20.19	.25	17.56	.06	17.76	.67	19.24	.17	...	...	17.97	.21
8.07	20.08	.20	20.38	.29	17.82	.06	17.53	.57	19.46	.20	...	...	18.17	.24
8.69	20.43	.27	20.74	.39	18.02	.07	17.88	.72	19.78	.25	...	...	18.44	.29
9.31	20.67	.32	21.37	.61	18.27	.08	...	...	19.70	.24	...	...	18.57	.32
9.93	21.04	.43	...	...	18.49	.10	...	...	19.95	.29	...	...	18.69	.34
10.54	21.18	.48	...	...	18.71	.11	...	...	21.19	.71	...	...	18.83	.38
11.16	21.81	.74	...	...	18.80	.12	...	...	20.53	.45	...	...	18.88	.39
11.78	...	...	...	...	19.01	.14	...	...	...	...	...	...	19.10	.45
12.40	...	...	...	...	19.19	.16	...	...	...	...	...	...	18.78	.35
13.02	...	...	...	...	19.45	.20	...	...	...	...	...	...	19.33	.53
13.64	...	...	...	...	19.71	.25	...	...	...	...	...	...	19.74	.70
14.26	...	...	...	...	20.00	.31	...	...	...	...	...	...	...	...
14.88	...	...	...	...	20.11	.34	...	...	...	...	...	...	...	...
15.50	...	...	...	...	20.40	.43	...	...	...	...	...	...	...	...

Table 1.5: E. Continued

	Mrk 841		Mrk 845		Mrk 871		Mrk 975		NGC 5548		Mrk 5940	
r''	μ	$\delta\mu^-$	μ	$\delta\mu^-$	μ	$\delta\mu^-$	μ	$\delta\mu^-$	μ	$\delta\mu^-$	μ	$\delta\mu^-$
.40	12.83	.04	14.39	.04	13.37	.04	12.83	.04	11.94	.04	13.73	.05
.73	13.22	.04	14.76	.04	13.74	.04	13.40	.04	12.34	.04	14.29	.05
1.29	14.23	.04	15.46	.04	14.47	.04	14.46	.04	13.31	.04	15.11	.05
1.88	15.39	.04	16.12	.04	15.34	.04	15.71	.05	14.49	.04	16.00	.07
2.49	16.23	.05	16.50	.05	15.98	.05	16.49	.07	15.25	.04	16.49	.09
3.11	16.82	.06	16.92	.05	16.45	.05	16.97	.08	15.72	.04	16.96	.11
3.73	17.26	.07	17.25	.05	16.79	.05	17.34	.10	16.07	.05	17.18	.13
4.35	17.55	.09	17.54	.06	16.97	.05	17.64	.12	16.36	.05	17.43	.15
4.97	17.64	.09	17.86	.06	17.06	.06	17.91	.14	16.59	.05	17.59	.16
5.59	17.96	.11	18.01	.07	17.27	.06	18.20	.18	16.79	.05	17.75	.18
6.21	18.52	.17	18.24	.08	17.53	.07	18.56	.23	17.02	.05	17.81	.18
6.83	18.48	.16	18.59	.10	17.78	.08	18.79	.27	17.26	.06	17.90	.19
7.45	19.14	.28	18.70	.10	17.91	.09	19.07	.32	17.45	.06	18.17	.23
8.07	19.06	.26	18.84	.12	18.16	.10	19.19	.35	17.68	.07	18.20	.23
8.69	19.10	.27	19.00	.13	18.55	.14	19.50	.44	17.90	.08	18.13	.22
9.31	18.95	.23	19.33	.17	18.64	.15	19.60	.46	18.01	.08	18.58	.31
9.93	19.38	.33	19.36	.17	19.14	.22	19.76	.51	18.26	.10	18.37	.26
10.54	20.46	.72	19.57	.20	19.09	.21	19.82	.53	18.43	.11	18.54	.29
11.16	19.95	.50	19.85	.25	19.75	.36	19.80	.52	18.62	.13	18.54	.29
11.78	19.72	.42	19.79	.24	20.24	.52	19.82	.52	18.85	.15	19.16	.47
12.40	19.75	.43	20.12	.31	20.12	.48	19.99	.58	19.21	.21	19.15	.46
13.02	...	...	20.00	.28	20.68	.71	19.28	.34	19.52	.26	19.68	.67
13.64	...	...	19.98	.28	...	...	19.50	.40	19.61	.28	19.60	.63
14.26	...	...	20.55	.43	...	...	20.05	.59	20.36	.50	19.87	.75
14.88	...	...	21.15	.66	...	...	...	...	20.43	.53	...	...
15.50	...	...	...	...	...	...	...	...	20.57	.59	...	...

Table 1.5: F. Continued

Chapter 2

Near–IR: Interpretations of Results

Summary. [1]The imaging and photometric IR data, presented in Chapter 1, are used to discuss the properties of nuclei and hosting galaxies of a well defined and large sample of optically selected Seyfert 1 galaxies. The K band luminosity distribution of the galaxies hosting the active nuclei is derived and the comparison with the local luminosity function of the spirals confirms that the probability of a spiral galaxy hosting bright AGN increases with the luminosity. On average the colors of the galaxies are slightly redder than those of spirals suggesting that hosting galaxies usually have moderately enhanced star formation rates. The analysis of the correlation of the K band to the IRAS fluxes demonstrates that the nuclei largely dominate the 12 μm emission, whereas the galaxies are the major contributors at $\lambda \geq 60$ μm. It is also shown that galaxies having a 12 to 60 μm spectral index flatter than -1.5 are likely hosting an active nucleus. The IR spectral data of the nuclei as well as the correlation of the X–ray to the IR emissions are briefly discussed. We conclude that the IR emission of the nuclei is probably dominated at $\lambda \geq 2.2$ μm by thermal dust radiation.

[1]This Chapter is based on a paper published in collaboration with L. Danese, V. Zitelli, N. Mandolesi, R. Wade and G. De Zotti (Danese et al. 1992)

2.1 Introduction

In the last decade the general improvement of the astronomical detectors both in sensitivity as well as in spatial resolution has allowed reliable spectral energy distributions (SEDs) of AGNs over a wide range of frequencies to be obtained (see e.g. Edelson and Malkan 1986; Ward et al. 1987; Carleton et al. 1987; Neugebauer et al. 1987), casting light on the fact that other emission mechanisms operate in addition to non–thermal processes.

Evidences of a generalized presence of a blue bump possibly due to an accretion disc have accumulated (see e.g. Band and Malkan 1989; Osterbrock 1991 and references therein). Many recent observations suggest that absorption and reradiation by material around the nuclei are relevant processes in shaping the AGN spectra. The spectra obtained in the X–ray band with *Exosat* and *Ginga* point toward the existence of a reflected component due to the presence of cold and/or warm matter. The column density of such material may be very high ($N_H \geq 10^{24}\,\mathrm{cm}^{-2}$) as suggested by a possible high energy bump found in several observed spectra (Piro et al. 1990; Inoue 1989). Several authors (see e.g. Pounds et al. 1990; Sanders et al. 1989) envisaged that the presence of a torus or a warped disc around the central engine can explain many observed spectral properties within a unified picture of the AGN phenomenon.

Presence of obscuring material around the nuclei has been discussed by many authors on the basis both of the continuum emission (Rieke 1978; Lawrence and Elvis 1982; Cheng et al. 1983; Lawrence et al. 1985; Ward et al. 1987) and of the emission–line ratios and polarization (Wampler 1971; De Zotti and Gaskell 1985; Miller and Antonucci 1985; Ward et al. 1987; Dahari and De Robertis 1988; Berriman 1989).

In this framework the dust reradiation is expected to play a relevant role in the IR region of the AGN spectra. Actually Neugebauer et al. (1979) called attention to the fact that some objects show a radiation excess at 3.5 μm. Edelson & Malkan (1987) and Edelson, Malkan & Rieke (1987) noted the presence of a bump around 5 μm in several AGNs. Barvainis (1987) substantiated previous hints of many authors in a model which naturally explains the bump in the near IR with the reradiation by dust heated to the evaporation temperature by primary optical and ultraviolet continuum emissions. Sanders et al. (1989) presented the observations of the continuum of 109 bright QSOs of the Palomar–Green survey in the frequency range from $\nu \sim 10^{10}$ to $\nu \sim 10^{18}$ Hz. They noticed that the shapes of the SEDs are quite similar and, in particular, that an IR bump and a minimum at

around 1 μm are usually present. They concluded that dust heated to the sublimation temperature can account for the observed spectra and suggested that the absorbing material is distributed in a warped disc. In the same framework detailed spectral fits from 0.3 to 100 μm have been done by Barvainis (1990). On the other hand Band & Malkan (1989) fitted spectral observations from X–ray to IRAS bands of 12 AGNs with a non–thermal source plus an accretion disk. However they argued that their fits leave room for a further component in the near–IR bands. Indeed in Seyfert galaxies and even in QSOs the contributions by the host galaxy in the infrared bands are not at all negligible.

Therefore we decided to investigate the IR properties of a well defined sample of faint active galactic nuclei harbored in Seyfert 1 galaxies. With the UK Infrared Telescope (UKIRT) using both photoelectric photometer and imaging camera, we observed almost all the objects of the homogeneous sample used to derive the optical luminosity function of low luminosity AGNs (Cheng et al. 1985). In the previous Chapter (see also Zitelli et al. 1993) we have reported the observations and we have also presented a method for a reliable separation of the emissions of the nuclei and of the galaxies using the K–band images. The computed magnitudes have typical errors of 0.2 and 0.3 for nuclei and galaxies respectively. We have also obtained optical CCD frames of the same objects and the corresponding results are reported in a Chapter 3. Observations in other bands from the X–ray to the radio are largely available for the sample objects and the SEDs will be discussed and modelled in Chapter 5.

2.2 Data

We concentrated our observations on the optically selected sample of Seyfert 1 and 1.5 galaxies defined by Cheng et al. (1985), when deriving the optical luminosity function of low luminosity AGNs. The sample, limited to $U \leq 16.3$, $M_u \leq -18.5$ and $z \leq 0.08$, comprises 56 objects and has been shown to be *homogeneous* (see also Chapter 4) in the sense that there is no significant correlation of the apparent magnitudes with the absolute magnitudes, or with the ratios of the fluxes of the nuclei to those of the underlying galaxies. High resolution images with a scale of 0.62″/pixel have been obtained on January and on July 1988 with the IRCAM system for 41 objects randomly chosen out of the sample. The intensity profiles computed from the two–dimensional images have been reported in Chapter 1.

A

Name	K_n	δK_n	J_n	J_n(tp)	H_n	H_n(tp)	$\frac{N}{G}(5'')$	$\frac{N}{G}(7.''8)$	K_g	δK_g	$(J-K)_g$	$(J-K)_a$	$(H-K)_g$	$(H-K)_a$
(1)	(2)	(3)	(4)	(5)	(6)	(7)	(8)	(9)	(10)	(11)	(12)	(13)	(14)	(15)
0048+29 .	12.15	0.27	14.26	13.67	12.87	12.57	1.50	1.05	11.50	0.24	0.77	0.67	0.32	0.27
2237+07 .	11.83	0.23	14.76	14.30	12.82	12.65	2.24	1.43	11.30	0.24	0.58	0.36	0.20	0.10
II Zw 1 ..	13.77	0.32	16.50	16.50	15.58	15.57	0.58	0.36	11.85	0.20	1.20	1.15	0.42	0.37
II Zw 136	11.49	0.23	13.72	13.86	12.79	12.94	4.41	3.08	12.19	0.42	1.74	1.85	0.69	0.82
Mrk 9 ...	11.03	0.21	13.20	13.14	12.22	12.16	7.11	3.73	11.38	0.33	1.77	1.38	0.89	0.57
Mrk 110 .	12.33	0.24	...	...	...	...	...	...	...	...	...	...	...	...
Mrk 290 .	12.06	0.29	13.39	13.49	12.70	12.80	2.36	1.79	11.66	0.37	2.07	1.87	1.29	1.12
Mrk 304 .	12.00	0.24	14.01	13.88	13.21	13.08	2.63	1.98	12.11	0.31	1.23	1.35	0.43	0.55
Mrk 382 .	13.16	0.29	...	...	...	...	...	...	12.89	0.28	...	...	...	...
Mrk 506 .	12.55	0.28	15.11	14.71	13.76	13.51	1.46	0.97	10.82	0.42	0.96	0.90	0.30	0.25
Mrk 509 .	10.50	0.23	12.70	12.39	11.57	11.37	3.40	2.49	9.79	0.47	1.12	0.99	0.64	0.56
Mrk 530 .	11.99	0.34	14.80	13.68	13.38	12.64	0.59	0.39	10.20	0.18	1.25	1.25	0.48	0.48
Mrk 704 .	11.07	0.23	13.44	13.80	12.67	13.08	5.20	3.16	11.49	0.36	1.12	1.28	0.14	0.31
Mrk 739 .	11.80	0.24	...	...	13.30	...	2.09	1.08	10.64	0.23	1.03	0.88	0.47	0.37
Mrk 975 .	11.64	0.27	14.54	14.55	12.84	12.91	2.96	2.05	11.46	0.30	1.02	1.17	0.55	0.63

Table 2.1: B: Nuclear and galactic magnitudes of objects for which we have K–band frames and single aperture photometry.

To disentangle the nuclear from the galactic fluxes, we have modeled the profiles of the host galaxies as the sum of two components: a bulge following the $r^{1/4}$ law and an exponential disc. The model of Seyfert galaxy is fully described by 5 parameters: the total flux of the nucleus F_n, the effective radius r_e which encloses half of the total light of the bulge, the surface brightness I_e at r_e, and the two parameters modeling the disc, namely the scale length r_D and the central surface brightness I_D. For each object the fitting profile has been calculated taking into account the effect of the galaxy inclination and of the seeing on both the galaxy and the nucleus. The best fit parameters obtained by χ^2 minimizations have been reported in Chapter 1.

We have observed 27 objects from the same sample using the photometers UKT9 in two nights in April and UKT6 in two nights in August 1987 in the J H K L' bands with 5″ and 7.8″ apertures. The data have been reported in Chapter 1, where the photometric data have been used to get estimates of the nuclear magnitudes to be compared to those derived from K-band frames. In the following we will use the photometric data to derive

B

Name	K_n	δK_n	J_n	H_n	Ap (″)	N/G	K_g	δK_g	References
(1)	(2)	(3)	(4)	(5)	(6)	(7)	(8)	(9)	(10)
I Zw 1 ...	10.20	0.22	13.13	11.60	8.5	3.40	11.02	0.45	1
Mrk 79 ...	11.19	0.23	13.57	12.34	8	1.87	10.57	0.37	2,3
Mrk 335 ..	10.04	0.30	12.87	11.42	6	3.40	11.02	0.60	4
Mrk 352 ..	12.42	0.29	13.82	13.11	8.5	1.26	11.77	0.24	1,5
Mrk 359 ..	12.35	0.24	14.26	13.07	8	0.47	10.74	0.18	6
Mrk 374 ..	12.30	0.23	13.87	13.11	5	2.47	11.48	0.22	7
Mrk 376 ..	11.07	0.24	13.81	12.63	5	3.70	11.58	0.42	7
Mrk 464 ..	13.35	0.27	14.96	14.29	5	1.38	...	...	7
Mrk 478 ..	11.28	0.23	13.70	12.63	5	3.37	11.88	0.42	7
Mrk 486 ..	11.39	0.23	13.64	12.74	5	3.94	...	...	8,9
Mrk 493 ..	12.69	0.27	14.66	14.20	8.5	0.63	11.36	0.23	10
Mrk 504 ..	14.27	0.68	16.65	15.20	8.5	0.21	11.86	0.23	1,11
Mrk 584 ..	14.71	0.74	...	...	7.8	0.16	11.94	0.17	7
Mrk 618 ..	11.54	0.22	13.79	12.68	7	4.37	11.34	0.33	8
Mrk 634 ..	13.24	0.31	15.41	14.15	5	1.74	12.60	0.24	7
Mrk 705 ..	11.58	0.22	13.30	12.40	5	2.94	...	...	7
Mrk 734 ..	11.98	0.22	13.76	12.95	10	2.07	12.36	0.35	10
Mrk 766 ..	11.30	0.28	13.75	12.89	8.5	1.01	...	...	1,10
Mrk 771 ..	12.74	0.32	...	...	10	0.42	11.42	0.20	8,12
Mrk 783 ..	14.06	0.41	15.62	14.89	7.8	1.21	...	...	7
Mrk 817 ..	11.21	0.32	...	...	10	0.72	10.31	0.22	10
Mrk 841 ..	11.59	0.23	13.85	12.98	5	1.87	11.03	0.27	7,10
Mrk 845 ..	13.51	0.41	14.97	14.08	5	0.52	11.34	0.20	7,10
Mrk 871 ..	12.50	0.25	14.96	...	8.5	0.38	10.70	0.18	10
NGC 5548	10.64	0.23	12.63	11.65	7.9	1.49	10.19	0.24	1,13
NGC 5940	12.53	0.23	14.63	13.64	5	1.47	...	...	7

Table 2.1: B: Nuclear and galactic magnitudes of objects for which we have K–band frames and single aperture photometry. The ratio N/G is computed within the aperture in col. (6). References for the photometry: (1) Balzano & Weedman, 1981; (2) McAlary et al., 1979; (3) Ward et al., 1987; (4) Rudy et al., 1982a; (5) Stein & Weedman, 1976; (6) Lawrence et al., 1985; (7) Our data; (8) Ward et al., 1982; (9) Neugebauer et al., 1985; (10) Rudy et al., 1982b; (11) Rieke, 1978; (12) Worrall et al., 1984; (13) McAlary et al., 1983.

the J and H band fluxes for the nuclei and the host galaxies, starting from the K band frames. The uncertainties in the L band data are too large to permit reliable separation of nuclear from galactic fluxes.

The nuclear magnitudes K_n with their errors δK_n and the *total* galactic magnitudes K_g with their errors δK_g reported in Table 2.1A and 2.1B have been taken from the previous Chapter. For the 15 galaxies listed in Table 2.1A, in addition to K–band frames we have JHK photometry with two apertures. These data can be combined to estimate the colors of the nuclei and of the surrounding galaxies. Assuming that the colors of the latter are aperture–independent (cf. Griersmith et al. 1982) and that the seeing is essentially the same both for K–band frames and for aperture photometry, we can write for $(J-K)$ colors:

$$(J-K)_n = -2.5\log \left[\frac{(a_K(r_1)+1)\,10^{-0.4c(r_1)} - (a_K(r_2)+1)\,10^{-0.4c(r_2)}}{a_K(r_1)-a_K(r_2)}\right] \quad (2.1)$$

$$(J-K)_g = -2.5\log \left[(a_K(r_2)+1)\,10^{-0.4c(r_2)} - a_K(r_2)10^{-0.4(J-K)_n}\right] \quad (2.2)$$

where $a_K(r) = F_n f_n(r)/F_g f_g(r)$ is the ratio of the nuclear to galactic flux within the aperture r and can be derived from the analysis of K–band frames, and the color $c(r)$ is obtained from aperture photometry. Analogous relationships hold for the $(H-K)$ and $(K-L)$ colors.

It is not straightforward to evaluate the uncertainties on nuclear fluxes derived using Eq. 2.1.

A direct check of the validity of the method is possible in the case of Mrk 704, for which we have also obtained a J frame with IRCAM. The analysis of the frame has given $J_n = 13.36$ to be compared with $J_n = 13.45$ obtained using the above equations.

A very interesting comparison is possible with the results obtained by Koitilainen et al. (1992a,b), who have analyzed with a technique very similar to ours their IR images of hard X–ray selected AGNs. In particular we have one object in Table 2.1A, Mrk 509, in common with them. The results are in very good agreement for the K and J bands, while our estimate of the H band magnitude is 0.16 mag brighter.

The statistical comparison of nuclear colours of the objects listed in Table 2.1A with those of the objects observed by Koitilainen et al. (1992b)

shows their distributions are very similar, with almost identical median values $(J-K)_n \simeq 2.3$ and $(H-K)_n \simeq 1.2$.

For 12 objects we have reported in Table 2.1A the J_n(tp) and H_n(tp) nuclear magnitudes (in columns 5 and 7 respectively), computed assuming a template profile for the hosting galaxies (see Chapter 1). The results obtained using Eq. 2.1 are in decent agreement ($\Delta J_{max} \simeq 0.6$ and $\Delta H_{max} \simeq 0.4$) except in the case of Mrk 530 ($\Delta J \simeq 0.9$ and $\Delta H \simeq 0.7$). It is likely that the uncertainties of the J and H fluxes are larger than the uncertainties in K fluxes by no more than 50%. Of course the uncertainties of nuclear fluxes increase with decreasing ratio of the nuclear to the galactic contributions that are presented in columns 8 and 9 of Table 2.1A.

Using Eq. 2.2 we have also computed the colors $(J-K)_g$ and $(H-K)_g$ of the underlying galaxies. The results have been reported in columns 12 and 14 of Table 2.1A. For comparison we have also reported the colors of the rings between the two angular radii of 2.5″ and 3.9″ (obtained subtracting out the observed flux within the 5″ aperture from that measured within 7.8″), which, at the median redshift of the sample ($z \simeq 0.035$), correspond to $r \simeq 2.5$ kpc and $r \simeq 4$ kpc, respectively. It is apparent that the agreement is good, because the largest discrepancy is 0.3 magnitudes and the color distributions are quite similar. The median values are $(J-K)_g \simeq 1.13$ and $(H-K)_g \simeq 0.45$. Neugebauer et al. (1985) have measured the IR colors of the rings between the two angular radii of 2.5″ and 5″ of 10 QSOs . Their results have median values $(J-K)_g \simeq 1.13$ and $(H-K)_g \simeq 0.48$ in nice agreement with our findings.

These values are redder than observed in normal early–type spirals ($\langle J-K\rangle \simeq 1.0$, $\langle H-K\rangle \simeq 0.25$; Griersmith et al. 1982; Devereux et al. 1987).

Using Spearman rank correlation coefficient and Kendall's coefficient of concordance W, we have tested that there is no correlation of the galactic with nuclear colors. Morever there is no significant correlation of these colors with the ratios of the nuclear to the galactic flux. The only relevant correlation is between these ratios and the *observed* colors, as it is expected.

In the case Mrk 110 no reliable estimate of the integral galactic magnitude has been obtained (see Chapter 1). Moreover the observed IR colors of Mrk 110 and Mrk 382 within the 7.8″ aperture are redder than those in the 5″ aperture. This would imply the implausible circumstance that the hosting galaxies are much redder than the nuclei. Therefore the J and H magnitudes derived using Eq. 2.1 would have been unreliable and have not been reported.

The median colors of the underlying galaxies ($(J-K)_g \simeq 1.13$, $(H-$

$K)_g \simeq 0.45$) have been used to derive J and H band nuclear magnitudes, through Eq. 2.2, when only single aperture photometry (in addition to K–band images) was available. This is the case for objects listed in Table 2.1B. In a few cases no results have been found for the J and/or H magnitudes.

Of course, the uncertainties in the fluxes derived in this way are larger than those derived from the K band frames and the evaluation of the errors is not easy. It is clear that the uncertanties are smaller when the underlying galaxy gives only a small contribution to the observed flux. Actually all the objects lacking estimates of nuclear magnitudes in Table 2.1B have nuclear to the galactic flux ratios $N/G < 1$ (see column 7). Moreover the J and H magnitudes of objects with small N/G ratios are quite sensitive to the assumption of the galactic colors. On the contrary the results of objects with $N/G > 1$ are quite independent of galaxy colors.

Among the objects of Table 2.1B, NGC 5548 is the only object observed also by Koitilainen et al. (1992b). The difference is very small in K band (0.04 mag.), but increases to 0.34 mag in J and and reaches 0.45 magnitudes in H band.

The comparison of the distributions of nuclear colors of objects listed in Table 2.1A and 2.1B shows that have have been drawn from the same parent populations.

The nuclear colors of all objects listed in Table 2.1A and 2.1B have been compared with the colors of the sample of Koitilainen et al. (1992b). The results of the statistical tests show that they have very similar distributions.

Note that no K–corrections have been applied, so that the results refer to the observer's frame. On the other hand, owing to the relatively low redshifts of the galaxies, such corrections are bound to be small.

2.3 Discussion

2.3.1 Characteristics of the Host Galaxies

As mentioned above, we have described the light distribution of the underlying galaxies as the superposition of bulge and disc. Using the best fit parameters, we found that both bulge and disc give in general appreciable contributions to the total K–band galactic emission (see Chapter 1). This fact is consistent with the claim that the large majority of the Seyfert nuclei reside in early type spiral or S0 galaxies (Adams 1977; Simkin et al. 1980; Yee 1983; MacKenty 1990).

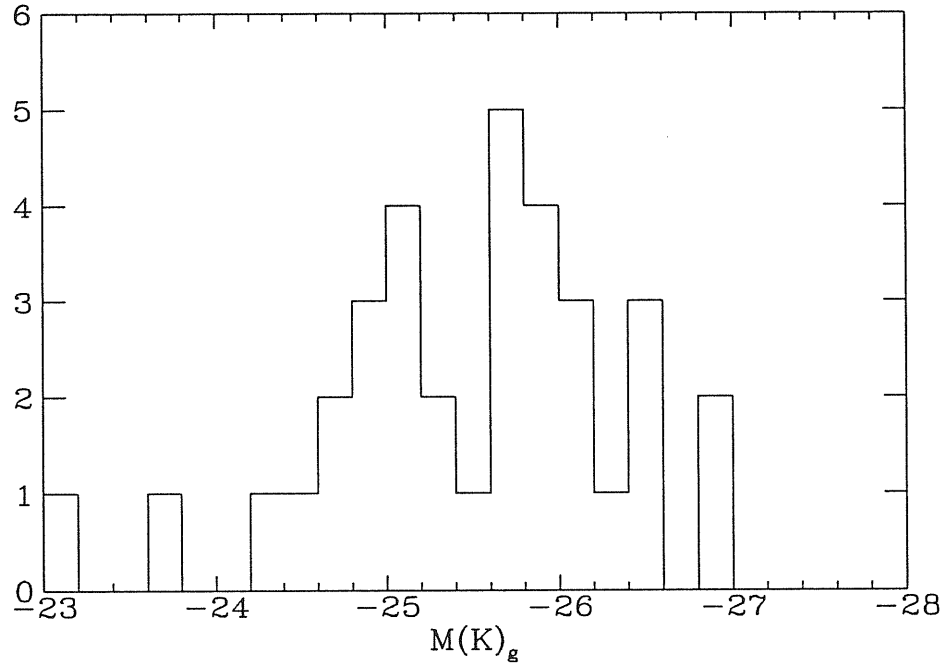

Figure 2.1: Distribution of the total K-band absolute magnitudes of the host galaxies.

We have obtained a reliable determination of the total absolute magnitude for 34 objects. In Fig 2.1 we present the K–band luminosity distribution of host galaxies in our sample. The median value is $M_{Kg} = -25.6$. This value falls in the exponentially decreasing tail of the K–band local luminosity function of spiral galaxies computed by Franceschini et al. (1991). This outcome confirms the results obtained by Neugebauer et al. (1985) in near IR. It is also in keeping with the results found by authors who have investigated the *optical* luminosity distribution function of galaxies hosting AGNs for optically selected samples (Yee 1983; Malkan 1984a; MacKenty 1990), and for a X–ray selected sample (Kruper and Canizares 1989). Similar investigations have also been performed on galaxies harboring radio–quiet and radio–loud QSOs (Hutchings et al. 1984; Geheren et al. 1984; Smith et al. 1986; Veron-Cetty and Woltjer 1990).

Nine out of these 34 objects are PG QSOs (Schmidt and Green 1983); for them we find a median $M_{Kg} = -25.7$. For the remaining 25 objects

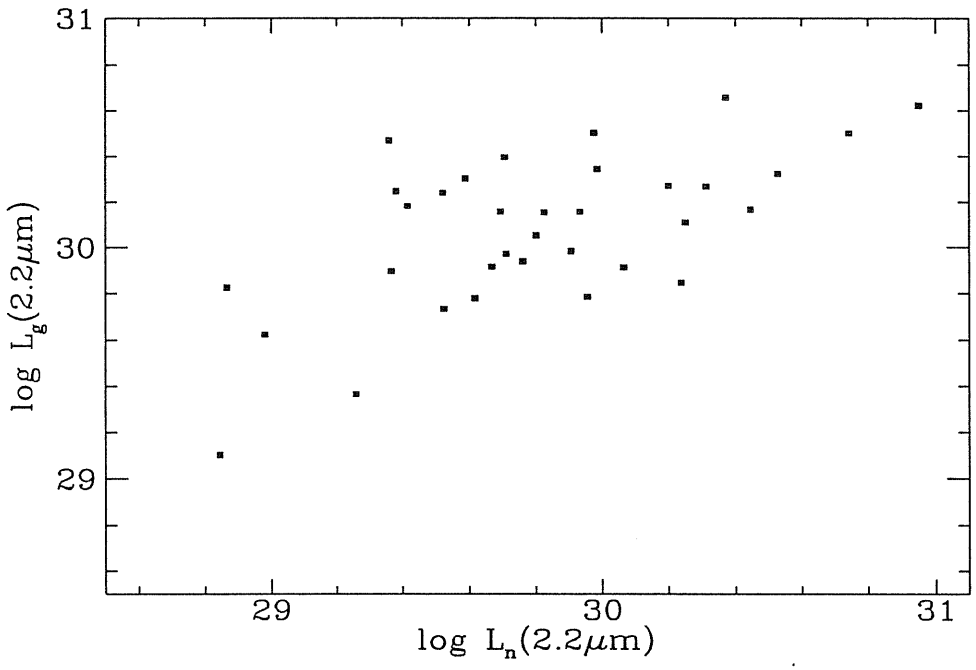

Figure 2.2: Galactic versus nuclear luminosities (erg/s/Hz) at 2.2 μm.

("Seyferts") we get a median $M_{Kg} = -25.5$.

Assuming that the colors of galaxies hosting an active nucleus are similar to those of normal early type spirals ($B-K = 4.15$, $V-K = 3.2$, Griersmith et al. 1982) the M_{Kg} corresponds to $M_{Bg} = -21.55$ and to $M_{Vg} = -22.5$ in the case of galaxies hosting PG QSOs; to $M_{Bg} = -21.35$ and to $M_{Vg} = -22.30$ for "Seyferts".

In Fig. 2.2 we have plotted the monochromatic luminosities at 2.2μm of the host galaxies against those of the nuclei; there is a clear correlation, significant at the 99.9% confidence level, that might at least partly be accounted for by selection effects. In particular, bright galaxies with low luminosity nuclei, which would populate the upper left corner, are likely to be under–represented in our sample of UV excess objects. On the other hand, the correlation is still significant if we confine ourselves to bright nuclei. Using the K–band local luminosity function of spiral galaxies (Franceschini et al. 1991) we find that the fraction of such galaxies hosting a nucleus brighter than $M_{Kn} = -25$ (corresponding to $M_{Bn} \approx -22.5$) strongly decreases with

galactic luminosity: it is $\simeq 3 \times 10^{-3}$ for $-27 < M_{Kg} < -26$, it falls to $P \simeq 3 \times 10^{-4}$, for $-26 < M_{Kg} < -25$, and becomes very small for galaxies fainter than $M_{Kg} = -25$.

It thus appears that bright AGNs tend to live in bright galaxies, whereas low luminosity nuclei may reside in galaxies of any luminosity.

As mentioned above, on average the $J-K$ and $H-K$ colors of galaxies in our sample are slightly redder than those of the normal galaxies. On the other hand, they turn out to be slightly bluer than those of starbursting and HII galaxies: based on the samples of such galaxies observed by Lawrence et al. (1985) and Glass & Moorwood (1985) we find: $< J-K >= 1.25$ and $< H-K >= 0.5$. Similar results have been derived by Joseph et al. (1984) for a sample of interacting galaxies.

It is also interesting to note that the average values of $(J-H)_g$ and $(H-K)_g$ of the host galaxies are close to the values measured along the major axis of NGC 253 at distance of 1 to 3 kpc by Scoville et al. (1985), who argued that the colors are probably due to reradiation by hot dust associated with star forming regions. They are also compatible with the observed distribution of colors across the center of M82 (Telesco et al. 1991).

In conclusion our data are consistent with the suggestion that nuclear activity in galaxies is often associated with moderate starbursting activity in central regions.

The possible correlation of the nuclear with starburst activity is matter of debate (see e.g. Heckman 1987; Terlevich and Melnick 1987; Scoville 1988). On the other hand evidences of circumnuclear starbursting activity in AGNs have been accumulated. For instance recent high resolution optical and radio observations of NGC 7469 support the presence of a starbursting region confined within 1 kpc (Wilson et al. 1991).

Moreover observations of CO emission in Seyfert galaxies detected molecular gas in the circumnuclear regions that could fuel both the nuclear activity as well as a moderate star forming activity. Heckman et al. (1989) have shown that Seyfert galaxies of both types exhibit a well defined correlation between the CO and far–infrared luminosity, as normal and starburst galaxies do. They also pointed out that Seyfert 1 galaxies look relatively normal in the overall abundance of CO. Meixner et al. (1990) observed three nearby Seyfert 1 galaxies at high resolution and found that a large portion of their CO emissions comes from regions within a few kpc of the nucleus. Taniguchi et al. (1990) found that there is no significant difference in circumnuclear molecular gas densities between Seyferts and starburst nuclei.

2.3.2 The Emission at IRAS Wavelengths

Using the IR luminosities of the nuclei and underlying galaxies, we can explore the problem of the respective contributions also in the far IR. More than half of the objects we observed in IR have been detected by IRAS and for the others reliable upper limits are often available.

Ground observations at 10 μm with small apertures ($\leq 5''$) compared to IRAS 12 μm data have been used by many authors to illustrate the relative importance of the nuclear and galactic emissions (Edelson et al. 1987; Neugebauer et al. 1987; McAlary and Rieke 1988; Roche et al. 1991). Following Edelson, Malkan & Rieke (1987), we can define the *compactness parameter* R as the ground–based to IRAS flux at 12 μm for 14 objects of our sample. The minimum value of R is 0.53 (it refers to Mrk 530 which has a nucleus particularly faint respect to the galaxy) and the median is 0.8. This result is indicative of the predominance of the nuclear emission at 12 μm. However spiral galaxies are known to be strong emitters in the far IR and this circumstance could reverse the relative importance of the nuclear to the galactic contribution with increasing wavelength.

In order to investigate this possibility, we have reported in in Figs. 2.3–2.6 the luminosities (and upper limits) in the IRAS bands against the nuclear and the galactic luminosities at 2.2 μm. It is apparent that the correlation between the 2.2 μm nuclear and IRAS luminosities tends to weaken with increasing wavelength, whereas the opposite holds for the galactic luminosities $L_g(2.2\ \mu\mathrm{m})$. Of course in analyzing the correlations it should be kept in mind that nuclear and galactic luminosities are correlated (see above).

We have investigated the correlations using various statistics: Kendall's coefficient of concordance W, Kendall's rank correlation coefficient τ and partial correlation coefficient $\tau_{xy;z}$, Spearman partial rank correlation coefficient (Macklin 1982) and the usual correlation coefficient. In particular we used a generalized version of Kendall's rank correlation and of the usual correlation coefficient statistics which take into account also the upper limits in the observations (see Schmitt 1985; Isobe et al. 1986). In Table 2.2 we have reported the results.

All the tests indicate that the strongest correlation is between the nuclear luminosities $L_n(2.2\,\mu\mathrm{m})$ and 12 μm luminosities $L(12\,\mu\mathrm{m})$. For example the probability of reproducing the correlation by chance is $P_k \leq 10^{-5}$ both for W and τ statistics, and the correlation coefficient is high ($r = 0.8$). The analysis with the partial correlation coefficient confirms that the correlation between $L_n(2.2\,\mu\mathrm{m})$ and $L(12\,\mu\mathrm{m})$ is relatively independent of the galac-

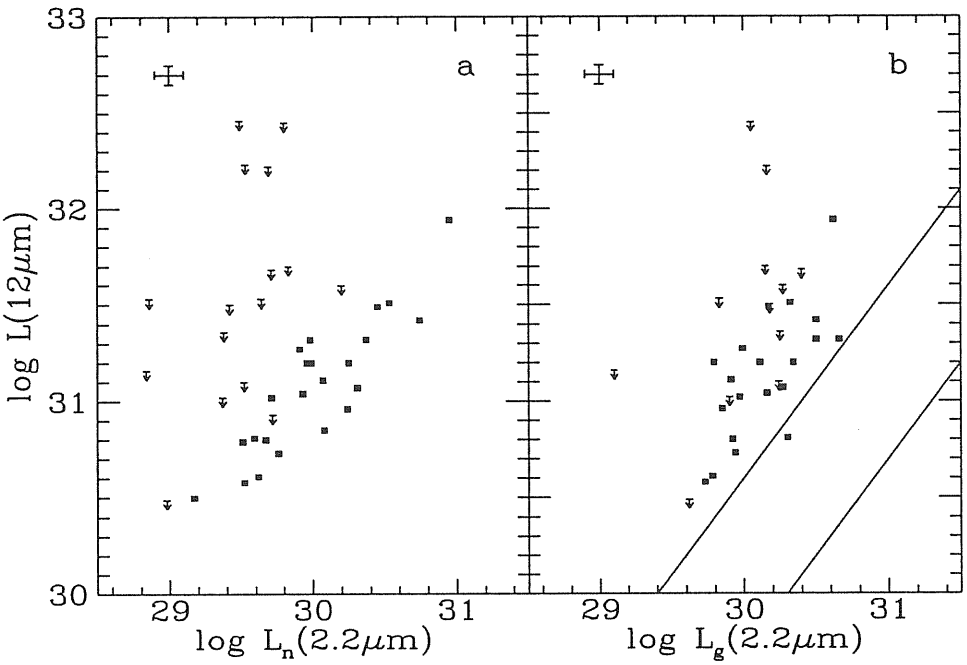

Figure 2.3: IRAS 12 μm luminosities (erg/s/Hz) versus nuclear (panel a) or galactic (panel b) luminosities (erg/s/Hz) at 2.2 μm. The upper and lower lines bound the range of galaxian contributions inferred from the distribution of 2.2 μm to 12 μm luminosity ratios for a sample of normal spiral galaxies (see text). The typical error bars of the data along the two axes are also shown (upper left corner)

tic K luminosities: keeping $L_g(2.2\,\mu m)$ constant the correlation coefficient changes from 0.66 to 0.53 and the probability (computed using the Spearman partial rank correlation coefficient) that the correlation entirely arises from the $L_n(2.2\,\mu\mathrm{m})$– $L_g(2.2\,\mu\mathrm{m})$ and $L_g(2.2\,\mu\mathrm{m})$–$L(12\,\mu\mathrm{m})$ ones separately is $P_{xy;z} \simeq 5.6 \times 10^{-4}$. The correlation between $L_g(2.2\,\mu\mathrm{m})$ and $L(12\,\mu\mathrm{m})$ is a little less significant ($\tau = 0.57$ and $r = 0.63$) and decreases substantially ($\tau = 0.39$) at constant $L_n(2.2\,\mu\mathrm{m})$. The above results is in keeping with the large compactness ratios R we have found. The statistical predominance of the nuclear emission is confirmed even at 25 μm, whereas at 60 μm a clear change occurs. The correlation coefficient between $L_n(2.2\,\mu\mathrm{m})$ and $L(60\ \mu\mathrm{m})$ is $\tau = 0.47$, smaller than that between $L_g(2.2\ \mu\mathrm{m})$ and

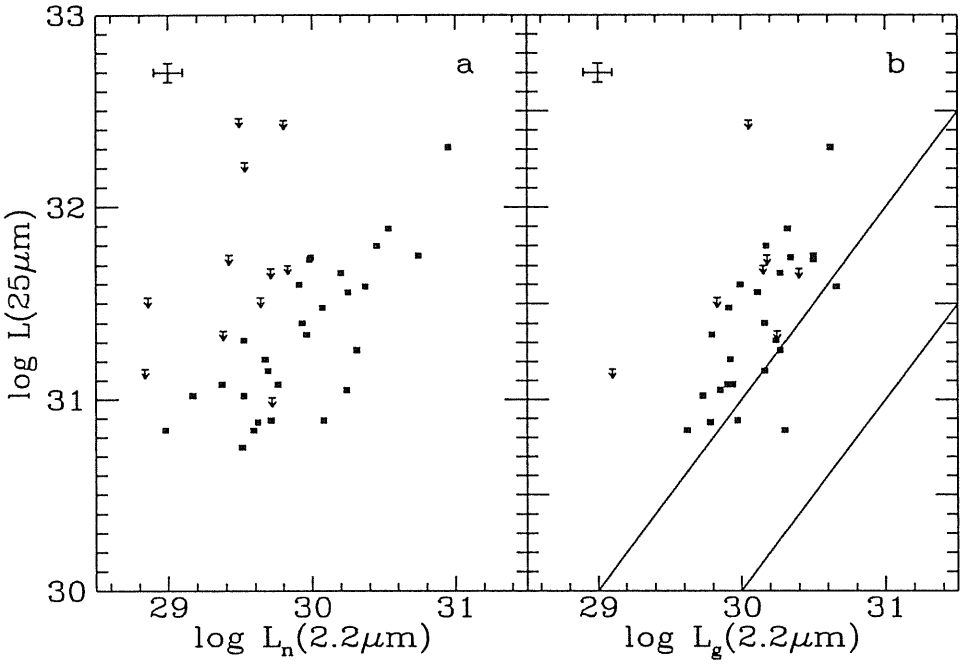

Figure 2.4: Same as the previous figure but for 25 μm luminosities.

	Detections and Limits		Detections only		
Values Correlated	P_k	r	τ	$\tau_{x,y;z}$	$P_{x,y;z}$
$L_{2.2,n}$—L_{12}	8×10^{-6}	0.82	0.66	0.53	5.6×10^{-4}
$L_{2.2,g}$—L_{12}	8×10^{-4}	0.63	0.57	0.39	1.1×10^{-2}
$L_{2.2,n}$—L_{25}	7×10^{-6}	0.80	0.61	0.48	7.4×10^{-4}
$L_{2.2,g}$—L_{25}	3×10^{-4}	0.67	0.52	0.34	2.7×10^{-2}
$L_{2.2,n}$—L_{60}	4×10^{-3}	0.46	0.47	0.32	0.18
$L_{2.2,g}$—L_{60}	4×10^{-4}	0.71	0.51	0.37	1.4×10^{-2}
$L_{2.2,n}$—L_{100}	0.25	0.27	0.42	0.27	0.22
$L_{2.2,g}$—L_{100}	7×10^{-3}	0.40	0.50	0.39	2.1×10^{-2}

Table 2.2: 2.2 μm–IRAS correlations

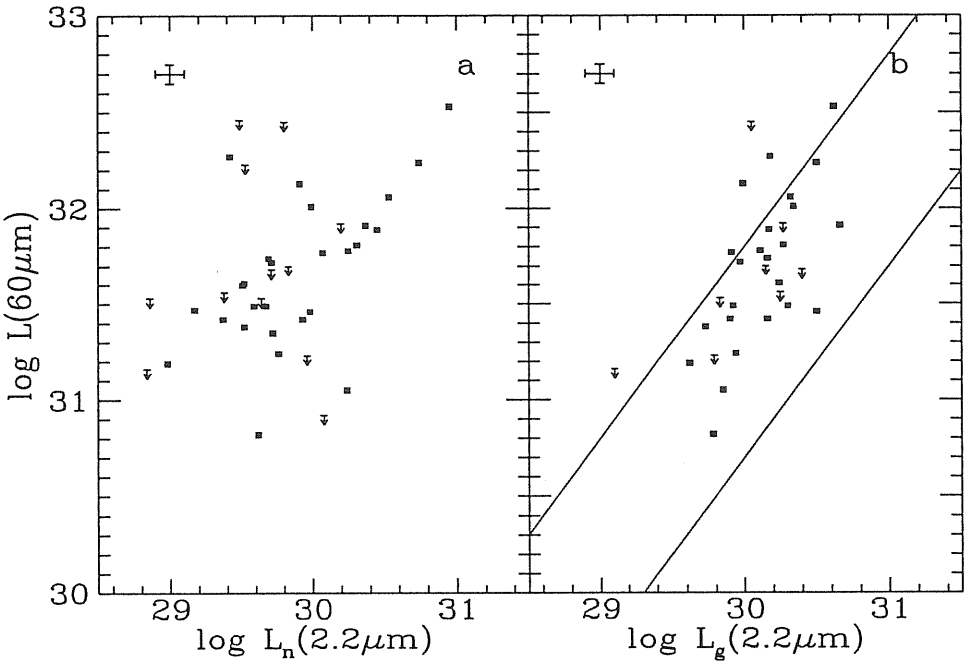

Figure 2.5: Same as the previous figure but for 60 μm luminosities.

$L(60\,\mu\mathrm{m})$ ($\tau = 0.51$). Moreover the partial correlation coefficient between $L_n(2.2\,\mu\mathrm{m})$ and $L(60\,\mu\mathrm{m})$, at constant $L_g(2.2\,\mu\mathrm{m})$, is only $\tau = 0.32$. The probability that the correlation $L_n(2.2\ \mu\mathrm{m})$ and $L(60\,\mu\mathrm{m})$ entirely arises from the $L_n(2.2\,\mu\mathrm{m})$–$L_g(2.2\,\mu\mathrm{m})$ and $L_g(2.2\ \mu\mathrm{m})$–$L(60\,\mu\mathrm{m})$ ones separately is $P_{xy;z} \simeq 0.18$, whereas in the case of $L_g(2.2\,\mu\mathrm{m})$ and $L(60\ \mu\mathrm{m})$ the probability of a completely induced correlation drops to $P_{xy;z} \simeq 1.3 \times 10^{-2}$. The trend of an increasing statistical relevance of the galactic contribution to the far IR emission with increasing wavelengths is confirmed by the 100 μm data. In this case the correlation coefficient of $L(100\,\mu\mathrm{m})$ with $L_g(2.2\,\mu\mathrm{m})$ is $r = 0.40$, but is only $r = 0.27$ in the case of $L(100\,\mu\mathrm{m})$ versus $L_n(2.2\,\mu\mathrm{m})$.

We conclude that the nuclear contribution to the far IR emission of Seyfert galaxies is definitely decreasing with increasing wavelength. As a further test of this conclusion we have examined the distribution of the ratios of the IRAS to the K–band luminosities of a sample of normal early type spirals. From a sample of normal spiral galaxies collected by Devereux (1987, 1989) we chose the objects observed in the K band with apertures large

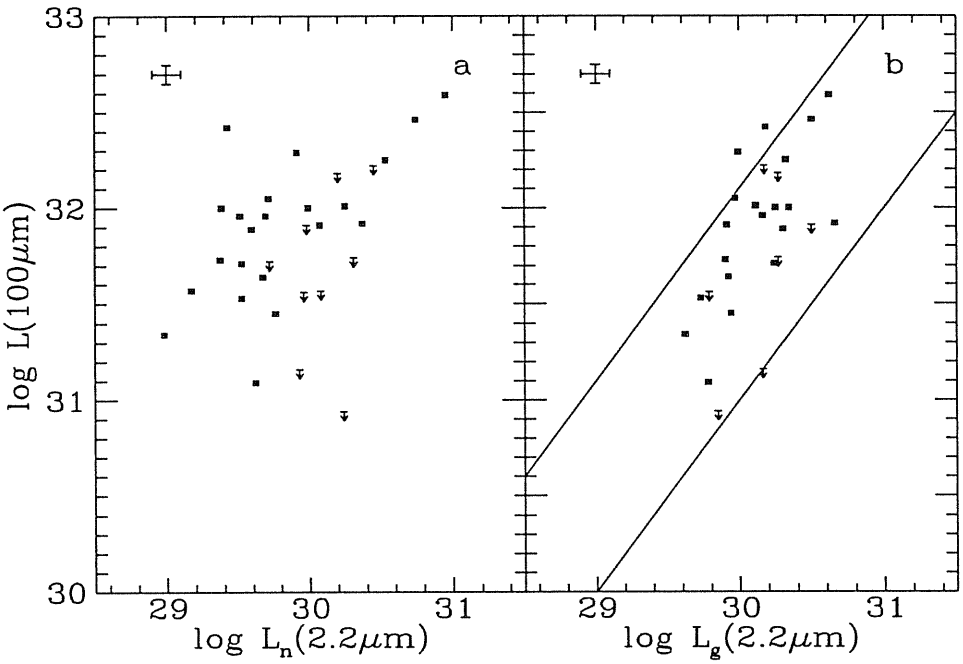

Figure 2.6: Same as the previous figure but for 100 μm luminosities.

enough to allow for a reliable determination of their total luminosities. The ratios $L(12\,\mu\mathrm{m})/L(2.2\,\mu\mathrm{m})$ range from 0.5 to 4.5 with a median $r_{12-2.2} \simeq 2$; the $L(25\,\mu\mathrm{m})/L(2.2\ \mu\mathrm{m})$ ratios vary from 1 to 10 with a median value $r_{25-2.2} \simeq 4$; at 60 μm the ratios fall between 5 to 65 and the median value is $r_{60-2.2} \simeq 22$; finally, the ratios $L(100\,\mu\mathrm{m})/L(2.2\,\mu\mathrm{m})$ are in the interval 10 to 120 with a median value $r_{100-2.2} \simeq 50$. For sake of comparison we notice that a small subsample of IRAS selected luminous bright galaxies observed by Carico et al. (1988, 1990) have $100 \leq r_{60-2.2} \leq 700$. Using these results we have reported in Figs. 2.3, 2.4, 2.5, 2.6 the maximum and minimum possible contribution (upper and lower lines) of the host galaxies to the total luminosities. While the observed luminosities at 12 and 25 μm are mostly above the maximum, at 60 and 100 μm they are well within the possible contributions of the host galaxies.

Rodriguez Espinosa, Rudy & Jones (1986, 1987) pointed out that the spectral indices between 60 and 100 μm, α_{60-100}, ($f_\nu \propto \nu^\alpha$) of Seyfert and starburst galaxies are quite similar. We confirm their result for our sample

of Seyferts, which has a α_{60-100} distribution similar to that of the starburst galaxies of the optically selected sample investigated by Sekiguchi (1987). However their claim that 75% of the Seyfert galaxies in their sample have *massive* starburt episodes, is based on a rather arbitrary choice for the lower limit of the luminosities of the starburst galaxies ($L_{fir} > 10^{44}\,\mathrm{erg\,s^{-1}}$). Actually, as we have shown above, the galaxies hosting AGNs are usually brighter than L_* (the typical luminosity where the luminosity function is falling exponentially) and the 60 and 100 μm emissions of the Seyferts are compatible with the emission from the host galaxies, with ratios between the IR (stellar) and the far–IR (dust) luminosities typical of normal or moderate starburst galaxies.

In conclusion there is statistical evidence that in Seyfert 1 galaxies the nuclear emission largely dominates at 12 μm and is still important at 25 μm, while longward of 60 μm the emission from the host galaxies is overwhelming. This result is also in keeping with the fact that in a 12 μm flux–limited sample the percentage of galaxies harboring active nuclei can be higher than 20% (Spinoglio and Malkan 1989).

A similar conclusion has been drawn by Berriman (1989) on the basis of the correlation of the polarization with the luminosities at 12 and 25 μm.

If the observed IR and mid–IR spectrum is ascribed to synchrotron emission, as suggested by Band & Malkan (1989), a consequence of the galaxy dominance at 60 μm is that the turnover in the synchrotron self–absorbed power law must occur at shorter wavelengths. At longer wavelengths the spectrum of Seyfert 1 is likely to be dominated by the cold dust emission in the host galaxies, in agreement with the steep fall–off of the spectrum of Seyfert 1 galaxies and QSOs in the submillimeter regions observed by several authors (Engargiola et al. 1988; Chini et al. 1989; Edelson et al. 1987; Lawrence et al. 1991).

As expected from the above discussion, the Seyfert 1 galaxies of our sample exhibit a slope α_{12-60} definitely flatter than those of normal and starburst galaxies. The flatness of the IR spectra of AGNs has been noticed by many authors (e.g. Miley et al. 1985; Edelson 1986; Edelson et al. 1987). In particular Edelson (1986) showed that the spectral indices α_{12-60} of AGNs are much flatter than those of normal galaxies.

As it is apparent from Fig. 2.7, the distributions of α_{12-60} for our sample and for an optically selected sample of normal spiral galaxies detected at 12 μm are quite different with a negligible probability $P(F1 = F2) \leq 4 \times 10^{-5}$ that they have been drawn from the same parent population (here and in the following we will use the Gehan's test and the Peto–Prentice generalized

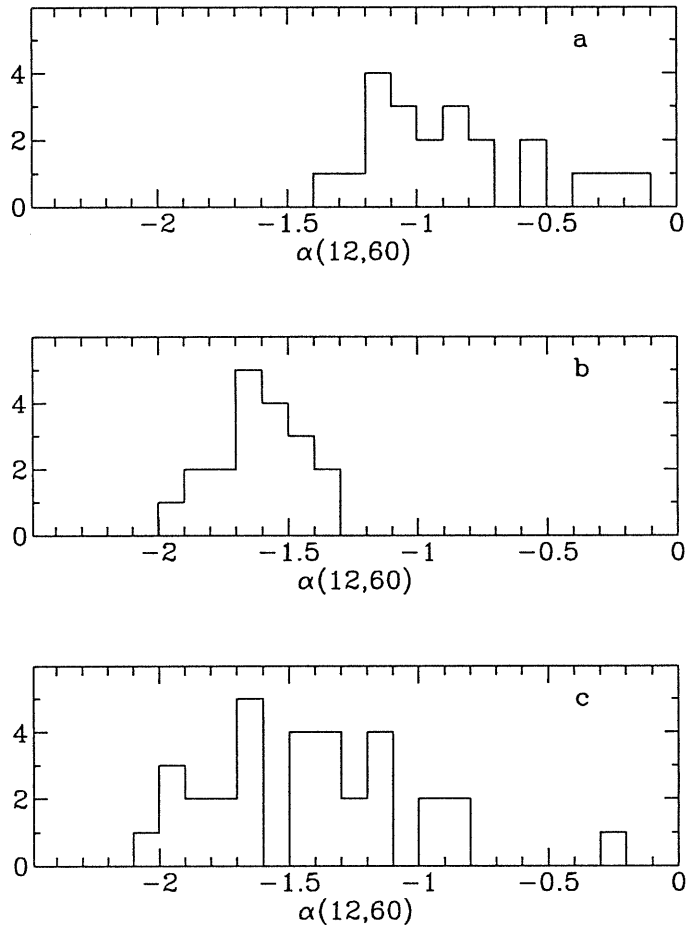

Figure 2.7: Distributions of the α_{12-60} slopes. Panel a: type 1 Seyferts in our sample; panel b: normal optically selected spirals; panel c: type 2 Seyferts selected at 12 μm (Spinoglio and Malkan 1989).

Wilcoxon statistic in comparing distributions).

For starburst galaxies Xu & De Zotti (1989) found an average $\alpha_{12-60} \simeq -1.9$, while the median value of our Seyfert galaxies is -0.9 (for both classes we used in the statistics only objects detected at both wavelengths).

On the other hand the distribution of the slopes α_{12-60} for the Seyfert 1 galaxies in the CfA sample looks very similar to that of our Seyferts ($P(F1 = F2) \simeq 0.15$), as might be expected on the basis of the fact that about half of the objects are common to the two samples. However in the CfA sample there are five objects out of nineteen with $\alpha_{12-60} < -1.5$, the minimum value for our sample; three objects, NGC 2992, NGC 3227 and NGC 5033, have very low total luminosities ($M_B > -19.4$) and two others, Mrk 231 and NGC 7469, have large starbursts (Aitken et al. 1981; Cutri et al. 1984; Wilson et al. 1991).

The IRAS data on the hard X–ray selected AGN sample of Piccinotti et al. (1982) again confirm that the AGNs have α_{12-60} slopes flatter than normal and starburst galaxies; the statistical tests on this distribution in comparison to ours give $P(F1 = F2) \simeq 0.20$.

It is worth noticing that the Seyfert 1 galaxies selected on the basis of their 12 μm emission by Spinoglio & Malkan (1989) show a distribution of α_{12-60} quite similar to those of our optically selected sample ($P(F1 = F2) \sim 0.2$).

Seyfert 2 galaxies in the CfA sample (Edelson et al. 1987) and those selected at 12 μm (Spinoglio and Malkan 1989) exhibit distributions much broader than those of Seyfert 1 samples (the probability that they are drawn for the same parent distribution is only $P \sim 2 \times 10^{-3}$), probably because of a larger variety of luminosity ratios among different emission mechanisms. However in this context it is quite interesting to note that NGC 1068 has a slope $\alpha_{12-60} \simeq -1$, close to the average value of our sample.

In a sample of optically selected non–active spiral galaxies the objects with $\alpha_{12-60} \geq -1.5$ are only 15% of the total number; the percentage reaches 20% if the primary selection has been done at 12 μm. Contrariwise, less than 15% of Seyfert 1 galaxies have $\alpha_{12-60} \leq -1.5$, independently of the primary selection (optical or mid–IR); these objects usually possess faint nuclei or exhibit large starbursts. No non–active spiral galaxy has a slope flatter than -1.1, while more than 50% of the Seyfert 1 galaxies do. Therefore we can conclude that extragalactic objects with $\alpha_{12-60} > -1.5$ are good AGN candidates.

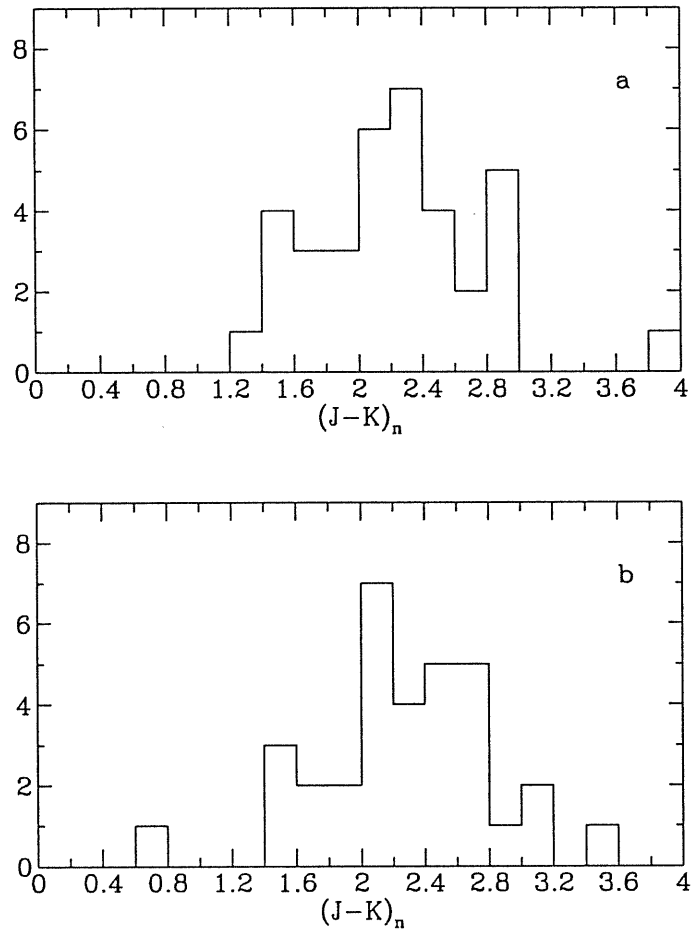

Figure 2.8: Distribution of nuclear (J-K) colors. Panel a: our sample; panel b: hard X-ray selected sample (Koitilainen et al. 1991b).

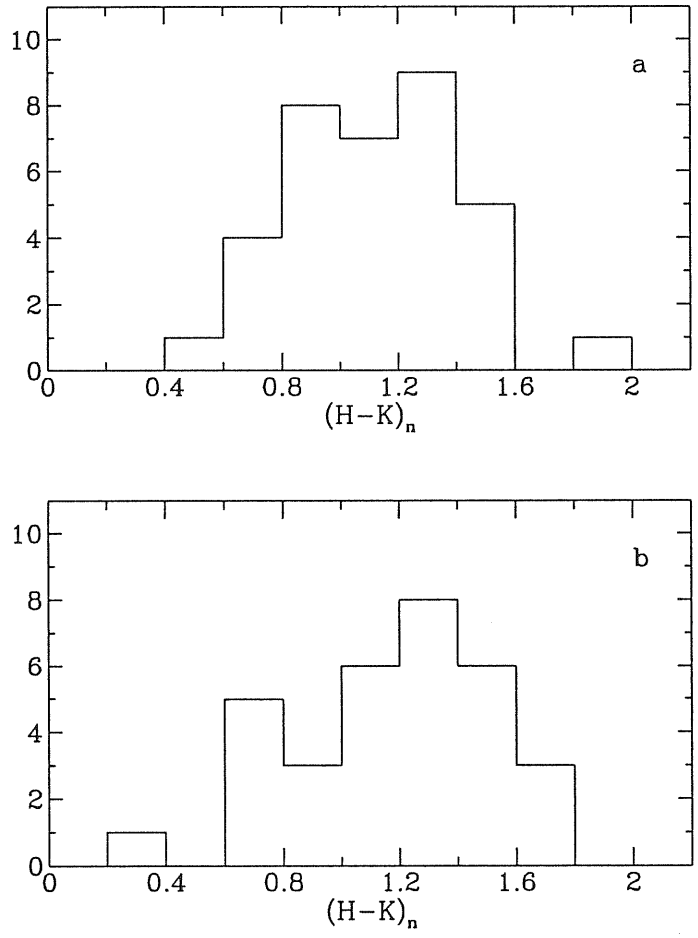

Figure 2.9: Same as the previous figure but for (H-K).

2.3.3 Near and Mid–IR Colors of the Nuclei

The distributions of the $(J-K)_n$ and $(H-K)_n$ colors of the nuclei of our sample are presented in Figs. 2.8 and 2.8a. The average values, $< J-K >= 2.25 \pm 0.1$ (rms), $< H-K >= 1.19 \pm 0.06$ for our sample are quite close to the median values, but it is evident that there is a considerable spread. For sake of comparison we have reported in Figs. 2.8 and 2.8b the IR colors of the nuclei of an X–ray selected sample of Seyfert galaxies (Koitilainen et al. 992b). The distributions of (J-K) and (H-K) colors are very similar; as an example, for $(J-K)_n$ colors the statistical tests give $P(F1 = F2) \simeq 0.7$. Moreover the slopes between the 2.2, 12 and 25μm of the two samples are compatible.

A detailed modellistic analysis of the nuclear SEDs will be presented in Chapter 5. A few general points are worth noticing here. Many nuclei in the sample exhibit curved IR spectra, with an excess at 3-5 μm already noted by several authors (see e.g. Neugebauer et al. 1979). Our optical and IR data confirm the claim by Sanders et al. (1989) that a minimum in νf_ν around 1 μm is a common feature in AGN spectra. This minimum suggests that the emission mechanism dominating the optical part of the spectrum fades at longer wavelengths, where a different process is emerging.

If we take into account the emission by the host galaxies at $\lambda \geq 60$ μm discussed above, the nuclear spectra are remarkably curved. Synchrotron models have many drawbacks in fitting this kind of spectra, because they require high magnetic fields (larger than hundred Gauss), small sizes of the emitting regions (smaller than several light–days) and large ratios of the photon–to–magnetic energy density (see Band and Malkan 1989; Lawrence et al. 1991). On the other hand, dust emission models naturally reproduce the raising in the near IR (dust grains sublimate at 1000–1500 K) and the fall off at $\lambda \geq 60$ μm (Barvainis 1987; Barvainis 1990; Sanders et al. 1989).

2.3.4 The Relation of IR and X–Ray Nuclear Luminosity

The correlation between near IR and X–ray luminosities of AGNs has been explored by many authors (e.g. Glass 1979; Malkan 1984b; Wilkes and Elvis 1987; Carleton et al. 1987; McAlary and Rieke 1988; Kriss 1988; Mushotzky and Wandel 1989; Sanders et al. 1989), to probe the relevance of the non–thermal emission in the IR band. So far no definite conclusion has been reached.

Although the objects of our sample detected in X–rays span only two

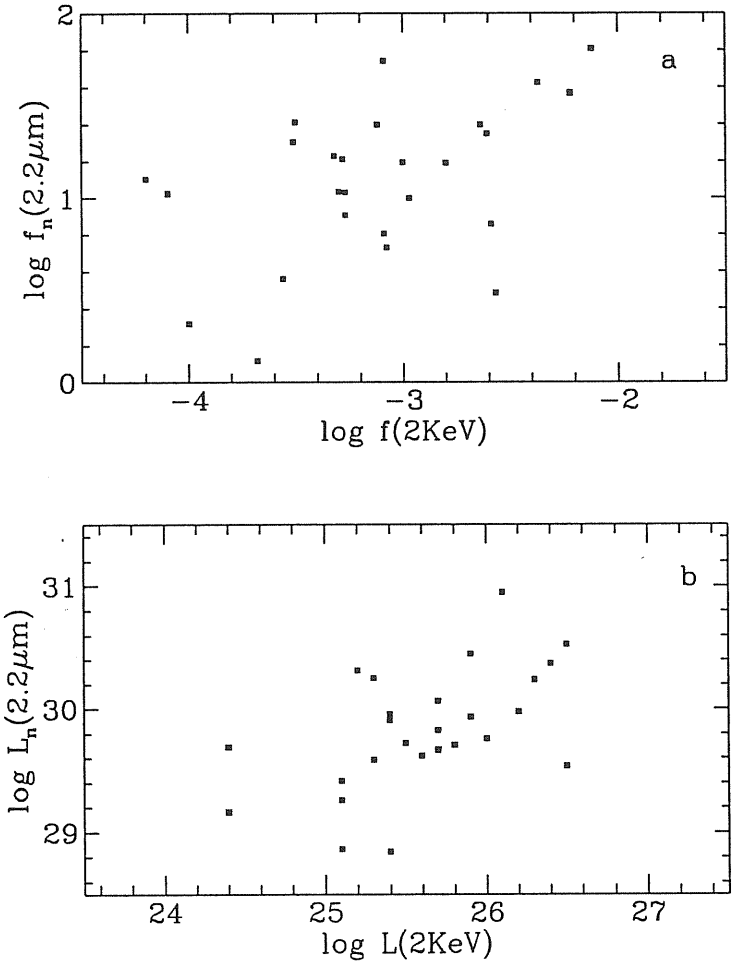

Figure 2.10: Panel a: nuclear fluxes (mJy) at 2.2 μm versus fluxes at 2 keV. Panel b: same as in panel a but in terms of luminosities (erg/s/Hz).

decades in flux or in luminosity both at 2.2 μm and at 2 keV (Figs. 2.10), a positive correlation is discernible. Kendall's rank test gives a probability of 0.03 that the correlation of the fluxes is spurious. As for the luminosities the probability of a spurious correlation falls to $P \leq 0.003$. The classical correlation coefficient is also significant ($r = 0.58$) and the fit suggests that the correlation is not linear: $L_{2\mathrm{keV}} \propto L_{2.2}^{0.63\pm0.17}$. The result is in reasonable agreement with that found by Kriss (1988), who explored the correlation of the 2 keV luminosity with the luminosity at 1 μm for a sample of 88 AGNS and radio–quiet QSO's. Indeed, using the 1.26 μm monochromatic luminosities, we found $L_{2\mathrm{keV}} \propto L_{1.26}^{0.75\pm0.20}$ quite close to Kriss' result ($L_{2\mathrm{keV}} \propto L_{1\ \mu\mathrm{m}}^{0.73}$). A closer to linear correlation has been found by Mushotzky & Wandel (1989) between the X–ray and 0.75 μm rest frame luminosities ($L_x \propto L_{0.75}^{0.85}$). On the contrary, Sanders et al. (1989) claimed that there is no evidence of any correlation between the 2 keV and the 3.5 μm fluxes of PG QSOs, and argued that objects covering a narrow range of fluxes occupy a strip in luminosity–luminosity plots, thus mimicking a correlation. All these authors have used *Einstein Observatory* X–ray data.

Hard X–ray data were used by McAlary & Rieke (1988) who concluded that the emission at 6 keV of their *hard X–ray* selected sample of Seyfert 1 galaxies doesn't show any significant correlation with the emission at 3.5 μm. On the other hand, Carleton et al. (1987), using a similar sample, found a strict correlation between the hard X–ray and the infrared *baseline* luminosity. They exploited this correlation to derive a rough estimate of the possible non–thermal IR component.

Our statistical analysis suggests that the correlation between X–ray and IR emission is significant at $\lambda = 2.2\ \mu m$ and increases both in significance and in linearity with decreasing IR wavelength. These facts are not in contrast with an IR continuum dominated by thermal dust reradiation. Actually many models predict a tight connection between X–ray and UV–optical emissions of AGNs: X–ray photons can be produced by Compton upscattering of UV–optical photons by high energy electrons, or, alternatively, X–ray primary photons may be reprocessed into UV–optical photons (see e.g. Collin-Souffrin 1991). On the other hand thermal dust emission is directly powered by the UV emission of the nucleus. Therefore is not surprising that a significant correlation between the IR and X–ray emissions exists. Of course this argument also implies that the variability in the three bands are related (see below).

A further interesting fact, on which we will return in Chapter 5, is that an important fraction of the total luminosity of the nuclei is emitted in

the near and mid–IR: for the majority of our objects the IR (1.2–25 μm) luminosity is more than 3 times their X–ray luminosity (2–10 keV) and can reach 30 – 40% of the bolometric luminosity. Therefore any model which attributes the IR emission to dust must solve the problem of producing such huge amount of light at shorter wavelengths and enough dust to absorb it.

2.4 Conclusions

We have analyzed new IR data on 41 Seyfert 1 galaxies out of the 56 comprised by the *homogeneous* optically selected sample defined by Cheng et al. (1985).

Almost all the galaxies exhibit detectable bulge and disk components, confirming that AGNs are preferentially located in early type spirals. The average luminosity of the host galaxies falls in the high luminosity tail of the K band luminosity function of the spiral galaxies. The probability that a spiral galaxy hosts a bright AGN increases with its luminosity. The average colors of the hosts are close to the colors of moderately starbursting galaxies.

The galaxian 2.2 μm luminosities correlate with 60 and 100 μm luminosities, whereas the 12 and 25 μm luminosities show a tighter correlation with the nuclear luminosities. This fact statistically demonstrates the predominance of the disc emission longward of 25 μm. As a consequence, any synchrotron emission must fall off at these wavelengths. The total 60 and 100 μm luminosities can be easily accounted for if the host galaxies have $L(60\,\mu\mathrm{m})/L(2.2\,\mu\mathrm{m})$ and $L(100\,\mu\mathrm{m})/L(2.2\,\mu\mathrm{m})$ ratios similar to those of galaxies with normal or moderately enhanced star formation rates.

The curved IR spectra of the nuclei are more easily modelled by dust emission rather than by synchrotron. Moreover synchrotron emission would imply variability on time scales of order of several light–days, whereas at IRAS wavelengths radio–quiet QSOs and AGNs show no evidence of variability (Edelson and Malkan 1987) at least on time scales of up to few months.

We also substantiated the suggestion that the slope α_{12-60} can be used to efficiently select AGN candidates. In particular only 15% of Seyfert 1 galaxies in our sample (either hosting a weak nucleus or undergoing a violent starbust) have $\alpha_{12-60} < -1.5$, whereas 85% of the normal galaxies do.

Our data confirm that there is correlation between the IR (K band) and the X–ray (2 keV) emissions. We have also found that the correlation strengthens with decreasing wavelength. We argued that this is not inconsis-

tent with dust emission dominating the IR. Actually almost all the models of AGN continua predict a strict correlation between the UV–optical and X–ray luminosities, thus the correlation between X–ray and IR can be induced by the fact that dust is heated by UV–optical radiation. The studies on the variability of Fairall 9 (Clavel et al. 1989) support the dust emission model: while the optical and the J fluxes varied in the same sense and almost in phase with the UV continuum, the K and L emissions show a delay of about 400 days.

Our data support a picture in which the nuclear emission of optically selected AGNs in the IR is the sum of two components. The first one is the fading part of the UV–optical emission. At $\lambda \geq 3$ μm it is overwhelmed by the emission of the *circumnuclear* dust, which is important up to $\lambda \simeq 60$ μm, where the galactic disc contributions start to dominate the total emission.

Chapter 3

Optical Observations

Summary. We[1] present CCD observations in BVR optical bands of the homogeneous sample of 42 Seyfert 1 galaxies, that we also observed in near–IR JHK bands (Chapters 1 and 2). We have applied to these data the same analysis procedure used for the infrared images, with the aim of separating the galaxian and nuclear fluxes, as well as investigating the main characteristics of the hosts. Nuclear fluxes have been estimated with typical global errors of 0.15 mag, while 0.3 mag errors are on average associated to host galaxy magnitudes. It is shown that in half of the host galaxies the bulge contribute more than 40% to the total observed fluxes even within small apertures. In the sample galaxies disks are dominating over the bulge in the large majority of the cases, suggesting that a significant fraction of Seyfert galaxies could be late type spirals. Moreover the galactic morphological parameters are in the ranges of typical spiral galaxies. The statistics of galactic colors show that the host galaxies tend to be bluer than the normal ones. This fact added to redder colors found in the IR–bands strengthens the suggestion that in Seyfert galaxies the star formation is on average enhanced.

[1]This Chapter is based on a paper published in collaboration with V. Zitelli, L. Danese, F. Bonoli, F. Delpino and C. Bonoli (Granato et al. 1993)

3.1 Introduction

Low luminosity local Active Galactic Nuclei (AGN) such as Seyfert 1 nuclei are important clues on nuclear activity. Their continuity with QSOs is now well assessed, increasing the interest in their properties. Therefore studies on local AGN have considerably expanded and a large wealth of data has been accumulated in the last few years thanks to improved sensitivity and spatial resolution of the astronomical detectors.

The nuclear continuum extends over the entire observable spectrum, and various emission mechanisms are expected to work at different wavelengths. In particular it has been suggested by many authors that the optical and IR emissions could well be ascribed to thermal rather than non-thermal mechanisms (see for instance Bregman 1990 and references therein). However in the optical and infrared bands the host galaxies often may add relevant contributions to the total light even in the case of photometric observations with small apertures. In the past, many efforts have been made in order to solve this problem deriving magnitudes of the bare nucleus using photometric data (Sandage 1973; Penston et al. 1974; Cheng et al. 1985; McAlary and Rieke 1988; Simons et al. 1988) together with assumptions about the host galaxy and/or the nucleus. With these methods, the information about the host were completely lost, and the results even for the nucleus had in general quite large (systematic) error bars, though they might still give useful information at least for statistical purposes.

More recently many studies (see e.g. Yee 1983; Ward et al. 1987; Geheren et al. 1984; Malkan 1984; Malkan et al. 1984; Hutchings et al. 1984; Smith et al. 1986; Kruper and Canizares 1989; Veron-Cetty and Woltjer 1990; Koitilainen et al. 992a; Zitelli et al. 1993) have exploited the information contained in two dimension images to separate nuclear and galaxy fluxes both for QSOs and Seyfert galaxies. Methods based on imaging can give, if carefully implemented, much more reliable results, but they have the obvious disadvantage of requiring much more time consuming data reduction and analysis procedures. On the other hand relationships and interactions between nuclear activity and properties of host galaxies can be investigated using the opportunity of resolving nuclei from underlying galaxies.

Precise evaluation of the local Luminosity Function of the optically selected AGN, particularly at the faint end, is obtainable only in the case of accurate separation of the nuclear from the galactic luminosity. Moreover accurate estimates of the nuclear optical and IR emissions are also needed for meaningful correlations with other wavelength nuclear emissions. The

determination of truly nuclear fluxes of a well defined and statistically significant sample of AGN is of course extremely important, when discussing the possible emission mechanisms operating in the IR and optical bands.

As in the previous Chapters, we have concentrated ourselves on the sample of Seyfert 1 and 1.5 galaxies defined by Cheng et al. (1985), from which they derived the luminosity function of low luminosity AGN. We remind again that the sample comprises 56 AGNs in the area covered by the first nine Markarian lists (see references in Cheng et al. 1985), with the restrictions $U \leq 16.3$, $M_u \leq -18.5$ and $z \leq 0.08$. It has been shown that there is no significant correlation of the apparent magnitudes with the absolute magnitudes, or with the ratios of the fluxes of the nuclei to those of the underlying galaxies. Following Neyman and Scott (1961, 1974) the sample is called *homogeneous* (see also Chapter 4) in the sense that the probability for an objects to be included depends solely on apparent magnitude.

In this Chapter we will present the observations of 42 objects in BVR filters obtained with a CCD camera in the Cassegrain focus of the Bologna Observatory 1.52 m telescope at Loiano. We have already presented and discussed the results of IR observations (K-band frames and JHKL photometry) for 41 sample objects (Chapters 1and 2or Zitelli et al. 1993; Danese et al. 1992). Moreover about 70% of the sample objects have been detected in one of the IRAS bands and the same percentage has been detected also in radio. X-ray observations allow for the computation of 2 keV fluxes for about 60% of the objects.

3.2 Observations and Initial Reduction

3.2.1 Observations

The observations were obtained with the Bologna Observatory's 1.52m telescope at Loiano. The Cassegrain f/8 focus was equipped with a 512×320 thinned, back illuminated CCD RCA SID501. The final image scale is $0''.50$ pixel^{-1}. The chip bias is 246 ± 3 ADU/pixel (at a gain of 17 electrons/ADU) and the dark current is negligible in the adopted exposure times.

The observations were made during many nights from March 1986 to May 1990, but we have selected only those observations taken during 19 nights with satisfactory photometric conditions and reliable standard star observations.

These observations regard 42 Seyfert 1 galaxies. Two of these objects

Name (1)	E_{B-V} (2)	z (3)	b/a (4)
0048+29 ..	0.00	0.036	0.60
1503	0.01	0.036	0.48
2237+07 ..	0.00	0.025	0.71
I Zw 1	0.03	0.061	0.96
II Zw 1 ...	0.01	0.054	0.93
III Zw 2 ...	0.04	0.090	0.90
VII Zw 118	0.04	0.080	0.91
Mrk 6	0.08	0.018	0.50
Mrk 10	0.03	0.029	0.54
Mrk 79	0.06	0.022	0.57
Mrk 141 ..	0.02	0.039	0.86
Mrk 231 ..	0.01	0.041	0.80
Mrk 279 ..	0.02	0.031	0.68
Mrk 290 ..	0.01	0.031	0.97
Mrk 304 ..	0.05	0.067	0.95
Mrk 335 ..	0.03	0.025	0.91
Mrk 352 ..	0.03	0.025	0.92
Mrk 359 ..	0.01	0.017	0.86
Mrk 372 ..	0.10	0.031	0.82
Mrk 376 ..	0.09	0.056	0.69
Mrk 478 ..	0.00	0.079	0.88
Mrk 486 ..	0.01	0.039	0.55
Mrk 506 ..	0.03	0.043	0.67
Mrk 530 ..	0.03	0.029	0.76
Mrk 584 ..	0.00	0.078	0.91
Mrk 590 ..	0.00	0.027	0.92
Mrk 595 ..	0.00	0.028	0.69
Mrk 618 ..	0.05	0.034	0.59
Mrk 668 ..	0.00	0.079	0.71
Mrk 704 ..	0.01	0.029	0.68
Mrk 705 ..	0.01	0.028	0.87
Mrk 734 ..	0.01	0.050	0.62
Mrk 766 ..	0.01	0.013	0.81
Mrk 817 ..	0.01	0.032	0.98
Mrk 841 ..	0.00	0.036	1.00
Mrk 871 ..	0.03	0.034	0.40
Mrk 876 ..	0.02	0.129	0.91
Mrk 975 ..	0.04	0.050	0.66
NGC 3516	0.02	0.009	0.81
NGC 5548	0.00	0.019	0.82
NGC 5940	0.00	0.034	1.00
NGC 7469	0.03	0.017	0.75

Table 3.1: The observed sample.

(III Zw 2 and Mrk 876) do not belong to the homogeneous sample, but we present observations also for them, even if they are excluded from the final discussion. For 28 objects we have obtained images through the B V Johnson and R Kron-Cousins filters, for 12 objects we have observations in two bands, and for the reminder two objects (III Zw 2 and VII Zw 118) we have only an R frame. In Tab. 3.1 we have reported for each observed object the redshift, the reddening within our own galaxy E_{B-V}, and the axial ratio b/a. We have estimated the latter parameter using the outermost well defined isophotes in our R frames, i.e. the isophotes corresponding to a level above that of the sky by 3σ.

Typical exposure times range from 10 to 20 minutes in B and from 7 to 15 minutes in V and R. These values were usually a good compromise between the two opposite requirements of avoiding saturation in the nuclear region while tracing as far as possible the outer regions of the underlying galaxy. This compromise is more difficult to reach in the B band, where the nuclei are usually more prominent with respect to the host galaxies. As a consequence data on the outermost regions of our sample galaxies are of lower quality in the B–band.

3.2.2 Preliminary Reductions

The reduction of the CCD frames followed standard procedures which we have carried out using the MIDAS environment. The images were corrected for instrumental effects by subtracting an averaged bias frame, obtained as a mean of 10 bias exposure each night. The resulting frames were then divided by a mean flat field, in order to correct for the variations in the sensitivity of the CCD from pixel to pixel. The flat frames were a mean of 3 to 5 exposures in each filter, obtained inside the dome.

Direct inspection to the frames allowed cosmic rays and bad pixels removal. Subtraction of contaminating objects was necessary only in few cases.

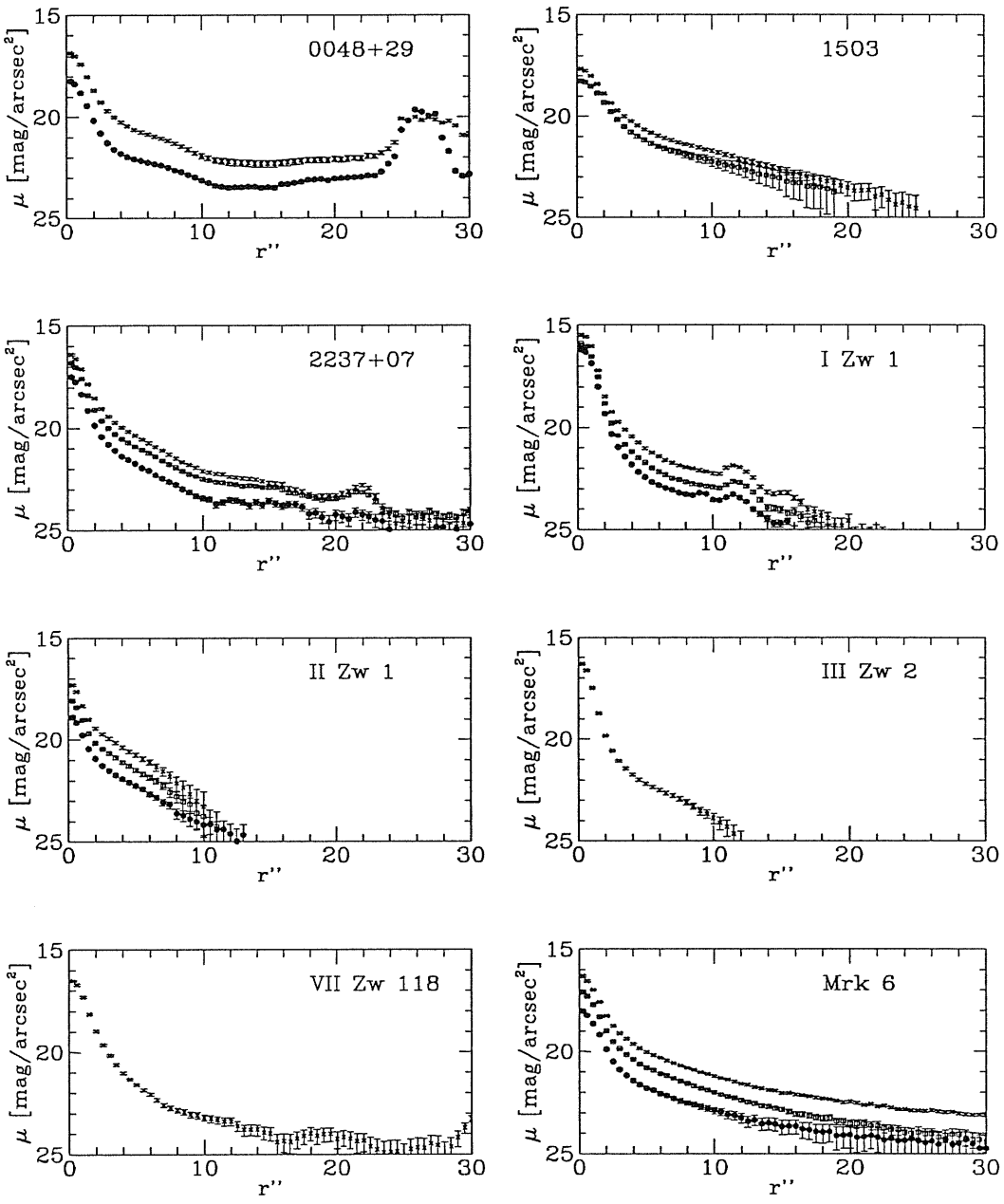

Figure 3.1: The B (filled circles), V (empty squares) and R (crosses) band surface brightness profiles for sample galaxies.

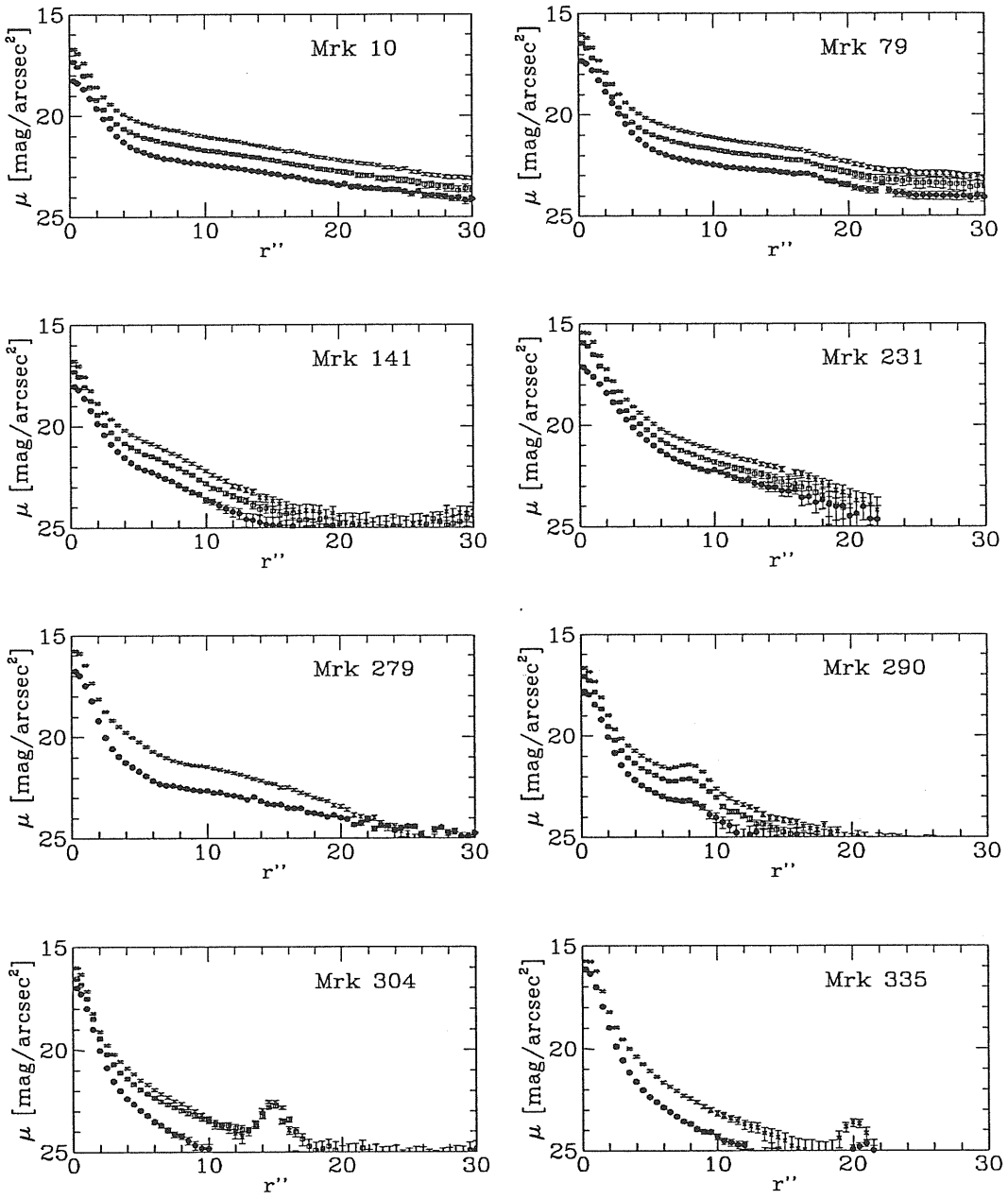

Figure 3.1: Continued

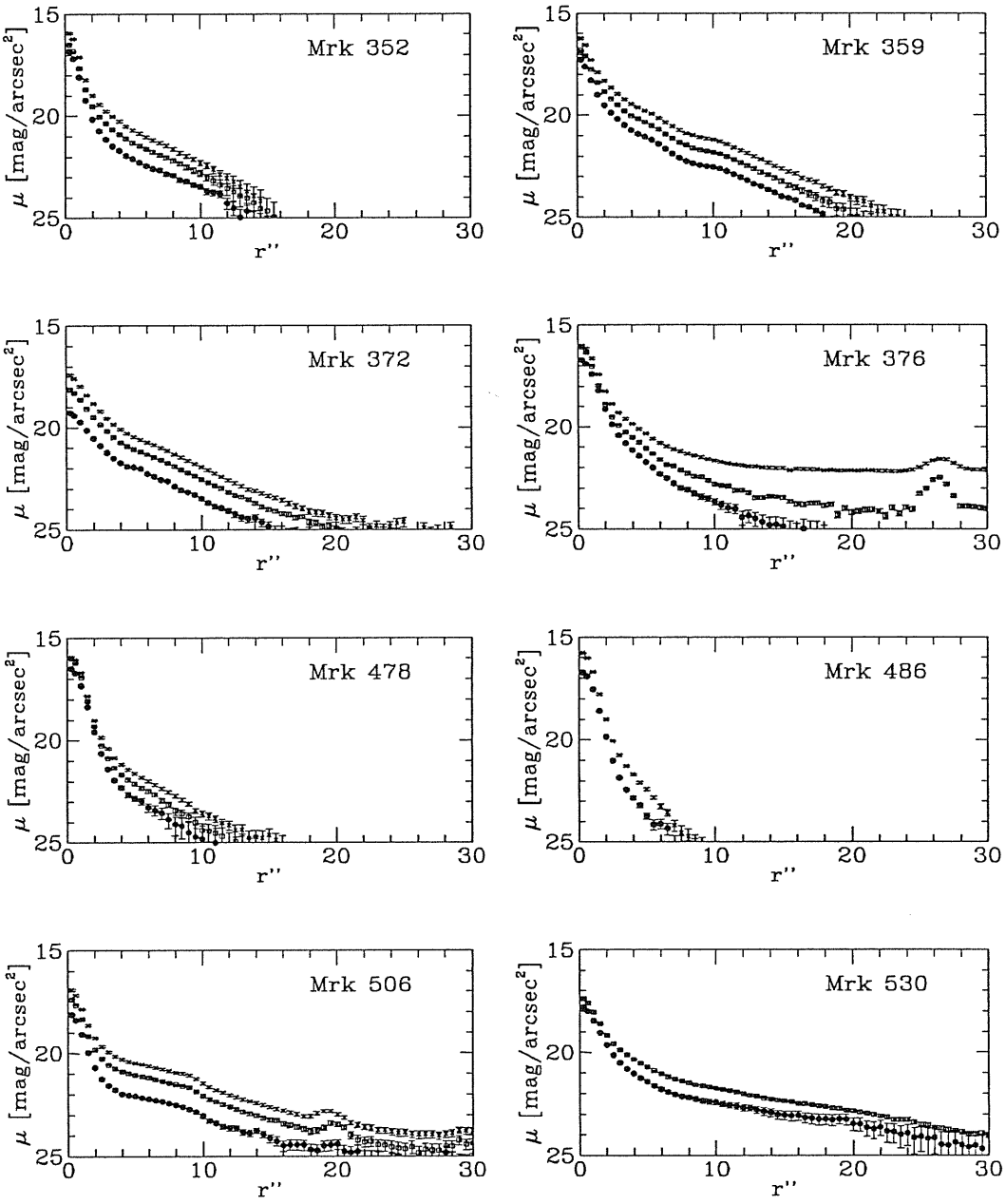

Figure 3.1: Continued

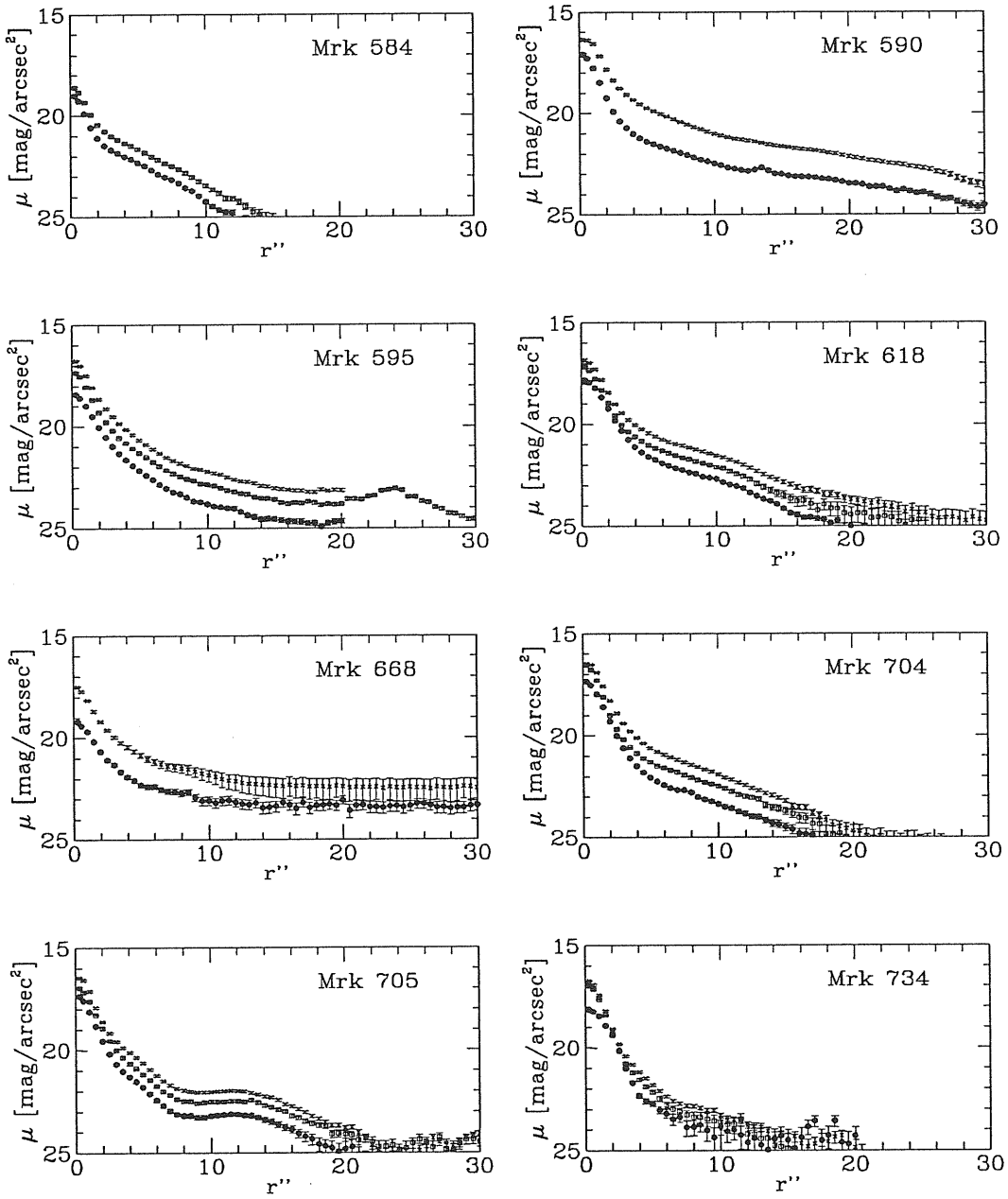

Figure 3.1: Continued

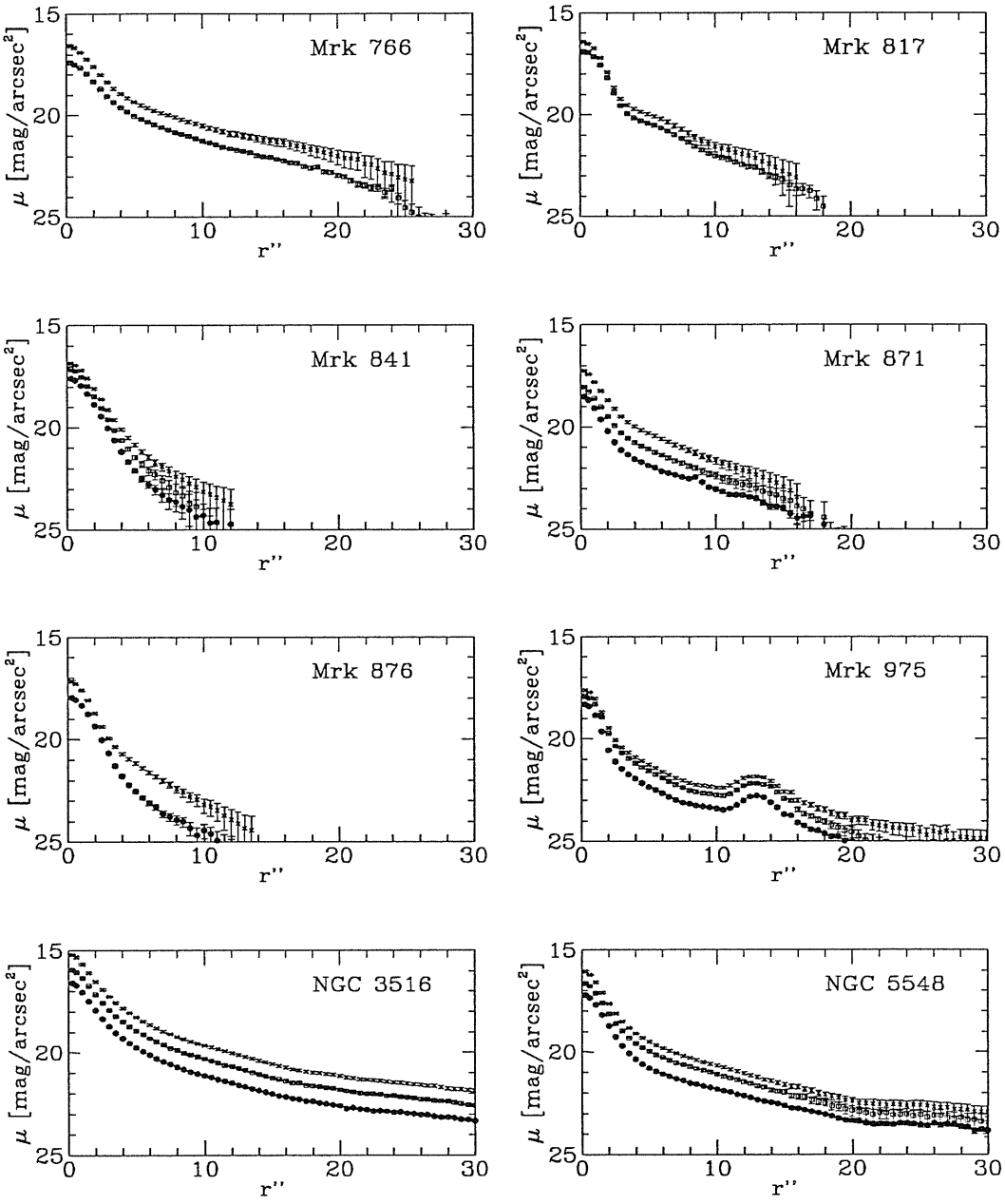

Figure 3.1: Continued

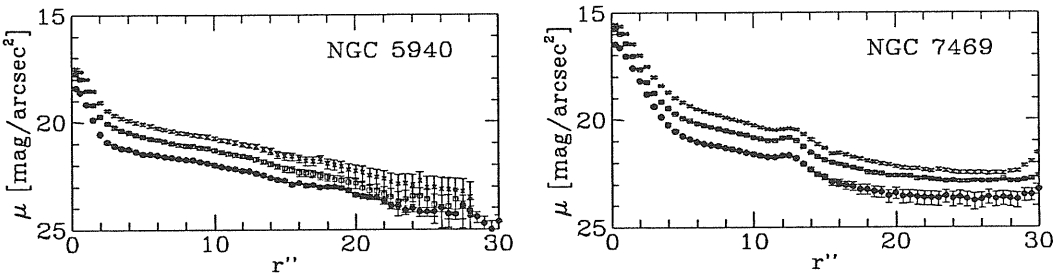

Figure 3.1: Continued

3.2.3 Background Subtraction

To determine the background level, we have usually chosen 4 boxes of at least 1000 pixels in regions of the frames free from contaminations by the galaxy or other field objects. Thanks to the large field of view of the optical frames, these conditions were easy to fulfill. We found that the pixel to pixel variations in each box were of the order expected from the poissonian statistics of the counts, and the differences between the mean values determined in different boxes were of the order of 1%–2%. We choose therefore to subtract a flat sky, with level given by the value averaged over all boxes, and uncertainty estimated by the box to box variation. This uncertainty is the dominant source of error in the outermost part of our profiles.

The average sky brightness we found are 21.1 mag/arcsec^2 in B, 20.2 in V and 19.7 in R, with a standard deviation from frame to frame $\sim$ 0.4 mag/arcsec^2 in the three bands.

3.2.4 Calibration

The observations were calibrated and transformed into the UBVRI system using standard sequences in the clusters M92, NGC2264, NGC 2419, NGC 4147, NGC 7790 and NGC 7006 (Christian et al. 1985). CCD frames of standard were taken every few frames (typically every 2 hours). The uncertainty in zero points, estimated from the statistic of the calibration constants derived from different standard stars in the same frame, turns out to be a few hundredths of magnitude in the three bands. However we observed several standards in different nights and we found that the measurements show rms $\simeq$ 0.08. This increased uncertainty likely is due to the extinction corrections and changes in photometric conditions from night to night. All in all we

have assumed that the calibration error is $\simeq 0.1$ mag.

3.2.5 Intensity profiles

With the aim of increasing the signal to noise ratio in the outer regions and to smooth out small scale irregularities, we have reduced the data on individual pixels to intensity profiles, properly averaging the intensity in concentric rings. The concentric annular rings are spaced by 1 pixel. It should be noted that our sample galaxies are, as optically selected Seyfert 1s, strongly biased toward high b/a values (e.g. Keel 1980; Danese and De Zotti 1984). The position of the nucleus has been determined by the use of the first moment of the brightness distribution on a 20×20 pixels grid around the brightest one. Individual pixels contribute to ring brightness depending on their brightness, weighted by the area in common with the ring. This procedure is extremely important in the central regions of the objects, where the pixel size is comparable to the scale of significant variation of the intensity profile.

In Fig. 3.1 we have plotted the resulting surface brightness μ (mag arcsec^{-2}) as a function of the angular distance from the centre for the 113 observed frames. The errors associated to the points of the profile are comprehensive of photon noise of the source, of the uncertainty in the background subtraction, and of the read-out noise of the detectors:

$$\frac{\sigma^2_{<I>}}{< I >^2_{ring}} = \frac{\sigma_f^2}{f^2} + \frac{\bar{n}_e + \sigma^2_{ron}}{N_{ring}\,(\bar{n}_e - \bar{n}_{bk})^2} + \frac{\bar{n}_{bk} + \sigma^2_{ron}}{N_{bk}\,(\bar{n}_e - \bar{n}_{bk})^2} + \frac{\sigma^2_{bk}}{(\bar{n}_e - \bar{n}_{bk})^2} \quad (3.1)$$

where $f \pm \sigma_f$ is the conversion factor from electronic counts to ADU, N_{ring} and N_{bk} are the number of pixel in the ring and in the region used for the background determination respectively, $\bar{n}_e$ is the mean number of electrons counted in the pixels of the ring, $\bar{n}_{bk}$ is the mean number of electrons per pixel due to the background and σ_{ron} is the read-out noise. These errors do not include the uncertainty in the calibration of the frames discussed above, which we added to all the integrated quantities derived from the profiles (see below).

As it is apparent, the profiles are quite well determined in the inner regions, where the effect of the seeing clearly shows up. Errors in surface brightness increase in the outer regions, mainly because of uncertainties in the background estimate.

As a result of combination of exposure times, CCD efficiency and backgrounds, uncertainties are $\delta\mu \sim 0.2 - 0.3$ mag/arcsec^2 at surface brightness levels $\mu \sim 23 - 24$ mag/arcsec^2 on average. This fact entails that it is possible for the large majority of the objects of the sample to trace reliable outer profiles at least up to $r \sim 16''$, corresponding to an average physical distance $r \sim 15$ kpc.

3.3 Data Analysis

Our scope in analyzing imaging data is to obtain reliable estimates of nuclear fluxes and of the main characteristics of the galaxies hosting AGN, such as their total luminosity, the relative importance of the bulge and the disk components and the morphological parameters. Here we briefly describe the technique that we have developed for this purpose. Additional details can be found in Chapter 1 and in Granato (1988).

3.3.1 Model

Several authors have noticed that Seyfert galaxies can be classified as spiral in the large majority of the cases but also that they often exhibit bars or generally disturbed features such as rings and jets (see e.g. Adams 1977; Dahari 1985; MacKenty 1990). Complex structures are often present also in our CCD frames. Nevertheless we have assumed that the intensity profiles of the host galaxies are similar to those of normal galaxies and reasonably approximated by the superposition of a bulge following the $r^{1/4}$ law and of an exponential disk (Kent 1985; Kodaira et al. 1986). Such a model of the intrinsic radial profile has four free parameters: the effective radius r_e, which encompasses half of the total light of the bulge, the surface brightness at this radius I_e, the scale length of the disk r_D, and its central surface brightness I_D.

This approximated model is only one of the possible descriptions of the light distribution in galaxies. However it has been largely used in photometric studies of normal galaxies, proving to be adequate for the majority of the analyzed objects. Indeed there is a wealth of decomposed profiles of normal galaxies available from the literature that allows for comparison with our studies. Moreover the ratio B/D of the bulge over disk luminosity (or equivalently the ratio between the bulge and the total galactic luminosity $B/G = B/(B + D)$) is a relevant model outcome, significantly correlated with morphological type (see e.g. Boroson 1981; Kodaira et al. 1986). Bars

and lenses, mimicking large bulges, could partly affect the decomposition. As a consequence in some cases the ratio B/D has to be interpreted as the ratio of the non-disk to the disk component. On the other hand it should be noted that we are primarily interested on the separation of the nuclear from the galactic flux.

We have also assumed that the galactic surface brightness is symmetric with respect to the central axis perpendicular to the galactic plane and, as a consequence, that the isophotes are concentric circles on the galactic plane. Thus the isophotes of a galaxy whose fundamental plane is tilted by an angle i with respect to the line of sight become concentric ellipses with axial ratio $\epsilon = b/a = \sin i$. Therefore by measuring the isophotal axial ratio we can estimate the galaxy inclination on the plane of the sky.

By adding up a nuclear pointlike component we get a model for Seyfert galaxies. We have taken into account the effects of the atmospheric seeing plus instrumental effects. In order to choose a proper functional form of the PSF, we considered, under many different seeing conditions, the CCD profiles of a number of stars, having magnitude comparable to those of typical nuclei of our sample. We found (Granato 1988) that the best representation for our purposes is given by the sum of two gaussians:

$$I(r) = \frac{F_T}{2\pi\sigma^2(1+as^2)}\left[\exp\left(\frac{-r^2}{2\sigma^2}\right) + a\exp\left(\frac{-r^2}{2s^2\sigma^2}\right)\right] \qquad (3.2)$$

where F_T is the total flux of the star, σ is the s.d. of the main gaussian and a and s are the ratios of the central peaks and of the standard deviations of the two gaussians respectively. While σ is of course a variable parameter depending on the seeing conditions, we have found that a and s can be considered as constants in our frames, fixed to the values of 0.05 and 2.2 respectively. The only adjustable seeing parameter is therefore σ, which, when possible, was determined for each frame by considering the profiles of two or three field stars in the same frame. The mean σ we found in our optical frames is $0''.95 \pm 0''.22$ (s.d.). The seeing profile of the nucleus is then given by Eq. 3.2, where F_T must be replaced by F_n, the total flux of the nucleus.

The effects of inclination of the galaxian planes with respect to the line of sight have been properly included in the decomposition. Using the PSF given by Eq. 3.2 and introducing a cartesian reference frame with x axis defined by the intersection of the plane of the sky with that of the galaxy, z axis directed along the line of sight and y axis in the plane of the sky, it

can be shown (see Granato 1988) that the expected surface brightness of a host galaxy at a point (x, y) in the sky is given by

$$I_{obs}(x,y) = \frac{1}{2\pi\sigma^2(1+as^2)\epsilon} \times \int\int_{-\infty}^{\infty} I(r') \left[\exp\left(-\frac{\rho'^2}{2\sigma^2}\right) + a\exp\left(-\frac{\rho'^2}{2s^2\sigma^2}\right)\right] dx'dy' \quad (3.3)$$

2 where $\rho'^2 = (x-x')^2 + (y-y')^2$, and $r' = \left(x'^2 + \frac{y'^2}{\epsilon^2}\right)^{1/2}$.

The surface brightness is then integrated to obtain the expected intensity profile to be compared with that derived from the observations. Thus the model depends on five parameters to be determined by matching it to the observed images: the total flux of the nucleus F_n, the effective radius r_e which encloses half of the total light of the bulge, the surface brightness I_e at r_e, and the two parameters modelling the disk, namely the scale length r_D and the central surface brightness I_D. The two additional parameters ϵ and σ are instead determined before the fitting procedure, as described above.

3.3.2 Fitting Procedure

As described in Section 3.2.5, we reduced the observed images to intensity profiles properly averaging the surface brightness in annular concentric rings. In such a way we reduce the dimensionality of the problem, significantly decreasing the computing time needed to calculate the best–fit parameters, without squandering the bidimensional information, but in some sense averaging it.

The model intensity profile is obtained adding the nuclear to the galactic profile. While the contribution of the nucleus to the intensity of a ring at distance r from the centre is easily calculated (see Eq. 3.2), the computation of the galactic flux in each ring implies an integration of Eq. 3.3 over the ring, and therefore a 4–dimensional numerical integral. As a consequence the fitting procedure would still have required a lot of computing time. However the effect of the seeing on the galactic profile strongly decreases in regions with relatively shallow gradient of the surface brightness. We have checked that with our typical observational conditions, the seeing effect on the galactic component is negligible at distances from the centre $r \geq 8\sigma$. Thus exterior to this radius we have neglected the seeing effect.

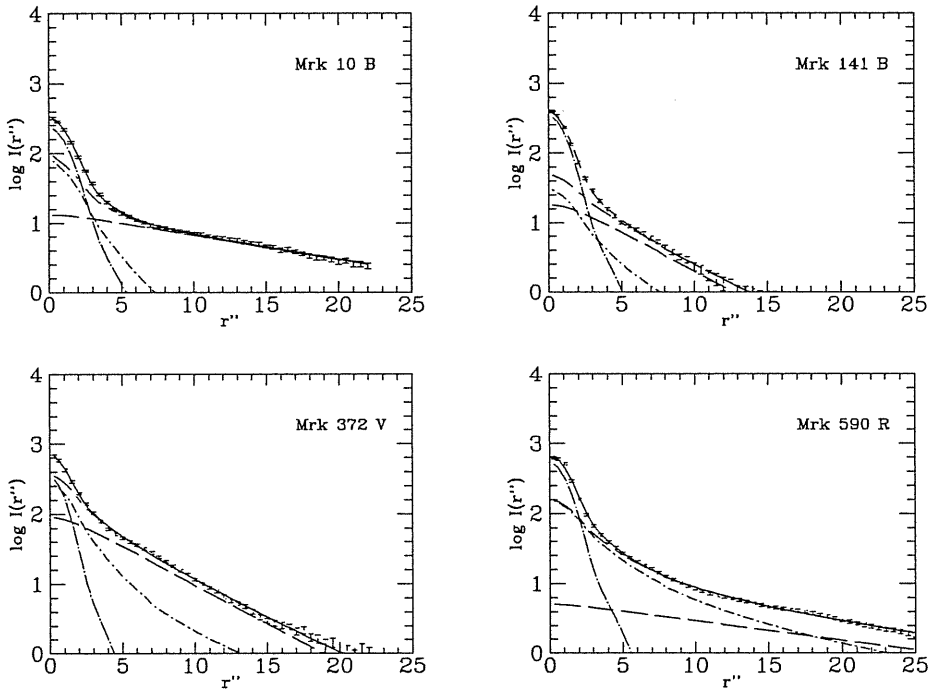

Figure 3.2: Four representative examples of intensity profile data (ADU/arcsec^2) and corresponding fits. The solid line is the best fitted profile. The dotted long dashed line is the nuclear profile, the bulge profile is the dotted dashed line, the disk profile is the dashed line, the galaxy profile is the short and long dashed line.

In the inner regions we only computed the flux in 100 properly distributed points of a quadrant, and used this 10×10 array in the x–y plane to interpolate the values required to calculate the intensity profile of the galaxy. This simplification also allowed us to compute the flux expected from the model in each of the 20×20 central pixels, taking into account the offset of the center of the observed image, as determined from the first moment of the brightness distribution, with respect to the center of the central pixel. Then we constructed the model intensity profiles averaged over concentric rings with the same technique used for the real data and described above in Sec. 3.2.5. In more external regions, the model intensity profile can be

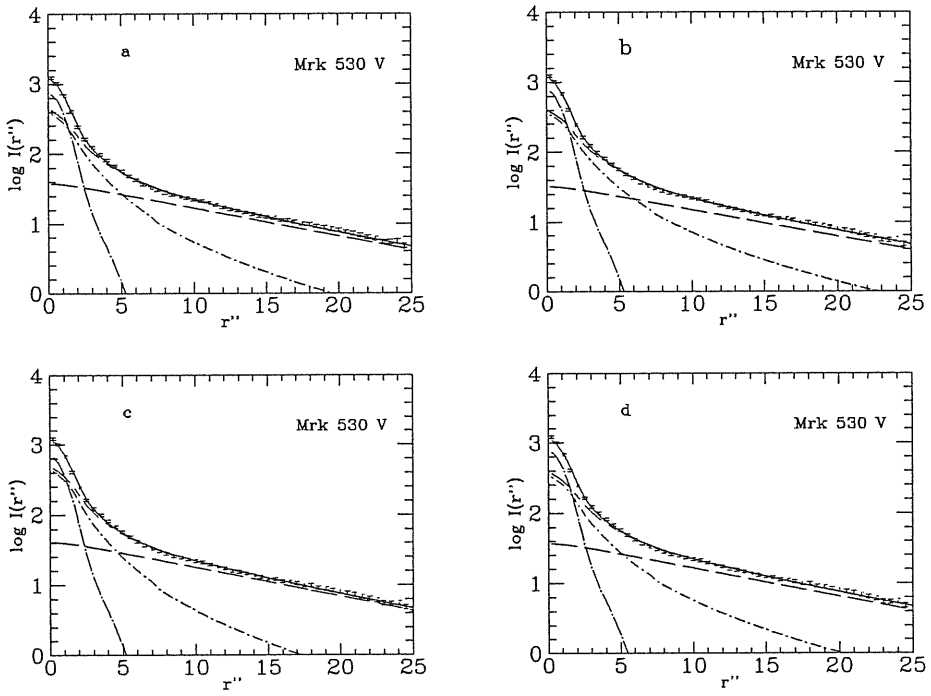

Figure 3.3: Intensity profile data and four alternative fits for Mrk 530 in the V band. The best fit is shown in panel a. In panel b we have reported a fit obtained by fixing the disk scale length r_D to a value greater than the best-fit one by 5% and minimizing the χ^2 with respect to the other 4 free parameters. Panel c reports a similar fits, but obtained by fixing the bulge scale length r_e to a value smaller than the best fitting one by 30%. Finally, panel d shows the best-fit obtained with a seeing parameter σ artificially increased by its typical uncertainty $0''.03$. The χ^2 is significantly greater in the three alternative fits than in the best one (by ≥ 2), while the galactic and the nuclear luminosities differ by no more than 10%.

instead directly averaged over circular rings.

The best fit parameters have been obtained by χ^2 minimizations. The initial values of the parameters have been selected using tentative fits by eye. Representative examples of fits are shown in Fig. 3.2 and 3.3.

3.3.3 Uniquiness of Solution and Parameter Uncertainties

It is natural to expect that the χ^2 function has several local minima in the five-dimension parameter space and, as a consequence, that singling out the *true* solution is a hard task. Fortunately there are usually distinct regions in the intensity profile dominated by only one among the three components. This circumstance favorably results in significant constraints on the possible range of the parameters of the dominating component.

In fact the very inner region, say interior to $r = 2''$, is usually dominated by the PSF of the pointlike nucleus (the mean σ used in our optical fits is $0''.95 \pm 0''.22$ (s.d.)), while outside about $10''$ the profile is almost invariably dominated by the exponentially decreasing disk. Therefore these regions often provide significant constrains on the contribution of the nucleus and the disk. This is apparent from Tab. 3.2B and C, where we present the results of changing the best-fit disk scale r_D and the seeing of a few representative profiles. More precisely, in these cases we have repeated the fits, fixing the parameter r_D to a value equal to the best fitting one multiplied by a factor f_D, which correspond to its statistical uncertainty as estimated by the fitting program, and mimimizing the χ^2 with respect to the other parameters. In Tab. 3.2B we have reported the factor f_D, the corresponding increase of the χ^2 and the maximum percentage variation of the bulge, disc, galactic (bulge + disc) and nuclear luminosity. The data reported in Tab. 3.2C refer to a similar computation, in which however we have artificially changed the seeing by its typical uncertainty $\pm 0''.03$, as estimated comparing the PSF of different stars in the same frame. As can be seen, small changes in the disk scales produce significant increments of the χ^2, while the disk luminosities do not change much and the total galactic luminosities as well as the nuclear ones even less. Tab. 3.2C shows that the uncertainty on the seeing parameter have a rather small effect on the disk, galactic and nuclear luminosities, while the effects on the bulge component can be larger (see below). Usually the fainter is the component the larger is the relative uncertainty, as expected.

The intermediate region is characterized by a more complex and variable behaviour, because in this portion of the intensity profile the bulge, when it

A

Name	f_b	$\Delta\chi^2$	δL_b (%)	δL_d (%)	δL_g (%)	δL_n (%)
Mrk 10 B	1.7	3.0	5	3	3	7
Mrk 141 B	2.4	1.5	32	14	1	3
Mrk 372 V	1.4	1.5	8	6	2	12
Mrk 530 V	1.3	1.8	8	6	1	8
Mrk 590 R	1.3	1.2	11	38	1	10

B

Name	f_d	$\Delta\chi^2$	δL_b (%)	δL_d (%)	δL_g (%)	δL_n (%)
Mrk 10 B	1.06	1.1	6	3	1	6
Mrk 141 B	1.13	3.5	28	10	3	4
Mrk 372 V	1.03	1.6	4	4	2	15
Mrk 530 V	1.05	3.6	12	8	0.7	7
Mrk 590 R	1.18	1.8	11	32	0.5	2

C

Name	$\Delta\chi^2$	δL_b (%)	δL_d (%)	δL_g (%)	δL_n (%)
Mrk 10 B	1.0	28	0.5	3	14
Mrk 141 B	4.0	40	15	4	5
Mrk 372 V	1.3	11	3	1	15
Mrk 530 V	6.8	1	2	1	5
Mrk 590 R	1.0	3	13	2	6

D

Name	$\Delta\chi^2$	δL_b (%)	δL_d (%)	δL_g (%)	δL_n (%)
Mrk 10 B	0.6	3	1	1	4
Mrk 141 B	0.4	10	3	0.3	0.8
Mrk 372 V	3.0	0.5	3	2.5	8
Mrk 530 V	0.5	0.5	1.5	0.3	1.8
Mrk 590 R	0.1	4	10	0.6	1

Table 3.2: Results of Alternative Fits for a Few Objects.

is a significant component, is prominent, but the other two components are usually not negligible. In many cases there is no region in the profile where the bulge is dominating, but nevertheless its presence remains necessary to obtain a good fit in the intermediate region. In such circumstances it can be seen that the parameters r_e and I_e are individually not well determined, while their combination $I_e r_e^2$, which is proportional to the bulge luminosity, is much better constrained. This can be seen by inspection of Tab. 3.2A, which is analogous to Tab. 3.2B, but obtained fixing r_e. For instance in the case of Mrk 141 we have multiplied or divided the best-fit value of r_e by a factor of 2.4 and we have computed the minimum χ^2 with respect to the other parameters. It turns out that the bulge luminosity varies by no more than 32%. In other words, when, as often is the case, the bulge is a detectable but nowhere a dominant component, we can obtain equivalently good fits by varying the single bulge parameters by a large factor. However the corresponding bulge luminosities are much better constrained. This is somewhat analogous to what already reported by other authors, when dealing either with profiles of normal galaxies (e.g. Kent 1985), or those of active galaxies (Malkan 1984; Veron-Cetty and Woltjer 1990; Abraham et al. 1992). We explicitly note that an uncertainty of this kind in the bulge luminosity partly reflects in that of the nucleus and partly in that of the host galaxy, depending also on the relative importance. Indeed Tab. 3.2C shows that the seeing can significantly affect the evaluation of the luminosities of faint bulges, as in the case of Mrk 10 and Mrk 141. However we have found no significant correlation between seeings and ratios B/T of bulge over total flux (see below).

The uncertainty of the best fit parameters associated to uncertainties on the axial ratio b/a is weak. Actually the estimates of axial ratios for 15 objects in common with MacKenty (1990) well agree giving $\Delta b/a \simeq 0.00 \pm 0.07(s.d.)$. Tab. 3.2D illustrate the quite small effects on the luminosities of the three components when the adopted axial ratio is artificially changed by as much as 20%.

For two objects we have obtained two frames in different nights and we can compare the results of the analysis. We have analysed two B–band frames of Mrk 705 with different seeings. Although this galaxy presents a feature in the profile in the range between $r \sim 10''$ to $16''$ that makes the adopted light distribution model inadequate, nevertheless the difference of the nuclear fluxes is smaller than the error. By the way even the galaxy fluxes within 20 Kpc agree within the error. The same galaxy has also been observed twice in R–band and once more there is good agreement. Mrk 704

has also been observed twice in R–band. In this case the host galaxy is more *regular* and we can compare the results in more details. The nuclear and galactic magnitudes agree within the errors, the main difference being in the relative importance of the bulge in the galaxy. Actually in one case the analysis yields a ratio of bulge over total galaxy of about 0.1, while in the other case the ratio is 0.26. The disk central surface brightnesses differ by 0.4 mag and the disk scale lengths by about 20%, whereas the total disk luminosities ($\propto I_D r_D^2$) agree within 8%.

With the aim of looking for seeing effects, we have explored correlations among galaxy parameters, redshifts and seeing. A rather intriguing fact is that we have found a significant correlation between linear disk scale lengths r_D and redshifts. Because of the sky coverage of the CCD, this seems hardly attributable to wrong background subtractions. Correlation at a level of about 97% is also present between *angular* disk scale lengths and seeing parameters in the sense that larger disk lengths correspond to large σ seeing parameters. These facts suggests the presence of a systematic effect, which likely is increasingly important with increasing redshifts. However it must be noted that the large majority of our sample objects are Markarian *galaxies* and the presence of the fuzziness around the nuclear regions was a condition for inclusion in Markarian lists. Therefore we may expect that our sample exhibits a bias toward extended objects with increasing redshifts. We have also investigated the possible effects of this bias on the fractions over total fluxes of nuclei, bulges and disks. There is not any significant correlation of these fractions with seeing parameters or with redshifts.

In conclusion nuclear and host galaxy luminosities usually have been rather well determined; bulge and disk luminosities have larger uncertainties especially when they are a small fraction ($f \lesssim 20\%$) of the total (this is often the case for the bulge component due to the morphology of the host galaxies). The individual disk and bulge parameters usually are more uncertain. The most important source of uncertainty have been the seeing conditions, that seldom have been very good at our observing site.

The difficulty to characterize the bulge component has forced other authors (Yee 1983; MacKenty 1990) to leave out its determination. On the other hand it is plausible that in early type spiral galaxies, such as Seyfert galaxies are thought to be (see below), the bulge can give a significant contribution to the brightness in the nuclear region. Almost half of the objects of our sample have bulges that contributes more than 20% to the total fluxes within 30″ apertures.

Name	Band	Date	σ	μ_e	r_e	μ_D	r_D	B/G	$N/T(5'')$	$N/T(7''.8)$	Q
			asec	$\frac{\text{mag}}{\text{asec}^2}$	kpc	$\frac{\text{mag}}{\text{asec}^2}$	kpc				
(1)	(2)	(3)	(4)	(5)	(6)	(7)	(8)	(9)	(10)	(11)	(12)
0048+29 ..	B	Oct 20, 86	0.93	...	...	21.80	7.87	0.00	0.87	0.77	1
0048+29 ..	R	Oct 20, 86	0.94	21.65	2.74	20.33	6.76	0.15	0.76	0.65	1
1503	V	Jul 3, 86	1.20	23.40	5.84	21.47	9.56	0.18	0.68	0.57	1
1503	R	Jul 3, 86	1.12	22.19	5.18	21.03	9.45	0.27	0.59	0.48	1
2237+07 ..	B	Jul 22, 88	0.85			20.54	2.74	0.00	0.87	0.75	1
2237+07 ..	V	Jul 22, 88	0.86	...	...	19.77	2.87	0.00	0.86	0.74	1
2237+07 ..	R	Jul 22, 88	0.87	29.18	69.60	19.08	2.57	0.19	0.82	0.69	1
I Zw 1	B	Nov 5, 88	0.78	...	...	...	...	...	0.93	0.92	3
I Zw 1	V	Nov 5, 88	0.82	...	...	...	...	...	0.94	0.94	3
I Zw 1	R	Nov 5, 88	0.78	...	...	...	...	...	0.95	0.92	3
II Zw 1 ...	B	Sep 5, 88	0.71	...	...	...	...	...	0.55	0.40	3
II Zw 1 ...	V	Sep 5, 88	0.66	...	...	19.54	3.98	0.00	0.50	0.36	1
II Zw 1 ...	R	Sep 5, 88	0.62	...	...	18.78	3.88	0.00	0.50	0.35	1
III Zw 2 ...	R	Oct 20, 86	0.65	...	...	20.69	8.28	0.00	1.00	0.96	1
VII Zw 118	R	Mar 4, 86	0.80	20.00	4.08	22.59	20.22	0.61	0.71	0.65	1
Mrk 6	B	Mar 4, 86	0.65	25.04	10.04	...	...	1.00	0.46	0.37	1
Mrk 6	V	Mar 4, 86	0.65	23.42	6.49	...	...	1.00	0.43	0.34	1
Mrk 6	R	Mar 4, 86	0.65	22.94	7.35	...	...	1.00	0.44	0.35	1
Mrk 10	B	Jan 8, 88	1.10	21.20	0.00	22.12	13.87	0.10	0.64	0.54	1
Mrk 10	V	Jan 8, 88	0.92	20.95	1.96	21.29	12.08	0.11	0.57	0.47	1
Mrk 10	R	Jan 8, 88	0.88	20.69	2.29	20.53	10.70	0.12	0.59	0.48	1
Mrk 79	B	Jan 8, 88	1.00	20.74	1.63	22.28	12.28	0.20	0.70	0.61	1
Mrk 79	V	Jan 8, 88	0.85	18.89	0.90	21.23	9.30	0.22	0.53	0.47	1
Mrk 79	R	Jan 8, 88	0.85	18.23	0.89	20.53	8.14	0.26	0.46	0.39	1
Mrk 141 ..	B	Jan 8, 88	0.97	23.65	5.47	21.06	4.44	0.33	0.80	0.68	1
Mrk 141 ..	V	Jan 8, 88	0.82	24.17	9.78	19.99	3.94	0.32	0.73	0.61	1
Mrk 141 ..	R	Jan 8, 88	0.81	24.04	11.22	19.20	3.71	0.27	0.71	0.57	1
Mrk 231 ..	B	May 10, 86	1.30	20.98	4.11	21.88	10.39	0.56	0.73	0.65	1
Mrk 231 ..	V	May 10, 86	1.00	19.77	3.03	20.65	7.35	0.58	0.73	0.65	1
Mrk 231 ..	R	May 10, 86	1.00	19.18	2.77	19.94	7.18	0.52	0.74	0.66	1
Mrk 279 ..	B	May 10, 86	0.85	20.80	1.23	21.86	9.29	0.14	0.88	0.83	1
Mrk 279 ..	R	May 10, 86	0.80	19.39	1.58	20.22	6.36	0.32	0.72	0.63	1
Mrk 290 ..	B	May 30, 90	0.89	...	...	21.55	3.92	0.00	0.97	0.90	1
Mrk 290 ..	V	May 30, 90	0.80	...	...	20.37	3.43	0.00	0.93	0.84	1
Mrk 290 ..	R	May 30, 90	0.84	...	...	19.71	3.27	0.00	0.91	0.82	1
Mrk 304 ..	B	Jul 22, 88	0.71	...	...	...	...	...	0.94	0.90	3
Mrk 304 ..	V	Jul 22, 88	0.72	...	...	...	...	...	0.89	0.83	2
Mrk 304 ..	R	Jul 22, 88	0.65	...	...	...	...	...	0.83	0.75	2

Table 3.3: A. Fitting Parameters. Q indicates the fit quality as follows. 1: the bulge–disk–nucleus decomposition can be considered successfully achieved; 2: the nucleus and the galaxy are both well determined but the bulge–disk decomposition of the galaxy is uncertain; 3: only the nuclear magnitude is reliably computed.

Name (1)	Band (2)	Date (3)	σ (4) sec	μ_e (5) $\frac{\text{mag}}{\text{asec}^2}$	r_e (6) kpc	μ_D (7) $\frac{\text{mag}}{\text{asec}^2}$	r_D (8) kpc	B/G (9)	$N/T(5'')$ (10)	$N/T(7''.8)$ (11)	Q (12)
Mrk 335	B	Aug 9, 86	0.77	...	...	...	...	...	1.00	0.98	3
Mrk 335	R	Aug 9, 86	0.83	21.72	2.94	20.21	2.10	0.64	0.88	0.84	1
Mrk 352	B	Sep 5, 88	0.65	...	...	20.51	2.68	0.00	0.91	0.82	1
Mrk 352	V	Sep 5, 88	0.66	22.04	1.27	19.78	2.52	0.10	0.84	0.73	1
Mrk 352	R	Sep 5, 88	0.60	...	...	18.97	2.51	0.00	0.73	0.63	1
Mrk 359	B	Nov 5, 88	0.64	20.77	1.13	20.26	2.08	0.40	0.37	0.28	1
Mrk 359	V	Nov 5, 88	0.63	20.21	1.21	19.55	2.08	0.40	0.29	0.21	1
Mrk 359	R	Nov 5, 88	0.60	19.61	1.14	18.96	2.11	0.37	0.26	0.19	1
Mrk 372	B	Nov 5, 88	0.89	22.25	2.37	20.63	3.73	0.24	0.32	0.23	1
Mrk 372	V	Nov 5, 88	0.85	21.25	2.71	19.87	3.68	0.35	0.29	0.21	1
Mrk 372	R	Nov 5, 88	0.82	20.28	2.32	19.37	3.66	0.38	0.24	0.18	1
Mrk 376	B	May 30, 90	0.80	...	...	...	...	...	0.89	0.82	3
Mrk 376	V	May 30, 90	0.74	...	...	...	...	...	0.90	0.81	3
Mrk 376	R	May 30, 90	0.80	...	...	...	...	...	0.77	0.67	3
Mrk 478	B	May 30, 90	0.75	...	...	...	...	...	1.00	1.00	3
Mrk 478	V	May 30, 90	0.73	...	...	...	...	...	0.97	0.96	3
Mrk 478	R	May 30, 90	0.74	...	...	...	...	...	0.97	0.93	3
Mrk 486	B	May 10, 86	0.73	...	...	...	...	...	1.00	1.00	3
Mrk 486	R	May 10, 86	0.73	...	...	...	...	...	0.95	0.95	3
Mrk 506	B	May 30, 90	0.72	...	...	21.43	8.06	0.00	0.86	0.72	1
Mrk 506	V	May 30, 90	0.71	...	...	20.32	7.40	0.00	0.78	0.63	1
Mrk 506	R	May 30, 90	0.74	...	...	19.79	7.54	0.00	0.76	0.60	1
Mrk 530	B	Sep 9, 88	0.92	22.01	3.54	21.97	10.85	0.27	0.58	0.47	1
Mrk 530	V	Sep 9, 88	0.90	21.65	4.15	21.24	9.91	0.30	0.49	0.38	1
Mrk 584	B	Nov 5, 88	0.73	...	...	20.80	6.64	0.00	0.60	0.44	1
Mrk 584	V	Nov 5, 88	0.75	...	...	20.09	6.60	0.00	0.52	0.38	1
Mrk 590	B	Oct 1, 86	0.85	23.84	11.87	23.07	15.28	0.51	0.80	0.71	1
Mrk 590	R	Oct 1, 86	1.00	21.60	8.17	21.55	12.12	0.61	0.62	0.53	1
Mrk 595	B	Nov 6, 88	0.93	...	...	...	...	...	0.38	0.31	2
Mrk 595	V	Nov 6, 88	0.75	...	...	...	...	...	0.36	0.30	2
Mrk 595	R	Nov 6, 88	0.78	...	...	...	...	...	0.34	0.28	2
Mrk 618	B	May 30, 90	1.18	...	...	20.87	5.67	0.00	0.91	0.83	1
Mrk 618	V	May 30, 90	1.03	...	...	20.30	5.72	0.00	0.89	0.79	1
Mrk 618	R	May 30, 90	1.04	...	...	19.84	5.89	0.00	0.85	0.73	1
Mrk 668	B	May 10, 86	1.05	24.46	15.38	22.51	24.50	0.19	0.63	0.49	1
Mrk 668	R	May 10, 86	0.88	21.72	8.72	20.95	16.94	0.32	0.48	0.37	1
Mrk 704	B	Feb 21, 88	1.03	...	...	21.61	4.98	0.00	0.99	0.93	1
Mrk 704	V	Mar 4, 86	0.81	23.15	2.77	20.65	4.55	0.12	0.91	0.83	1
Mrk 704	R	Feb 21, 88	0.97	20.03	0.80	19.86	4.20	0.10	0.92	0.83	1
Mrk 704	R	Mar 4, 86	0.79	21.82	3.34	20.31	5.29	0.26	0.86	0.78	1

Table 3.3: B. Continued.

Name	Band	Date	σ	μ_e	r_e	μ_D	r_D	B/G	$N/T(5'')$	$N/T(7''.8)$	Q
			sec	$\frac{\text{mag}}{\text{asec}^2}$	kpc	$\frac{\text{mag}}{\text{asec}^2}$	kpc				
(1)	(2)	(3)	(4)	(5)	(6)	(7)	(8)	(9)	(10)	(11)	(12)
Mrk 705 ..	B	Feb 21, 88	0.81	...	...	...	...	...	0.57	0.50	2
Mrk 705 ..	B	Jan 8, 88	0.96	...	...	...	...	...	0.66	0.59	2
Mrk 705 ..	V	Jan 8, 88	0.87	...	...	...	...	...	0.41	0.35	2
Mrk 705 ..	R	Feb 21, 88	0.80	...	...	...	...	...	0.37	0.32	2
Mrk 705 ..	R	Jan 8, 88	1.14	...	...	...	...	...	0.32	0.27	2
Mrk 734 ..	B	May 10, 86	1.20	...	...	...	...	...	0.96	0.96	3
Mrk 734 ..	V	May 10, 86	0.85	21.00	2.42	22.73	11.21	0.45	0.84	0.79	1
Mrk 734 ..	R	May 10, 86	0.85	21.00	3.14	22.52	11.49	0.52	0.80	0.75	1
Mrk 766 ..	V	May 28, 86	1.35	21.37	1.77	19.97	2.65	0.31	0.60	0.50	1
Mrk 766 ..	R	May 28, 86	1.29	20.89	2.21	19.54	3.06	0.35	0.60	0.50	1
Mrk 817 ..	V	Jun 3, 86	1.19	...	...	19.37	3.72	0.00	0.82	0.79	1
Mrk 817 ..	R	Jun 3, 86	1.10	...	...	19.08	4.11	0.00	0.86	0.80	1
Mrk 841 ..	B	Jun 2, 86	1.20	...	...	...	...	...	0.81	0.75	3
Mrk 841 ..	V	Jun 2, 86	1.14	...	...	...	...	...	0.72	0.64	3
Mrk 841 ..	R	Jun 2, 86	1.24	...	...	...	...	...	0.64	0.59	3
Mrk 871 ..	B	May 9, 86	0.85	20.53	0.93	21.56	7.11	0.14	0.48	0.38	1
Mrk 871 ..	V	May 9, 86	0.90	21.58	2.72	20.96	6.76	0.25	0.36	0.28	1
Mrk 871 ..	R	May 9, 86	0.88	20.68	2.57	20.14	6.40	0.26	0.34	0.26	1
Mrk 876 ..	B	Aug 9, 86	1.21	...	...	...	...	...	0.96	0.93	3
Mrk 876 ..	R	Aug 9, 86	1.08	24.51	16.25	19.85	9.97	0.12	0.88	0.81	1
Mrk 975 ..	B	Nov 5, 88	0.83	23.40	6.25	22.43	12.20	0.28	0.74	0.64	1
Mrk 975 ..	V	Nov 5, 88	0.96	22.85	5.55	21.43	9.97	0.23	0.75	0.65	1
Mrk 975 ..	R	Nov 5, 88	1.00	23.17	8.37	21.55	13.05	0.25	0.74	0.65	1
NGC 3516	B	Jan 8, 88	0.98	20.78	2.02	22.79	6.76	0.67	0.39	0.30	1
NGC 3516	V	Jan 8, 88	0.96	19.70	1.74	21.73	5.74	0.68	0.26	0.19	1
NGC 3516	R	Jan 8, 88	0.88	19.18	1.92	21.59	7.73	0.67	0.24	0.18	1
NGC 5548	B	Jun 2, 86	1.12	23.88	8.82	21.27	4.69	0.53	0.82	0.72	1
NGC 5548	V	Jun 2, 86	1.12	23.66	12.54	20.02	3.28	0.65	0.78	0.66	1
NGC 5548	R	Jun 2, 86	1.05	21.15	3.65	19.71	4.02	0.44	0.69	0.57	1
NGC 5940	B	May 10, 86	0.75	...	...	20.75	7.81	0.00	0.71	0.53	1
NGC 5940	V	May 10, 86	0.77	...	...	19.93	6.98	0.00	0.65	0.47	1
NGC 5940	R	May 10, 86	0.92	...	...	19.40	7.21	0.00	0.67	0.50	1
NGC 7469	B	Jul 22, 88	1.00	21.19	1.02	20.33	3.87	0.10	0.89	0.80	1
NGC 7469	V	Jul 22, 88	0.94	19.53	0.69	19.34	3.44	0.11	0.83	0.72	1
NGC 7469	R	Jul 22, 88	1.05	19.66	1.07	18.68	3.18	0.14	0.78	0.67	1

Table 3.3: C. Continued.

Name (1)	Band (2)	m_n (3)	δm_n (4)	m_g (5)	δm_g (6)	$m_g(20)$ (7)	$\delta m_g(20)$ (8)
0048+29	B	16.23	0.18	15.26	0.33	15.62	0.19
0048+29	R	14.96	0.17	13.97	0.25	14.20	0.12
1503	V	15.86	0.20	14.31	0.34	14.77	0.12
1503	R	15.58	0.17	13.77	0.31	14.19	0.08
2237+07	B	15.82	0.16	15.56	0.22	15.57	0.22
2237+07	V	15.08	0.14	14.69	0.17	14.71	0.17
2237+07	R	14.64	0.12	14.01	0.26	14.20	0.15
I Zw 1	B	14.40	0.15	...	...	...	...
I Zw 1	V	14.05	0.13	...	...	...	...
I Zw 1	R	13.63	0.11	...	...	...	...
II Zw 1	B	17.61	0.16	...	...	...	...
II Zw 1	V	16.97	0.18	15.31	0.13	15.37	0.10
II Zw 1	R	16.27	0.22	14.61	0.09	14.67	0.08
III Zw 2	R	14.87	0.12	15.86	0.31	16.27	0.47
VII Zw 118	R	14.96	0.13	14.57	0.26	15.06	0.24
Mrk 6	B	16.26	0.15	15.16	0.45	15.57	0.29
Mrk 6	V	15.51	0.14	14.50	0.36	14.75	0.23
Mrk 6	R	14.81	0.12	13.74	0.38	14.04	0.23
Mrk 10	B	16.11	0.22	13.81	0.53	14.62	0.23
Mrk 10	V	15.72	0.19	13.27	0.49	13.93	0.20
Mrk 10	R	15.11	0.16	12.75	0.45	13.30	0.19
Mrk 79	B	15.08	0.16	13.53	0.52	14.12	0.32
Mrk 79	V	14.95	0.19	13.05	0.44	13.43	0.29
Mrk 79	R	14.64	0.20	12.59	0.39	12.87	0.26
Mrk 141	B	16.01	0.16	15.50	0.23	15.62	0.20
Mrk 141	V	15.63	0.13	14.71	0.20	14.87	0.13
Mrk 141	R	15.16	0.13	14.12	0.17	14.26	0.10
Mrk 231	B	14.78	0.15	14.12	0.30	14.45	0.20
Mrk 231	V	14.02	0.15	13.61	0.22	13.79	0.17
Mrk 231	R	13.45	0.14	13.09	0.21	13.28	0.15
Mrk 279	B	14.92	0.16	14.50	0.42	14.91	0.28
Mrk 279	R	14.17	0.15	13.43	0.24	13.59	0.16
Mrk 290	B	15.81	0.15	16.24	0.34	16.29	0.34
Mrk 290	V	15.28	0.18	15.35	0.25	15.39	0.24
Mrk 290	R	14.80	0.17	14.79	0.21	14.82	0.21
Mrk 304	B	15.29	0.15	...	...	...	...
Mrk 304	V	14.90	0.13	...	...	15.55	0.31
Mrk 304	R	14.64	0.12	...	...	15.02	0.21

Table 3.4: A. Derived nuclear and galactic magnitudes. The quoted uncertainties on the magnitudes are downward errors. The corresponding upward errors are given by $\delta m^+ = -2.5\log(2 - 10^{0.4\delta m^-})$.

Name (1)	Band (2)	m_n (3)	δm_n (4)	m_g (5)	δm_g (6)	$m_g(20)$ (7)	$\delta m_g(20)$ (8)
Mrk 335	B	14.31	0.14	...	...	...	...
Mrk 335	R	13.79	0.12	14.71	0.31	14.77	0.31
Mrk 352	B	15.49	0.16	15.54	0.26	15.55	0.26
Mrk 352	V	15.16	0.13	14.86	0.17	14.87	0.17
Mrk 352	R	14.78	0.13	14.15	0.13	14.16	0.12
Mrk 359	B	16.59	0.16	14.52	0.15	14.54	0.15
Mrk 359	V	16.30	0.20	13.81	0.14	13.83	0.13
Mrk 359	R	15.91	0.20	13.25	0.14	13.26	0.13
Mrk 372	B	17.62	0.20	15.12	0.16	15.16	0.14
Mrk 372	V	16.77	0.22	14.23	0.14	14.28	0.11
Mrk 372	R	16.39	0.24	13.68	0.14	13.72	0.10
Mrk 376	B	14.57	0.15	...	...	...	...
Mrk 376	V	14.27	0.17	...	...	...	...
Mrk 376	R	14.11	0.12	...	...	...	...
Mrk 478	B	14.84	0.16	...	...	...	...
Mrk 478	V	14.48	0.14	...	...	...	...
Mrk 478	R	14.28	0.13	...	...	...	...
Mrk 486	B	15.04	0.15	...	...	...	...
Mrk 486	R	14.24	0.12	...	...	...	...
Mrk 506	B	16.49	0.18	15.21	0.29	15.60	0.17
Mrk 506	V	15.83	0.14	14.29	0.25	14.60	0.11
Mrk 506	R	15.37	0.12	13.72	0.26	14.05	0.08
Mrk 530	B	16.12	0.18	13.97	0.45	14.45	0.25
Mrk 530	V	15.91	0.17	13.38	0.43	13.80	0.24
Mrk 584	B	17.70	0.18	16.17	0.15	16.42	0.21
Mrk 584	V	17.28	0.15	15.48	0.11	15.73	0.20
Mrk 590	B	15.35	0.15	13.73	0.55	14.46	0.33
Mrk 590	R	14.36	0.12	12.48	0.47	12.97	0.27
Mrk 595	B	17.21	0.19	...	...	15.47	0.18
Mrk 595	V	16.42	0.16	...	...	14.56	0.16
Mrk 595	R	15.89	0.16	...	...	13.94	0.14
Mrk 618	B	15.15	0.15	14.95	0.28	15.11	0.24
Mrk 618	V	14.91	0.13	14.35	0.24	14.52	0.16
Mrk 618	R	14.52	0.12	13.77	0.25	14.00	0.13
Mrk 668	B	17.30	0.24	14.85	0.46	16.28	0.65
Mrk 668	R	16.13	0.25	13.90	0.30	14.76	0.46
Mrk 704	B	15.16	0.15	15.64	0.36	15.75	0.35
Mrk 704	V	14.76	0.13	14.74	0.25	14.83	0.22
Mrk 704	R	14.35	0.14	14.14	0.20	14.22	0.17
Mrk 704	R	14.23	0.13	13.87	0.25	14.00	0.19

Table 3.4: B. Continued.

Name (1)	Band (2)	m_n (3)	δm_n (4)	m_g (5)	δm_g (6)	$m_g(20)$ (7)	$\delta m_g(20)$ (8)
Mrk 705	B	15.99	0.19	...	...	14.95	0.24
Mrk 705	B	15.82	0.17	...	...	14.99	0.27
Mrk 705	V	15.83	0.17	...	...	14.22	0.20
Mrk 705	R	15.52	0.20	...	...	13.77	0.17
Mrk 705	R	15.51	0.27	...	...	13.51	0.20
Mrk 734	B	15.50	0.18	...	...	...	...
Mrk 734	V	15.18	0.15	15.45	0.30	15.82	0.31
Mrk 734	R	15.03	0.13	15.05	0.25	15.40	0.23
Mrk 766	V	15.00	0.17	13.29	0.29	13.31	0.28
Mrk 766	R	14.27	0.17	12.47	0.33	12.51	0.32
Mrk 817	V	14.40	0.15	14.23	0.22	14.28	0.21
Mrk 817	R	14.05	0.15	13.73	0.22	13.79	0.19
Mrk 841	B	15.18	0.16	...	...	...	...
Mrk 841	V	14.94	0.22	...	...	...	...
Mrk 841	R	14.64	0.18	...	...	...	...
Mrk 871	B	16.98	0.27	14.98	0.24	15.23	0.13
Mrk 871	V	16.71	0.25	14.34	0.21	14.55	0.09
Mrk 871	R	16.03	0.29	13.62	0.19	13.80	0.08
Mrk 876	B	15.34	0.16	...	...	...	...
Mrk 876	R	14.83	0.14	15.13	0.23	15.71	0.52
Mrk 975	B	16.43	0.16	15.27	0.34	15.87	0.23
Mrk 975	V	15.81	0.15	14.78	0.28	15.25	0.18
Mrk 975	R	15.54	0.13	14.28	0.37	14.98	0.18
NGC 3516	B	15.07	0.16	12.48	0.43	12.59	0.39
NGC 3516	V	14.82	0.17	11.74	0.40	11.82	0.37
NGC 3516	R	14.26	0.15	10.99	0.43	11.13	0.38
NGC 5548	B	14.98	0.15	13.71	0.43	13.94	0.35
NGC 5548	V	14.44	0.13	12.94	0.43	13.25	0.30
NGC 5548	R	14.10	0.13	12.69	0.31	12.78	0.26
NGC 5940	B	16.85	0.20	14.12	0.43	14.48	0.27
NGC 5940	V	16.24	0.17	13.54	0.38	13.82	0.25
NGC 5940	R	15.60	0.34	12.95	0.39	13.25	0.25
NGC 7469	B	14.21	0.15	13.68	0.35	13.72	0.33
NGC 7469	V	13.76	0.13	12.94	0.29	12.97	0.28
NGC 7469	R	13.27	0.15	12.40	0.26	12.42	0.25

Table 3.4: C. Continued.

3.3.4 Results

In Tab. 3.3 we have reported for each objects the seeing and the best-fit parameters for each frame, the ratio B/G between the bulge and the galactic luminosities and the ratios N/T between the nuclear an the total (nucleus plus galaxy) luminosity within two small apertures, 5″ and 7″.8, which are the apertures we used for our near–IR photometry (Chapters 1 and 2). The last column of this table reports a code Q indicating the quality of the fit: 1 means that the bulge–disk–nucleus decomposition can be considered successfully achieved, 2 means that the nucleus and the galaxy are both reasonably well determined but the bulge–disk decomposition of the galaxy is quite uncertain, while 3 indicates that only the nucleus is detected.

In Tab. 3.4 we have reported the magnitudes of the nuclei and the galaxies. The errors of the nuclear magnitudes δm_n include the following contributions added up in quadrature: (1) a first contribution due to the typical uncertainty in seeing parameter $\Delta\sigma = \pm 0''.03$, (2) uncertainty in the final values of the fitting parameters, and (3) uncertainty of calibration. The global errors are usually in the range between 0.15 and 0.20 magnitudes.

As for the galaxies we have computed the total magnitudes m_g as well as the magnitudes within $r \leq 20$ kpc $m_g(20)$ using the best-fit parameters of bulge and disk. Of course, m_g is computed only for the best quality fits (Q=1). The corresponding errors have been estimated adding to the uncertainties already quoted for the nuclei also the uncertainty in the profiles of the outermost radii. We have taken up as a conservative estimate of this uncertainty the difference between the galactic flux within the last observed point and the reported flux. Because these conservative errors depend on a number of circumstancies, they span a range much larger than that spanned by nuclear uncertainties.

The magnitudes and the brightness parameter have been corrected for the galactic extinction using the values of E_{B-V} given by Cheng et al. (1985) and reported in the Tab. 3.1. No K–corrections have been applied, so that the results refer to the observer's frame. On the other hand, owing to the relatively low redshifts of the galaxies, such corrections are largely negligible with respect to the typical uncertainty.

3.3.5 Comparison to Previous Results

Yee (1983) has analysed surface photometry of 20 Seyfert galaxies obtained with a SIT-vidicon camera. He reported nuclear and host galaxy magnitudes

in g band (Gunn system, see Thuan and Gunn 1976). For 7 objects in common with our sample we have translated these magnitudes to the V-band using transformation laws of Thuan & Gunn (1976) and we have compared them to our results. For 4 objects (Mrk 10, Mrk 79, Mrk 290, Mrk 304) the nuclear magnitudes nicely agree with differences well within the errors and the galactic magnitudes are in reasonable agreement with discrepancies not larger than 2 σ errors. Nuclear g and/or v magnitudes have been estimated for Mrk 290 and 304 also by Malkan (1984) using SIT frames and similar analysis. For both objects Malkan's estimates disagree with Yee's and our evaluations. On the other hand Mrk 304 has been observed with CCD camera at CTIO 4m telescope by Smith et al. (1986), who found $B = 15.31$ for the nucleus, very close to Yee's ($B = 15.39$) and our value ($B = 15.29$). Malkan (1984) and Smith et al. (1986) have one more object in common II Zw 136 and they have estimated the nuclear flux ($B = 14.61$) and ($B = 15.31$) respectively. Of course differences in nuclear magnitudes could be ascribed to time variability.

In the case of Mrk 618 our estimate of the galactic magnitude is close to Yee's value ($\Delta m \sim 0.1$ mag), but we have found that the nucleus is brighter by $\Delta m \simeq -0.5$ mag. For Mrk 376 we have got a reliable estimate only of the nuclear magnitude that resulted to be brighter than Yee's estimate by $\Delta m = -0.64$ mag. The largest difference we have found with the results reported by Yee (1983) refers to the nucleus of Mrk 352, that we have estimated to be brighter by about -1.3 mag in B as well as in V-band. It should be noted that our analysis yields a fainter host galaxy and that discrepancy of about -0.6 mag is also present for the global magnitude of the nucleus plus galaxy.

In our sample we have one more object in common with Malkan's sample, Mrk 478; the estimated nuclear magnitudes are within 0.3 mag corresponding to 2σ error in our case and 1σ for Malkan's analysis. Much larger discrepancy we have found between our estimate of I Zw 1 nuclear magnitude ($m_B = 14.4$) with Smith et al. (1986) analysis ($m_B = 13.8$).

Ward et al. (1987) have estimated the nuclear fluxes of several Seyfert 1 galaxies with various methods. For two objects in common with our sample they have used CCD frames to subtract the galaxy contributions. For Mrk 590 they have found $B = 15.28$ and $R = 14.22$ to be compared to our findings $B = 15.35$ and $R = 14.36$; for NGC 7469 their results are $B = 14.02$ $V = 13.63$ and $R = 13.17$, while we have found $B = 14.21$, $V = 13.76$ and $R = 13.27$.

As a further check we can also compare our estimates of host galaxy

magnitudes to those derived by similar methods. For Mrk 10, Mrk 79, Mrk 290, Mrk 304 and Mrk 618 we have found R-band magnitudes in agreement with the results obtained by Yee (1983) within 1.5σ errors. The discrepant case of Mrk 352 has already been illustrated above. The agreement is decent also for objects in common with Malkan (1984) and Smith et al. (1986) and Hutchings, Crampton & Campbell (1984).

There is also the opportunity of comparing disk parameters and magnitudes to results obtained by Yee (1983), Malkan (1984), Smith et al (1986) and MacKenty (1990). In particular MacKenty (1990) has collected CCD frames in BVR for a sample of 51 Seyfert galaxies, fitting the external regions of 39 galaxies with an exponential disk model. We have data good enough for significant comparisons of disk characteristics for 10 objects, some of them in two or even three bands. As for the host galaxies R–band is the most suitable for comparisons. In the case of disk scale length r_D typical fractional difference is about 20%. On the other hand the estimates of central surface brightnesses are often quite different with a maximum difference of about 2 mag in the case of Mrk 290. However the comparison of disk fractional luminosities within 32 kpc aperture show large differences only in 3 out of 13 cases.

It should be noticed that there are results from various authors clearly at variance among them. For instance Mrk 290 has a much shorter scale length in our and Yee's analysis than in MacKenty's and Malkan's analysis. However Malkan's estimate of the central disk surface brightness ($\mu_D(B) \simeq 21.5$ mag/arcsec^2) is quite close to ours ($\mu_D(B) \simeq 21.6$ mag/arcsec^2) and rather discordant with MacKenty's result ($\mu_D(B) \simeq 23.2$ mag/arcsec^2). Moreover Yee (1983) has found for the same object ($\mu_D(B) \simeq 20.6$ mag/arcsec^2).

We have one more object, Mrk 279, in common with the sample observed by Malkan (1984): our estimate of the disk scale length is a factor about 1.6 larger, while we have found $\mu_D(B) \simeq 21.8$ mag/arcsec^2 about 0.9 mag fainter. However the galactic magnitudes agree within 0.25 magnitudes. Note that Malkan (1984) assumes no bulge component, while bulge contibution of about 15% is predicted by our fit.

We also have compared the galactic colors derived from our fits, to those computed by MacKenty integrating in the annulus between 7.5 and 15 Kpc in radius, in which the contribution from the nucleus is negligible. The mean difference from our colors is -0.09 ± 0.20 (s.d.) in $B - V$ and 0.03 ± 0.13 (s.d.) in $V - R$.

The above discussion confirms that data and analysis yield reliable estimates of nuclear and galaxy fluxes, while the individual parameters of the

galactic components are controversial.

Comparisons are also possible with estimates of nuclear fluxes based on aperture photometry. McAlary and Rieke (1988) have computed nonstellar flux densities of 16 Seyfert galaxies. We have 4 objects in common and the agreement is acceptable for 3 of them (Mrk 6, Mrk 79, NGC 7469). In the case of NGC 5548 our results in all the three bands is fainter, suggesting a dimming of the nucleus at the time of our observations.

Particularly interesting is the comparison with the results obtained by Cheng et al. (1985) on the same sample. Cheng et al. (1985), using a collection of heterogeneous photometric data taken from the literature, and by applying two raw correction methods (the *color given* and *galaxy given* methods), computed the B nuclear magnitudes for all the objects in our sample, with an estimated error of 0.5 mag. The mean difference between our magnitudes and those given by Cheng is 0.19 ± 0.76 (s.d.) for the color given method and 0.49 ± 0.75 for the galaxy given method. The large dispersion of these discrepancies is clearly connected to the crude assumptions made with these methods. The relatively large systematic shift between our results and those of the galaxy given method is easily accounted for: that method consists in fact in subtracting to the observed magnitude the fixed contribution of a template host galaxy. Cheng et al. (1985) have taken $M_B = -21$ for the total absolute magnitude of the galaxy, while we have found from our fits an average of $M_B \simeq -21.6$.

3.4 Discussions and Conclusions

The estimate of truly nuclear fluxes of Seyfert galaxies is a relevant step toward understanding the cosmological evolution of the AGN optical luminosity function (see e.g. Boyle 1991). Although we are partially limited by the typical seeing of our telescope site, nevertheless we have been able to reliably separate galactic and nuclear fluxes. To substantiate the importance of the galactic contribution in small aperture observations of the nuclei, we have computed for the objects of our sample the nuclear over total flux N/T ratios in a $7''.8$ aperture (column 11 Tab. 3.3). The median value is $N/T \simeq 0.7$ in B–band and 0.6 in R–band, implying overestimated fluxes by about 40% and 70% respectively for half of the objects in case of no galaxy subtraction.

The analysis and discussion of the nuclear properties will be presented elsewhere (Granato et al. in preparation). Here we want to focus our atten-

tion on the properties of the host galaxies. As mentioned above, the most reliable parameter is the total magnitude. However even colors and parameters related to the morphology such as the ratio B/G of bulge over total galactic flux have been reliably estimated in many cases.

In particular the B/G ratios of our sample have a relatively narrow distribution in all the three bands (see Fig. 3.4), with median values ranging from 0.17 to 0.27. In the R band only 25 % of the sample object show B/G larger than 0.4 and less than 15% of the sample have B/G larger than 0.6. Even taking into account of possible bias against bulges, comparison of our statistics to those found by Boroson (1981), by Kent (1985) and by Kodaira et al. (1986) for normal galaxies suggests that the large majority of the host galaxies are spirals. This result is in agreement with the general conclusions of previous morphological studies (Adams 1977; Simkin et al. 1980; Whittle 1992) and with the results obtained with similar techniques by Yee (1983), MacKenty (1990) and by ourselves (Chapter 1). It should be noted that we have found about 40% of the objects have $B/G \lesssim 0.2$, which seems typical of galaxies of late type such as Sb-Sc. Indeed Whittle (1992) noticed that about 30% of Seyfert galaxies could be typed as Sb or later. Our statistics seems to exclude that a significant fraction of galaxies typed S0 or earlier among the hosts, opposite to the results based on visual classifications. On the other hand Whittle (1992) has noted that amorphous galaxies, that could be about 20% of the hosts (MacKenty 1990), are often classified as S0 galaxies. Indeed we have found a large spread of B/T ratio among galaxies classified as amorphous by MacKenty (1990).

Although disk and even more bulge parameters are affected by large uncertainties (see Sec. 3.3.3), it is interesting to compare our findings on host galaxies to the results found for normal spiral galaxies.

In the B–band our median value of central brightness $\mu_D(B) \simeq 21.6$ mag/arcsec^2 is somewhat brighter than the results found by Freeman (1970) $\mu_D(B) \simeq 21.7$ mag/arcsec^2 and Boroson (1981) $\mu_D(B) \simeq 21.8$ mag/arcsec^2. The same trend is also present in R–band, where our median central brightness $\mu_D(B) \simeq 19.9$ mag/arcsec^2 is 0.3 magnitudes brighter than that found by Kent (1985) for spiral galaxies (using $R - r \sim 0.3$, see Thuan and Gunn 1976). The difference is actually rather small, well within the standard deviations of the distributions, which are presented in Fig. 3.5. In balance we can conclude that the disks of host galaxies exhibit rather normal central surface brightnesses.

Our sample objects show significant correlation between central bright-

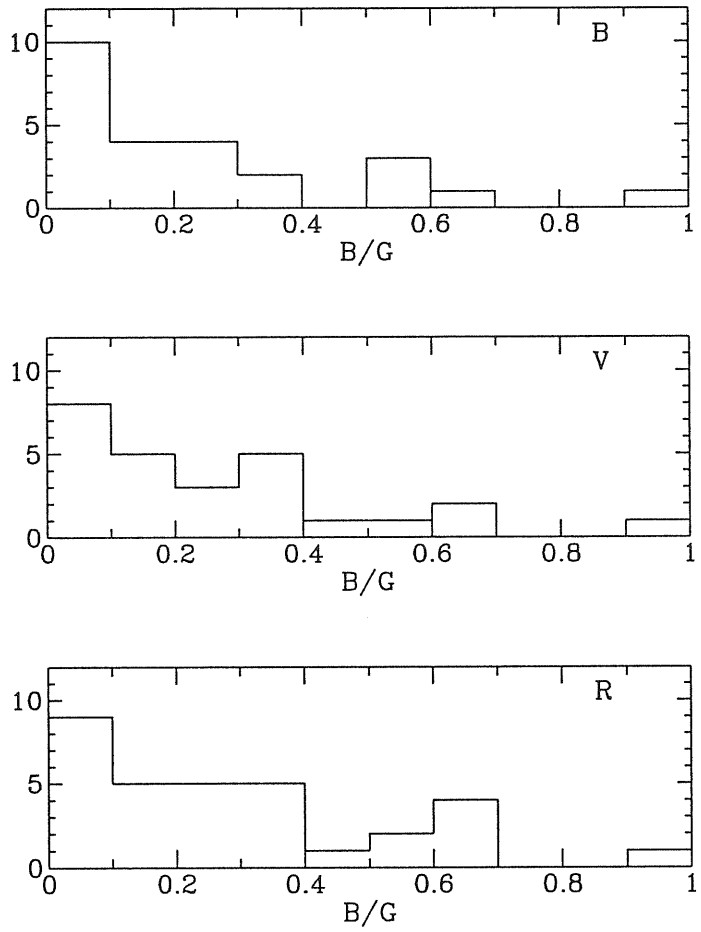

Figure 3.4: Distributions of the ratios B/G between the bulge and the galactic luminosities in the B, V and R bands.

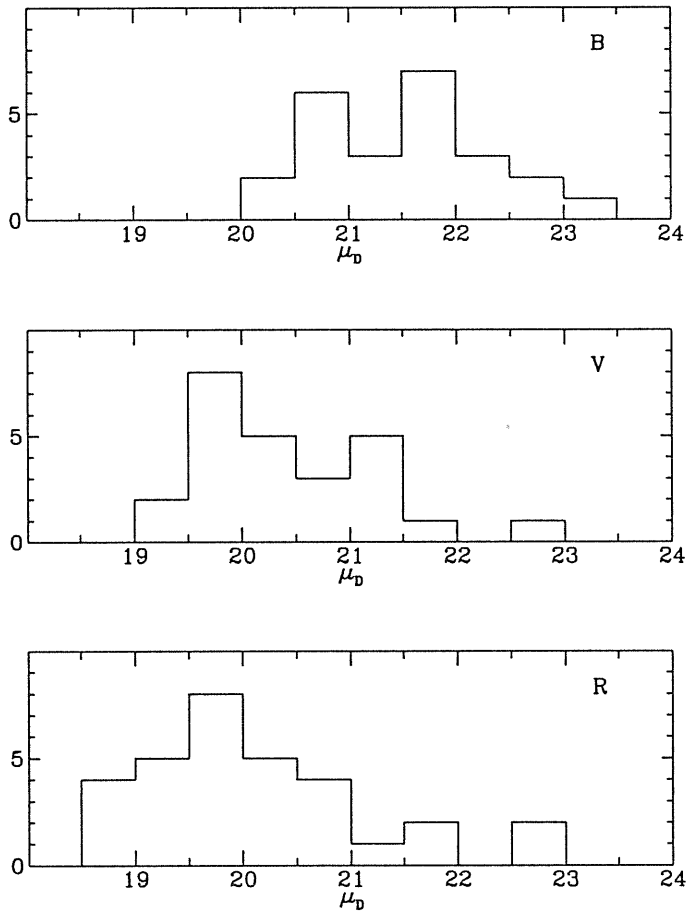

Figure 3.5: Distributions of the disk central surface brightness μ_D in the B, V and R bands.

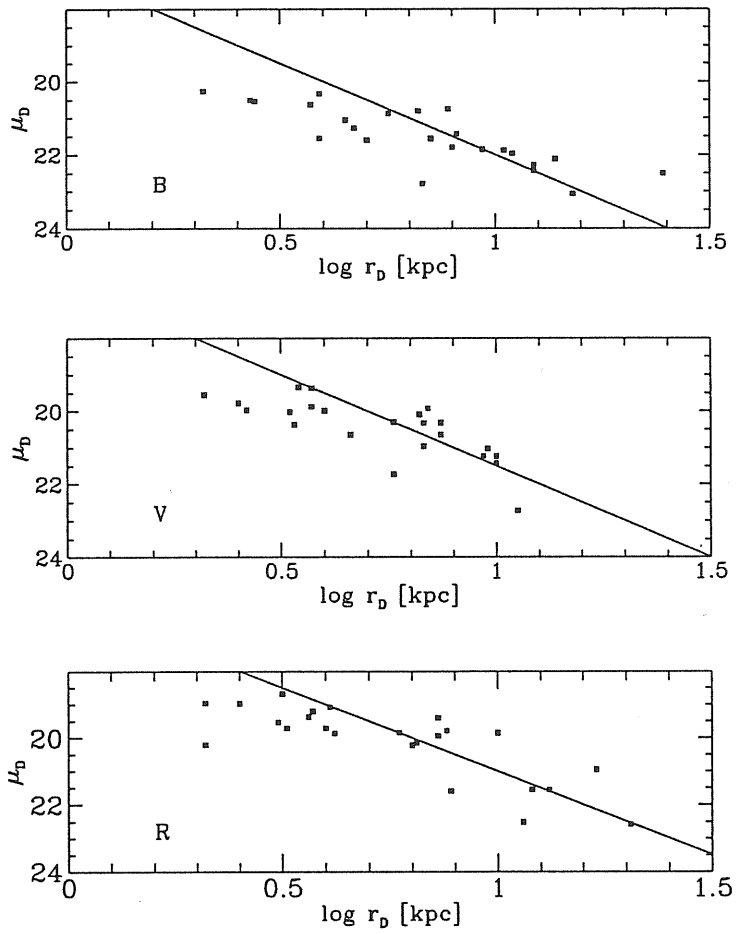

Figure 3.6: Plots of the disk central surface brightness μ_D against the disk scale length r_D. Lines of constant integrated luminosity of the disks are drawn (i.e. $\mu_D r_D^2 = \text{const}$).

ness and disk length (see Fig. 3.6), like that found for normal spiral galaxies and similar to a line of constant disk luminosity (Kent 1985). This fact reflects the fact that the disk luminosities span a relatively narrow range, though the disk parameters have a larger spread.

Even for the characteristic surface brightness μ_e our median result in R–band $\mu_e(R) \simeq 20.8$ is in satisfactory agreement with the result $\mu_e(R) \simeq 20.7$ found by Kent (1985) for spiral galaxies.

Interestingly enough the host galaxies are distributed in the planes B/T—$\log(r_e)$ and B/T—$(\mu_e - \mu_D)$ in a way quite similar to that found by Kent (1985) for normal spirals.

In Fig. 3.7 host galaxy color (within 20 kpc) distributions $(B-V)_g$, $(V-R)_g$ and $(R-K)_g$ are shown. Median optical colors, $(B-V)_g \simeq 0.72$ and $(V-R)_g \simeq 0.57$ are slightly bluer than normal Sa–Sb galaxies. Therefore we have compared our $(B-V)_g$ distribution to that of the *morphological sample* of non–Seyfert Markarian defined by Huchra (1977), confining ourselves to objects of morphological classes $0 \leq T \leq 4$. The median is 0.67, very close to our result, and the probability of the hypothesis that the two distributions are drawn from the same parent population, computed with the standard Kolmogorov–Smirnov test, is high. Moreover in Chapter 2 we have found that the IR colors of host galaxies are slightly redder than those of normal spirals. Therefore our statistics reinforce the suggestion that nuclear activity in galaxies is often associated with moderate starbursting activity possibly in central regions, according to high resolution optical and radio observations of nearby objects (see e.g. Wilson et al. 1991).

The total absolute magnitude distributions of the host galaxies in the three bands are presented in Fig. 3.8. Our median value $M_g(B) \simeq -21.6$ is in reasonable agreement with the average absolute magnitude $M_g(B) \simeq -21.4$ estimated for a sample of 39 objects with nuclear absolute magnitudes $M_n(B) \geq -23.0$ collected from various authors (Boroson et al. 1982; Geheren et al. 1984; Malkan et al. 1984; Hutchings et al. 1984; Smith et al. 1986). Kruper & Canizares (1989) have found a fainter median luminosity $M_g(B) \simeq -21.1$ for their sample of soft X-ray selected AGN. In the V–band our median value $M_g(V) \simeq -22.1$ is close to the result $M_g(V) \simeq -22.0$ derived from the sample studied by Yee (1983). In the R–band our median value is $M_g(R) \simeq -22.8$.

As already noticed by a number of authors (see e.g. Smith et al. 1986), the median absolute magnitude of hosts is brighter than the value of the characteristic magnitude of the Schechter function ($M_g^\star(B) \simeq -21.2$ see Efstathiou et al. 1988). This is in keeping with the results we found in the

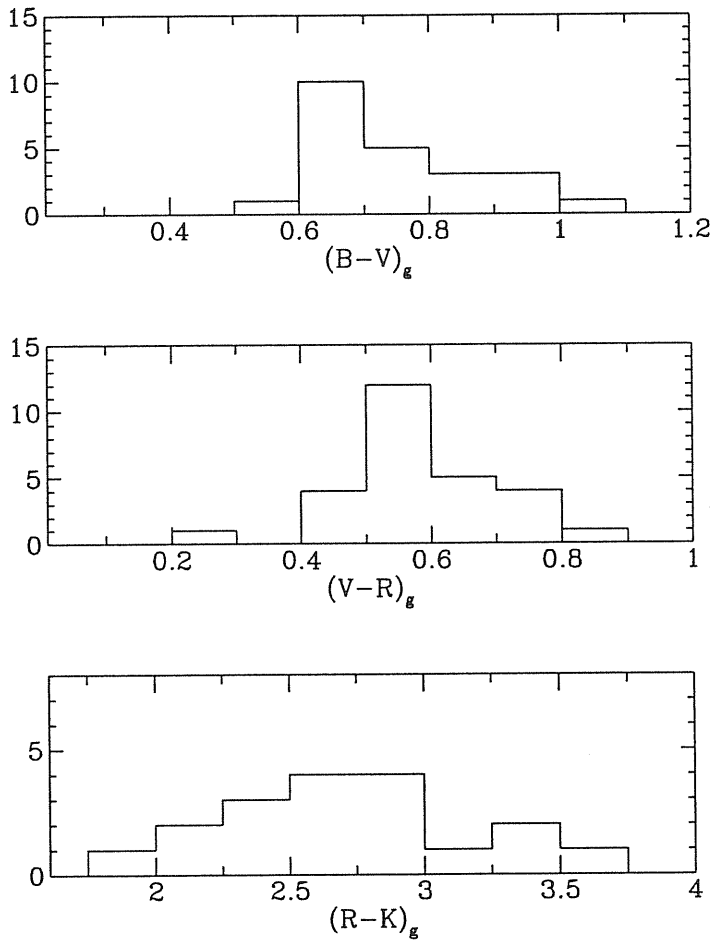

Figure 3.7: Distributions of the galactic colors.

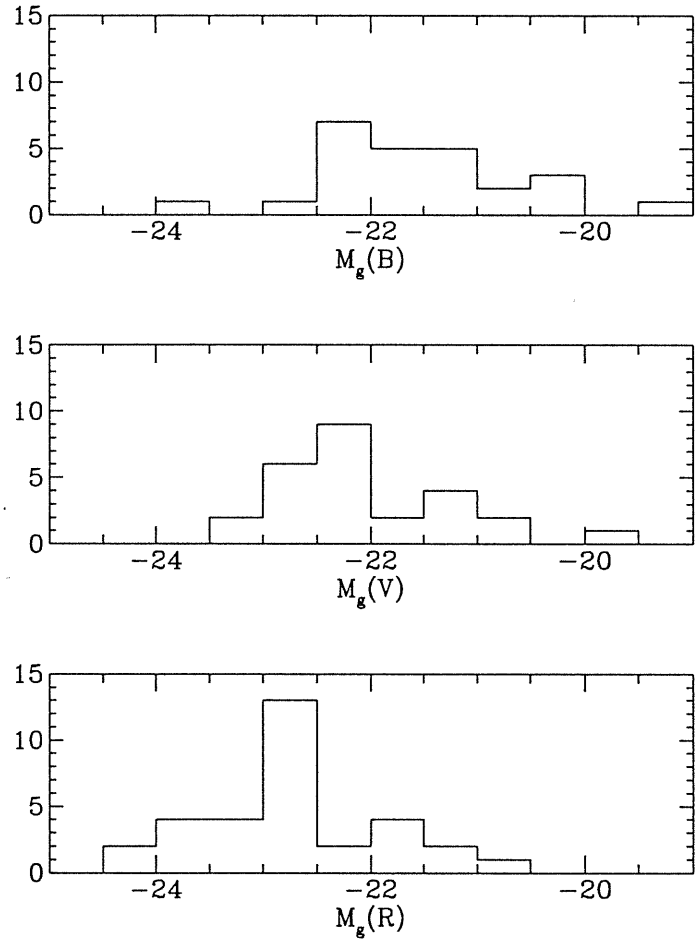

Figure 3.8: Distributions of the galactic absolute magnitudes.

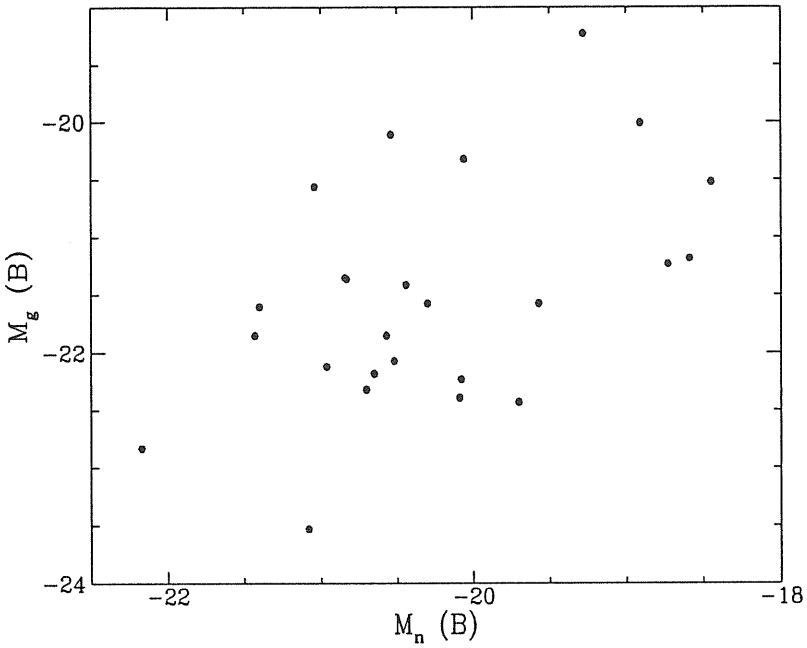

Figure 3.9: Plot of galactic absolute magnitudes against those of the nuclei.

K band (Chapter 2) and may be interpreted as a bias of the AGN toward bright galaxies.

Fig. 3.9 shows that nuclear and galaxy luminosity are correlated, at least apparently. Actually it should be noted that low luminosity active nuclei hosted by bright galaxies could have missed by a survey based on UV excess. However, Koitilainen and Ward (1993) have found that this kind of objects are lacking also in their hard–X selected sample, where this bias should not be present (see Fig. 4.1). On the other hand the deficiency of bright nuclei in low luminosity galaxies, already noted by several authors with studies in optical bands (see e.g. Smith et al. 1986; Veron-Cetty and Woltjer 1990) and by ourselves (Chapter 2) in the K–band, is almost certainly real. This implies significantly increasing probability of hosting a bright active nucleus with increasing galaxy luminosity.

Chapter 4

The Luminosity Function

Summary. We use the B and K nuclear magnitudes, derived in the previous Chapters from imaging data, to estimate the B, K and 12 μm Luminosity Function of Seyfert 1s nuclei. The former is determined following the treatment given by Cheng et al. (1985), whose result is confirmed. The effects of the use of nuclear magnitudes, as opposed to integrated ones, are considered in some details. The 12 μm (or K–band) luminosity function is derived by means of the bivariate optical–infrared luminosity distribution. Our result is in good agreement to the LF estimated by Rush, Spinoglio and Malkan (1993) for a sample of Seyfert 1s selected at 12 μm.

4.1 Introduction

A basic starting point for evolutionary studies of AGNs is the determination of their local Luminosity Function (LF) which, given the observed continuity between Seyfert 1 nuclei and higher redshift QSOs, is represented in practise by the luminosity function of Seyfert 1s nuclei. This is a necessary piece of information to understand the cosmological role of AGNs, such as their contributions to backgrounds, in particular that observed in the X–ray, which is still poorly understood. These facts justify the high number of papers dealing with determinations of Seyfert luminosity functions which have been published in the last two decades. The systematic uncertainties

of the available estimates are still large, as demonstrated by the fact that they often do not agree within the quoted (when quoted) statistical errors. Indeed, there are many problems to address, often related to the fact that we deal with nuclei whose luminosity is not overwhelming with respect to the host galaxy (see Chapters 2 and 3). This circumstance is very likely to produce serious selection effects at some level. Moreover, as originally pointed out by Veron (1979), the relevant LF for AGNs evolutionary studies is that computed by using nuclear magnitudes, and the use of integrated magnitudes, which include the non negligible contribution of the surrounding galaxy, may cause substantial distortions. Another problem is that it is needed a sample sufficiently extended in redshift to include a reasonable number of AGNs and to smooth out density inhomogeneities due to the Local Supercluster, but at the same time not too much extended, in order to avoid the inclusion of an already evolved population.

In the previous Chapters we have presented and discussed near–IR and optical imaging of a statistically well defined sample of AGNs, which provided us with reliable estimates of the nuclear magnitudes in the B, V, R, J, H and K bands. Here we will use these data to provide determine the B–band, K–band and 12 μm LF of Seyfert 1 nuclei.

4.2 The Sample

The sample has been defined by Cheng et al. (1985) (hereafter CDDF). It comprises the 88 objects classified as Seyfert 1 or 1.5, in the area covered by the first nine Markarian lists, up to the end of 1983. More specifically, 68 objects have been discovered during the Markarian survey, 12 are nearby galaxies compensating for the fact that bright galaxies were systematically excluded from Markarian lists, and 5 come from the Zwicky lists of compact galaxies. The sample is therefore essentially UVx selected, and has a sky coverage of 3.39 sr, or 1.11×10^4 square degrees. However, in the following computation of the LF, we will employ an effective solid angle Ω_e, which takes into account that the extinction in our own galaxy introduces a dependence of the limiting magnitude on the direction. In the B–band, $\Omega_e = 2.94$ (CDDF). In Tab. 4.1 we report the coordinates (1950), the redshift and the Seyfert type of the objects.

It is interesting to compare the properties of this sample to those of another sample of local AGNs, extracted from the Center for Atrophysics (CfA) survey, which has also been used recently to compute the luminosity

functions of local AGNs (Huchra and Burg 1992). In this survey ($\simeq$ 400 galaxies) AGNs have been identified by means of low resolution spectroscopy. The sample, complete up to $m_{Zw} = 14.5$ mag, comprises 26 Seyfert 1s (20 of which are also included in our sample), 23 Seyfert 2s, 33 LINERs and one QSO. The following points are worth noticing:

- The AGNs in the CfA survey are more local than those in our sample. The advantage is that the evolutionary effects are more likely to be negligible, while the disadvantage is that an overestimate of the density can be induced by the Local Supercluster. Indeed, as we will see, in the LF function derived from our sample, there are clear signatures of evolution at high luminosity, while in that derived from the CfA sample there are probably distortions at low luminosities due to local density enhancements, as noticed by Hucra and Burg themselves.

- For our objects we have nuclear magnitudes, so that it is possible to compute a LF for the nuclei. As already remembered, this is the relevant quantity for evolutionary comparisons between the LF of local AGNs and that of higher z QSOs.

- The Hucra and Burg sample is statistically poorer: the objects used to compute our LF are about twice.

- On the other hand, the CfA sample is complete, so that there is not need to correct for incompleteness, as we are forced to do.

In conclusion both samples have their advantages as well as their shortcomings, so that they are at present in some sense complementary each other.

4.3 Computation of the B–Band LF

The method we use to compute the LF is basically that described by CDDF, to which the reader is referred for a more detailed description, and incorporates corrections for incompleteness, for random errors in the nuclear magnitudes and for the effect of binning. Procedures for some aspects similar have been used previously also by Veron (1979), Terebizh (1980) and by Meurs and Wilson (1984). In the following we will recall the basic steps, giving more emphasis to the points in which our analysis is affected by the new data and general knowledge gained in the intervening years.

Name	$\alpha(1950)$	$\delta(1950)$	z	Type	B_n	M_{Bn}
0048+2907	00 48 52.2	+29 07 38	0.036	1	16.23	−20.46
1503	15 05 56.4	+03 42 25	0.036	1	16.82	−19.87
2237+07	22 37 47.1	+07 47 35	0.025	1	15.82	−20.07
I Zw 1	00 50 56.4	+12 25 23	0.061	1	14.40	−23.45
II Zw 1	01 19 27.0	−01 18 02	0.054	1	17.61	−19.97
II Zw 136	21 30 01.0	+09 55 04	0.062	1	14.82*	−23.07
III Zw 2	00 07 56.7	+10 41 48	0.090	1	16.20*	−22.51
VII Zw 118	07 07 56.7	+64 37 21	0.080	1	16.59*	−21.86
Mrk 6	06 45 43.4	+74 29 07	0.018	1.5	16.26	−18.92
Mrk 9	07 32 42.0	+58 53 00	0.040	1	15.85	−21.07
Mrk 10	07 43 07.4	+61 03 23	0.029	1	16.11	−20.11
Mrk 40	11 22 48.0	+54 39 26	0.021	1	...	...
Mrk 42	11 51 05.3	+46 29 20	0.024	1	...	...
Mrk 50	12 20 50.9	+02 57 20	0.023	1	...	...
Mrk 69	13 43 51.3	+29 53 03	0.076	1	16.94*	−21.40
Mrk 79	07 38 46.9	+49 55 47	0.022	1.5	15.08	−20.53
Mrk 106	09 16 18.4	+55 34 21	0.122	1	16.44*	−22.95
Mrk 110	09 21 44.4	+52 30 14	0.036	1	...	...
Mrk 124	09 45 24.3	+50 43 26	0.057	1	16.24*	−21.46
Mrk 141	10 15 38.7	+64 13 14	0.039	1	16.01	−20.86
Mrk 142	10 22 23.1	+51 55 40	0.045	1	16.23*	−20.95
Mrk 205	12 19 31.8	+75 35 10	0.070	1	15.64*	−22.51
Mrk 231	12 54 05.0	+57 08 37	0.041	1	14.78*	−22.20
Mrk 236	12 58 18.0	+61 55 27	0.052	1	16.69*	−20.81
Mrk 279	13 51 51.9	+69 33 13	0.031	1.5	14.92	−21.44
Mrk 290	15 34 45.4	+58 04 00	0.031	1	15.81	−20.55
Mrk 291	15 52 54.1	+19 20 20	0.036	1	16.91*	−19.78
Mrk 304	22 14 45.2	+13 59 27	0.067	1	15.29	−22.77
Mrk 315	23 01 35.6	+22 21 20	0.039	1.5	...	...
Mrk 335	00 03 45.1	+19 55 27	0.025	1	14.31	−21.58

Table 4.1: The sample. The coordinates are taken from Mazzarella and Balzano (1986) for Markarian galaxies and from Paturel et al. (1989) for the reminder, except Tol 1059, Ton 524 A and X Comae whose coordinates have been taken from Della Ceca et al. (1990). The redshift is from Veron–Cetty and Veron (1989). The Seyfert type is the same reported in CDDF. The asterisks indicate magnitudes computed with the color–given method (typical uncertainty $\delta m \sim 0.5$ mag), otherwise the magnitude is computed from the profile fitting procedure (Chapter 3, $\delta m \sim 0.15 \div 0.20$ mag).

Name	$\alpha(1950)$	$\delta(1950)$	z	Type	B_n	M_{Bn}
Mrk 352	00 57 08.6	+31 33 27	0.015	1	15.49	−19.29
Mrk 358	01 23 45.1	+31 21 13	0.046	1	...	...
Mrk 359	01 24 50.1	+18 55 07	0.017	1	16.59	−18.46
Mrk 372	02 46 30.9	+19 05 54	0.031	1.5	17.62	−18.74
Mrk 374	06 55 33.9	+54 15 53	0.044	1	15.84*	−21.29
Mrk 376	07 10 35.8	+45 47 07	0.056	1	14.57	−23.09
Mrk 382	07 52 03.2	+39 19 07	0.034	1	16.21*	−20.36
Mrk 464	13 53 45.1	+38 48 54	0.051	1	...	...
Mrk 474	14 33 06.0	+48 52 47	0.041	1	...	...
Mrk 478	14 40 04.6	+35 38 53	0.079	1	14.84	−23.58
Mrk 486	15 35 21.5	+54 43 04	0.039	1	15.04	−21.83
Mrk 493	15 57 16.6	+35 10 13	0.031	1	16.40*	−19.96
Mrk 504	16 59 10.4	+29 28 47	0.036	1	16.19*	−20.50
Mrk 506	17 20 45.6	+30 55 30	0.043	1.5	16.49	−20.59
Mrk 509	20 41 26.4	−10 54 16	0.036	1	14.32	−22.37
Mrk 530	23 16 22.7	−00 01 48	0.029	1	16.12	−20.10
Mrk 541	23 53 28.2	+07 14 36	0.041	1	...	...
Mrk 543	23 59 52.9	+03 04 26	0.026	1	16.79*	−19.19
Mrk 584	01 57 51.1	+02 25 49	0.078	1	17.70	−20.69
Mrk 590	02 12 00.5	−00 59 57	0.027	1.	15.35	−20.71 5
Mrk 595	02 38 55.8	+06 58 27	0.028	1	17.21	−18.93
Mrk 618	04 33 59.7	−10 28 40	0.034	1	15.15	−21.42
Mrk 634	10 55 20.6	+20 45 03	0.066	1	17.64*	−20.38
Mrk 662	13 51 46.3	+23 40 29	0.055	1.5	17.91*	−19.71
Mrk 668	14 04 45.9	+28 41 35	0.079	1	17.30	−21.12
Mrk 699	16 22 05.0	+41 11 42	0.034	1	18.76*	−17.81
Mrk 704	09 15 39.5	+16 30 59	0.029	1.5	15.16	−21.06
Mrk 705	09 23 20.0	+12 57 03	0.028	1	15.99	−20.15
Mrk 707	09 34 26.5	+01 19 13	0.051	1	17.31*	−20.15

Table 4.1: Continued

Name	α(1950)	δ(1950)	z	Type	B_n	M_{Bn}
Mrk 716	10 07 27.5	+23 21 19	0.056	1.5	18.46*	−19.20
Mrk 734	11 19 10.9	+12 00 47	0.050	1	15.50	−21.91
Mrk 739	11 33 52.5	+21 52 24	0.030	1	...	...
Mrk 766	12 15 55.5	+30 05 27	0.013	1	15.78	−18.69
Mrk 771	12 29 33.1	+20 26 02	0.064	1	15.31*	−22.65
Mrk 783	13 00 30.4	+16 40 34	0.067	1	16.21*	−21.85
Mrk 813	14 25 05.8	+20 03 19	0.111	1	15.42*	−23.76
Mrk 817	14 34 58.0	+59 00 40	0.032	1.5	14.17*	−22.26
Mrk 841	15 01 36.4	+10 37 59	0.036	1.5	15.18	−21.51
Mrk 845	15 06 12.5	+51 38 41	0.046	1	17.03*	−20.20
Mrk 849	15 17 50.9	+28 45 26	0.082	1	17.78*	−20.72
Mrk 871	16 06 15.6	+12 27 41	0.034	1	16.98	−19.59
Mrk 876	16 13 36.2	+65 50 37	0.129	1	15.34*	−24.17
Mrk 877	16 17 56.6	+17 31 35	0.115	1	15.63*	−23.63
Mrk 885	16 29 43.1	+67 29 06	0.025	1	...	...
Mrk 975	01 11 12.7	+13 00 27	0.050	1	16.43	−20.98
NGC 2639	08 40 03.0	+50 23 24	0.011	1	...	...
NGC 3227	10 20 47.6	+20 07 00	0.003	1.5	...	...
NGC 3516	11 03 22.6	+72 50 25	0.009	1	15.07	−18.60
NGC 4051	12 00 35.9	+44 48 48	0.002	1	16.76*	−13.64
NGC 4151	12 08 00.8	+39 41 11	0.003	1.5	12.90*	−18.38
NGC 4235	12 14 35.7	+07 28 11	0.007	1	...	...
NGC 5273	13 39 55.1	+35 54 18	0.004	1	...	...
NGC 5548	14 15 44.0	+25 22 01	0.019	1.5	14.98	−20.31
NGC 5940	15 28 51.1	+07 37 38	0.034	1	16.85	−19.72
NGC 7469	23 00 44.0	+08 36 19	0.017	1.5	14.21	−20.84
Tol 1059	10 59 21.0	+10 33 48	0.034	1	...	...
Ton 524A	10 20 46.4	+29 02 27	0.060	1	17.03*	−20.78
X Comae	12 57 57.7	+28 40 10	0.092	1	17.88*	−20.88

Table 4.1: Continued.

4.3.1 Nuclear Magnitudes

In Chapter 3 we derived, using CCD frames, B band magnitudes for the nuclear pointlike component of 38 AGNs of the sample. These objects are less than one half of the whole sample, but 34 of them belong to the homogeneous subsample of 52 AGNs that will be used for the determination of the LF (see below). The typical overall uncertainties on these nuclear magnitudes, including both statistical noise as well as systematic effects, are rather low, usually less than 0.2 mag. For the reminder objects, we can obtain a less precise estimate of the nuclear magnitudes using the *color given method* (Sandage 1973) described by CDDF. The method works essentially starting from photometry in two bands, within the same aperture, and assuming the colors for both the nuclear and the galactic component. It is straightforward to derive an equation giving the nuclear magnitude in one of the two bands, in terms of the observed total magnitude and color and on the assumed components colors. For instance, denoting with the subscripts n, g and c the quantities referred to the nucleus, to the galaxy and to the observed combination of the two respectively, we have:

$$B_n = B_c + 2.5\log(1 + 1/a_B) \tag{4.1}$$

where

$$a_B \equiv \frac{L_n(B)}{L_g(B)} = \frac{1 - 10^{0.4[(B-V)_g-(B-V)_c]}}{10^{0.4[(B-V)_n-(B-V)_c]} - 1} \tag{4.2}$$

CDDF estimated that the typical uncertainty on the B magnitude derived in such a way is of the order of 0.5 mag. This is confirmed by the fact that, comparing their values to those we derived from the optical frames, we found a distribution of the differences having about this width (see Sec. 3.3.5). Thus, for the objects we did not observe in the B band, we have repeated their computations, using the same photometry but adopting slightly different assumptions, based on our results: (i) the intrinsic nuclear color is assumed to be $(B-V)_{n,0} = 0.4$, the mean value found from the B and V frames, rather than 0, and (ii) we do not correct for the reddening within the host galaxy, since the nuclear colors derived from the frames do not show any correlation with the axial ratio, suggesting that the reddening law used by CDDF (their Eq. (10)) is not reliable. Note that this two differences go in opposite directions and have a comparable absolute value, so that the final value is often similar. In Tab. 4.1 we have reported the

apparent and absolute B band magnitudes for the entire sample, marking with an asterisk those values obtained with the color–given method, which therefore are less precise. For 16 objects we do not have any estimate of B_n, since they have not been observed and the color–given method does not give any solution (the method works if the observed color is redder than that of the nucleus and bluer than that of the galaxy).

4.3.2 Definition of a Homogeneous Sample

The sample considered so far is clearly plagued by serious incompleteness, since it has been constructed simply collecting from the literature objects from different surveys, with the only requirements of belonging to the area covered by the first nine Markarian lists and of being classified as Sy 1 or 1.5. Even the major source for the sample, the Markarian survey, becomes progressively incomplete at magnitudes fainter than $m_{ph} \sim 15$ (Sargent 1972). Neyman and Scott (1961,1974) showed that it is possible to compute the LF even from an incomplete sample, provided that its incompleteness is sufficiently "well understood", so that it can be corrected in the computations. More specifically the sample need to be *homogeneous*, in the sense that the probability for an object to be selected depends only on its apparent magnitude. While in a complete sample this probability is identically equal to one, in a homogeneous sample it is a decreasing function of the magnitude $p(m)$, equal to one at sufficiently low m (i.e. high flux). If the sample has this property, $p(m)$ can be estimated, assuming a spatially homogeneous distribution, with the standard $V/V_{\max}$ test, and then the LF can be computed dividing the surveyed volume of each object $V_{\max}(M, m_l)$ for $P(m)$, where m and M are respectively the apparent and absolute magnitudes of the object, and

$$P(m) = 0.6 \ln(10) \int_{-\infty}^{m} 10^{0.6(m'-m)} p(m')\, dm' \qquad (4.3)$$

(see equation (17) in CDDF). The sample must be restricted to a suitable limiting magnitude m_l, such that the correction factor $1/P(m)$ is not too large, say $\lesssim 2$.

The operational criterion indicated by Neyman and Scott to judge the homogeneity of a sample is the lack of correlation between the absolute and apparent luminosity.

It is worth noticing that our considerations concerning the completeness and homogeneity of the sample refers always to the bare nuclear component.

In order to define a homogeneous subsample, we repeated on the new data the analysis made by CDDF. There are at least two problems that could introduce, in the sample listed in Tab. 4.1, a dependence of the probability for an objects to be selected on circumstances other than its apparent luminosity, giving raise to "inhomogeneity":

- a first contrast effect between the nuclear and galactic luminosity, which would not allow to recognize the Seyfert optical properties when the nuclear luminosity is too low with respect to that of the galaxy;
- a second opposite contrast effect, so that nuclei very prominent with respect to the host may appear starlike and as such be excluded from the Markarian lists. This problem is likely to be more severe for more distant objects.

According to CDDF, these problems can be avoided confining ourselves to nuclei satisfying the conditions $z \leq z_c$, $B_n \leq B_l$ and $M_{Bn} \leq M_B^*$, with proper choices of the cut–off redshift z_c, of the limiting magnitude B_l and of the maximum absolute magnitude M_B^*.

As we pointed out in the Chapter 3, the first effect could account in part for the sharp correlation observed in our data between the galactic and nuclear luminosity. However, this bias should not be present in the hard–X selected sample observed recently by Koitilainen and Ward (1993), in which instead the correlation is again very strong (see Fig. 4.1), leading to the conclusion that the observed lack of faint AGNs hosted in bright galaxies is mostly real, and the contrast effect does not introduce any serious inhomogeneity in our sample. The cut–off of the luminosity distribution of objects in Tab. 4.1, at magnitudes fainter than $\simeq -18.0$, is not due to this bias, so that we can compute the LF down to luminosities at which the statistic is adequate. We set $M_B^* = -18.0$, a value which excludes only two nuclei from the sample.

The second bias becomes important when the redshift is sufficiently high, and can be eliminated confining ourselves to nuclei below a given *cut–off* redshift z_c, above which objects tend to be missed in the Markarian survey due to the difficulty to identify the surrounding nebulosity. This cut–off redshift can be estimated, following CDDF, comparing the z distribution of the objects in Tab. 4.1 to that of the objects in the BQS sample (Schmidt and Green 1983) with an associated nebulosity. As discussed in details by CDDF, and as can be guessed by an inspection of Fig. 4.2, a reasonable value of z_c is 0.08, which eliminates 8 objects of Tab. 4.1.

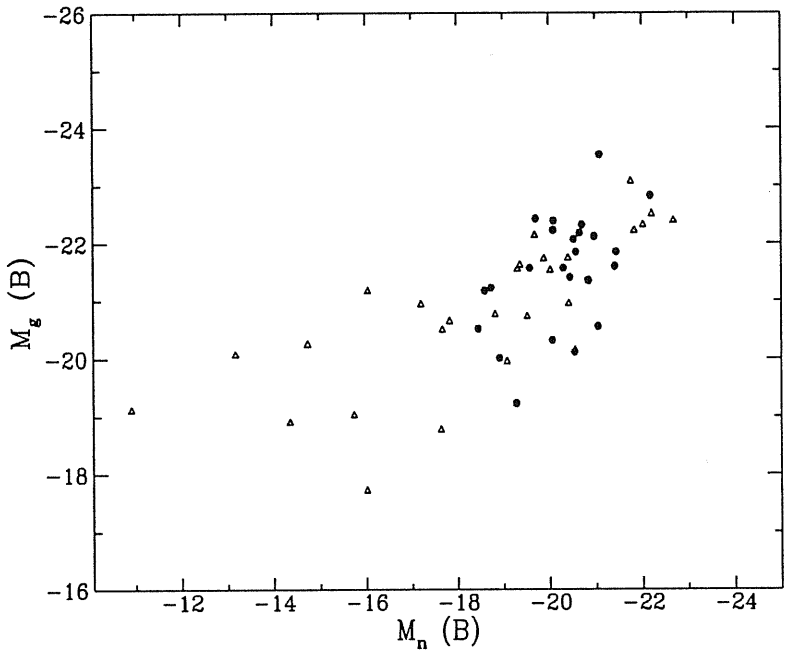

Figure 4.1: Plot of galactic absolute magnitudes against those of the nuclei. Filled circles represent our data, while empty triangles represent data taken from Koitilainen and Ward (1993).

We checked for the homogeneity of the subsamples defined by $z_c = 0.08$, $M_B^* = -18$, and B_l with different choices of B_l, using the test indicated by Neyman and Scott. In doing this, it must be taken into account that the presence of a cut–off redshift introduces itself a certain degree of correlation, not due to a lack of homogeneity, between M_{Bn} and B_n. Indeed, at any value of B_n an object has a redshift less than z_c only if $M_{Bn} \geq \hat{M}(B_n) \equiv B_n - 5\log z_c - 43.89$, a fact that produces a forbidden zone in the plane M_{Bn}–B_n (see Fig 4.3). Thus the correlation analysis must be confined to $\hat{M}(B_l) \leq M_{Bn} \leq M_B^*$.

We found, in keeping with the results of CDDF, that the subsample of 52 nuclei defined by the conditions $z \leq 0.08$, $B_n \leq 17.0$ and $M_{Bn} \leq -18.0$ turns out to be reasonably homogeneous. Our estimate of the B band LF is based on this subsample. The probability that the observed degree of correlation

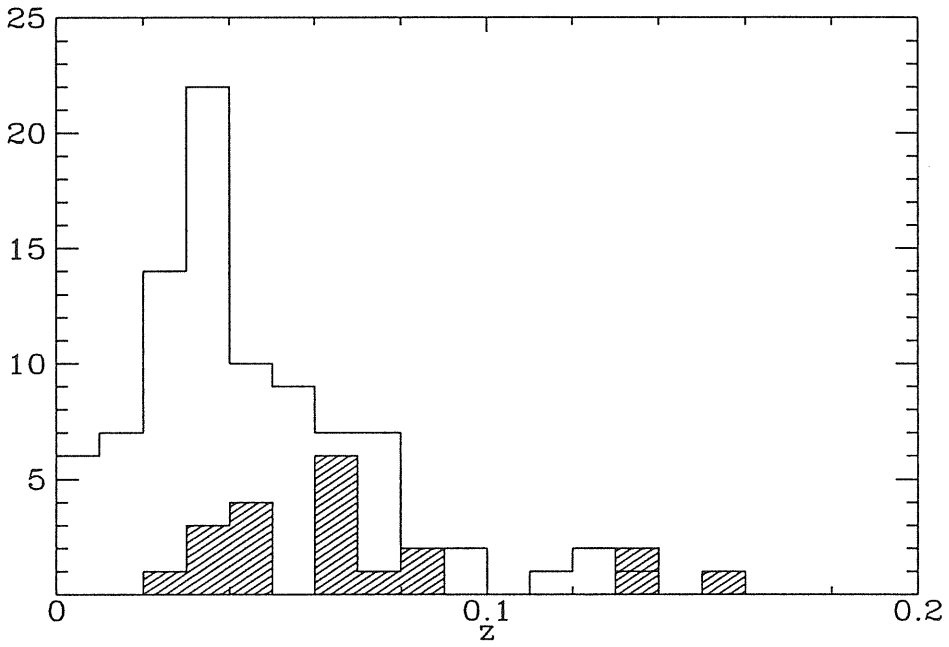

Figure 4.2: Distribution of the redshift in our sample (empty histogram) compared to that of the objects in the BQS sample showing an associated nebulosity (hatched histogram).

between M_{Bn} and B_n arises by chance, as given by the Kendall's τ test on 33 data points, is equal to 0.8. Moreover, the minimum value of $P(m)$ is 0.464, giving a maximum incompleteness correction factor $F_i(m) = 1/P(m)$ of 2.15, which means that at the limiting magnitude of 17 we would expect a total of 112 objects if the sample was complete. The incompleteness analysis has been performed in steps of 0.05 mag. starting at 14.5, and the results are reported in Tab. 4.1, from which it can be seen that the sample is complete only up to $B_n = 15.55$.

4.3.3 Results and Comparisons

Our determination of the LF is reported in Tab. 4.2 and in Fig. 4.4, together with estimates from other authors. The result is rather stable with respect to the chosen values of the parameters. Halving or doubling the step for

B	$<V/V_{max}>$	$N_{obs}(<B)$	$P(B)$	B	$<V/V_{max}>$	$N_{obs}(<B)$	$P(B)$
14.50	0.639	6	1.000	15.80	0.423	24	0.857
14.55	0.596	6	1.000	15.85	0.502	29	0.879
14.60	0.614	7	1.000	15.90	0.477	29	0.879
14.65	0.573	7	1.000	15.95	0.454	29	0.853
14.70	0.535	7	1.000	16.00	0.450	30	0.857
14.75	0.499	7	1.000	16.05	0.445	31	0.838
14.80	0.529	8	1.000	16.10	0.424	31	0.795
14.85	0.546	9	1.000	16.15	0.437	33	0.805
14.90	0.513	9	1.000	16.20	0.433	34	0.773
14.95	0.530	10	1.000	16.25	0.483	39	0.796
15.00	0.541	11	1.000	16.30	0.470	40	0.800
15.05	0.548	12	1.000	16.35	0.445	40	0.769
15.10	0.579	14	1.000	16.40	0.436	41	0.745
15.15	0.573	15	1.000	16.45	0.427	42	0.724
15.20	0.587	17	1.000	16.50	0.420	43	0.705
15.25	0.552	17	1.000	16.55	0.400	43	0.662
15.30	0.547	18	1.000	16.60	0.395	44	0.647
15.35	0.561	20	1.000	16.65	0.376	44	0.611
15.40	0.529	20	1.000	16.70	0.373	45	0.592
15.45	0.499	20	1.000	16.75	0.356	45	0.556
15.50	0.518	22	1.000	16.80	0.355	46	0.541
15.55	0.488	22	1.000	16.85	0.352	47	0.522
15.60	0.463	22	0.957	16.90	0.350	48	0.505
15.65	0.462	23	0.958	16.95	0.348	49	0.485
15.70	0.439	23	0.885	17.00	0.346	50	0.467
15.75	0.418	23	0.852				

Table 4.1: Results of the V/V_{max} test. The incompleteness factor $F_i(B) = 1/P(B)$ is approximated by the ratio between $N_{obs}(< B)$, the number of observed objects with apparent magnitude less than B, and $N_{un}(< B)$, the number expected for a complete sample in case of a uniform space distribution (see equation (17) in CDDF).

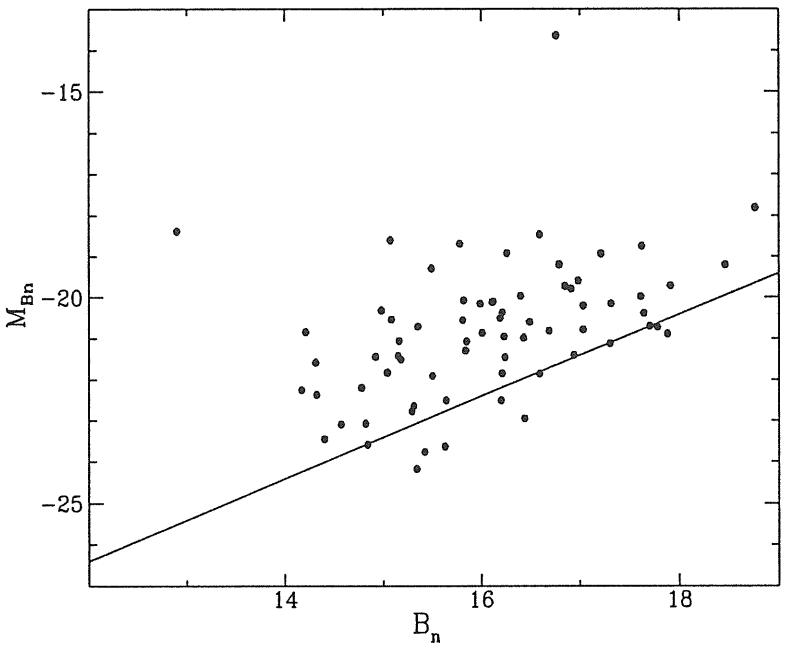

Figure 4.3: Plot of absolute against the apparent magnitudes for our sample nuclei. The diagonal line represents the equation $M_{Bn} = B_n - 5\log z_c - 43.89$. Objects below this line tend to be excluded from the sample due to the existence of a cut–off redshift z_c above which it becomes very difficult to recognize the associated nebulosity.

the completeness analysis or the size of the bins, changing B_l from 16.5 to 17.5, the differences are always within 15%. The third and fourth columns of Tab. 4.2 report the upward and downward statistical errors on the LF, which have been computed from the formula:

$$\frac{\sigma(\varphi)}{\varphi} = \left[\frac{1 - N_b/N_t}{N_b}\right]^{1/2} \tag{4.4}$$

where N_b is the number of objects in the bin and N_t is total number of objects in the sample. This formula follows from the binomial character of the distribution of N_b.

The new determination is in good agreement, well within the quoted

M_{Bn}	$\log(\varphi(M_{Bn}))$ $[\mathrm{Mpc}^{-3}\mathrm{mag}^{-1})]$	σ^+ N	σ^-	N
−23.50	−7.51	0.18	−0.30	4
−22.50	−7.24	0.15	−0.23	6
−21.50	−6.62	0.11	−0.14	13
−20.50	−5.92	0.09	−0.12	17
−19.50	−5.66	0.13	−0.19	8
−18.50	−5.36	0.18	−0.30	4

Table 4.2: Luminosity function of Seyfert 1 and 1.5 nuclei in the B band, with associated statistical upward and downward errors. The last column reports the number of objects of the homogeneous sample in the magnitude bin.

$M_{B,c}$	$\log(\varphi(M_{B,c}))$ $[\mathrm{Mpc}^{-3}\mathrm{mag}^{-1})]$	σ^+ N	σ^-	N
−23.50	−7.65	0.23	−0.53	2
−22.50	−6.68	0.10	−0.13	14
−21.50	−5.94	0.07	−0.09	30
−20.50	−5.55	0.08	−0.10	22
−19.50	−5.57	0.16	−0.26	5
−18.50	−5.42	0.23	−0.53	2

Table 4.3: Luminosity function of Seyfert 1 and 1.5 galaxies derived using integrated photometry.

errors, to those reported by CDDF, in particular the one they obtained using the color–given method applied to $(B-V)$ colors. In this case, the greatest difference, corresponding to a factor 1.4, occurs at $M_{Bn} = -21.5$. This nice agreement is not unexpected, provided that the sample and the method are the same and the adopted nuclear magnitudes have differences often within the adopted errors. On average this difference amounts to 0.09 ± 0.72 mag (s.d.), to compare with the estimated uncertainties of 0.2 and 0.5 mag respectively for our and their magnitudes.

To study the effects introduced by the use of total magnitudes (nucleus plus galaxy), we computed, with the same technique, the LF simply using the integrated photometry collected from the literature by CDDF. The result is reported in Tab 4.3. As can be appreciated from Fig. 4.4, the use of integrated magnitudes, introduces a severe distortion in the shape of the

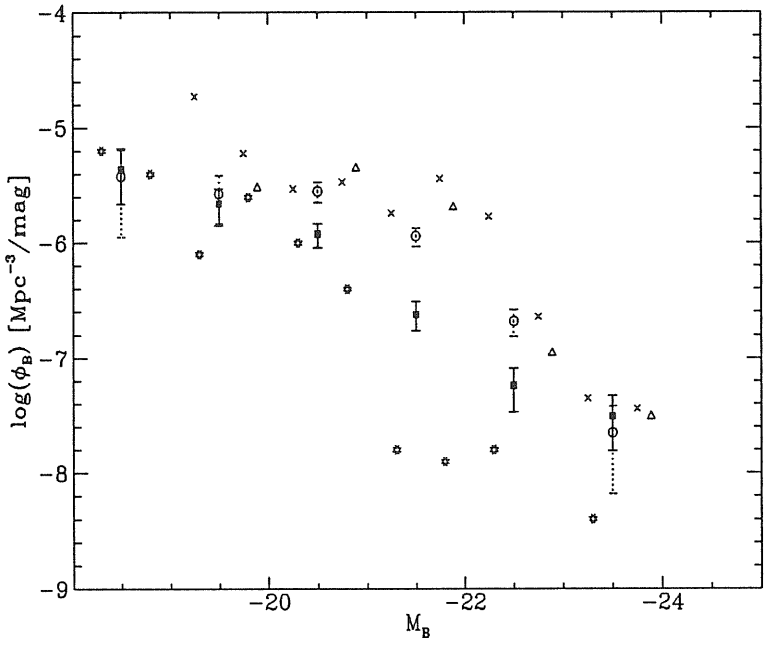

Figure 4.4: Luminosity function of Seyfert 1 in the B band. Filled squares with solid error bars: our estimate using nuclear magnitudes; open circles with dotted error bars: our estimate using integrated total magnitudes; Stars: Veron (1979); open triangles: Meurs & Wilson (1984); crosses Huchra & Burg (1992). Error bars are reported only for our result. Note however that they usually would be greater than ours, due to poorer statistic.

LF. For $-20.5 \geq M_B \geq -22.5$, the galactic contribution shifts significantly the LF toward higher values, up to a factor ~ 5. The difference becomes less important at increasing luminosities, where the nucleus tends to prevail, and in the highest luminosity bin it is well within the error bars. The differences are also negligible at low luminosity, where the objects lost to higher luminosities are balanced by those coming from lower ones.

In Fig. 4.4, our results are compared to the determinations of Veron (1979), Meurs and Wilson (1984) and Huchra and Burg (1992). The Veron's LF, derived using a sample of only 34 Seyfert 1s from the first five Markarian lists and the color–given method to obtain the nuclear magnitudes, has been

reported to the B band using the nuclear color $(B-V)_n = 0.2$ adopted in that paper. Note also that, according to a private communication, the space densities in Veron's Tab. 1 are wrong and must be reduced by a factor 2, and also that the densities in his Fig. 2 are per half–magnitude intervals. The small correction $B = m_p + 0.11$ has been applied to the blue photographic magnitudes used by Meurs and Wilson (1984). Their sample (101 objects) is also mainly extracted from the first 9 Markarian lists, and they used Zwicky magnitudes whenever possible to compute the LF. The Huchra and Burg (1992) result, which has been reported to $H_o = 50$ km/sec/Mpc, refers also to integrated magnitudes, but is based on a spectroscopically selected complete sample, namely the CfA sample.

As expected, the agreement of our nuclear LF is satisfactory only with the Veron's estimate, in particular at $M_B > -21$, where its statistic is sufficiently rich (its determination for the four bins at $M_B < -21$ is based only on 6 objects). By converse, the match between our nuclear LF and that of Meurs and Wilson, or that of Huchra and Burg, is good only in the highest luminosity bin, where the galactic luminosity has little effect. Indeed, the differences can be mostly explained by the use of integrated magnitudes, as indicated by the fact that our determination made with integrated magnitudes agrees reasonably well with Huchra and Burg's result. It is interesting to notice that the estimates of Huchra and Burg and that of Meurs and Wilson, although based on completely different selections, are in good agreement.

We wish to remark that in our sample with $z \leq 0.8$ evolutionary effects are probably already at work for the brightest objects. The calculated LF at $M_B = -23.5$ is considerably greater than the value that would be extrapolated from the lower luminosity bins, and indeed the mean z of the four objects falling in this bin (i.e. I Zw 1, II Zw 136, Mrk 376 and Mrk 478) is 0.06, much higher than the mean value 0.034 of the homogeneous sample.

4.4 Computation of the LF in Other Bands

4.4.1 General Method

In the following we will estimate the luminosity function of Seyfert 1 nuclei in the K–band (2.2 μm) and in the IRAS 12 μm band. The common method to obtain the LF function of a sample of objects, in a band different from that in which the sample has been originally selected, and in which therefore it is impossible to define the completeness limit, uses the bivariate luminosity

distribution in the two bands. This procedure has been originally employed by Elvis et al. (1978) in the problem of deriving an X–ray LF for optically selected Seyfert galaxies. More recent applications of the method have been described, among others, by Meurs and Wilson (1984) or Franceschini et al. (1988).

Suppose we want to compute the luminosity function in a generic band Y, for a sample of objects selected in the band X. Once derived the luminosity function in the X band, the plane L_X–L_Y is divided into N_X and N_Y bins of amplitude ΔL_X and ΔL_Y along the two axes respectively. Then the distribution of L_Y is computed in each L_X bin, by means of a suitable statistical estimator, and integrated in each L_Y bin, to give the quantities F_{ij}, i.e. the fractionary number of objects with L_X in the i–th L_X bin and L_Y in the j–th L_Y bin, with the normalization $\sum_i F_{ij} = 1$. Finally, the Y band LF is obtained, in each L_Y bin, by summing up along the L_X bins the product of the X band LF and of the bivariate distribution:

$$\varphi_Y(L_{Yj}) = \frac{\Delta L_X}{\Delta L_Y} \sum_i F_{ij} \varphi_X(L_{Xi}) \tag{4.5}$$

The corresponding uncertainty is

$$\delta\varphi_Y^2(L_{Yj}) = \frac{\Delta L_X^2}{\Delta L_Y^2} \sum_i \left[\delta F_{ij}^2 \varphi_X^2(L_{Xi}) + F_{ij}^2 \delta\varphi_X^2(L_{Xi})\right] \tag{4.6}$$

In our computations we took advantage also of the information contained in upper limits to the luminosities. To do this, the bivariate distributions have been computed by means of survival analysis techniques. In particular, the bivariate distributions have been derived with the *Kaplan-Meier Product-Limit Estimator* (Feigelson and Nelson 1985). We checked that the same results, within the quoted errors, are reached with the method described by Schmitt (Schmitt 1985).

4.4.2 K–Band Luminosity Function

In Chapters 1 and 2 we derived, using IRCAM frames, K–band nuclear magnitudes for 41 objects of the sample. As shown there, the galactic contribution to the observed near–IR magnitudes is often very important even within small aperture. For the objects we did not observe, we collected from the literature the available photometry within aperture $\leq 10''$. These data have been regarded as upper limits to the K–band fluxes.

Name	K_n	Ref.	$F(12\mu m)$	Ref.
0048+2907	12.15		0.186	1
1503	...		< 0.600	
2237+07	11.83		0.140	1
I Zw 1	10.20		0.540	1
II Zw 1	13.77		< 0.250	
II Zw 136	11.49		0.186	
III Zw 2	>11.41	1	< 1.500	
VII Zw 118	...		< 1.500	
Mrk 6	10.71		0.207	2
Mrk 9	11.03		0.230	
Mrk 10	>11.40	2	< 0.250	
Mrk 40	...		< 1.500	
Mrk 42	...		< 0.600	
Mrk 50	>12.71	3	< 1.500	
Mrk 69	...		< 1.500	
Mrk 79	11.19		0.313	2
Mrk 106	...		< 0.600	
Mrk 110	12.33		< 0.600	
Mrk 124	>11.62	3	< 0.250	
Mrk 141	>11.77	3	< 0.250	
Mrk 142	...		< 0.600	
Mrk 205	>11.68	1	< 0.070	1
Mrk 231	> 8.95	3	1.820	1
Mrk 236	>13.08	4	< 0.600	
Mrk 279	>11.66	5	0.199	1
Mrk 290	12.06		0.099	
Mrk 291	>12.67	4	< 0.600	
Mrk 304	12.00		0.061	
Mrk 315	>11.62	3	< 0.390	
Mrk 335	10.04		0.341	

Table 4.4: K–band magnitudes and IRAS 12 μm fluxes (Jy) used to compute the corresponding LF.
References: For objects we did not observe with IRCAM, we used K band photometry taken from the literature and treated as upper limits to the nuclear fluxes. The references are: 1. Neugebauer et al. 1979; 2. McAlary et al. 1979; 3. Rieke 1978; 4. Balzano & Weedman 1981; 5. McAlary et al. 1983; 6. Rudy et al. 1982; 7. Ward et al. 1987; 8. Glass 1979. The bulk of the 12 μm fluxes are taken directly from the catalogue (*Cataloged Galaxies and Quasar in the IRAS Survey, Jet Propulsion Laboratory, Second Edition, 1987*). Otherwise, when a reference code is given the meaning is the following: 1. Edelson and Malkan, 1987, 2. McAlary and Rieke, 1988 and Roche et al. 1991.

Name	K_n	Ref.	$F(12\mu m)$	Ref.
Mrk 352	12.42		< 1.500	
Mrk 358	...		< 1.500	
Mrk 359	12.35		< 0.250	
Mrk 372	...		< 0.600	
Mrk 374	12.30		< 0.600	
Mrk 376	11.07		0.240	
Mrk 382	13.16		< 1.500	
Mrk 464	13.35		< 1.500	
Mrk 474	>12.26	4	< 0.250	
Mrk 478	11.28		0.098	
Mrk 486	11.39		0.108	
Mrk 493	12.69		< 0.250	
Mrk 504	14.27		< 1.500	
Mrk 506	12.55		< 0.600	
Mrk 509	10.50		0.342	3
Mrk 530	11.99		0.180	1
Mrk 541	>11.64	4	< 1.500	
Mrk 543	>11.91	6	< 1.500	
Mrk 584	14.71		< 1.500	
Mrk 590	>10.92	7	0.169	1
Mrk 595	...		< 0.600	
Mrk 618	11.54		0.330	
Mrk 634	13.24		< 0.600	
Mrk 662	...		< 1.500	
Mrk 668	...		< 0.400	
Mrk 699	>11.81	4	< 1.500	
Mrk 704	11.07		0.370	
Mrk 705	11.58		< 0.250	
Mrk 707	...		< 0.600	

Table 4.4: Continued.

Name	K_n	Ref.	$F(12\mu m)$	Ref.
Mrk 716	>13.17	6	< 0.600	
Mrk 734	11.98		0.120	
Mrk 739	11.80		< 4.240	
Mrk 766	11.30		0.431	1
Mrk 771	12.74		0.117	
Mrk 783	14.06		< 1.500	
Mrk 813	...		< 1.500	
Mrk 817	11.21		0.357	1
Mrk 841	11.59		0.198	1
Mrk 845	13.51		< 0.250	
Mrk 849	>13.19	6	< 0.600	
Mrk 871	12.50		< 0.250	
Mrk 876	>11.90	6	< 0.250	
Mrk 877	...		< 0.600	
Mrk 885	...		< 0.600	
Mrk 975	11.64		< 0.370	
NGC 2639	...		< 0.600	
NGC 3227	>9.83	3	0.562	1
NGC 3516	>9.30	2	0.384	1
NGC 4051	>9.98	4	0.780	1
NGC 4151	>8.63	4	2.080	1
NGC 4235	>10.67	6	< 0.121	1
NGC 5273	...		0.134	1
NGC 5548	10.64		0.343	1
NGC 5940	12.53		0.124	1
NGC 7469	>9.26	8	1.300	1
Tol 1059	...		< 1.500	
Ton 524A	...		< 0.600	
X Comae	...		< 1.500	

Table 4.4: Continued.

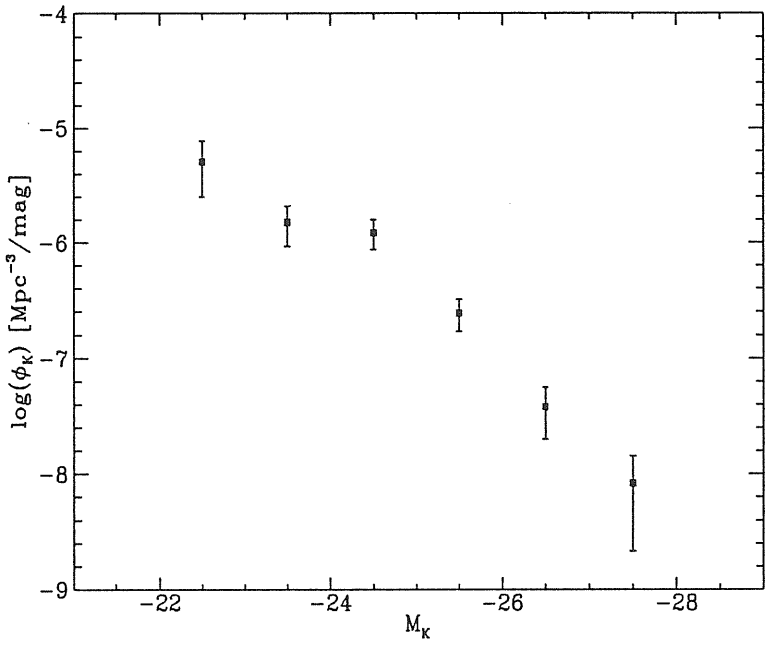

Figure 4.5: Luminosity function of Seyfert 1 nuclei in the K band.

The K–B bivariate luminosity distribution, its uncertainty and the resulting K–band luminosity function of Seyfert 1 nuclei are shown in Tab. 4.4 and in Fig. 4.5.

4.4.3 Luminosity Function at 12 μm

It is particularly interesting to compute the 12 μm LF for our sample of optically selected AGNs. As pointed out originally by Spinoglio and Malkan (1989) and subsequently by Rush et al. (1993), the spectral region between 7 and 12 μm carries an approximately constant fraction of the bolometric flux for all types of Seyfert galaxies and Quasars. In other words, the 12 μm luminosity is a good indicator of the bolometric luminosity for all the known type of AGNs, so that a selection based on a flux limit at 12 μm should minimize wavelength dependent selection effects. Moreover, the statistical analysis carried out in Chapter 2 has shown that the IRAS fluxes of Seyfert 1 galaxies in the two lowest wavelength bands, namely 12 and 25 μm, are

A

M_{Bn} / M_{Kn}	−23.50	−22.50	−21.50	−20.50	−19.50	−18.50
−27.50	0.269	0.000	0.000	0.000	0.000	0.000
−26.50	0.731	0.269	0.000	0.000	0.000	0.000
−25.50	0.000	0.731	0.635	0.043	0.000	0.000
−24.50	0.000	0.000	0.165	0.638	0.190	0.000
−23.50	0.000	0.000	0.200	0.186	0.561	0.000
−22.50	0.000	0.000	0.000	0.132	0.249	1.000

B

M_{Bn} / M_{Kn}	−23.50	−22.50	−21.50	−20.50	−19.50	−18.50
−27.50	0.147	0.000	0.000	0.000	0.000	0.000
−26.50	0.147	0.202	0.000	0.000	0.000	0.000
−25.50	0.000	0.202	0.113	0.042	0.000	0.000
−24.50	0.000	0.000	0.169	0.120	0.105	0.000
−23.50	0.000	0.000	0.126	0.132	0.159	0.000
−22.50	0.000	0.000	0.000	0.070	0.119	0.000

M_{Kn}	$\log(\varphi(M_{Kn}))$ $[\mathrm{Mpc}^{-3}\mathrm{mag}^{-1})]$	σ^+	σ^-
−27.50	−8.08	0.24	−0.59
−26.50	−7.42	0.17	−0.28
−25.50	−6.61	0.12	−0.16
−24.50	−5.91	0.11	−0.15
−23.50	−5.82	0.14	−0.21
−22.50	−5.29	0.18	−0.31

Table 4.4: A: The B–K bivariate luminosity distribution for Seyfert 1 nuclei; B: its uncertainty; C: the resulting K–band luminosity function.

A

M_{Bn} / $\log L_{12}$	−23.50	−22.50	−21.50	−20.50	−19.50	−18.50
32.00	0.071	0.064	0.000	0.000	0.000	0.000
31.60	0.679	0.082	0.000	0.000	0.000	0.000
31.20	0.250	0.854	0.554	0.096	0.000	0.000
30.80	0.000	0.000	0.446	0.567	0.308	0.000
30.40	0.000	0.000	0.000	0.337	0.692	0.244
30.00	0.000	0.000	0.000	0.000	0.000	0.756

B

M_{Bn} / $\log L_{12}$	−23.50	−22.50	−21.50	−20.50	−19.50	−18.50
32.00	0.062	0.058	0.000	0.000	0.000	0.000
31.60	0.225	0.146	0.000	0.000	0.000	0.000
31.20	0.216	0.133	0.125	0.083	0.000	0.000
30.80	0.000	0.000	0.125	0.142	0.218	0.000
30.40	0.000	0.000	0.000	0.115	0.218	0.200
30.00	0.000	0.000	0.000	0.000	0.000	0.200

L_{12}	$\log(\varphi(L_{12}))$ $[\mathrm{Mpc}^{-3}(\log L)^{-1})]$	σ^+	σ^-
32.00	−7.84	0.24	−0.57
31.60	−7.20	0.20	−0.39
31.20	−6.12	0.14	−0.21
30.80	−5.43	0.15	−0.22
30.40	−5.12	0.15	−0.24
30.00	−5.08	0.20	−0.36

Table 4.5: A: The 12μm–K bivariate luminosity distribution for Seyfert 1 nuclei; B: its uncertainty; C: the resulting 12 μm luminosity function.

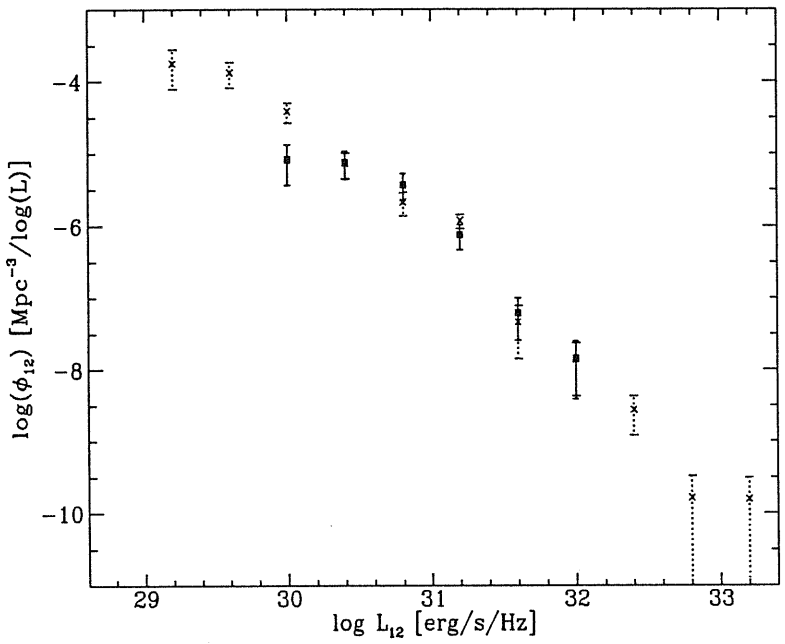

Figure 4.6: Luminosity function of Seyfert 1 nuclei at 12 μm. The squares with solid error bars represent our determination, while the crosses with dotted error bars the recent estimate made by Rush et al. (1993), using a sample selected at 12 μm.

mainly nuclear in origin.

The 12 μm fluxes of our sample objects are reported in Tab. 4.4. They are usually extracted directly from the IRAS catalogue (*Cataloged Galaxies and Quasar in the IRAS Survey, Jet Propulsion Laboratory, Second Edition, 1987*). Additional sources, which sometimes reports co–added survey data or more sensitive pointed observations, are Edelson and Malkan (1987), McAlary and Rieke (1988) and Roche et al. (1991). For a handful of objects in our sample these papers report detections where the IRAS catalogue reports only upper limits, and in these cases we made use of the detections.

The 12μm–B bivariate luminosity distribution, its uncertainty and the resulting 12 μm luminosity function of Seyfert 1 nuclei are shown in Tab. 4.5. In Fig 4.6 our LF is compared with that derived by Rush, Malkan and

Spinoglio (1993) from a sample directly selected at 12 μm (reported to $H_o = 50$ km/sec/Mpc and multiplied by 2.5 to take into account that their densities refers to one mag intervals). Although they do not give the errors on their determination, for a more meaningful comparison we have plotted the statistical errors bars even on their data, computed on the basis of the number of objects in each bin with Eq. 4.4. The two LF agree well within the uncertainties in all but the lowest luminosity bin of our determination. This fact and the behaviour of the LF of Rush et al. below $\log L_{12} = 30$ suggest that in optically selected samples very faint objects tend to be systematically lost.

Chapter 5

SEDs and Dust Models

Summary. We present and discuss the data collected from the IR to the UV of Seyfert 1 galaxies in a sample for which we presented previously optical and near–IR observations (Chapters 1–3). For the objects of this sample we have been able to derive the optical and near-IR *nuclear* fluxes and hence we can analyze the SEDs of their nuclei. We have worked out detailed calculations of the 0.1 to 100 μm Spectral Energy Distributions (SEDs) for the case of AGN surrounded by thick and thin dust torii with different opening angles. The dust mixture has been mimicked by using three silicate and three graphite grains of different sizes. The radiative transfer equation in a cloud having azimuthal simmetry and containing a mixture of dust grains has been solved by means of a numerical code that takes into account absorption, emission and scattering. We discuss the optimization of the free parameters comparing the spectra predicted by the code to the available data. We address the problem of the rather general absence of features in the IR spectra of AGNs, particularly the silicate feature around 10 μm. The ensuing constraints are discussed. Models of thick torii extended up to a few tens of parsecs, in which however shocks significantly reduce the silicate grain abundance within few parsecs, are fully consistent with available broad band data and high resolution IR spectra of Seyfert 1 and 2 nuclei, in the context of unified schemes.

5.1 Introduction

The origin of the large IR emission in AGN is still debated. However data collected in the last few years suggest that the role of the dust is particularly relevant, at least in radio quiet AGN. Indeed dust reprocessing of the primary optical–UV emission, as firstly suggested by Rees et al. (1969), is at present regarded as the most attractive possibility to produce the bulk of the IR continuum, which constitutes a significant portion of the bolometric luminosity (Sanders et al. 1989). Dust organized in an anisotropic optically thick distribution, such as a torus, may also originate the observed difference between some classes of AGNs, in particular Seyfert 1 and 2 nuclei, and is therefore a fundamental ingredient of the unification schemes for AGNs, as originally suggested by the Antonucci and Miller (1985) (see e.g. Pier and Krolik 1992b for other references).

Indirect arguments favoring the dust reprocessing picture for the origin of the IR emission are: (1) the observed steep rise of the submillimetric continuum between 1000 and 100 μm (Engargiola et al. 1988; Chini et al. 1989; Lawrence et al. 1991; Hughes et al. 1993), which is by far too steep for all current non–thermal models; (2) the nearly universality of the local minimum in νF_ν at $\log \nu = 14.5$, that is $\lambda \sim 1$ μm (Sanders et al. 1989), a feature arising naturally in models where dust reradiates a primary optical–UV thermal continuum with $T \sim 25000$ K; (3) studies on optical–IR variability which have shown that the observed behavior, in particular concerning time scales and delays between the different bands, is exactly as expected in the dust picture (Clavel et al. 1989; Glass 1992; Baribaud et al. 1992; Barvainis 1992); (4) the observed low level of polarization (e.g. Sitko and Zhu 1991).

On the other hand the elusivity of features in the IR spectra of the AGN (Roche et al. 1991) seems to partly contradict an important dust emission in AGNs, although several possible effects have been proposed for solving the contrast (see e.g. Laor and Draine 1993).

The increasing evidence of the relevance of dust in shaping the IR radiation from AGNs has prompted out several studies on possible models in the last few years. The first paper in this direction is due to Barvainis (1987), who substantiated previous hints of many authors in a simple model, which explains the IR continuum with reradiation by dust, heated by a primary optical and ultraviolet continuum emission. This model has been then successfully used to fit the 0.3 to 100 μm continuum of 11 sources (Barvainis 1990). More recently Barvainis (Barvainis 1992) introduced in its treatment

also time dependence, fitting the infrared light curves and spectra of Fairall 9 as a response to the observed UV light curve. However, Barvainis made use of several simplifications in his approach, which can be used therefore only to provide an order of magnitude estimate of the spectral shape. For instance, he used rough power-law approximations of the grain optical efficiency Q_ν, he ignored scattering and included in the cloud only one kind of dust grains, namely graphite grains with radius $a = 0.05$ μm. Moreover, he avoided the solution of the radiative transfer equation by assuming that the dust is transparent to its own radiation. This, while simplifying enormously the numerical task, puts strong limits to the accessible range of parameters, since the cloud cannot be optically thicker than ~ 10 in the optical–UV.

Loska et al. (1993) have provided reasonable fits to the SEDs of four AGNs by means of computations similar to those made by Barvainis, but with many refinements in the physical treatment. Here a range of grain sizes is used, graphite and silicate grains are both included and an angular dependence for the radiation of the central source (but not for the grain density) is considered. However, the authors follow again the easiest approach to radiative transfer, assuming that the dust is transparent to IR photons, so that the resulting spectrum is simply given by an integral over the emitting volume. The authors find that for a standard number ratio of silicate to graphite grains (1.13), the resulting spectra show very prominent 10 and 20 μm silicate features. Since in the observational data these features are weak or absent (Roche et al. 1991), they conclude that there is not evidence for the presence of silicate in AGN dust, and thus they adopted a pure graphite dust mixture for the fits.

Laor and Draine (1993) have used the lack of a significant 10 μm silicate emission feature in AGN to constrain dust emission models. Using newly computed optical properties for dust grains, they find, in agreement with Loska et al. (1993), that a standard mixture of graphite and silicate in a configuration optically thin at 10 μm produces necessarily a prominent feature which is clearly ruled out by observations. They also have studied optically thick configurations in a rather idealized slab geometry, finding that the feature may be indeed reduced, but remains still greater than the observational limits in most objects. They conclude that featureless IR spectra are produced only by dust with modified composition and/or size distribution.

In the model proposed by Sanders et al. (1989) and Phinney (1989), the dust responsible of the mid and far–IR radiation, say at wavelengths above 5 μm, is placed in a warped disk of gas associated to the host galaxy at

distances from the nucleus greater than about 10 pc, rather than in a torus or a more or less isotropically distributed population of clouds. The 0.5–5 μm radiation is instead interpreted as thermal emission from the outer accretion disk (0.1–1 pc) heated by the broad line cloud. The emission from 0.5 to 2 μm is attributed to free–free radiation from gas at smaller radii, while that between 2 and 5 μm would be due to dust grains associated to the accretion disk. However no detailed predictions on spectra expected from this model have been worked out.

Krolik and coworkers have investigated the properties of very thick ($\tau_{uv} \sim 10^3$) and compact (a few pc) dust torii that they believe to be responsible of observed differences between Sy 1 and Sy 2 galaxies and that they believe to form around AGN (Pier and Krolik 1992a). The same authors (Pier and Krolik 1992b) presented a computational method which they have developed in order to compute the emitted spectrum solving the radiative transfer equation, but ignoring scattering and using a single "equivalent" kind of grain.

In this Chapter we present and discuss the data collected from the IR to the UV of Seyfert 1 galaxies in a sample for which we reported previously optical and near–IR observations (Chapters 1, 2 and 3). For the objects of this sample we have been able to derive the optical and near-IR *nuclear* fluxes and hence we can analyze the SEDs of their active nuclei (Sec. 5.2).

To compare the observational data to the model outcomes, we have worked out detailed calculations of the 0.1 to 100 μm Spectral Energy Distributions (SEDs) for the case of AGN surrounded by thick and thin torii with different opening angles. The dust mixture has been mimicked by using three silicate and three graphite grains of different sizes. The radiative transfer equation in a cloud having azimuthal simmetry and containing a mixture of dust grains has been solved by means of a numerical code that takes into account absorption, emission and scattering (Sec. 5.3).

We discuss the optimization of the free parameters comparing the spectra predicted by the code to the available data. We also address the problem of the rather general absence of features in the IR spectra of AGNs, particularly the silicate feature around 10 μm. The ensuing constraints are discussed (Secs. 5.5 and 5.6).

A Hubble constant $H_0 = 50$ km sec^{-1} Mpc^{-1} has been assumed.

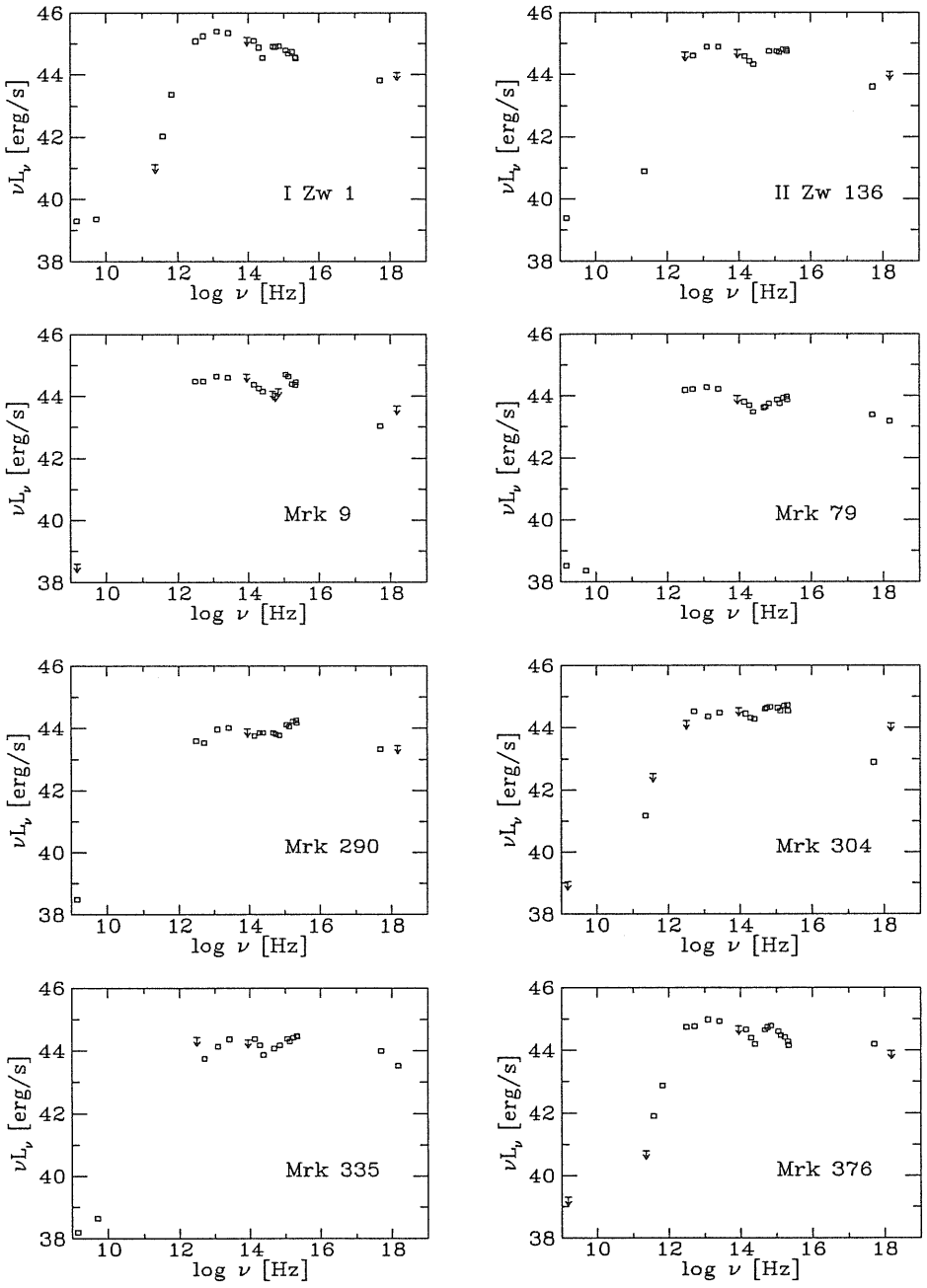

Figure 5.1: Radio to X–ray SEDs of sample objects.

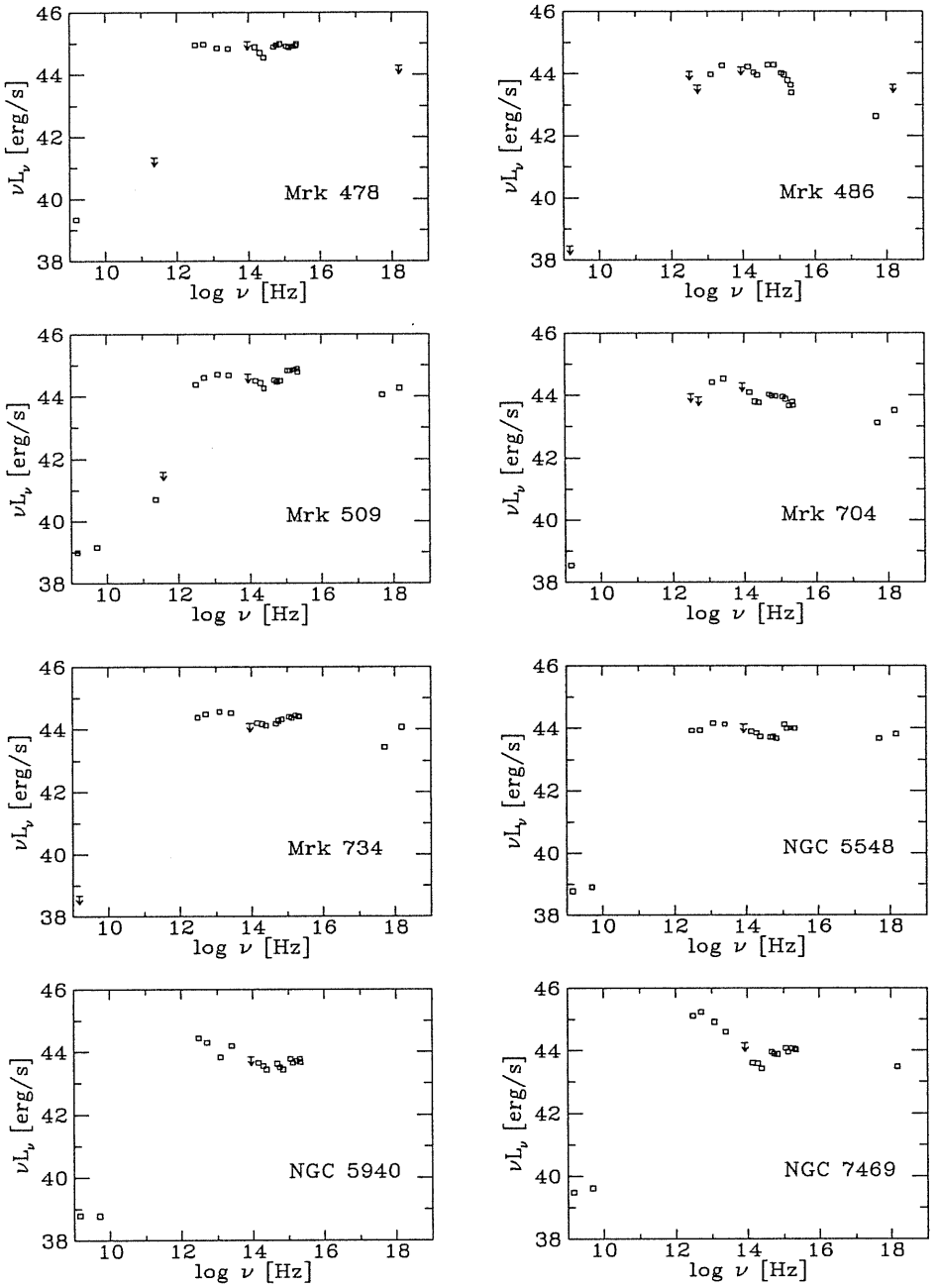

Figure 5.2: Radio to X–ray SEDs of other sample objects.

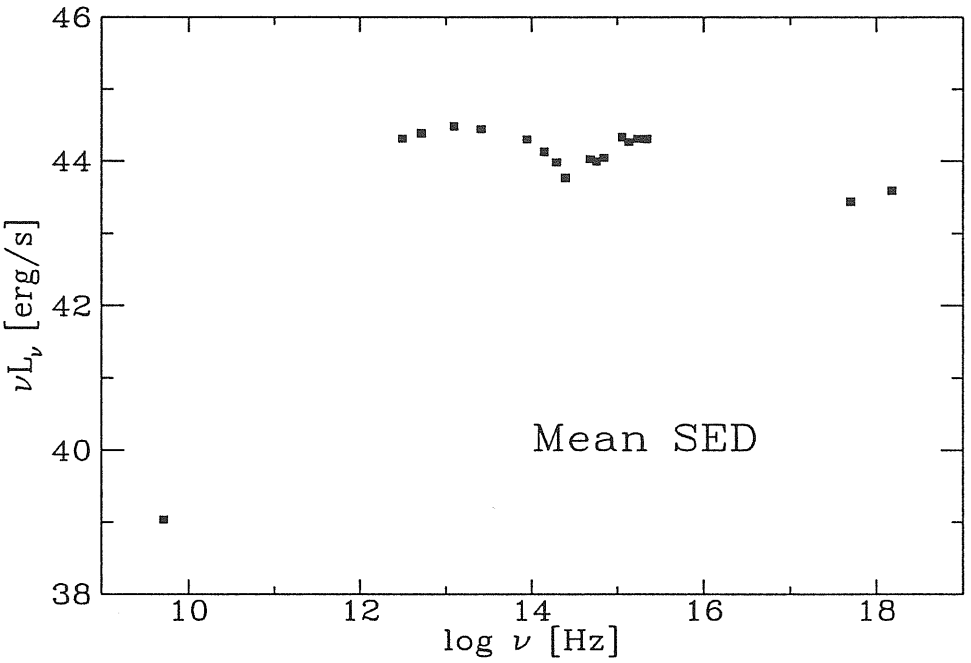

Figure 5.3: Average Radio to X–ray SED for the objects of the sample detected at 12 μm.

5.2 Radio to X–Rays Spectral Energy Distributions of Seyfert 1 Galaxies

The sample on which this study is based has been already described in the previous Chapters, together with its statistical properties. We remind that it has been originally defined by Cheng et al. 1985 and it is a sample of 56 local ($z \leq 0.08$) optically selected radio quiet AGNs, mainly Seyfert 1 nuclei. In the first three Chapters of this work we have derived, using new optical and near-IR imaging, nuclear (i.e. corrected for starlight) magnitudes in B V R J H K bands for many objects of the sample, with typical uncertainties of $0.15 \div 0.20$ mag. Combining these data with radio, IRAS, IUE and X–ray observations, which are largely available for our sample objects, it is possible to trace the radio to X–rays nuclear Spectral Energy Distributions (SEDs). The data and their sources are described in more details in Appendix A. Figs. 5.1 and 5.2 present the rest–frame SEDs of those objects for which a

large spectral coverage is available, while in Fig. 5.3 it is reported a SED obtained averaging the luminosities in the various bands.

We are well aware that a possible shortcoming of these spectra is the lack of simultaneity in the observations at different wavelengths, a problem which could distort the spectra particularly at $\lambda \lesssim 1$ μm. At present, it is unfeasible to provide simultaneous measurements in such a huge range of frequencies for a sample of a few tenths of objects. It is also worth noticing that, if the dust reprocessing picture is correct, the IR emission at a given time t is powered by the optical–UV emission at $t - \delta t$, where δt can range from a few months in the near–IR to hundreds of years at IRAS wavelengths, and thus it is perfectly possible that even simultaneous data does not characterize the SEDs much better than "randomly" time sampled data. The hope is that working on a relatively large sample of objects this problem can be minimized. In particular, we think that the averaged SED reported in Fig. 5.3 provides a reasonably good representation of the typical spectrum emitted by Seyfert 1 nuclei, and we will base our physical modeling on this ground.

A well known characteristic of the SEDs in radio quiet AGNs is the nearly universal presence of a well defined minimum in νL_ν around $\log \nu \simeq 14.5$ (1 μm) (Neugebauer et al. 1987; Sanders et al. 1989). This feature arises naturally in models where dust heated to sublimation temperature $T_s \sim$ 1500 K reradiates a primary optical–UV thermal continuum with $T \sim 25000$ K, and it is therefore regarded as a piece of evidence in favour of the thermal origin for the IR continuum. It has also been previously noticed that, in lower luminosity objects, the dip seems to be less prominent (Kriss 1988; Sanders et al. 1989), and it has been suggested that this may be due to the host galaxy emission. Our use of optical–IR fluxes subtracted from starlight gives clear evidence of the minimum even in low luminosity objects. The deepness of this feature can be measured from the ratio of the quantity νL_ν computed at 12 and 1 μm. Sanders et al. found, judging from their Fig. 1, this ratio to be $\simeq 2.5$ for high luminosity AGNs ($L_{bol} > 1.7 \times 10^{45}$ erg s^{-1}) but only $\simeq 1.3$ for low luminosity ones ($L_{bol} < 1.7 \times 10^{45}$ erg s^{-1}). In the SEDs shown in Fig. 5.3, there is not any indication of a systematic dependence of $\nu L_\nu(12\ \mu\text{m})/\nu L_\nu(1\ \mu\text{m})$ on the luminosity (see Fig. 5.4 and Tab. 5.1). For the ten AGNs brighter than 1.7×10^{45} erg s^{-1} the ratio averages to 3.0, while for the reminder six the mean value is 3.3. Our result, slightly larger than that derived for higher luminosity SEDs reported in Sanders et al. paper, suggests that the shape of the spectra are appreciably

Name	$\log L_{bol46}$	$L_{\rm ir}/L_{uv}$	$L_{\rm ir}(< 25\ \mu{\rm m})/L_{uv}$	d
(1)	(2)	(3)	(4)	(5)
I Zw 1 ...	0.00	3.53	2.34	0.80
II Zw 136 .	−0.30	1.05	0.75	0.57
Mrk 9	−0.54	1.30	0.92	0.46
Mrk 79 ...	−1.05	1.86	1.12	0.74
Mrk 290 ..	−1.03	0.56	0.45	0.16
Mrk 304 ..	−0.52	0.76	0.55	0.21
Mrk 335 ..	−0.73	0.69	0.56	0.50
Mrk 376 ..	−0.39	2.48	1.66	0.72
Mrk 478 ..	−0.12	0.87	0.58	0.28
Mrk 486 ..	−1.06	1.63	1.35	0.30
Mrk 509 ..	−0.36	0.73	0.51	0.43
Mrk 704 ..	−0.93	2.96	2.33	0.76
Mrk 734 ..	−0.66	1.07	0.66	0.40
NGC 5548	−1.04	1.19	0.84	0.40
NGC 5940	−1.16	2.34	1.23	0.76
NGC 7469	−0.51	5.98	1.87	1.18

Table 5.1: Bolometric luminosities in units of 10^{46} erg/s and relative importance of the IR and UV bumps if not intrinsic absorption is assumed. The quantity $d \equiv \log \nu L_\nu(12\ \mu{\rm m})/\nu L_\nu(1\ \mu{\rm m})$ is a measure of the deepness of the 1 μm local minumum.

affected by the host galaxy even in high and intermediate luminosity AGNs.

Following Pier and Krolik (1992b), we take as a measure of the width of the IR bump the logarithmic interval of frequency W in which the power emitted is no less than one third of its peak value. Even allowing for a generous contribution from the underlying galaxy longward $\sim$ 30 μm, as indicated by our statistical analysis presented in Chapter 2, W is bound to be greater than 1.5 in most objects.

From Fig 5.3 it is apparent that the flux νF_ν in the B, V and R bands is on average 40% lower than in the UV band. In many, if not all, the SEDs displayed in Figs. 5.1 5.2 and there seems to be a certain degree of optical–UV absorption, as suggested by the frequent presence of the 2200

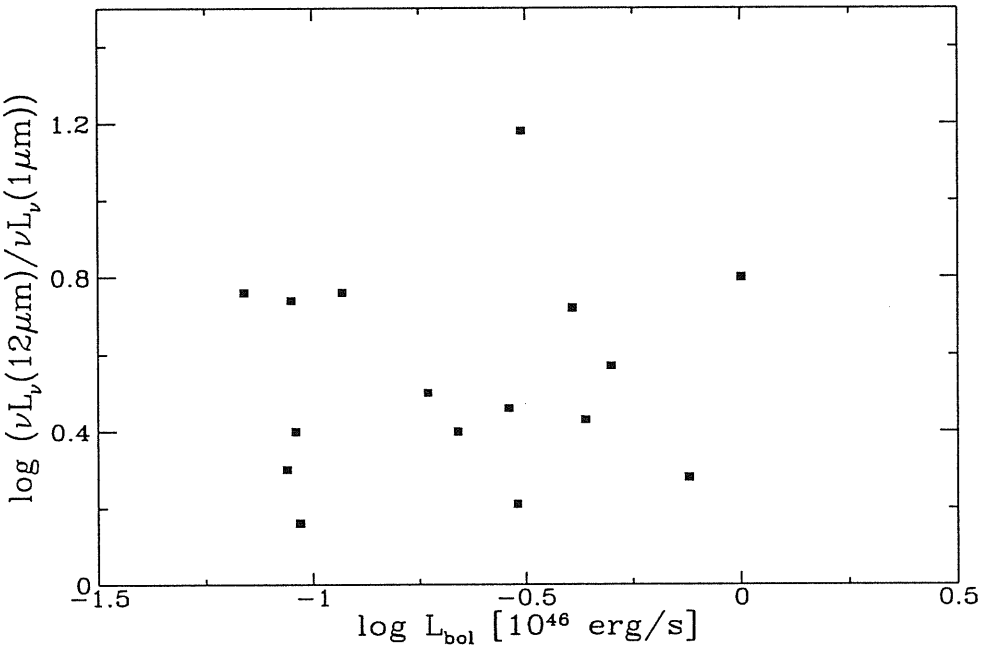

Figure 5.4: The ratio $\nu L_\nu(12\ \mu\text{m})/\nu L_\nu(1\ \mu\text{m})$, which measures the deepness of the local minimum around 1 μm plotted against the bolometric luminosity.

Å graphite absorption feature, by the sharp UV decline observed in a few cases, and by the fact that in color–color plots our nuclei tend to cluster along reddening line. For instance, in Fig. 5.5 we have plotted the "colors" L_R/L_B against L_V/L_B. The points are concentrated in proximity of the segment along which a nucleus would move for the effect of an increasing absorption, up to $E(B-V) \simeq 0.5$ ($A_V \simeq 1.5$). This result is in agreement with the findings of Carleton et al. (1987), except that those authors have found a larger maximum reddening $E(B-V) \simeq 1.0$. The difference is not surprising, provided that our sample is optically selected, and therefore the more heavily absorbed objects are missed, while that considered by Carleton et al. is dominated by members of an hard X–ray selected sample. The 2200 Å dip, if interpreted in terms of the standard galactic reddening law (Seaton 1979; Savage and Mathis 1979), would imply a typical color excess $E(B-V) \simeq 0.05 \div 0.15$, but the universal applicability of this law is at least questionable, in particular to the environment of AGNs and in the UV spectral region.

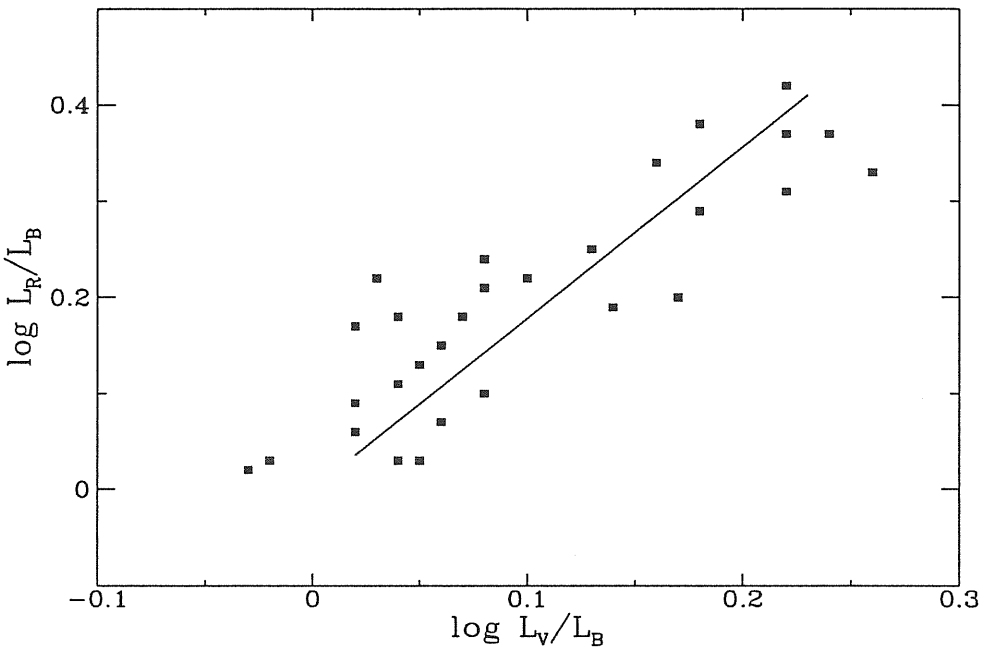

Figure 5.5: Optical color–color plot for our sample nuclei. The segment represents a reddening vector corresponding to $E(B-V) = 0.5$.

In addition, many authors have pointed out that the 2150–2250 Å IUE "continuum" window is often contaminated by the blending of Fe II emission lines (e.g. Francis et al. 1991), resulting in an underestimate of the reddening (De Zotti and Gaskell 1985). For these reasons the estimates given above should be taken as lower limits. In conclusion, there are indications that we receive typically less than 50% of the optical–UV flux emitted by the nucleus, but to estimate the individual amount of absorption remains at the moment a very difficult task. This relatively moderate absorption is on the other hand to be expected, since the kind of nuclei with which we are dealing here are usually hosted in the center of early type spirals, even if the AGN may well be capable of destroy the dust at least along certain directions (Chang et al. 1987; Laor and Draine 1993).

5.3 General Model

With the aim of modeling the observed SEDs of our sample objects, we have developed a code which computes numerically the outcome of realistic and general models. Even if at the moment the scanty coverage of the SEDs allows to obtain rather good fits even with simpleminded computations, the few conclusions that one can reach in this way are affected by the crude assumptions, whose effects must be tested. Moreover our observational knowledge is expected to improve quickly in the next future. With realistic modeling it is also possible to explore with more dynamical range the parameter space. In particular, we have discussed in the previous sections motivations to consider torii optically thick in the IR.

Our code solves numerically for the transfer equation of radiation in a cloud having an axial symmetry. Its main properties are the following: (i) takes into account both thermal emission as well as scattering from dust grains; (ii) uses accurate tabulations of grain optical efficiencies Q_ν; (iii) requires only axial symmetry for both the dust distribution and the primary continuum; (iv) can include in the cloud several different dust grains (size and composition) at the same time, in order to mimic the behavior of a realistic mixture of dust; (v) it is capable of compute the outcome of very thick dust clouds, at least up to $\tau <$ few $\times$ 100 in the UV region (depending on the resolution of the spatial grids, and therefore on available CPU time), so that the dust is not necessarily transparent to its own radiation. In the previous models quantitatively compared to observed SEDs of AGNs at least one, but usually more, of the previous point are not satisfied. Although there are good reasons to believe that the dust distribution should be clumpy (e.g. Krolik and Begelman 1988), here we adopt a smooth representation, which is a good approximation as long as the overall size of the system is much greater than the typical intercloud distance.

We assume azimuthal symmetry for the dust distribution and the primary continuum, with respect to an axis passing trough the location of the primary source, as well as planar symmetry with respect to an equatorial plane containing the primary source. Fig. 5.6 delineates the geometry: the position of a generic point P is given by the three polar coordinates r, Θ, Φ, while a generic direction is specified by the two angles θ, the polar angle with respect to $\hat{r}$, and ϕ, which is the azimuth measured from the plane defined by $\hat{z}$ and $\hat{r}$. The cloud is composed by a given mixture of dust grains, in thermal equilibrium with the radiation field, and it is extended out to a maximum radius r_m. The inner boundary of the cloud is set by the

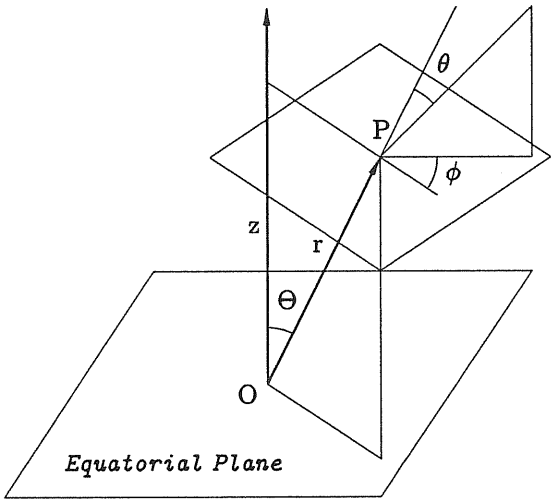

Figure 5.6: The geometry of the model.

sublimation of dust above a given temperature T_s, depending on the type of grain under consideration. The radius at which a given grain would have an equilibrium temperature equal to T_s is the evaporation radius for that grain, and no grains of that kind can survive interior to this radius. Since in general the radiation field depends on Θ, so does the sublimation radius. We indicate with r_o the minimum radius of the dust distribution, that is the radius within which all dust grains sublimate in any direction. Moreover, we introduce the possible presence of a "conical hole" in the dust distribution, i.e. the possibility that the dust density is zero for $\Theta < \Theta_h$ and $\Theta > \pi - \Theta_h$, in order to have directions along which the central source is seen unaffected by dust absorption. In this case, the covering factor $f \equiv \Omega/4\pi$ of the dust cloud is given by $f = \cos\Theta_h$.

5.3.1 Numerical Method

For this general problem of radiative transfer, which despite the axial simmetry is tridimensional, analytical solutions do not exist. The usual approach is to employ an iterative numerical technique, sometimes referred to as lambda–iteration method: the temperature is computed at each iteration from the condition of local radiative equilibrium of dust grains, i.e. balancing the energy thermally emitted by the grains with the power they absorb from the radiation field, where the radiation field is that computed at the previous iteration. Versions of this method, in the specific context of circumnstellar dust shells, are described in Efstathiou and Rowan-Robinson (1990), Dent (1988), Collison and Fix (1991), but have never been extensively applied to AGNs. We have introduced in these treatments a few straightforward modifications, in particular with respect to the following points: (i) the inclusion in the cloud of a mixture of dust grains with different sizes and chemical compositions; (ii) the possible presence of an anisotropic primary source, in which the luminosity depends on the polar angle Θ.

Grids

The physical quantities entering into the transfer equation depends on (at most) r, Θ, θ, ϕ and ν. In the numerical method they are more or less precisely computed only in a grid of points and then interpolated whenever necessary. Even the mixture of dust grains is discretized: we consider a few (of the order of 10) different kinds of spherical grains, where kind means radius and chemical compositions. We adopt the following convention: any quantity with a greek upper index refers to the grain of kind numbered by the index. In particular, X^α is the mass fraction of the grain α-nth in the mixture, which we consider independent of position (but our treatment could easily be extended to the more general case). In other words, the mass density of the grain α is given by

$$\rho^\alpha(r,\Theta) = \rho(r,\Theta)X^\alpha \tag{5.1}$$

The radial grid is defined by

$$r_i = r_o \exp(\gamma i^\delta), \qquad i \in [1, N_i] \tag{5.2}$$

with

$$\gamma = \frac{\ln(r_m/r_o)}{N_i^\delta} \tag{5.3}$$

where r_o is the minimum radius of the dust distribution, that is the radius within which all kinds of grain in all the directions do not survive, r_m is the outer radius of the shell and δ is an index depending on the radial behavior of the dust density. For instance, in the case of a power law density $\rho \propto r^{-\beta}$ (the usual choice), we find convenient to set $\delta = (\beta + 2)/2$.

For models without conical holes around the axis, i.e. with $\Theta_h = 0$, a simple equispaced angular grid is defined:

$$\begin{cases} \Theta_j = (j-1) \times \delta\Theta & \text{if} \quad 1 \le j \le N_j \\ \Theta_j = \pi - \Theta_{2N_j - j + 1} & \text{if} \quad N_j + 1 \le j \le 2N_j \end{cases} \tag{5.4}$$

with

$$\delta\Theta = \frac{\pi}{2N_j - 1} \tag{5.5}$$

When instead $\Theta_h > 0$, two additional grid points are defined, one just inside the hole and the other just outside it, in order to follow more carefully the discontinuity at $\Theta = \Theta_h$.

Reasonable indicative values for N_i and $2N_j$ are 30 and 16 respectively. Depending on the particular class of model under consideration, we have slightly varied these parameters in order to get a reasonably good solution with the minimum CPU time. As a general rule, the grids must be finer for more thick and extended models. Similarly a frequency grid, consisting typically of $N_k \sim 30$ points, is constructed almost equispaced in $\log \nu$, but with individual points slightly adjusted, in order to optimize the description of the opacity spectrum of the dust mixture under consideration employing the minimum numbers of points.

Fundamental Equations

The radiation field $I_\nu(r, \Theta, \theta, \phi)$ and the grain temperature $T^\alpha(r, \Theta)$ in the cloud are obtained at grid points by solving the equation of radiative transfer:

$$\hat{\omega} \bullet \nabla I_\nu = -\alpha_\nu I_\nu + j_\nu \tag{5.6}$$

where $\hat{\omega}$ is the unit vector of the direction specified by θ and ϕ, α_ν is the extinction coefficient and j_ν the emission coefficient. For the dust mixture,

these quantities can be written explicitly, assuming LTE and denoting with B_ν the Planck function, as follows

$$\alpha_\nu = \sum_\alpha Q^\alpha_{\nu,e}\varsigma^\alpha \tag{5.7}$$

$$j_\nu = \sum_\alpha Q^\alpha_{\nu,a}\varsigma^\alpha B_\nu(T^\alpha) + \\ + \sum_\alpha Q^\alpha_{\nu,s}\varsigma^\alpha \frac{1}{4\pi}\int_{4\pi} I_\nu(\omega')\xi(\theta')d\Omega' \tag{5.8}$$

The first term in the expression of j_ν represents true emission, while the second one represents scattering. The quantities $Q^\alpha_{\nu,e}$, $Q^\alpha_{\nu,a}$ and $Q^\alpha_{\nu,s}$ are the extinction, absorption and scattering efficiencies of the grains, and $\xi(\theta)$ the scattering phase function, identically equal to one for isotropic scattering. We have also introduced, for each kind of dust grain, the quantity

$$\varsigma^\alpha = \pi(a^\alpha)^2 n^\alpha \tag{5.9}$$

where a^α is the radius of the grain and n^α its number density, which, if D^α is the specific mass of the grain, is given by

$$n^\alpha = \frac{3}{4\pi}\rho\frac{X^\alpha}{(a^\alpha)^3 D^\alpha} \tag{5.10}$$

Q_e and Q_s are related to Q_a and to the albedo $\omega = Q_s/Q_e$, which are the quantities usually given in literature, by

$$Q_s = \frac{\omega}{1-\omega}Q_a \tag{5.11}$$

$$Q_e = \frac{1}{1-\omega}Q_a \tag{5.12}$$

It is convenient to split the specific intensity into two terms

$$I_\nu = I^{(1)}_\nu + I^{(2)}_\nu \tag{5.13}$$

where $I^{(1)}_\nu$ is the specific intensity of the radiation emitted by the central source, while $I^{(2)}_\nu$ is that thermally emitted or scattered by the dust. $I^{(1)}_\nu$

satisfies Eq. 5.6 with $j_\nu = 0$, which has the trivial solution for the mean specific intensity[1]

$$J_\nu^{(1)}(r,\Theta) = \frac{1}{(4\pi)^2}\frac{L_\nu^c(\Theta)}{r^2}\exp(-\tau_\nu(r,\Theta)) \tag{5.14}$$

where $L_\nu^c(\Theta)$ is the luminosity that the central source would have if emitted in all directions as it does along Θ (i.e. $L_\nu^c(\Theta) = 4\pi r^2 F_\nu^c(\Theta)$), and $\tau_\nu(r,\Theta)$ is the optical depth from the origin to (r,Θ).

Instead $I_\nu^{(2)}$ must be obtained from the full transfer equation 5.6, which can be *formally* solved (e.g. Rybicky and Lightman 1979) to get:

$$\begin{aligned} &I_\nu^{(2)}(r,\Theta,\theta,\phi) = \\ &= \int_{(r,\Theta)}^{(r_b,\Theta_b)} S_\nu(r',\Theta')\, e^{-\tau_\nu(r',\Theta')} d\tau_\nu \end{aligned} \tag{5.15}$$

where the integration is extended from (r,Θ) to the outer boundary of the cloud (r_b,Θ_b) along the direction specified by $(\pi-\theta,\pi+\phi)$ and τ_ν is the optical depth from (r,Θ) to (r',Θ'). The quantity $S_\nu \equiv j_\nu/\alpha_\nu$ on the right hand side is the source function, which depends nonlinearly on I_ν, and this is the reason why Eq. 5.15 does not represent a true solution.

Assuming from now on isotropic scattering, the source function can be written, from Eq. 5.7 and Eq. 5.8, as

$$S_\nu = \frac{\sum_\alpha \varsigma^\alpha \left[Q_{\nu,a}^\alpha B_\nu(T^\alpha) + Q_{\nu,s}^\alpha J_\nu(r,\Theta)\right]}{\sum_\alpha Q_{\nu,e}^\alpha \varsigma^\alpha} \tag{5.16}$$

We explicitly note that the mean specific intensity appearing in the right hand side of Eq. 5.16 refers to the global radiation field, i.e. (1)+(2).

Finally, since we assume a condition of radiative equilibrium for the dust grains, their temperature distribution $T^\alpha(r,\Theta)$ can be derived, once given $J_\nu(r,\Theta)$, by solving numerically the following set of equations:

$$\int_0^\infty Q_{\nu,a}^\alpha J_\nu d\nu = \int_0^\infty Q_{\nu,a}^\alpha B_\nu(T^\alpha) d\nu \qquad \forall\alpha \tag{5.17}$$

[1]It is convenient to treat the primary source as pointlike, since r_o is for AGNs (but not for circumnstellar shells) much greater than the dimension of the source itself.

Iterative Method

The iterative process starts with trial values of the mean specific intensity $J_\nu(r,\Theta)$. The obvious choice is to start with $J_\nu^{(1)}$, the specific intensity due to the primary source, from which the first estimate of the temperature distributions of the various species of grains $T^\alpha(r,\Theta)$ can be computed by solving Eq. 5.17. At this point, the source function $S_\nu(r,\Theta)$ is given by Eq. 5.16 and with the formal solution Eq. 5.15 together with Eq. 5.14, it is possible to compute an updated $J_\nu(r,\Theta)$ and repeat the process until consistency between the radiation field and the temperature distribution is achieved and the luminosity is constant at each level in the shell and is equal to the luminosity of the primary source L_p.

This method leads to a converged solution usually in 5–10 iterations (the conditions under which a solution is regarded as converged are discussed in the next section). However we found that the same solution can be reached more quickly (say 2–5 iterations) employing the technique proposed by Collison and Fix, which is a generalization of the method applied by Pollack and Ohring (1973) to the study of planetary atmospheres.

If we denote with $J_\nu^{(n)}$ the starting guess of the mean specific intensity at the n-th iteration, and with $J_\nu^{\prime(n)}$ the corresponding function obtained from the formal solution of the transfer equation Eq. 5.15 and from Eq. 5.14, in such a way that the method described above consists simply in setting $J_\nu^{(n+1)} = J_\nu^{\prime(n)}$, the convergence is speeded up by setting:

$$J_\nu^{(n+1)}(r_i,\Theta) = J_\nu^{\prime(n)}(r_i,\Theta) f_i \tag{5.18}$$

where f_i are correction factors depending only on the radius. These factors are given by recursion relations, which are a slightly modified version of eq. 20 given by Collison and Fix (1991), but are derived in a strictly analogous way[2]:

$$f_i = f_{i+2}\frac{Y_{i+2}}{Y_i} + \frac{L_p}{L_{i+1}^{(n)}}\left(1 - \frac{Y_{i+2}}{Y_i}\right) \tag{5.19}$$

$$f_N = \frac{L_p}{L_N^{(n)}} \qquad f_{N-1} = \frac{L_p}{L_{N-1}^{(n)}} \tag{5.20}$$

[2]We adopt this form since we prefer to avoid, for speed reasons, the computation of the luminosity trough the *boundary radii* $r_{b,i}$, which are radii defined by these authors at intermediate positions with respect to r_i.

where N is the total number of radial grid points N_i, $L_i^{(n)}$ is the luminosity trough the spherical surface at r_i, computed using the specific intensity given by the formal solution Eq. 5.15 and by Eq. 5.14, and

$$Y_i = \int_{4\pi} d\Omega \int_0^{\infty} d\nu \, \alpha_\nu J_\nu'^{(n)}(r_i, \Theta) \tag{5.21}$$

An additional complication comes from the fact that the temperature of the grains increases between successive iterations, so that it can surpass the sublimation temperature. If this happens for a given kind of grain at a given grid location, that grain is eliminated at that point. This effect, often neglected in similar computations, occurs frequently in the interior of the cloud and considerably slows down the achievement of a converged solution, but it must be taken into account at least in very thick and compact models, where the final temperature may exceed the initial one by a few hundreds of degrees.

Convergency Checks

As we stated above, a solution of our radiative transfer problem is represented by a radiation field and a temperature distribution satisfying the condition of radiative equilibrium (Eq. 5.17). From an analytical point of view, once this condition is satisfied, the global condition of constant luminosity at each level in the shell is also granted. However, in an approximate numerical solution it is safer to check for both the conditions (see e.g. Efstathiou and Rowan-Robinson 1990). In our program, we stop the iterative process when the temperature corrections between successive iterations fall below 1 K and the luminosity through the shells is conserved to better than 5%. All the models discussed in this work satisfy these criteria. When we found it impossible to obtain such a solution with certain spatial and frequency grids, the goal was attained by using finer ones. Typical computing times are of the order of several tenth of minutes on an Alpha DEC3000/400, or several hours on 486 based systems.

Once the radiation field and the temperature distributions have been determined, the spectrum that would be seen by a distant observer is computed evaluating the flux trough a point at a distance much greater (10^3 times) than the outer radius r_m of the dust distribution, in the required direction, in order to avoid distortions due to the geometry of the cloud.

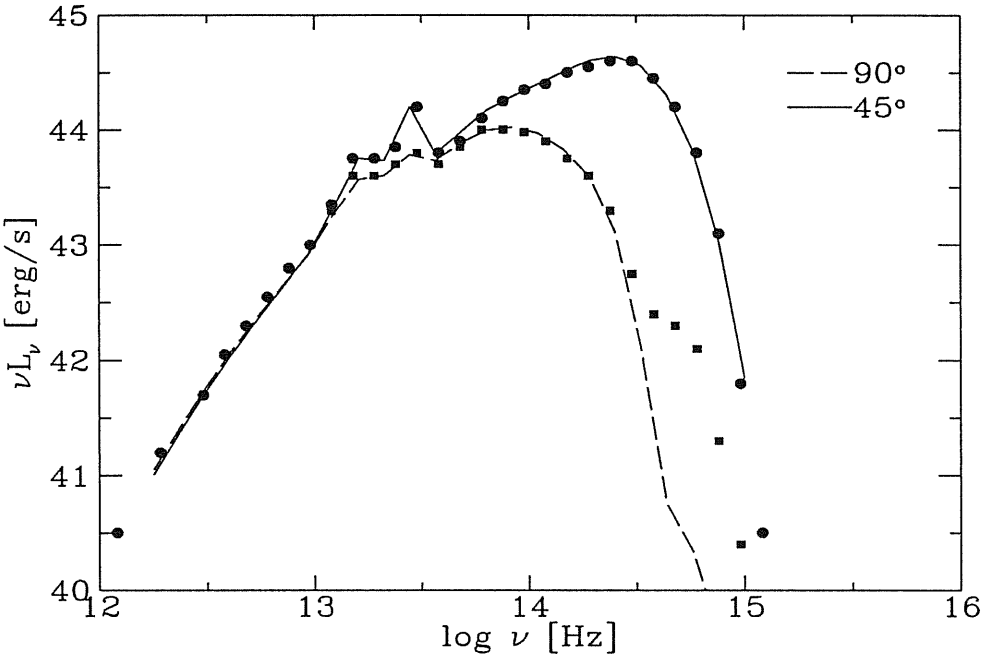

Figure 5.7: Comparison between the emitted spectra predicted by our code (solid and dashed line) and by that of Efstathiou and Rowan–Robinson (1990, circles and squares) for a circumnstellar dust shell.

5.3.2 Comparisons with Previous Works

We have compared our spectra with the results obtained in previous works, introducing the same assumption and approximations, which usually are less general. We found a rather good agreement. For instance, in Fig. 5.7 we report the $\Theta = 90^o$ and $\Theta = 45^o$ spectra emitted by model 3 in Efstathiou and Rowan–Robinson (1990), which is a circumnstellar dust shell composed only by dirty silicate grains with radius $a = 0.1$ μm. As can be seen, the agreement is very good, except at $\log\nu > 14.4$ for the edge–on spectrum. This difference arises from the fact that we treat the central source as point-like, while Efstathiou and Rowan–Robinson did not. As already pointed out, our approximation is a good one for AGNs but not for stars, and in this case produces a noticeable underestimate of the scattered light.

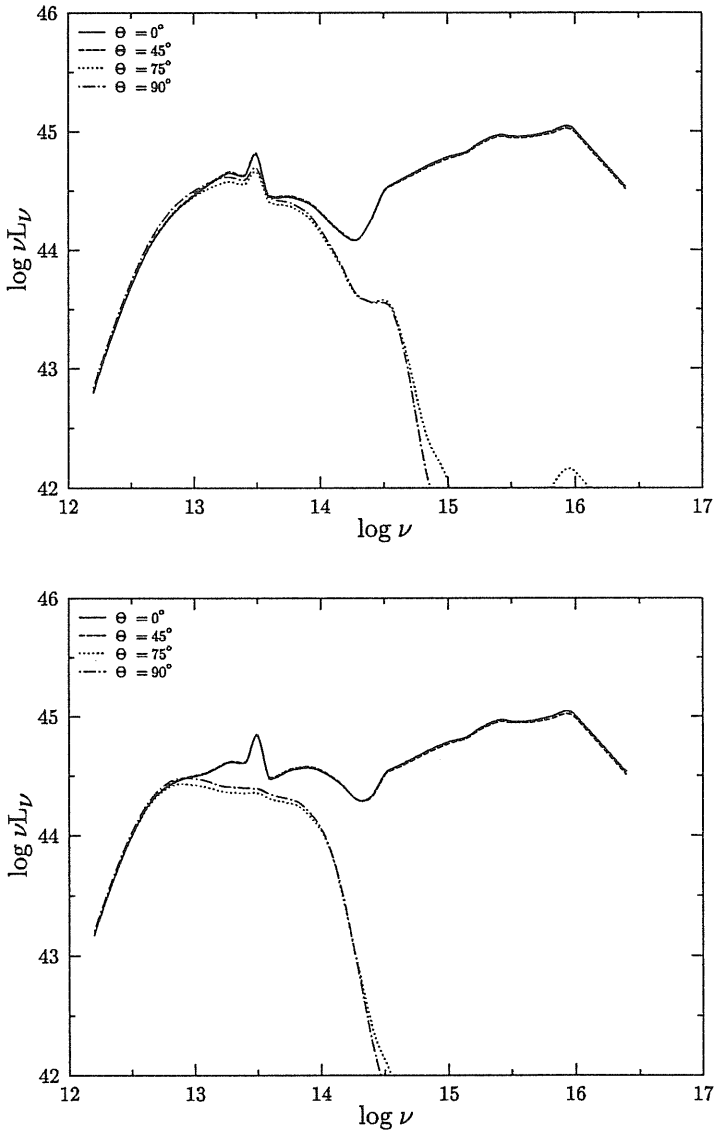

Figure 5.8: Examples of spectra emitted by thick torii (model B) in different directions. The parameters have the following values. Upper panel: $\tau_e = 10$, $r_m/r_o = 1000$, $f = 0.5$ (i.e. $\Theta_h = 60°$), $\beta = 0$. Lower panel: same of upper panel but with $\tau_e = 30$.

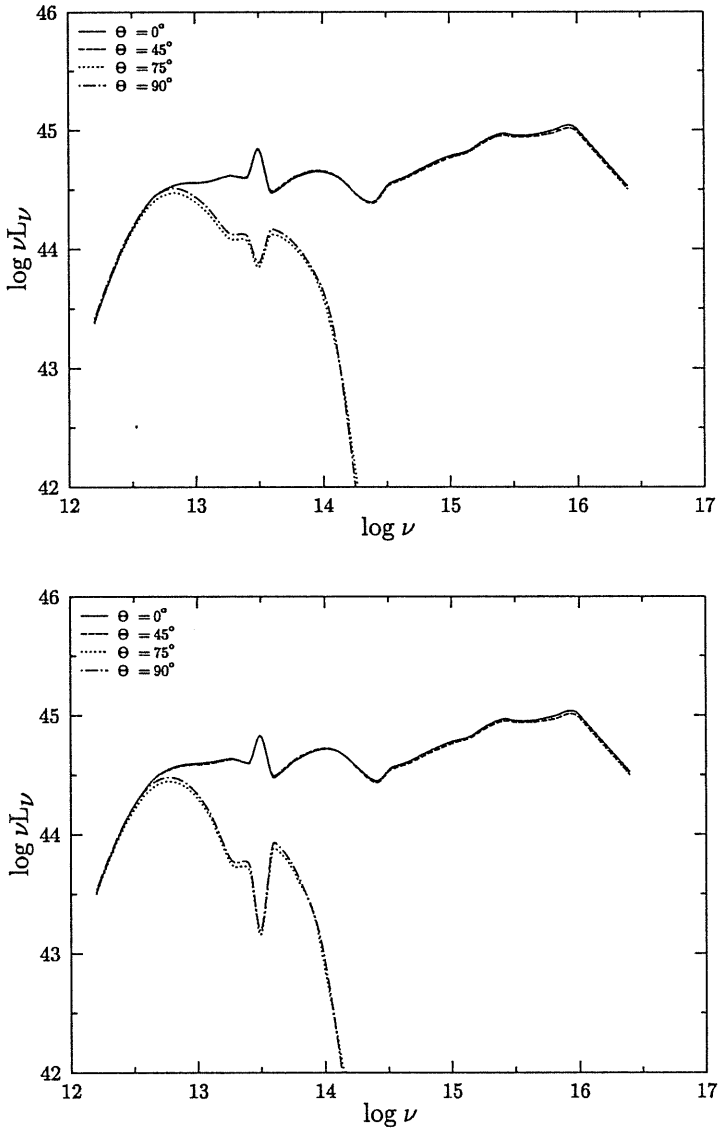

Figure 5.9: Same of the previous figure but with the following parameters. Upper panel: $\tau_e = 60$, $r_m/r_o = 1000$, $f = 0.5$ (i.e. $\Theta_h = 60°$), $\beta = 0$. Lower panel: same of upper panel but with $\tau_e = 100$.

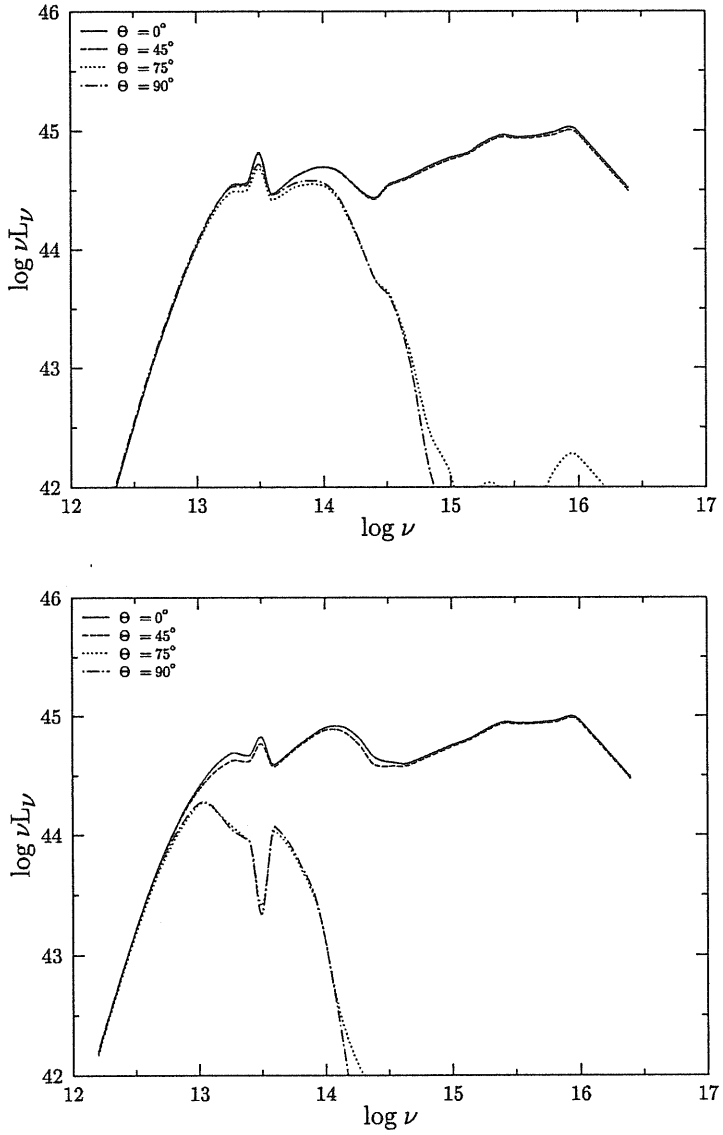

Figure 5.10: Same of the previous figure but with the following parameters. Upper panel: $\tau_e = 10$, $r_m/r_o = 100$, $f = 0.5$ (i.e. $\Theta_h = 60°$), $\beta = 0$. Lower panel: same of upper panel but with $\tau_e = 100$.

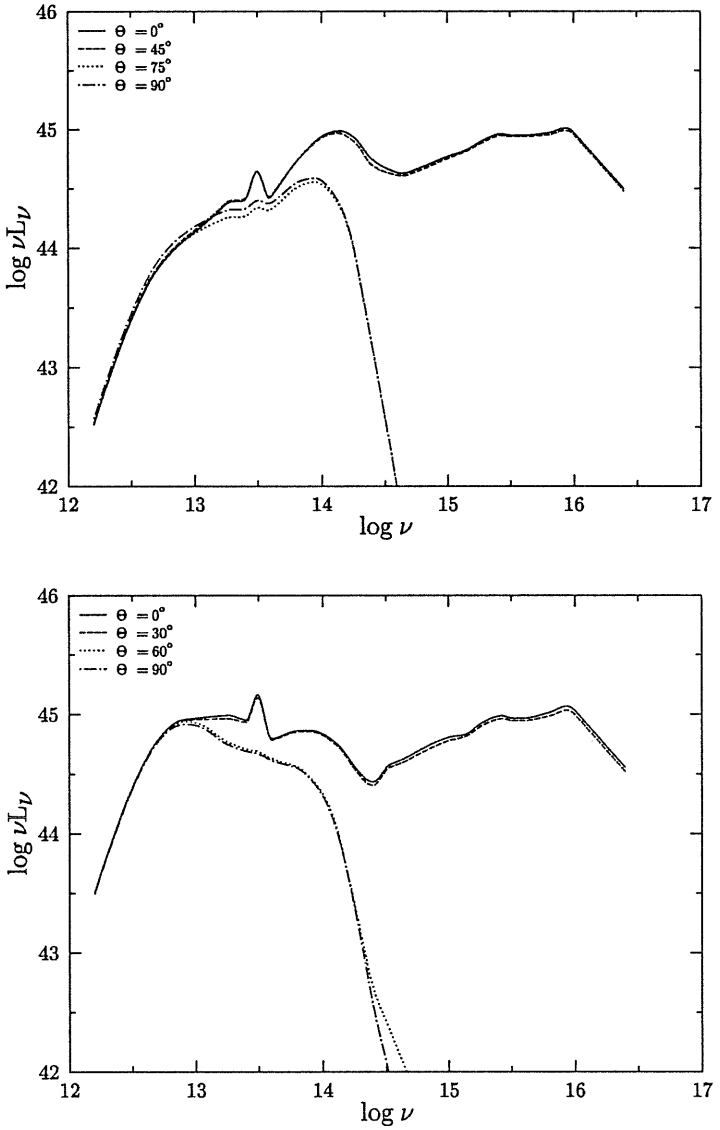

Figure 5.11: Same of the previous figure but with the following parameters. Upper panel: $\tau_e = 30$, $r_m/r_o = 1000$, $f = 0.5$ (i.e. $\Theta_h = 60^o$), $\beta = 1$. Lower panel: same of upper panel but with $f = 0.8$ (i.e. $\Theta_h \simeq 37^o$)

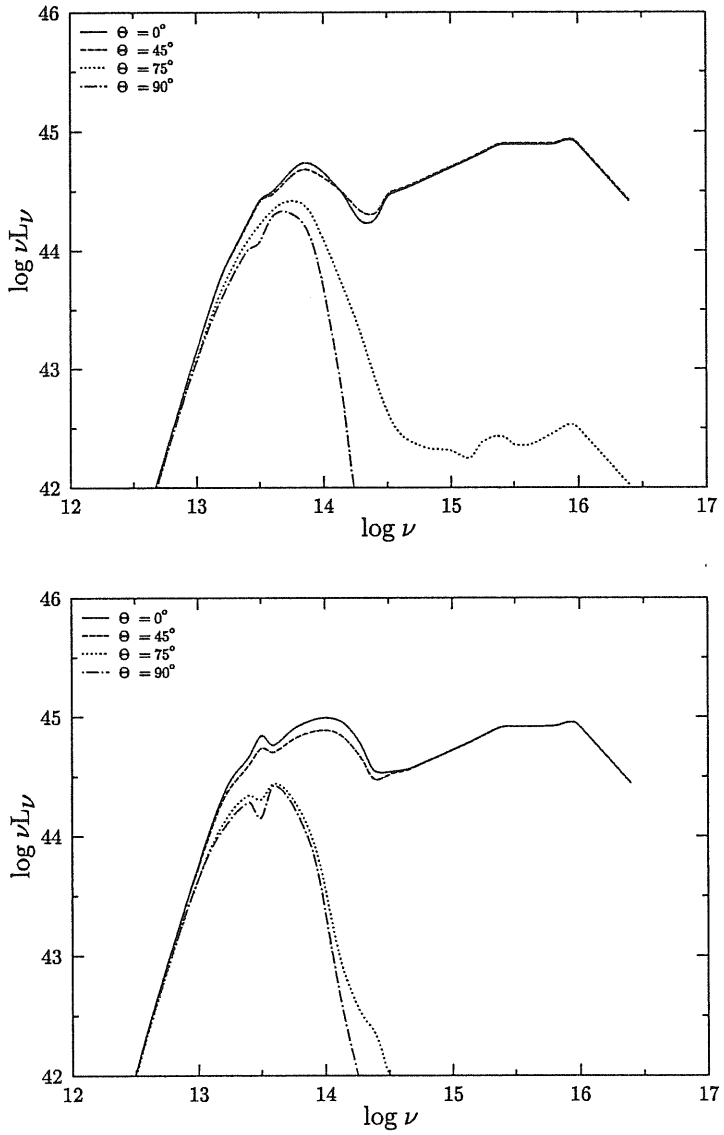

Figure 5.12: Other examples of spectra emitted by thick torii (model B) in different directions. Here very thick and compact configurations are considered. Upper panel: $\tau_e = 100$, $r_m/r_o = 3$, $f = 0.5$ (i.e. $\Theta_h = 60°$), $\beta = 1$. Lower panel: same of upper panel but with $r_m/r_o = 10$.

5.3.3 Fitting Program

We have included in the code the ability to produce formal fits to the observed SEDs by χ^2 minimization, in order to improve approximated fits obtained with the "ocular estimation method" (Barvainis 1990). Given the large amount of computing time needed to compute a single model, a very efficient algorithm was required. We made use of the routine MRQMIN described by Press et al. (1986), which implements the Levenberg–Marquardt method. The program is constructed in such a way that at each run one can specify which model parameters are adjustable and which are "froozen". A satisfying fit can be attained in 5–10 iterations, with reasonably good starting guesses, and at each step the computation of N+1 models is needed, where N is the number of parameters left free, usually 3–5. Thus a single fit requires typically 10–30 hours of CPU on an Alpha DEC3000/400.

5.4 Specific Models

There are many parameters whose effect can in principle be tested with our program. One must specify the dust mixture composition, the condensation temperatures of the various grains, the density distribution and the angular and frequency dependence of the primary spectrum. Given the large amount of CPU time needed to compute any single model, we are forced to put some limitations to these choices.

5.4.1 Dust Properties

The average transmission properties of dust in our galaxy between 0.1 and 10 μm are well reproduced by the Mathis, Rumpl and Nordisiek (1977, hereafter MRN) mixture of silicate and graphite grains (Mathis et al. 1977; Draine and Lee 1984). According to MRN, the grains have a broad power–law size distribution of the form

$$dn_i(a) = A_i\, n_{\rm H}\, a^{\gamma}\, da \qquad (a_{\rm min} \le a \le a_{\rm max}) \tag{5.22}$$

where the subscript i stands for either graphite (gra) or silicate (sil) and $n_{\rm H}$ is the number density of H nuclei. The distribution is extended between $a_{\rm min} \simeq 0.005$ μm and $a_{\rm max} \simeq 0.25$ μm, the power law index γ is equal to -3.5 and the normalization constants are $A_{\rm sil} = 10^{-25.10}$ cm$^{2.5}$/H and $A_{\rm gra} = 10^{-25.13}$ cm$^{2.5}$/H. More recently several lines of evidence, in particular the diffuse galactic emission at IRAS wavelength, have suggested the

Type	a [μm]	D [gr/cm^3]	X	T_s [K]
(1)	(2)	(3)	(4)	(5)
Amorph. Carbon	0.1	2.26	0.1119	1500
Graphite	0.03	2.26	0.0727	1500
Graphite	0.01	2.26	0.0969	1500
Amorph. Silicate	0.1	2.50	0.5609	1000
Silicate	0.03	2.50	0.1361	1000
Silicate	0.01	2.50	0.0215	1000

Table 5.2: Parameters of the grain mixture used to reproduce the absorption properties of standard galactic dust.

additional presence of very small particle ($\sim$ 10 Å), which were identified by Leger and Puget (1984) with polycyclic aromatic hydrocarbon molecules (PAH). However, this component is plausibly destroyed up to large distances from the nuclear region (see e.g. Voit 1991), and indeed IR spectroscopy of most AGNs does not show the characteristic features associated with PAHs emission (Roche et al. 1991). Therefore we do not include them in our models.

The straightforward approach to introduce in the code a discretized mixture reproducing the standard galactic extinction law, would be to define a grid of grain sizes between $a_{\rm min}$ and $a_{\rm max}$ and then to compute the mass fractions X^α of each kind of grain according to the MRN distribution. However we find that the number of grains necessary to obtain a satisfying fit to the reddening law with this method turns out to be rather high, at least $\gtrsim$ 20. A better way to reproduce the properties of dust in our galaxy, using a number of grain kinds N_k significantly lower than this, is the model proposed by Rowan–Robinson (1986, 1992). In our program, we have therefore adopted the six grains model described by Rowan–Robinson (1986), with the same absorption and scattering efficiencies. The relevant properties of grains and their relative abundance are reported in Table 5.2. In the following, this mixture will be referred to as *standard*, in the sense that it fits the galactic average absorption law.

We have assumed a sublimation temperature T_s = 1500 K for graphite grains and T_s = 1000 K for silicate ones but we have also tested T_s = 1800 K and T_s = 1200 K for graphite and silicate grains respectively. At least for the

sublimation temperatures in this ranges, the main spectral characteristics of the dust emission do not appreciably change, except for a faster declining at short wavelengths ($\lesssim 2$ μm) with lower T_s.

5.4.2 Density Distributions

The general density distribution we have considered has the form

$$\begin{cases} \rho(r,\Theta) = Cr^{-\beta}e^{-\alpha|\cos\Theta|} & \text{if} \quad \Theta_h \leq \Theta \leq \pi - \Theta_h \\ \rho(r,\Theta) = 0 & \text{otherwise} \end{cases} \tag{5.23}$$

for $r_o \leq r \leq r_m$. The distribution is parameterized by the four constants C, α, β and Θ_h. In place of the normalization constant C, we use the equatorial optical thickness of the cloud computed at 0.3 μm which hereafter we will indicate as τ_e ($A_V \simeq 0.61\tau_e$). In practise we have singled out the following limiting cases of this distribution:

A) Setting $\Theta_h = 0$ and $\alpha = 0$ we have an isotropic cloud completely surrounding the nucleus. Since the primary continuum is observed, this case is more directly interesting for our purposes when the optical thickness is not large, say $\lesssim 1$ in the optical–UV, and thus the outcoming spectrum can be computed neglecting dust self–absorption. The adjustable parameters of the distribution are β, τ_e and r_m/r_o.

B) With $\Theta_h > 0$ and $\alpha = 0$ the dust distribution becomes a torus–like configuration whose density is independent off the polar angle. This class of models is intended as the simplest kind of torii envisaged by the AGN unification schemes. The primary source is seen unobscured by dust at $\Theta < \Theta_h$, thus for the considerations reported in Sec. 5.5.1 this case is likely to be more interesting when the optical thickness of the torus is sufficiently large, say $\gtrsim 10$ in the optical–UV. Here the free parameters are β, τ_e, r_m/r_o and Θ_h, or equivalently the covering factor $f = \cos\Theta_h$.

C) Finally, when $\Theta_h = 0$ and $\alpha > 0$ we get a distribution of dust completely surrounding the nucleus, but thicker at the pole than at the equator. If α is sufficiently large the anisotropy can be very pronounced, so that this class of models could provide a somewhat more sophisticated version of the torii required by unification schemes. The adjustable parameters are β, α, τ_e, and r_m/r_o.

5.4.3 Primary Continuum

In the framework of dust reprocessing models, a fundamental point to consider is the relative power emitted by the AGN in the IR and in the blue bumps.

Since we are not directly interested here to the physical modeling of the primary optical–UV continuum, a reasonable functional description of the blue bump is fully satisfactory for our purposes. As for the observed optical–UV portion of the blue bump, we used either a black body spectrum with adjustable T ($\sim 2 \times 10^4$ K) or a power law with an adjustable spectral index.

Much more uncertain is the behavior of the intrinsic SEDs in the Extreme UV (EUV) region $15.5 < \log \nu < 17$, where the photon energy coincides with the natural scale energy of atomic physic, enforcing severe technological and observational limitations. We can in principle have indirect indications from the following arguments: (i) observations of high–z QSOs (e.g. Francis et al. 1991), (ii) photoionization models for the emission lines (e.g. Krolik and Kalmann 1988; Mathews and Ferland 1987) and (iii) computations of accretion discs spectra (e.g. Ross et al. 1992). However, the information gained by means of these arguments are scanty. The spectra of distant QSOs show apparently a sharp decline at energies above the Lyman limit (912 Å), which is however believed to be not intrinsic. Emission line diagnostic puts rather weak constrains on the spectral shape of the EUV emission, while something more precise can be said about its integrated luminosity. Spectra emitted by thin accretion discs around supermassive black holes have been computed by many authors in recent years (e.g. Czerny and Elvis 1987; Sun and Malkan 1989; Laor and Netzer 1989; Ross et al. 1992), and some work has been published also on alternative models such as thick accretion discs (e.g. Madau 1988). Unfortunately the spectra depend particularly in the EUV regime on the adopted relativistic geometry (Kerr or Schwarzschild), on the mass and accretion rate of the black hole, on the viewing angle and on the physical assumptions on the locally emitted spectrum. As a result, the published spectra show a variety of shapes, but we can say that they usually have a local spectral index between -0.5 and -1.5 from $\log \nu = 15.4$ and $\log \nu = 16 \div 16.5$ and then they cut off very steeply.

In conclusion the above cited arguments are all consistent with the usual assumption (e.g. Mathews and Ferland 1987; Sanders et al. 1989; Laor and Draine 1993), according to which the intrinsic spectrum should remain almost flat or slowly rising in νF_ν, with a spectral index $\alpha \simeq -1.0$ up to

$\log\nu = 16 \div 16.5$, and then cut off sharply ($\alpha = -2 \div -3$) in order to join the much lower flux at X–rays frequencies, in such a way that the contribution given by the unobserved portion of the blue bump to the bolometric luminosity should be of the same order as that given by the observed one (Krolik and Kalmann 1988). The integrated luminosity in the EUV region can thus be estimated as:

$$L_{\rm EUV} = (\nu L_\nu)_{15.4} \times C \tag{5.24}$$

where $(\nu L_\nu)_{15.4}$ is the value of νL_ν computed at $\log\nu = 15.4$ and C is a multiplicative factor equal to 2.2 if the cut off occurs at $\log\nu = 16$ or 2.8 if it occurs at $\log\nu = 16.5$. The corresponding integrated blue bump luminosity L_{uv} usually would not change by more than 20% in our sample objects, in absence of local absorption.

Note also that if we assume that the IR radiation is mainly due to an optically thick dust torus heated by the primary optical–UV continuum, which we are viewing through the "hole" of the torus, its contribution should not be considered in the budget of the primary energy source, since it is a sort of reflected component, due to power that has been emitted in direction of the torus and subsequently redirected toward us.

5.5 Results

5.5.1 Thick Torii

With the aim of exploring with reasonable resolution and width the parameter space, we have computed models B (Section 5.4.2) in correspondence of all (270) the possible combinations of the following values of the free parameters:

$$\begin{aligned} \beta &= 0, 1, 2 \\ \tau_e &= 3, 10, 30, 100, 300 \\ r_m/r_o &= 3, 10, 30, 100, 300, 1000 \\ f &= 0.2, 0.5, 0.8 \end{aligned}$$

We have also considered a few intermediate cases, for instance some models with $\tau_e = 60$. In these computations we used a broken power–law continuum described by $\alpha = -0.5$ for $14.5 < \log\nu \leq 15.4$, $\alpha = -1$ for

$15.4 < \log\nu \leq 16$ and $\alpha = -2.2$ for $\log\nu > 16$. The adopted power–law in the range $14.5 < \log\nu \leq 15.4$ approximates well the observed portion of the blue–bump in our mean SED (Fig. 5.3). In the IR, we assumed a very sharp decline of the primary continuum at $\log\nu \leq 14.5$ ($\lambda \geq 1$ μm), with a spectral index $\alpha = 2$, so that the emission from the dust largely dominates the spectrum immediately below this limit. It is worth noticing that realistic changes in these choices have very little effects, if any, on the shape of the spectrum emitted by the dust.

In Figs. 5.8–5.12 are shown a few representative examples of the emitted radiation. A first point to notice is that, for values of the optical depth $\tau_e >$ few, models with density distribution described by $\beta \geq 1$ produce rather narrow IR bumps peaking at few μm and then rapidly declining, in contrast with the observations showing on average increasing or flat spectra in the few to 30 μm region (Fig. 5.15 and Sec. 5.5.1). By converse with smaller values of optical depth a more concentrated density distribution is needed. For instance a reasonable fit to the average IR spectrum is obtained with $\tau_e = 1.5$ and $\beta = 0.7$. Therefore the broadness of the observed spectra requires almost homogeneous density distributions.

In the following of this section, unless otherwise explicitly stated, all the considerations will refer more specifically to $\beta = 0$ models, i.e. homogeneous torii.

The dependence on the covering factor f manifests mainly through the relative importance of the UV to the IR luminosity, while the main characteristics of the IR spectrum and silicate features keep quite similar when only f varies.

Angular Dependence

The continuum observed from directions along which the torus obscures the primary source and its interior portion, i.e. from $\Theta > \Theta_h$, is very different from that seen from directions along which it does not. At long wavelengths the differences are negligible, but at lower λ, when the dust becomes increasingly opaque to its own radiation, the torus turns out to be more and more luminous at $\Theta < \Theta_h$. Due to the geometry the SED does not depend strongly on Θ as long as it remains less than Θ_h, or greater than Θ_h. As expected, the ratio p between the integrated flux emitted by the dust at the equator and that emitted at the pole is a strongly decreasing function of τ_e (Fig. 5.13).

Generally speaking, if one assumes that the bulk of the IR radiation

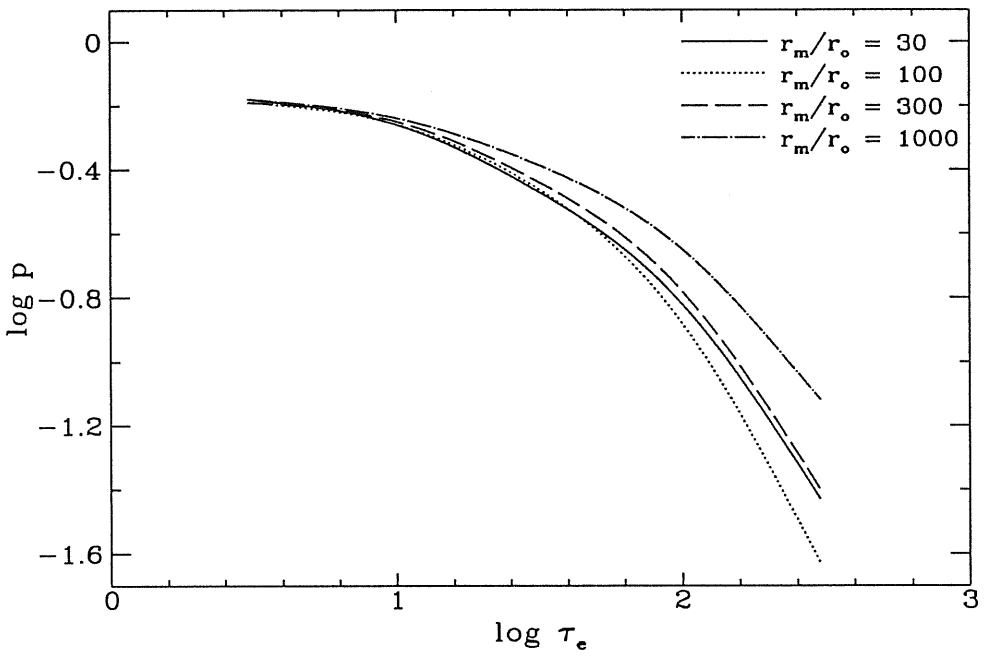

Figure 5.13: The plotted quantity p is the ratio between the integrated fluxes emitted by dust at $\Theta = 90^o$ (equator) and $\Theta = 0^o$ (pole) by optically thick torii (model B) with $\beta = 0$ and $f = 0.5$.

at least up to 25 μm is produced by optically thick dust, geometrically organized in a torus with a covering factor f, and reradiating the power absorbed from the optical–UV continuum, which we see essentially along an absorption free line of sight (Seyfert 1 case), then the parameter p is related to the covering factor f in a simple way. Indeed we can define the ratio $R = L_{\rm ir}(< 25\ \mu{\rm m})/L_{\rm uv}$ between the integrated luminosity from 1 to 25 μm and the luminosity in the blue bump from 1 μm to $\log\nu = 17$, where the contribution of EUV region is estimated by means of Eq. 5.24, with the intermediate choice $C = 2.5$. The distribution of this quantity among our SEDs is shown in Fig. 5.14. The energy balance yields

$$f \simeq \frac{R}{1 + R(1-p)} \tag{5.25}$$

Therefore for a torus essentially transparent to the infrared ($p \simeq 1$) $f \simeq R$,

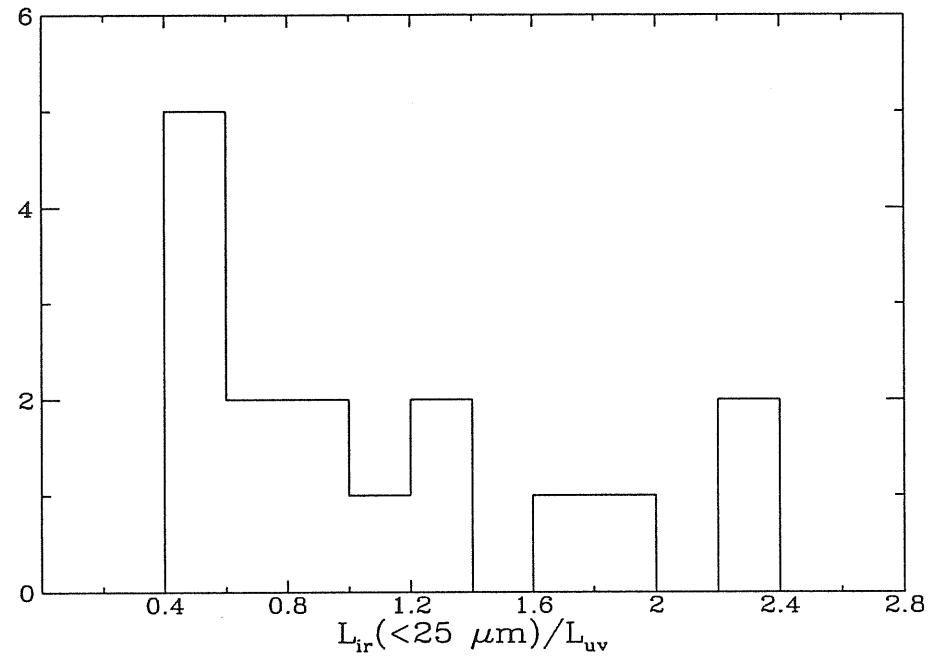

Figure 5.14: Distribution among our SEDs of the ratio $L_{\rm ir}(< 25\ \mu{\rm m})/L_{\rm uv}$ between the integrated luminosity from 1 to 25 μm and the luminosity in the blue bump from 1 μm to $\log\nu = 17$.

while at the opposite extreme if the torus is very thick to its own radiation, p decreases and the required covering factor can be lowered. Thus the covering factor required by thicker torii to produce a given ratio between the IR and the UV bumps is lower than that required by thinner ones.

Width of the IR Bump

The width of the IR bump is an important property of the various proposed models. It can be studied quantitatively by using the logarithmic interval of frequency W in which the power emitted is no less than one third of its peak value. We remind that observed spectra are usually broader than $W = 1.5$ (see Fig. 5.3).

In the hypothesis of homogeneous dust distribution in the torii the width W depends basically on the optical depth τ_e and on the radial extension

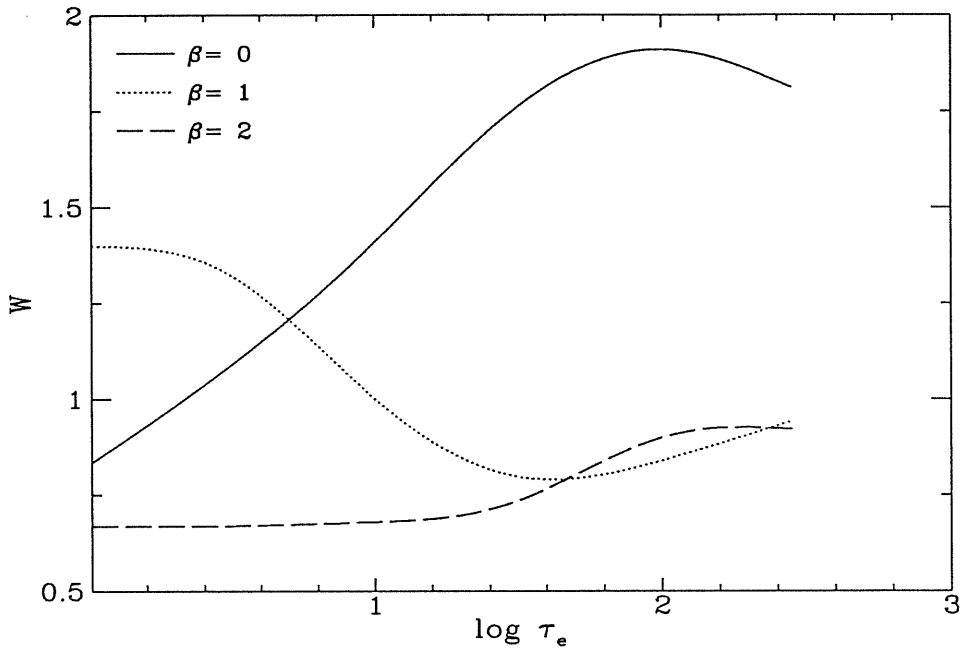

Figure 5.15: Width of the IR bump produced by optically thick pole–on torii (model B) with $r_m/r_o = 1000$ and $f = 0.5$. The curves refer to the bare dust component. W is the logarithmic interval of frequency in which the power emitted is no less than one third of its peak value.

r_m/r_o. Fig. 5.16 displays the predicted width of the bump produced by the dust distribution against its radial extension r_m/r_o, for different choices of τ_e, the equatorial optical thickness at 0.3 μm. For definiteness the curves refer to configurations with a covering factor $f = 0.5$, but, as already remarked, the dependence on f is weak. The width increases with increasing r_m/r_o, increases when τ_e increases for $\tau_e \lesssim 100$ and then decreases slowly, reflecting the broadness of the dust equilibrium temperature. The width is comparable to that of observed SEDs only when $r_m \gtrsim$ few $\times\, 10^2\, r_o$.

We confirm the findings of Pier and Krolik (1992b) who have pointed out that their extremely thick ($\tau_e \geq 100$) and compact ($r_m/r_o \leq 10$) torii produce IR spectra with $W \leq 1$.

Centrally concentrated distributions ($\beta > 0$ in Eq. 5.23) tend to produce

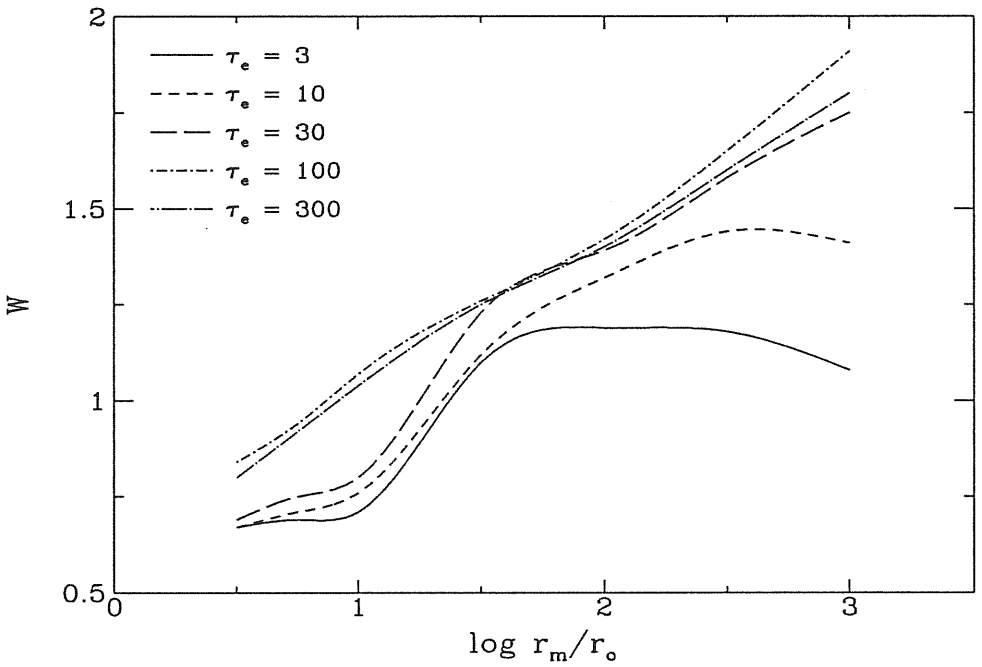

Figure 5.16: Same of the previous figure but for optically thick pole–on torii (model B) with $\beta = 0$, $f = 0.5$ and different values of τ_e. The width is comparable to that of observed SEDs for sufficiently extended ($r_m \gtrsim 100 \times r_o$) systems.

narrower spectra for thick torii at fixed optical depth (see Fig. 5.15). By contrast we confirm that optically thin cases produce the broadest spectra for $\beta \sim 0.7$ (Barvainis 1987; Loska et al. 1993).

10 μm Feature

The absence of a significant 10 μm silicate emission feature in the spectra of bright AGNs (Roche et al. 1991) has been invoked in the past as an argument for the nonthermal origin of the IR radiation, even if it is sufficient to assume a modified size and/or composition for the dust mixture to reconcile the predicted amplitude of the feature to observational limits. These modifications are quiet plausible, if not unavoidable, in the AGN environment, since small grains are more easily destroyed than big ones, and silicate more

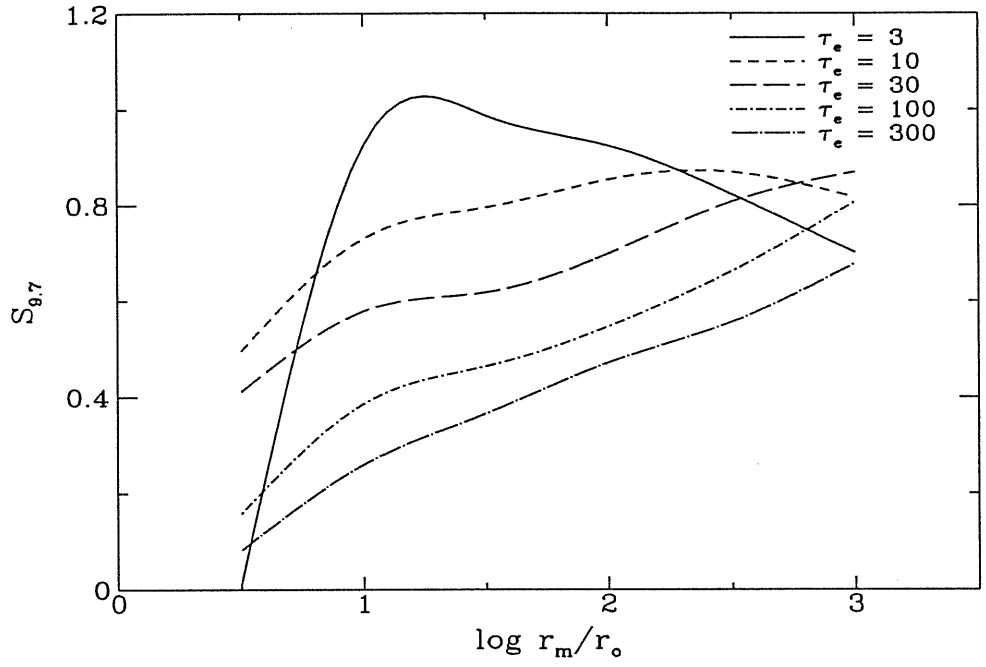

Figure 5.17: Amplitude of the 10 μm silicate emission feature as a function of the radial extension of the dust distribution. The curves refer to optically thick pole–on torii (model B) with $\beta = 0$ and $f = 0.5$ seen face–on. $S_{9.7}$ is the ratio of the actual flux emitted at 9.7 μm to that interpolated with a power law extended between 6.8 and 13.9 μm. The feature is weak only for very compact ($r_m \lesssim 10\, r_o$) and thick ($\tau_e \gtrsim 100$) configurations.

than graphite (Seab and Shull 1983; Aitken and Roche 1985; Voit 1991). It seems therefore more interesting to investigate to what extent the present and future observations in this spectral region can constrain the composition and geometry of the emitting dust, or in other words to search for ways other than small silicate depleted dust to produce a nearly featureless emission. This question has been addressed recently by Laor and Draine (1993), but their results for dust optically thick to the infrared continuum are presumably affected by the very idealized slab geometry they considered.

As can be seen from the examples, a prominent silicate emission feature is to be expected almost invariably when torii are seen from $\Theta < \Theta_h$. This

fact is made clearer from inspection of Fig. 5.17, in which we have reported the amplitude of the emission feature. Following Pier and Krolik (1992b), we have adopted as a measure of this amplitude $S_{9.7}$, the natural logarithm of the ratio between the actual flux emitted at 9.7 μm to that interpolated with a power law extended between 6.8 and 13.9 μm. The quantity $\exp(S_{9.7}) - 1$ is rather similar to the definition of the feature amplitude given by Laor and Draine (1993), if the average spectral index is $\alpha \sim 1$. So far data suggest that for Seyfert 1 galaxies $S_{9.7} < 0.4$ (see Roche et al. 1991 and references therein).

Figure 5.17 refers to pole–on ($\Theta = 0°$) spectra emitted by torii with $\beta = 0$ and $f = 0.5$. The feature turns out to be as weak as suggested by the observations only for very compact ($r_m \lesssim 10\, r_o$) and thick ($\tau_e \gtrsim 100$) configurations. This result is in keeping with that found by Pier and Krolik (1992b). Indeed, in their models, which have a cylindrical geometry with $r_m \lesssim 30\, r_o$ and $\tau_e \gtrsim 10^2$, the feature disappears in some cases. However we have seen in the previous section that very compact models do not produce bumps broad enough to account for the observed SEDs at $\lambda \gtrsim 12\mu$m.

The trend of the 10 μm feature to decrease with increasing optical depth is also present in the slab model presented by Laor and Draine (1993), although they conclude that the emission feature can never be smaller than the observational limits.

On the other hand Roche et al. (1991) pointed out that most of the galaxies with strong silicate absorption features are classified as Seyfert 2 galaxies, consistently with the unified model of Seyfert nuclei. Data collected by Roche et al. (1991) show that distinct absorption features of Seyfert 2 galaxies range from $-1.4 < S_{9.7} < -0.3$. From the reported examples of emitted spectra, it is apparent that optical depths $\tau_e \gtrsim$ few$\times 10$ can produce such features, provided that the line of sight has $\Theta > \Theta_h$.

5.5.2 Models with Optical Depth Dependence on Direction

Some amount of absorption is present even in Seyfert 1 nuclei (see e.g. De Zotti and Gaskell 1985). Therefore we have also decided to explore models with dust completely surrounding the nucleus, but with optical depths much higher along the equatorial plane than in polar direction (model C in Section 5.4.2). In particular we have reported in Fig. 5.18 two cases with $\tau_e = 100$ for line of sight in the equatorial plane and $\alpha = 5$ and 6, yielding along the polar direction optical depths of $\tau_e = 0.67$ and $\tau_e = 0.25$ respec-

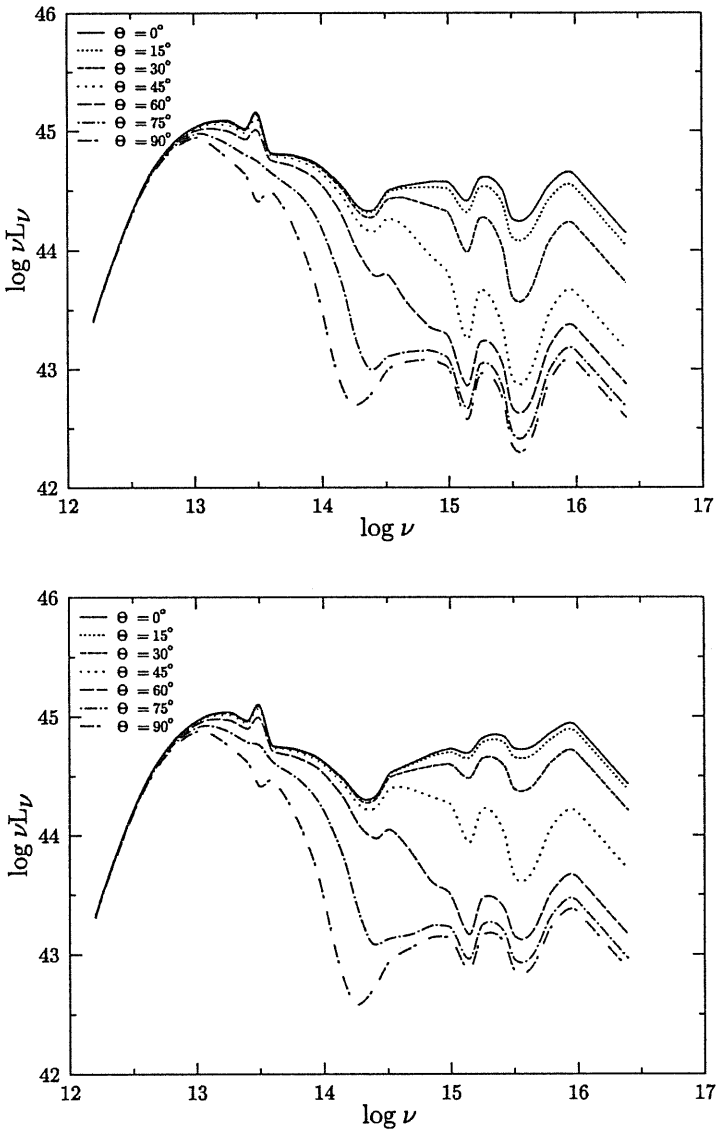

Figure 5.18: Examples of spectra emitted by torii with optical depth dependence on direction (model C). The parameters have the following values. Upper panel: $\tau_e = 100$, $r_m/r_o = 1000$, $\beta = 0$, $\alpha = 5$. Lower panel: same of upper panel but with $\alpha = 6$.

tively. The two cases have quite different ratios $R = L_{\rm ir}(< 25\ \mu{\rm m})/L_{\rm uv}$, as expected, but rather similar IR continuum and features.

Comparison to similar cases ($\tau_e = 100$) of thick torii with covering factor $f = 0.5$ shows that (i) the minimum at 1 μm is present only with viewing angles $\theta \leq 30°$; (ii) the continuum is much steeper with no bump at 3 μm whatever the line of sight is; (iii) the silicate feature at 10 μm is present in emission for $\theta \lesssim 70°$ and only for lines of sight close to the equatorial plane the feature appears in absorption.

5.6 Confrontation with Observations

In the following we shall compare the results of our calculations to the available data also at the light of unified schemes of narrow and broad–line AGNs, that means in our case unified schemes for Seyfert 1 and 2 nuclei. Spectropolarimetric observations have already shown that several narrow–line nuclei in Seyfert 2 galaxies are indeed heavily obscured broad–line nuclei (Antonucci and Miller 1985; Miller and Goodrich 1990). Moreover Maulchaey et al. (1992) pointed out that hard X–ray observations of a sample of UV detected Seyfert 2 galaxies show large column density $N_H \sim 10^{22} - 10^{24}$ and rapid variability. This could be a clue of the presence of an axisymmetric structure around the nucleus yielding values of visual extinction as high as $A_V \sim 250$ or more. The simplest version of unified schemes assumes that the difference between narrow and broad–line AGN depends only on the viewing angle. Indeed the relative frequency of the two classes of objects (Lawrence 1991) and hard X–ray observations of UV detected Seyfert 2 galaxies (Maulchaey et al. 1992) strongly suggest that the simplest unified scheme is not consistent with the data. However these authors showed that unification could be reconciled to their data, if allowance is made for dependence of the geometrical and optical thickness of the torii on luminosity.

A relevant role of the dust in broad–line AGNs has been suggested on the basis of their IR emission. As we already mentioned in the introduction, there are several indirect arguments favouring dust reradiation as origin of the bulk of the IR emission of the broad–line AGNs and particularly of the Seyfert 1 nuclei. On the other hand fits to Seyfert 1 nuclei and QSO SEDs have been often worked out by use of models that are transparent in the IR (Barvainis 1990, Loska et al. 1993). However the observed broad IR bump ($W \gtrsim 1.5$) may be obtained even in the case of high optical depth, provided that the radial dimension of the thick torus ($\tau_e \gtrsim 30$) is extended enough

($r_m/r_o \gtrsim 30$), as shown in Fig. 5.16. Both the optical thick as well as the thin case have problems in minimizing the strength of the 10 μm feature.

For the thin case the only possible solution is that the dust is significantly depleted in silicate grains with respect to the usually assumed composition of the interstellar dust (see e.g. Loska et al. 1993). However this solution is rather unsatisfactory because in all the cases of obscured broad–line AGNs the silicate feature is clearly seen in absorption (Roche et al. 1991). Even assuming that the Seyfert 1 nuclei have no thick torii around the nuclei, whereas type 2 have, a strong difference in dust composition can hardly be justified.

In the case of an optically thick ($\tau_{9.7\mu m} \geq 1$) slab Laor and Draine (1993) have suggested possible modifications of the standard dust model proposed by Mathis et al. (1977) that could reduce the silicate emission below the observational limits: (i) depletion of the silicates by a factor of 2 or more; (ii) significant reduction of small grains fraction. We have tested these hypotheses for our model of thick torus and the results are in agreement with Laor and Draine conclusions, as expected. However the already mentioned presence of the feature in absorption in obscured broad–line AGNs argues against these solutions, because both the proposed changes affect the silicate feature in emission as well as in absorption.

Pier and Krolik (1992b) have explored cylindrical torii with optical depths $100 \lesssim \tau_e \lesssim 10000$. They showed that extremely large optical depths and small r_m/r_o ($\lesssim 30$) tend to suppress the silicate emission features even in the case of almost dust free line of sight. All their cases fall in the lower left corner of our Fig. 5.17. On the other hand torii with very large optical depths produce IR spectra rather peaked with $W \lesssim 1$ inconsistent with the observations of broad–line AGN ($W \gtrsim 1.5$). Large optical depths have also problems in fitting the SEDs of Seyfert 2 nuclei. Indeed Koitilainen and Ward (1993) have been able to determine the near IR nuclear magnitudes of several Seyfert 2 galaxies. Their IR spectra are only somewhat steeper than those of Seyfert 1 nuclei, increasing by a factor $\sim 10 \div 20$ in νf_ν when passing from 1 to 25 μm and then flattening up to 60 μm. By converse, in cases like those envisaged by Pier and Krolik (1992b), the spectra predicted for significantly obscured lines of sight tend to be significantly peaked with the maximum at $\lambda \lesssim 10$ μm.

The solutions so far proposed to the absence of significant emission feature at 10 μm are not satisfactory in several aspects, if a unified scheme is adopted.

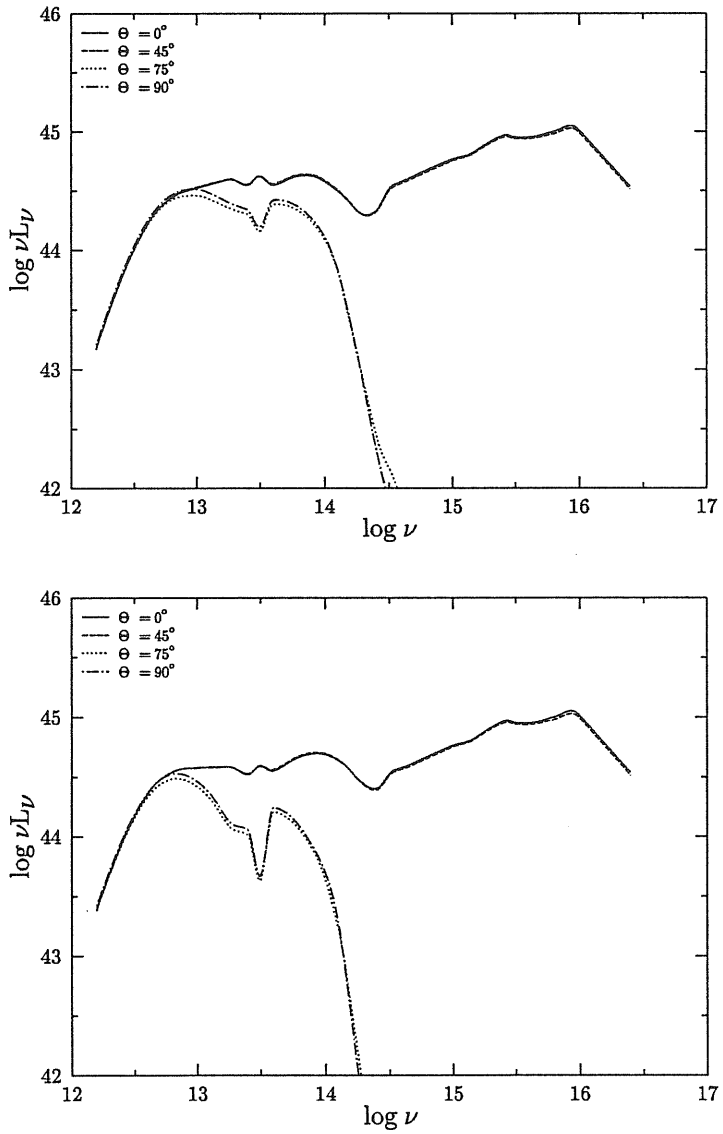

Figure 5.19: Spectra emitted by thick torii (model B) in which the dust is depleted in silicate grains within $r = 50 \times r_o$, where their equilibrium temperature is around 200 K, and has a standard composition outside this limit. The parameters are $r_m/r_o = 1000$, $\beta = 0$, $f = 0.5$ ($\Theta_h = 60°$), $\tau_e = 30$ in the upper panel and $\tau_e = 60$ in the lower one. The silicate feature is significant in absorbtion at $\Theta > \Theta_h$ while at the same time it is very weak in emission at $\Theta < \Theta_h$.

A significant modification of the dust properties is suggested by the studies on the effects of shocks on composition and dimension of the grains. Seab and Shull (1983) have shown that for shock speeds around 60 km/s, about 40% of the silicate grains is returned to the gas phase. It is not implausible that in the innermost regions of the torus shocks develop, significantly decreasing the silicate abundance. Therefore we have computed models in which the dust is depleted in silicate grains within a fixed radius. The results (Fig 5.19) show that it is possible to obtain spectra with large widths W, without emission feature in the case of dust free line of sight (Seyfert 1 nuclei), and with significant absorption 10 μm feature in the case of obscured lines of sight (Seyfert 2), provided that the silicate grain abundance is significantly depressed within $r \lesssim 40 \div 60\, r_o$ and the torus extends to $r \gtrsim 500 \div 1000$.

This solution is consistent with the unified scheme of Seyfert 1 and 2 nuclei. Indeed torii with large optical depths are suggested by Seyfert 2 spectropolarimetric and hard X–ray observations. Torii of large opacity are also called for by the observed ratios R of the infrared to UV flux of the Seyfert 1 nuclei (see Eq. 5.25). The SEDs computed for these models are in agreement with the available data of both Seyfert 1 and 2 nuclei. These models also predict that the silicate feature is negligible for Seyfert 1 nuclei, while it appears in absorption in Seyfert 2 nuclei.

Of course dependence of optical depth and covering factor on luminosity as suggested by observations (Lawrence 1991; Mulchaey et al. 1992) adds further free parameters and flexibility to the proposed model.

5.7 Summary and Conclusions

The presence in narrow–line AGN of anisotropic emission, large gas column densities and large amounts of dust has been demonstrated by observations (see e.g. Miller and Antonucci 1985; Roche et al. 1991; Mulchaey et al. 1992). The IR spectra of Seyfert 1 nuclei strongly suggest a relevant role of dust reradiation (see e.g. Barvainis 1990; Danese et al. 1992). All these observations are consistent with the unified schemes of broad and narrow–line AGN. However the elusivity of the silicate emission feature casted doubts on the importance of the dust reradiation in Seyfert 1 nuclei (Roche et al. 1991). Several possible solutions to this problem have been envisaged (see e.g. Pier and Krolik 1992b; Laor and Draine 1993). We have tested these solutions for the case of optically thick torii like those required by unification

models. Our predictions are based on computations that fully solve the transport equation in a cloud having azimuthal simmetry and containing a mixture of dust grains.

Adopting a standard dust composition, a prominent 10 μm silicate emission feature for dust free lines of sight is avoided only with extremely compact and optically thick configurations, which however are unable to produce bumps broad enough to account for the observed SEDs longword 12 μm. Thus the suggestion of extremely compact and thick torii (Pier and Krolik 1992a,b) is not satisfactory.

The possibility of modifying the dust mixture decreasing the silicate abundance has been also suggested. However the presence of the feature in absorption in obscured broad–line AGN argues against this proposal at least in the framework of unified models.

A viable alternative is connected to the finding of Seab and Shull (1983). They showed that shocks destroy more efficiently silicate than graphite grains. We suggest that similar mechanisms significantly reduce the silicate grain abundance within few parsecs, while the torii extend up to few tens of parsecs. Including these assumptions in models of optically thick torii we have found that in unabsorbed lines of sight the silicate feature is negligible, while it shows up in absorption for dust obscured lines of sight. In conclusion these models of thick torii are fully consistent with available broad band data and high resolution IR spectra of Seyfert 1 and 2 nuclei in the context of unified schemes.

Appendix A

Data for SEDs

The data used to construct the spectral energy distributions of our sample objects are described with some details in the following sections. Continuum levels estimated from IUE spectra are reported in Tab. A.1. New optical and near–IR data have been presented in Chapters 1–3. Radio, sub-mm, IRAS and X–ray data have been collected from published literature.

A.1 Radio

The $\lambda \simeq 20$ cm data have been taken from the *Westerbork Survey of Seyfert Galaxies* (Wilson and Meurs 1982) when available. These 21.2 cm observations have been made with the Westerbork Synthesis Radio Telescope, whose declination dependent Half Power Beam Width (HPBW) is $\sim 25''$ in R.A. and $25''/\sin\delta$ in Dec. For objects not included in this compilation we used the 20 cm measures reported by Edelson (1987) , which have HPBW = $90''$. From this paper we took also 6 cm data with HPBW = $15''$. The fraction of the flux originating from the underlying galaxy in large beams is uncertain. At 6 cm Edelson (1987) estimated that the galactic disc is responsible on average of about one fourth of the total $90''$ flux.

A.2 Millimeter and Sub–Millimeter

Observations in this spectral region have become available only very recently and for few AGNs. Chini et al. (1989) reported 1.3 mm detections for three objects of the sample (Mrk 304, Mrk 509 and II Zw 136), as well as upper limits for other four (Mrk 376, Mrk 478, Mrk 876 and I Zw 1). More recently,

Hughes et al. (1993) published detections at 450 and 800 μm of I Zw 1 and Mrk 376, and 800 μm upper limits of Mrk 304 and Mrk 509. Finally, a 1.1 mm detection of III Zw 2 and an upper limit of Mrk 590 is given by Lawrence et al. (1991).

A.3 Far–Infrared (IRAS)

IRAS fluxes at 12, 25, 60 and 100 μm are usually extracted directly from the IRAS catalogue (*Cataloged Galaxies and Quasar in the IRAS Survey, Jet Propulsion Laboratory, Second Edition, 1987*). Additional sources, which sometimes report co–added survey data or more sensitive pointed observations, are Edelson and Malkan (1987), McAlary and Rieke (1988) and Roche et al. (1991). For a handful of objects in our sample these papers report detections where the IRAS catalogue reports only upper limits, and in these cases we made use of the detections. We remind that the wavelength dependent IRAS beam size (typically $\sim 4' \times 2'$) includes the whole galaxy, so that all the fluxes reported are strictly speaking upper limits to the nuclear emission. In Chapter 2 we have presented strong evidences indicating that the 12 and 25 μm observed emission is mainly nuclear in origin, while in the two higher wavelength bands the galactic contribution is substantial.

A.4 Near–Infrared and Optical

Almost all the fluxes in the optical B R V and infrared J H K bands have been presented and discussed in Chapter 1–3, and refer to the bare nuclear pointlike component. There are a few exceptions: J H K nuclear fluxes for Mrk 590 and NGC 7469 are taken from Koitilainen et al. (1992a,b), who used analysis techniques strictly analogous to ours. Optical B V R fluxes of Mrk 9, Mrk 10 and Mrk 315 are taken from MacKenty (1990), who subtracted the galactic disk, but not the bulge component. Therefore, we treat these last data as upper limits.

As for the L band, where the starlight contribution is believed to be negligible, we used our photometry within 5″ aperture for 26 objects (Chapter 2), while for other 22 objects we employed photometry collected from the published literature (Granato 1988), with aperture $\leq 10''$.

Name	F_{uv1} [mJy]	F_{uv2} [mJy]	F_{uv3} [mJy]	F_{uv4} [mJy]	F_{uv5} [mJy]	N_S	N_L
(1)	(2)	(3)	(4)	(5)	(6)	(7)	(8)
I Zw 1	1.0	1.1	2.1	2.3	3.4	8	7
II Zw 1 ...	0.3	0.5	0.6	...	...	5	0
II Zw 2 ...	1.3	0.7	1.4	1.3	2.3	8	4
II Zw 136	1.6	1.9	2.3	2.3	3.1	7	7
VII Zw 118	2.0	2.1	2.6	2.6	3.4	2	1
Mrk 9	2.0	1.7	2.1	5.0	6.7	1	1
Mrk 10 ...	0.7	0.7	0.8	0.9	1.8	1	1
Mrk 79 ...	1.7	2.1	2.4	2.0	3.2	1	1
Mrk 279 ..	2.2	2.7	3.0	2.4	3.5	11	4
Mrk 290 ..	1.7	2.1	2.4	2.1	2.8	2	4
Mrk 304 ..	0.8	1.4	1.6	1.4	2.1	2	4
Mrk 335 ..	4.9	5.6	5.9	5.4	7.8	10	11
Mrk 352 ..	1.1	1.0	1.4	1.3	2.1	2	1
Mrk 359 ..	0.7	0.7	0.9	1.0	1.4	5	4
Mrk 376 ..	0.5	0.7	1.1	1.7	2.7	2	2
Mrk 478 ..	1.7	1.6	1.8	2.1	2.7	5	9
Mrk 486 ..	0.2	0.3	0.5	1.0	1.4	3	3
Mrk 506 ..	0.9	0.9	1.2	1.4	1.5	1	1
Mrk 509 ..	5.2	6.8	7.7	8.9	11.0	21	11
Mrk 704 ..	0.6	0.8	0.8	1.6	2.2	1	1
Mrk 734 ..	1.1	1.2	1.6	1.6	2.1	3	3
Mrk 771 ..	1.9	1.9	2.1	2.0	2.7	3	3
Mrk 876 ..	1.1	1.1	1.5	1.7	2.6	4	5
NGC 3516	1.1	1.3	1.8	2.2	4.1	15	11
NGC 5548	2.9	3.1	3.8	4.7	7.7	36	2
NGC 5940	0.4	0.6	0.6	0.7	1.0	2	2
NGC 7469	3.8	4.3	5.4	5.4	8.6	27	14

Table A.1: F_{uv1}–F_{uv5} are average IUE fluxes integrated in the following five continuum windows: 1340–1370 Å, 1430–1460 Å, 1690–1790 Å, 2150–2250 Å and 2600–2700 Å.

A.5 Ultraviolet (IUE)

Using the package ULDA, we have extracted from the IUE archives the good quality SWP, LWP and LWR spectra of our sample objects, and we have integrated the fluxes in the following rest–frame wavelength windows: 1340–1370 Å, 1430–1460 Å, 1690–1790 Å, 2150–2250 Å and 2600–2700 Å. Usually many spectra were available, in which case we averaged the results. The overall noise, including that due to genuine source variability, can be estimated for objects with a sufficient number of spectra (say $\gtrsim 5$) from the distribution of the different measurements. The typical standard deviation decreases clearly with wavelength, from 20–40% at 1350 Å to 10–20% at 2650 Å. The windows have been defined by Chapman et al. (1985) for the specific purpose of measuring the continuum flux level. The contamination arising from unresolved emission lines, or from the wings of resolved ones, have been estimated by these authors, probably somewhat optimistically, to be less than 10 %. Particularly the window around 2200 Å, which is crucial to define the deepness of the graphite absorption feature, is thought to be contaminated by the blending of Fe II emission lines much more severely than this (e.g. Francis et al. 1991). Tab. A.1 reports the fluxes corrected for the extinction within our galaxy, which have been computed using the standard absorption law (Seaton 1979). The table gives also the number of SW and LW spectra employed for each object, respectively N_S and N_L.

A.6 X–Ray

IPC flux levels at 2 keV have been mainly taken from Kruper et al. 1990. Additional soft–X data, as well as A–2 hard–X data (usually upper limits) reported to 6 keV, have been extracted from the catalog by Della Ceca et al. (1990).

Bibliography

Abraham, R. G., Crawford, C. S., and McHardy, I. M. 1992, ApJ, in press.

Adams, T. F. 1977, ApJS, 33, 19.

Aitken, D. K. and Roche, P. F. 1985, MNRAS, 213, 777.

Aitken, D. K., Roche, R. J., and Phillips, M. M. 1981, MNRAS, 196, 101P.

Antonucci, R. R. J. and Miller, J. S. 1985, ApJ, 297, 621.

Balzano, W. A. and Weedman, D. W. 1981, ApJ, 243, 756.

Band, D. L. and Malkan, M. A. 1989, ApJ, 345, 122.

Baribaud, T., Alloin, D., Glass, I. S., and Pelat, D. 1992, A&A, page 256.

Barvainis, R. 1987, ApJ, 320, 537.

Barvainis, R. 1990, ApJ, 353, 419.

Barvainis, R. 1992, ApJ, 400, 502.

Berriman, G. 1989, ApJ, 345, 713.

Boroson, T. A. 1981, ApJS, 46, 177.

Boroson, T. A., Oke, J. B., and Green, R. 1982, ApJ, 263, 32.

Boyle, B. J. 1991. In Barrow, J. D., Mestel, L., and Thomas, P. A., editors, *Texas/ESO-CERN Symposium on Relativistic Astrophysics, Cosmology, and Fundamental Physics*, page 14. New York: NY Acad. Sci.

Bregman, J. N. 1990, Astron. Astrophs. Rev., 2, 125.

Campins, H., Rieke, G. H., and Lebofsky, M. J. 1985, AJ, 90, 896.

Carico, D. P., Sanders, D. B., Soifer, B. T., Elias, J. H., Matthews, K., and Neugebauer, G. 1988, AJ, 95, 356.

Carico, D. P., Sanders, D. B., Soifer, B. T., Matthews, K., and Neugebauer, G. 1990, AJ, 100, 70.

Carleton, N. P., Elvis, M., Fabbiano, G., Willner, S. P., Lawrence, A., and Ward, M. 1987, ApJ, 318, 595.

Chang, C. A., Schiano, A. V. R., and Wolfe, M. 1987, ApJ, 322, 180.

Chapman, G. N. F., Geller, M. J., and Huchra, J. P. 1985, ApJ, 297, 151.

Cheng, F. Z., Danese, L., and De Zotti, G. 1983, MNRAS, 204, 13P.

Cheng, F. Z., Danese, L., De Zotti, G., and Franceschini, A. 1985, MNRAS, 212, 857.

Chini, R., Kreysa, E., and Biermann, P. L. 1989, A&A, 219, 87.

Christian, C. A., Adams, M., Barnes, J. V., Butcher, H., Hayes, D. S., Mould, J. R., and Siegel, M. 1985, PASP, 97, 363.

Clavel, J., Wamsteker, W., and Glass, I. S. 1989, ApJ, 337, 236.

Collin-Souffrin, S. 1991, A&A, 243, 344.

Collison, A. J. and Fix, J. D. 1991, ApJ, 368, 545.

Cowie, L. L., Gardner, J. P., Lilly, S. J., and McLean, I. 1990, ApJ, 360, L1.

Cutri, R. M., Rudy, R. J., Rieke, G. H., Tokunaga, A. T., and Willner, S. P. 1984, ApJ, 280, 512.

Czerny, B. and Elvis, M. 1987, ApJ, 321, 305.

Dahari, O. 1985, ApJS, 57, 643.

Dahari, O. and De Robertis, M. M. 1988, ApJS, 67, 249.

Danese, L. and De Zotti, G. 1984, A&A, 140, 393.

Danese, L., Zitelli, V., Granato, G. L., Wade, R., De Zotti, G., and Mandolesi, N. 1992, ApJ, 399, 38.

De Zotti, G. and Gaskell, C. M. 1985, A&A, 147, 1.

Della Ceca, R., Palumbo, G. G. C., Persic, M., Boldt, E. A., De Zotti, G., and Marshall, F. E. 1990, ApJS, 72, 471.

Dent, W. R. F. 1988, ApJ, 325, 252.

Devereux, N. A. 1987, ApJ, 323, 91.

Devereux, N. A. 1989, ApJ, 346, 126.

Devereux, N. A., Becklin, E. E., and Scoville, N. 1987, ApJ, 312, 529.

Draine, B. T. and Lee, H. M. 1984, ApJ, 285, 89.

Edelson, R. A. 1986, ApJ, 309, L69.

Edelson, R. A. 1987, ApJ, 313, 651.

Edelson, R. A. and Malkan, M. A. 1986, ApJ, 308, 59.

Edelson, R. A. and Malkan, M. A. 1987, ApJ, 323, 516.

Edelson, R. A., Malkan, M. A., and Rieke, G. H. 1987, ApJ, 321, 233.

Efstathiou, A. and Rowan-Robinson 1990, MNRAS, 245, 275.

Efstathiou, G., Ellis, R. S., and Peterson, B. A. 1988, MNRAS, 232, 431.

Elvis, M., Maccacaro, T., Wilson, A. S., Ward, M. J., Penston, M. V., Fosbury, R. A. E., and Perola, G. C. 1978, MNRAS, 183, 129.

Engargiola, G., Harper, D. A., Elvis, M., and Willner, S. P. 1988, ApJ, 332, L19.

Feigelson, E. D. and Nelson, P. I. 1985, ApJ, 293, 192.

Franceschini, A., Danese, L., De Zotti, G., and Toffolatti 1988, MNRAS, 233, 157.

Franceschini, A., Toffolatti, L., Mazzei, P., Danese, L., and De Zotti, G. 1991, A&AS, 89, 285.

Francis, P. J., Hewett, P. C., Foltz, C. B., Chaffee, F. H., Weymann, R. J., and Morris, S. L. 1991, ApJ, 373, 465.

Freeman, K. C. 1970, ApJ, 160, 811.

Geheren, T., Fried, J., Wehinger, P. A., and Wyckoff, S. 1984, ApJ, 278, 11.

Giovanardi, C. and Hunt, L. K. 1988, AJ, 95, 408.

Glass, I. S. 1979, MNRAS, 186, 29P.

Glass, I. S. 1981, MNRAS, 197, 1067.

Glass, I. S. 1992, MNRAS, 256, 23P.

Glass, I. S. and Moonrwood, A. F. M. 1985, MNRAS, 211, 461.

Granato, G. L. 1988. *Degree Thesis Universitá di Padova.*

Granato, G. L., Zitelli, V., Bonoli, F., Danese, L., Bonoli, C., and Delpino, F. 1993, ApJS, 89, In Press.

Griersmith, D., Hyland, A. R., and Jones, T. J. 1982, AJ, 87, 1106.

Heckman, T. M. 1987. In Thuan, T. X., Montmerle, T., and Van, T. T., editors, *Starbursts and Galaxy Evolution*, page 381. Paris: Editions Frontières.

Heckman, T. M., Blitz, L., Wilson, A. S., Armus, L., and Miley, G. K. 1989, ApJ, 342, 735.

Huchra, J. and Burg, R. 1992, ApJ, 393, 90.

Huchra, J. P. 1977, ApJS, 35, 171.

Hughes, D. H., Robson, E. I., Dunlop, J. S., and K, G. W. 1993, MNRAS, in Press.

Hutchings, J. B., Crampton, D., and Campbell, B. 1984, ApJ, 280, 41.

Inoue, H. 1989. In Hunt, J. and Battrick, B., editors, *Proc of the* 23^d *ESLAB Symposium on X-Ray Astronomy ESA SP-296*, page 783. ESA SP–296.

Isobe, T., Feigelson, E. D., and Nelson, P. I. 1986, ApJ, 306, 490.

Joseph, R. D., Meikle, W. P. S., Robertson, N. A., and Wright, G. S. 1984, MNRAS, 209, 111.

Keel, W. C. 1980, AJ, 85, 198.

Kent, S. 1985, ApJS, 59, 115.

Kodaira, K., Watanabe, M., and Okamura, S. 1986, ApJS, 62, 703.

Koitilainen, J. K. and Ward, M. J. 1993, MNRAS, in Press.

Koitilainen, J. K., Ward, M. J., Boisson, C., DePoy, D. L., and Bryant, L. R. 1992a, MNRAS, 256, 125.

Koitilainen, J. K., Ward, M. J., Boisson, C., DePoy, D. L., and Smith, M. G. 1992b, MNRAS, 256, 143.

Kriss, G. A. 1988, ApJ, 324, 809.

Krolik, J. H. and Begelman, M. C. 1988, ApJ, 329, 702.

Krolik, J. H. and Kalmann, T. R. 1988, APJ, 324, 714.

Kruper, J. S. and Canizares, C. R. 1989, ApJ, 343, 66.

Kruper, J. S., Urry, C. M., and Canizares, C. R. 1990, ApJS, 74, 347.

Laor, A. and Draine, B. T. 1993, ApJ, 402, 441.

Laor, A. and Netzer, H. 1989, MNRAS, 238, 897.

Lawrence, A. 1991, MNRAS, 252, 586.

Lawrence, A. and Elvis, M. 1982, ApJ, 256, 410.

Lawrence, A., Rowan-Robinson, M., Efstathiou, A., Ward, M. J., Elvis, M., Smith, M. G., Duncan, W. D., and Robson, I. E. 1991, MNRAS, 248, 91.

Lawrence, A., Ward, M., Elvis, M., Fabbiano, G., Willner, S. P., Carleton, N. P., and Longmore, A. 1985, ApJ, 291, 117.

Leger, A. and Puget, J. L. 1984, A&A, 137, L5.

Loska, Z., Szczerba, R., and Czerny, B. 1993, MNRAS, 261, 63.

MacKenty, J. W. 1990, ApJS, 72, 231.

Macklin, J. T. 1982, MNRAS, 199, 1119.

Madau, P. 1988, ApJ, 327, 116.

Malkan, M. A. 1984a, ApJ, 287, 555.

Malkan, M. A. 1984b. In Brinkmann, W. and Trumper, J., editors, *X-Ray and UV Emission from Active Galactic Nuclei*, page 121. Munich: MPI fur Extraterresriche Physik.

Malkan, M. A., Margon, B., and Chanan, G. A. 1984, ApJ, 280, 66.

Mathews, W. G. and Ferland, G. J. 1987, ApJ, 323, 456.

Mathis, J. S., Rumpl, W., and Nordsieck, K. H. 1977, ApJ, 217, 425.

Mazzarella, J. M. and Balzano, V. A. 1986, ApJS, 62, 751.

McAlary, C. W., McLaren, R. A., Dennis, R., and Crabtree, D. R. 1979, ApJ, 234, 471.

McAlary, C. W., McLaren, R. A., McGonegal, R. J., and J, M. 1983, ApJS, 52, 341.

McAlary, C. W. and Rieke, G. H. 1988, ApJ, 333, 1.

McLean, I. S., Chuter, T. C., McCaughrean, M. J., and Rayner, J. T. 1986, Proceedings of SPIE, 627, 430.

Meixer, M., Puchalsky, R., Blitz, L., Wright, M., and Heckman, T. 1990, ApJ, 354, 158.

Meurs, E. J. A. and Wilson, A. S. 1984, A&A, 136, 206.

Miley, G. K., Neugebauer, G., and Soifer, B. T. 1985, ApJ, 293, L11.

Miller, J. S. and Antonucci, R. R. J. 1985, ApJ, 297, 621.

Miller, J. S. and Goodrich, R. W. 1990, ApJ, 355, 456.

Molendi, S., Maraschi, L., and Stella, L. 1992, MNRAS, 255, 27.

Mulchaey, J. S., Mushotzky, R. F., and Weaver, K. A. 1992, ApJ, 190, L69.

Mushotzky, R. F. and Wandel, A. 1989, ApJ, 339, 674.

Neugebauer, G., Green, R. F., Matthews, K., Schimdt, M., Soifer, B. T., and Bennett, J. 1987, ApJS, 63, 615.

Neugebauer, G., Matthews, K., Soifer, B. T., and Elias, J. H. 1985, ApJ, 298, 275.

Neugebauer, G., Oke, J., Becklin, E., and Matthews, K. 1979, ApJ, 230, 79.

Neyman, J. and Scott, E. L. 1961. In *Proc of 4th Berkeley Symp. Math. Stat. and Prob., Vol. 3*, page 261. University of California Press, Berkeley.

Neyman, J. and Scott, E. L. 1974. In *Confrontation of Cosmological Theories with Observational Data, IUA Symp. No. 63*, page 129.

Osterbrock, D. E. 1991, Rep. Progr. Phys. 54, 579.

Paturel, G., Fauque, P., Bottinelli, L., and Gouguenheim, L. 1989. *Catalogue of Principal Galaxies.* Imprimerie de l'Observatoire de Paris.

Penston, M. V., Penston, M. J., Selmes, R. A., Becklin, E. E., and Neugebauer, G. 1974, MNRAS, 169, 357.

Phinney, E. S. 1989. In Meyer, J. S. e. a., editor, *Theory of Accretion Disks*, page 457. Kluwer Academic Publishers.

Piccinotti, G., Mushotzky, R. F., Boldt, E. A., Holt, S. S., Marshall, F. E., Serlemitsos, P. J., and Shafer, R. A. 1982, ApJ, 253, 485.

Pier, E. A. and Krolik, J. H. 1992b, ApJ, 401, 109.

Piro, L., Yamauchi, M., and Matsuoka, M. 1990, ApJ, 360, L35.

Pollack, J. B. and Ohring, G. 1973, Icarus, 19, 34.

Pounds, K. A., Nandra, K., Stewart, G. C., George, I. M., and Fabian, A. C. 1990, Nature, 344, 132.

Press, W. H., Flannery, B. P., Teukolsky, S. A., and Vetterling, W. T. 1986. *Numerical Recipes.* Cambridge University Press.

Rees, M. J., Silk, J. I., Werner, M. W., and Wickramsinghe, M. C. 1969, Nature, 223, 788.

Rieke, G. H. 1978, ApJ, 226, 550.

Roche, R. J., Aitken, D. K., Smith, C. H., and Ward, M. J. 1991, MNRAS, 248, 606.

Rodriguez Espinosa, J. M., Rudy, R. J., and Jones, B. 1986, ApJ, 309, 76.

Rodriguez Espinosa, J. M., Rudy, R. J., and Jones, B. 1987, ApJ, 312, 555.

Ross, R. R., Fabian, A. C., and Mineshige, S. 1992, MNRAS, 258, 129.

Rowan-Robinson, M. 1986, MNRAS, 219, 737.

Rowan-Robinson, M. 1992, MNRAS, 258, 787.

Rudy, R. J., LeVan, P. D., Puetter, R. C., Smith, H. E., Willner, S. P., and Tokunaga, A. T. 1982a, ApJ, 257, 570.

Rudy, R. J., LeVan, P. D., and Rodriguez-Espinosa, J. M. 1982b, AJ, 87, 598.

Rudy, R. J., LeVan, P. D., and Rodriguez-Espinosa, J. M. 1982c, AJ, 87, 598.

Rush, B., Malkan, M. A., and Spinoglio, L. 1993, ApJS, 89, Nov 1.

Rybicky, G. B. and Lightman, A. P. 1979. *Radiative Processes in Astrophysics.* John Wiley & Sons.

Sandage, A. R. 1973, ApJ, 180, 687.

Sanders, D. B., Phinney, E. S., Neugebauer, G., Soifer, B. T., and Matthews, K. 1989, ApJ, 347, 29.

Sargent, W. L. W. 1972, ApJ, 173, 7.

Savage, B. D. and Mathis, J. S. 1979, Ann. Rev. Astr. Ap. 17, 73.

Schmidt, M. and Green, R. F. 1983, ApJ, 269, 352.

Schmitt, J. H. M. M. 1985, ApJ, 293, 178.

Scoville, N. Z. 1988. In Pudritz, R. E. and Fich, M., editors, *Galactic and Extragalactic Star Formation*, page 541. Dordrecht: Kluwer.

Scoville, N. Z., Soifer, B. T., Neugebauer, G., Young, J. S., Matthews, K., and Yerka, J. 1985, ApJ, 289, 129.

Seab, C. G. and Shull, J. M. 1983, ApJ, 275, 652.

Seaton, M. J. 1979, MNRAS, 187, 73P.

Sekigichi, K. 1987, ApJ, 316, 145.

Simkin, S. M., Su, H. J., and Schwarz, M. P. 1980, ApJ, 237, 404.

Simons, D. A., Tokunaga, A. T., Rudy, R. J., and Stein, W. A. 1988, AJ, 96, 481.

Sitko, M. L. and Zhu, Y. 1991, ApJ, 369, 106.

Skrutskie, M. F., Shure, M. A., and Beckwith, S. 1985, ApJ, 299, 303.

Smith, E. P., Heckman, T. M., Bothun, G. D., Romashin, W., and Balick, B. 1986, ApJ, 306, 64.

Spinoglio, L. and Malkan, M. A. 1989, ApJ, 342, 83.

Stein, W. A. and Weedman, D. W. 1976, ApJ, 205, 44.

Sun, W. H. and Malkan, M. A. 1989, ApJ, 346, 68.

Taniguchi, Y., Kameya, O., Nakai, N., and Kawara, K. 1990, ApJ, 358, 132.

Telesco, C. M., Campins, H., Joy, M., Dietz, K., and Decher, R. 1991, ApJ, 369, 135.

Terebizh 1980, Astrofizika, 16, 45.

Terlevich, R. and Melnick, J. 1987. In Thuan, T. X., Montmerle, T., and Van, T. T., editors, *Starbursts and Galaxy Evolution*, page 393. Paris: Editions Frontières.

Thuan, T. X. and Gunn, J. E. 1976, PASP, 88, 543.

Veron, P. 1979, A&A, 78, 46.

Veron-Cetty, M. P. and Veron, P. 1989. *A Catalogue of Quasar and Active Galactic Nuclei, 5th edition.* ESO scientific Report Nr. 10.

Veron-Cetty, M. P. and Woltjer, L. 1990, A&A, 236, 69.

Voit, G. M. 1991, ApJ, 379, 122.

Wampler, E. J. 1971, ApJ, 164, 1.

Ward, M., Allen, T. A., Wilson, A. S., Smith, M. G., and Wright, A. E. 1982, MNRAS, 199, 953.

Ward, M., Elvis, M., Fabbiano, G., Carleton, N. P., Willner, S. P., and Lawrence, A. 1987, ApJ, 315, 74.

Whittle, M. 1992, ApJS, 79, 49.

Wilkes, B. J. and Elvis, M. 1987, ApJ, 323, 243.

Wilson, A. S., Helfer, T. T., Haniff, C. A., and Ward, M. J. 1991, ApJ, 381, 79.

Wilson, A. S. and Meurs, E. J. A. 1982, ApJS, 50, 217.

Worral, D. M., Puschell, J. J., Bruhweiler, F. C., Miller, H. R., Aller, M. F., and Aller, H. D. 1984, PASP, 96, 699.

Xu, C. and De Zotti, G. 1989, A&A, 225, 12.

Yee, H. K. C. 1983, ApJ, 272, 473.

Zitelli, V., Granato, G. L., Mandolesi, N., Wade, R., and Danese, L. 1993, ApJS, 84, 185.